

# **DEVELOPMENT OF NANOCONTAINER IMPREGNATED COATINGS FOR ACTIVE CORROSION PROTECTION**

*By*

**C. ARUNCHANDRAN**

**Enrolment No.: CHEM02200904002**

**Indira Gandhi Centre for Atomic Research, Kalpakkam**

*A thesis submitted to the  
Board of Studies in Chemical Sciences*

*In partial fulfillment of requirements  
For the Degree of*

**DOCTOR OF PHILOSOPHY**

*of*

**HOMI BHABHA NATIONAL INSTITUTE**



**November, 2014**

# Homi Bhabha National Institute

## Recommendations of the Viva Voce Committee

As members of the Viva Voce Committee, we certify that we have read the dissertation prepared by C. Arumchandran entitled "Development of Nanocontainer Impregnated Coatings for Active Corrosion Protection" and recommend that it may be accepted as fulfilling the dissertation requirement for the Degree of Doctor of Philosophy.

 Date: 29.06.15  
Chairman – Dr. C. Mallika

 Date: 29/6/15  
Guide / Convener – Dr. U. Kamachi Mudali

 Date: 29/6/15  
Examiner – Dr. M. A. Quraishi

 Date: 29.06.2015  
Member 1 – Dr. S. Rangarajan


 Date: 29/06/2015  
Member 2 – Dr. K.I. Gnanasekar

 Date: 29.06.2015  
Technology Advisor – Dr. S. Ramya

Final approval and acceptance of this dissertation is contingent upon the candidate's submission of the final copies of the dissertation to HBNI.

I hereby certify that I have read this dissertation prepared under my direction and recommend that it may be accepted as fulfilling the dissertation requirement.

Date: 29/6/15  
Place: Kalpakkam

  
Dr. U. Kamachi Mudali  
Guide

## STATEMENT BY AUTHOR

This dissertation has been submitted in partial fulfillment of requirements for an advanced degree at Homi Bhabha National Institute (HBNI) and is deposited in the Library to be made available to borrowers under rules of the HBNI.

Brief quotations from this dissertation are allowable without special permission, provided that accurate acknowledgement of source is made. Requests for permission for extended quotation from or reproduction of this manuscript in whole or in part may be granted by the Competent Authority of HBNI when in his or her judgment the proposed use of the material is in the interests of scholarship. In all other instances, however, permission must be obtained from the author.



**(C. ARUNCHANDRAN)**

# DECLARATION

I, hereby declare that the investigation presented in this thesis has been carried out by me. The work is original and has not been submitted earlier as a whole or in part for a degree /diploma at this or any other Institution/ University.

A handwritten signature in blue ink, appearing to read 'Arunchandran', with a long horizontal stroke extending to the right.

**(C. ARUNCHANDRAN)**

## List of publication arising from the thesis

### Journal:

- 1) “Self-Healing Corrosion Resistive Coatings Based on Inhibitor Loaded TiO<sub>2</sub> Nanocontainers”, C. Arunchandran, S. Ramya, R.P. George, U. Kamachi Mudali, *Journal of the Electrochemical Society*, **2012**, 159, C552-C559.
- 2) “Corrosion inhibitor storage and release properties of TiO<sub>2</sub> nanotube powder synthesized by rapid breakdown anodization method”, C. Arunchandran, S. Ramya, R.P. George, U. Kamachi Mudali, *Materials Research Bulletin*, **2013**, 48, 635-639.
- 3) “2-Mercaptobenzothiazole loaded hollow mesoporous silica based hybrid coatings for corrosion protection of modified 9Cr-1Mo ferritic steels”, C. Arunchandran, S. Ramya, R.P. George, U. Kamachi Mudali, *Corrosion*, **2014**, 70, 496-511.
- 4) “Hollow mesoporous zirconia nanocontainers for storing and controlled releasing of corrosion inhibitors”, C. Arunchandran, S. Ramya, R.P. George, U. Kamachi Mudali, *Ceramic International*, **2014**, 40, 10457-10463.
- 5) “Zirconia Nanocontainer Based Active Anticorrosion Coatings for 9Cr-1Mo Ferritic Steel”, C. Arunchandran, S. Ramya, R.P. George, U. Kamachi Mudali, communicated to *Surface Engineering* (Under Review)
- 6) “Nanocontainer Impregnated Hybrid Epoxy Coatings for Active Corrosion Protection of 9Cr-1Mo steel”, C. Arunchandran, R.P. George, U. Kamachi Mudali, communicated to *Corrosion* (Under Review)
- 7) “A Review on Inhibitor Loaded Nanocontainers Impregnated Coatings for Active Corrosion Protection”, C. Arunchandran, U. Kamachi Mudali, to be communicated to *Corrosion Reviews*

### Chapters in books and reports:

- 1) “Enhanced localized corrosion resistance of modified 9Cr-1Mo steel by hollow mesoporous silica based self healing coatings”, C. Arunchandran, S. Ramya, R.P. George, U. Kamachi Mudali, “*Strategies for Corrosion Prevention*” NIGIS South Zone Student Section Kalpakkam-Chennai, India, **2013**, 121-128.
- 2) “Inhibitor loaded nanocontainer based hybrid coatings for corrosion protection of modified 9Cr-1Mo ferritic steel”, C. Arunchandran, S. Ramya, R. P. George, U. Kamachi Mudali, , IGC Annual Report, **2013**, Article No: V.23, pp.154.

### Conferences:

- 1) C. Arunchandran, S. Ramya, Rajini. P. Antony, R.V. Subba Rao, R.K. Dayal, “*Surface Enhanced Raman Scattering of Sudan I from Ag doped TiO<sub>2</sub> nanoparticles*”, *International Symposium on Advances in Nanomaterials* (ANM-2010), CGCRI, Kolkata-700 032, December 6-7, 2010.
- 2) C. Arunchandran, S. Ramya, R.P. George, U. Kamachi Mudali, “*Self-Healing Corrosion Resistive Coatings Based on Inhibitor Loaded TiO<sub>2</sub> Nanocontainers*”, Oral presentation at *International Conference on Advanced Materials (ICAM 2011)*, PSG College of Technology, Coimbatore, India, December 12-16, 2011.
- 3) C. Arunchandran, S. Ramya, R.P. George, U. Kamachi Mudali, “*Nanocontainer impregnated Self-healing Surface Modification for Corrosion Protection*”, Poster presentation at poster presentation at *Workshop on Electrochemical Techniques for Nano-Scale Surface Engineering*, January 5-6, 2012, Anushaktinagar, BARC Mumbai - 400095.
- 4) C. Arunchandran, S. Ramya, R.P. George, U. Kamachi Mudali, “*Self-healing Surface Modification for Corrosion Protection*” Poster presentation at *NACE 5<sup>th</sup>*

- training program on Paints and Coating on 13<sup>th</sup>-15<sup>th</sup> July, 2012 at Hotel Jayapuspam, Chennai.*
- 5) C.Arunchandran, S. Ramya, R. P. George, U. Kamachi Mudali, “*Enhanced localized corrosion resistance of modified 9Cr-1Mo steel by hollow mesoporous silica based self healing coatings*”, paper presented at *International Corrosion Prevention Symposium for Research Scholars, CORSYM-2013* on February 28-March 02, 2013 at Chennai.
  - 6) C.Arunchandran, S. Ramya, R. P. George, U. Kamachi Mudali, “*Application of Hollow Mesoporous Silica Spheres as pH-responsive Nanocontainers for Controlled Release of Corrosion Inhibitor and Protection of Mod.9Cr-1Mo from Corrosion*” Poster presentation at *Theme Meeting on Recent Trends in Materials Chemistry*, July, 2013 at Vellore Institute of Technology, Vellore.
  - 7) C.Arunchandran, S. Ramya, R. P. George, U. Kamachi Mudali, “*Inhibitor Loaded Hollow Mesoporous Zirconia Nanocontainers Based Hybrid Coatings for Corrosion Protection of Modified 9Cr-1Mo Ferritic Steel*”, Oral presentation at *CORCORN-2013*, 30<sup>th</sup> September to 3<sup>rd</sup> October, 2013 at New Delhi.
  - 8) C.Arunchandran, S. Ramya, R. P. George, U. Kamachi Mudali, “*Hollow Mesoporous Zirconia Nanospheres for Active Corrosion Protection*”, Oral presentation at *NACE International EAP Area Conference & Expo-2013*, 19<sup>th</sup> November to 21<sup>st</sup> November, 2013 at Kyoto, Japan.
  - 9) C.Arunchandran, S. Ramya, R. P. George, U. Kamachi Mudali, “*Zirconia Nanocontainers for Active Corrosion Protection*”, Poster presentation at *NIGIS South Zone Student Poster Session during Short Term Training Course on Corrosion and its Control*, January 30-31, 2014 at SRM University.

### **Awards and Recognitions:**

- 1) **Best Young Researcher Paper Award** from the Indian Institute of Metal, Kalpakkam Chapter for the research paper “*Self-healing corrosion resistive coatings based on inhibitor loaded TiO<sub>2</sub> nanocontainers*”, Journal of the Electrochemical Society, 159 (11) C552-C559 (2012).
- 2) **Best Oral Presentation Award** – “*Enhanced localized corrosion resistance of modified 9Cr-1Mo steel by hollow mesoporous silica based self healing coatings*”, paper presented at international Corrosion Prevention Symposium for Research Scholars, CORSYM-2013 on February 28-March 02, 2013 at Chennai, India.
- 3) **Best Poster Presentation Award** - “*Nanocontainer impregnated Self-healing Surface Modification for Corrosion Protection*”, Poster presentation at poster presentation at Workshop on Electrochemical Techniques for Nano-Scale Surface Engineering, January 5-6, 2012, Anushaktinagar, BARC Mumbai-400095, India.
- 4) **Best Poster Presentation Award** - “*Self-healing Surface Modification for Corrosion Protection*” Poster presentation at NACE 5<sup>th</sup> training program on Paints and Coating on 13<sup>th</sup>-15<sup>th</sup> July, 2012 at Hotel Jayapuspam, Chennai.
- 5) **Best Poster Presentation Award:** “*Zirconia Nanocontainers for Active Corrosion Protection*”, Poster presentation at NIGIS South Zone Student Poster Session during Short Term Training Course on Corrosion and its Control on January 30-31, 2014 at SRM University.



**(C. ARUNCHANDRAN)**



## ACKNOWLEDGEMENTS

The work described in this thesis was carried out at Corrosion Science and Technology Group of Indira Gandhi Centre for Atomic Research (IGCAR), Kalpakkam.

Primarily, I express my sincerest gratitude to my research supervisor, Prof. Dr. U. Kamachi Mudali, who introduced me into the world of “Corrosion”. I am very much grateful to him for his understanding and support which helped me to do things at the best of my abilities. Only due to his constant patience, continuous guidance, and supervising, I could complete my research work and accomplish this thesis. Thanks are due to him for providing excellent research facility at CSTG, which enables me to complete my thesis work successfully.

I wish to thank my Doctoral Committee Chairperson, Dr. C. Mallika, and Committee members Dr. S. Rangarajan, Dr. K.I. Gnanasekar, for their meticulous evaluation of my research work and valuable suggestions during the course of my work. I would like to acknowledge the financial support by Department of Atomic Energy (DAE) for my Ph.D. during my stay at IGCAR, Kalpakkam. I thank Dr. P.R. Vasudeva Rao, Director, IGCAR, and Dr. T. Jayakumar, Director, MMG, for their support. I would like to thank Dr. M. Saibaba, AD, RMG, for taking care of administrative issues and providing excellent accommodation during my stay at Kalpakkam. I thank all the teachers of HBNI-IGCAR campus who taught me various subjects during my course work.

My warmest gratitude goes to Dr. Rani P. George for her timely assists and support in various aspects constantly with care and affection. She could spend her time to go through this dissertation and all my manuscripts with lot of patience. I would like to thank Dr. S. Ramya, Technology Advisor, for introducing me to Raman spectroscopy and teaching me to handle the instrument and allow me to do experiments independently. Thanks are due to her for those scientific discussions we had during the course of this thesis work. I am greatly thankful to Vinod Kumar, my friend and colleague at CSTG for making my life pleasurable and easy during the toughest time of my Ph.D life at IGCAR. Big thanks to Dr. M.G. Pujar for his endless kind suggestions and numerous informative discussions we had during teatime.

I am thankful to Dr. Kamaraj for teaching me the basics of epoxy coatings and helping me to paint epoxy-based coatings. I am extremely thankful to Mr. Sinu Chandran for his help in teaching and interpreting impedance spectroscopy. I would like to thank Dr. P. Chandramohan, WSCD, BARCF for BET analysis, Dr. Anuradha M. Ashok, PSG

Institute of Advanced Studies for HRTEM examinations, and Dr.S. Kalavathi, MSG, IGCAR for low angle XRD measurements.

A very special mention to my friends at CSTG, Dr. Jagadeesh Sure, Dr. Pradeep Kumar Samantaroy, Mrs. Rasmi, Mrs. Ezhil Vizhi, Dr. Indira and Dr. Lipika for their help, support and care during my Ph.D. work. Also, my acknowledgements are due to all staffs of CSTG which includes: Dr. N. Parvathavarthini, Dr. S. Ningshen, Mrs. Girija Suresh, Dr. J. Jayaraj, Dr. Ch. Jagadeswara Rao Dr. S.C. Vanithakumari, Dr. P. Priya, Dr. A. Ravishankar, Mr. Nanda Gopala Krishna, Mrs. Narmata Upadhyay, Mrs. Anita Toppo, Mrs. N. Shivai Bharasi, Dr. Anandkumar, Mrs. Sundari, Mr. Selvam, Mr. Thinakaran, Mrs. A. Poonguzhali, Mr. Srinivas, Mrs. Archana, Mr. Ravi Kumar Sole, Mr. Yogesh Kumar, Mr. Avinash, Mr. R. Rajendran, Mr. P.U. Jalendiran, Mr. T. Nandakumar and Mr. T.V. Balaji.

I thank my batch mates Mr. Shashwath, Mr. Ravi Kirana, and Mr. Srinivasan for their help, support and enjoyable company. Special thanks go to Priyadarsini who joined IGCAR along with me and helped me a lot in the initial and final stages of my doctoral study. Next, I would like to thank my friends at Kalpakkam: Special mention to Biju Joseph and Dr. Sandeepan for making my stay at JRF enclave a memorable period in my life. Those unforgettable footballing nights would not come back again! A special thank you to Sreejith and Mabin for giving me some special memories and good laughs over the last few years. Thanks to Jayarajettan, Rakesh, Anuraj, Arun, Jovin, Jobby, Bijoy, Shyam, Dijo, Suresh, Sandeep, Vijith, Dr. Feby Jose, Bineesh, Arun Aravind, Krishnachandran, Haneef, Anees, Shiva Srinivas, Anoop, Sujith, Meera, Sabeena, Dr. Rajini P. Antony, Dr. Shima, Sharath, and Dr. Ilaiyaraja for their affection and support. I would like to extend a special “thank you” to my brother, Unni and sisters Varada and Soumyedathi and uncle Sasi Kumar for their love and support. I would like to thank my wonderful wife, Priyada, who was always with me during my toughest times of my career lending great support. I would like to extend special thanks to my mother-in-law, Sobhana and father-in-law Vijayan for their love, care, and encouragement over the last few years. Finally, I want to thank my Amma and Achan, for their continuous love, support, care, and encouragement. My parents’ enormous support and sacrifices have brought me to this position.

Just in case, if I miss anyone, this may apply: Thank you to whomsoever it may concern!

# CONTENTS

S. No.	Title	Page No.
<b>I</b>	<b>Synopsis</b>	<b>XVI</b>
<b>II</b>	<b>List of figures</b>	<b>XXVI</b>
<b>III</b>	<b>List of tables</b>	<b>XXXIII</b>
<b>IV</b>	<b>List of Abbreviations</b>	<b>XXXIV</b>

## CHAPTER 1

<b>1</b>	<b>Introduction to Corrosion and its Prevention</b>	<b>1</b>
1.1	Corrosion and its Manifestation	1
1.2	Consequences of Corrosion	4
1.3	Atmospheric Corrosion Behaviour of Iron and Low Alloy Steels	5
1.4	Influence of Cr and Mo on Atmospheric Corrosion of Steels	11
1.5	Corrosion Prevention Methods	13
1.5.1	Materials Selection	13
1.5.2	Design	14
1.5.3	Cathodic and Anodic Protection	15
1.5.4	Inhibitors	16
1.5.5	Coatings	18
1.5.5.1	Metallic Coatings	19
1.5.5.2	Inorganic Coatings	21
1.5.5.3	Organic Coatings	23
1.6	The Organic Coating System	24
1.7	Recent Advances in Protective Coatings	26
1.8	Summary	29

## CHAPTER 2

<b>2</b>	<b>A Review on Protective Sol-Gel Coatings and Active Corrosion Protection Methods Based on Self-Healing Ability</b>	<b>30</b>
2.1	Fundamentals of Sol-Gel Coatings	30
2.1.1	Synthesis of Sol-Gel Coatings	31
2.1.2	Deposition and Curing of Sol-Gel Coatings	36
2.2	Types of Protective Sol-Gel Coatings	37

2.2.1	Inorganic Corrosion Protective Sol-Gel Coatings	37
2.2.2	Inorganic-Organic Hybrid Sol-Gel Coatings	38
2.2.3	Additives Doped Hybrid Sol-Gel Coatings	41
2.3	Smart Coatings for Active Corrosion Protection	42
2.4	Active Corrosion Protection Based on Nanocontainers	45
2.5	Motivation for the Present Study	55
2.6	Objective of the Present Study	56

### **CHAPTER 3**

<b>3</b>	<b>Experimental: Materials and Methods</b>	<b>57</b>
3.1	Materials and Chemicals	57
3.2	Equipments	59
3.3	Substrate for Coatings	60
3.3.1	Pre-treatment of Substrate	60
3.4	Synthesis of Nanocontainers	60
3.4.1	Synthesis of TiO <sub>2</sub> Nanocontainers	60
3.4.2	Synthesis of Hollow Mesoporous Silica (HMS) Nanocontainers	61
3.4.3	Synthesis of Hollow Mesoporous Zirconia (HMZ) Nanocontainers	62
3.5	Inhibitor Loading and Releasing	63
3.5.1	Loading of Inhibitors	64
3.5.2	Releasing of Inhibitors	65
3.6	Preparation of Hybrid Barrier Coatings	66
3.6.1	Silane-Titania Hybrid Barrier Coatings	66
3.6.2	Silane-Zirconia Hybrid Barrier Coatings	67
3.7	Deposition of Hybrid Barrier Coatings	68
3.8	Preparation of Epoxy Based Coatings for Long Term Corrosion Test	68
3.9	Characterization Methods	70
3.9.1	Scanning Electron Microscopy	70
3.9.2	Transmission Electron Microscopy	70
3.9.3	Laser Raman Spectroscopy	70

3.9.4	Nitrogen Adsorption/Desorption	71
3.9.5	Low Angle X-ray Scattering	71
3.9.6	UV-Visible Spectroscopy	71
3.9.7	Surface Profiler	72
3.9.8	Cross-Hatch Tape Adhesion Test	72
3.9.9	Salt Spray Test	72
3.9.10	Electrochemical Impedance Spectroscopy	73

## **CHAPTER 4**

<b>4</b>	<b>Hollow Mesoporous Zirconia Nanocontainers for Active Corrosion Protection</b>	<b>82</b>
4.1	Introduction	82
4.2	Experimental	84
4.2.1	Materials	84
4.2.2	Synthesis of HMZ Nanocontainers	84
4.2.3	Characterization of Silica Nanoparticles and HMZ Nanocontainers	85
4.2.4	Loading and Releasing of 2-MBT	85
4.2.5	Development of Coatings on Modified 9Cr-1Mo Ferritic Steels	86
4.2.6	Evaluation of Anticorrosion Efficiency of Coatings	86
4.3	Results and Discussion	87
4.3.1	Synthesis and Characterization of HMZ Nanocontainers	87
4.3.2	Inhibitor Loading and Releasing Properties of HMZ Nanocontainers	91
4.3.3	Anticorrosion Efficiency of Various Hybrid Coatings on Modified 9Cr-1Mo Ferritic Steels	96
4.4	Summary	109

## CHAPTER 5

<b>5</b>	<b>Hollow Mesoporous Silica Nanocontainers for Active Corrosion Protection</b>	<b>111</b>
5.1	Introduction	111
5.2	Experimental	114
5.2.1	Materials	114
5.2.2	Synthesis and Characterization of HMS Nanocontainers	114
5.2.3	Loading and Releasing of 2-MBT	114
5.2.4	Development of Coatings on Modified 9Cr-1Mo Ferritic Steels	115
5.2.5	Evaluation of Anticorrosion Efficiency of Coatings	116
5.3	Results and discussion	116
5.3.1	Synthesis and Characterization of HMS Nanocontainers	116
5.3.2	Inhibitor Loading and Releasing Properties of HMS Nanocontainers	121
5.3.3	Surface Characterization of the Sol-Gel Coatings	126
5.3.4	Protective Performance of Various Hybrid Coatings on Modified 9Cr-1Mo Ferritic Steels	127
5.4	Summary	142

## CHAPTER 6

<b>6</b>	<b>TiO<sub>2</sub> Nanocontainers for Active Corrosion Protection</b>	<b>143</b>
6.1	Introduction	143
6.2	Experimental	145
6.2.1	Materials	145
6.2.2	Synthesis and Characterization of TiO <sub>2</sub> Nanocontainers	145
6.2.3	Loading and Releasing of Inhibitors	146
6.2.4	Synthesis and Deposition of Sol-Gel Hybrid Coatings	146
6.2.5	Evaluation of Anticorrosion Efficiency of Coatings	147
6.3	Results and Discussion	147
6.3.1	Synthesis of TiO <sub>2</sub> Nanocontainers	147
6.3.2	Characterization of TiO <sub>2</sub> Nanocontainers	150
6.3.3	Inhibitor Loading and Releasing	152

6.3.4	Protective Performance of Various Hybrid Coatings on Modified 9Cr-1Mo Ferritic Steels	159
6.3.4.1	EIS Studies of SiO <sub>x</sub> -TiO <sub>x</sub> Hybrid Coating System	160
6.3.4.2	EIS Studies of SiO <sub>x</sub> -ZrO <sub>x</sub> Hybrid Coating System	168
6.4	Summary	182
<b>CHAPTER 7</b>		
<b>7</b>	<b>Comparison of Corrosion Protective Performance of Silica, Zirconia, and Titania Nanocontainers and Long Term Corrosion Protection Studies</b>	<b>183</b>
7.1	Introduction	183
7.2	Experimental	184
7.2.1	Materials and Methods	184
7.3	Results and Discussions	185
7.3.1	Comparison of Corrosion Protective Performance of Zirconia, Silica and Titania Nanocontainers	185
7.3.2	Cross-Hatch Tape Adhesion Test	188
7.3.3	Salt Spray Test for Nanocontainer Based Epoxy Coatings	189
7.3.4	Analysis of the Undercoat Corrosion	191
7.3.5	Raman Analysis of Salt Spray Exposed Coated Specimens	192
7.4	Summary	195
<b>CHAPTER 8</b>		
<b>8</b>	<b>Conclusions, Summary and Scope for Future Studies</b>	<b>196</b>
8.1	Conclusions and Summary	196
8.2	Scope for Future Study	200
	References	201

## SYNOPSIS

Corrosion of materials and structures is a hindrance to the development of society as it causes significant loss to the economy and hence its prevention and control is of great benefit for the humanity. Corrosion prevention by protective coatings has a greater role to play in curbing this menace for all metals and alloys used in industries. Application of organic/polymeric coating system is one of the widely used strategies to combat corrosion of metals and alloys under service conditions [1, 2]. A typical protective coating system includes a pre-treatment layer or conversion layer, a primer and a topcoat [3]. These pre-treatment or conversion layers are generally applied to improve the corrosion protection efficiency and impart good adhesion of organic coatings applied subsequently [4]. Chromate and phosphate conversion coatings are widely used strategies to obtain a pre-treatment layer to improve the adhesion of subsequent organic coatings for both ferrous and non ferrous alloys. But the extreme oxidation property of Cr (VI) causes several health problems to humans and it is carcinogenic in nature [5, 6]. The main disadvantage of inorganic corrosion inhibitors such as chromates, phosphates is their toxicity. The common usage of chromate is banned in several countries considering health and safety reasons and the protection of the environment. Similarly, the corrosion protection performance of zinc phosphate coating is not good enough for outdoor exposure. Hence, there is a strong necessity for developing an environmentally- friendly surface pre-treatment for all coatings.

One of the most promising alternatives to the above mentioned toxic surface treatment for corrosion protection is sol-gel coatings. A sol-gel based dip coating is a very simple method consisting of the withdrawal of a substrate from a fluid sol and the resulting deposition of a thin solid film due to gravitational draining, solvent evaporation and further condensation reactions [7]. The sol-gel process is a chemical synthesis method



based on hydrolysis and condensation reactions of metal alkoxides ( $M(OR)_n$ ). Sol-gel derived coatings possess lot of advantages such as high corrosion resistance, nontoxic and environmentally compatible, and good adhesion to both metallic substrate and organic topcoat [5, 8]. One of the fascinating features of sol-gel based coating is its functionalization and tailoring of the properties of the deposited sol-gel film.

The sol-gel process can be used to prepare either organic or inorganic based protective coatings. Moreover, the low reaction temperature required for sol-gel process provides ease of introduction of organic groups in the inorganic material leading to the fabrication of a new class of hybrid coatings consists of both organic and inorganic components. The functions imparted by both organic and inorganic components in hybrid coatings are different. The inorganic parts confer enhanced mechanical properties, scratch resistance, durability and adhesion to metallic substrate. On the other hand, the organic part contributes to the increase of density, flexibility and functional compatibility with polymeric paint systems applied as topcoats. Moreover, organically modified coatings are thick and pore free dense coatings [5, 8].

The corrosion resistance of sol-gel derived film is mainly due to its barrier property, which obstructs the entry of corrosive species and water through the coatings and protects the underlying metal surface. Corrosion protection provided by a barrier film, which avoids any interaction of metallic substrate with external environment, is known as passive protection [10, 11]. However, sol-gel coatings are not completely free from cracks and other defects (such as fissures and pores) and this leads to the penetration of electrolyte and water into metal surface for initiating corrosion reactions. Hence it is ideal to introduce active agents or corrosion inhibitors into the barrier coatings to enhance its anticorrosion property. Corrosion protection provided by active agents or corrosion inhibitors is known as active corrosion protection. In active corrosion

protection methods, corrosion inhibitors are incorporated into the protective barrier layers which become active and decrease the corrosion rate when the passive barrier layer starts deteriorating [9-11]. The corrosion inhibitor can be introduced into the coatings in two ways: (i) adding the inhibitors directly into the coating, (ii) loading or encapsulating the inhibitors in suitable containers or reservoirs and then incorporating them into the coating. It was proved that the direct addition of inhibitor had a negative effect on the stability of the sol-gel coating and thereby deteriorates the physical barrier functionality of the coating [9]. Hence the second approach, loading or encapsulating the inhibitors in containers prior to mixing with coating is widely adopted in recent times.

Recent developments in nanotechnology and surface engineering pave avenues for fabricating novel class of coatings which can impart both barrier protection and active functionalities. Nano or microcontainers with sustained release properties can be used in a new class of self-healing coatings [12-15]. When the environment around the coatings changes, nanocontainers senses the same and would release quickly the inhibitor for delaying corrosion activity. Several investigations with this novel approaches have been reported recently in the literature [16-19]. There are many advantages in adopting this novel strategy for corrosion protection as this avoids the direct contact between the inhibitor molecules and barrier coatings and hence reduces the negative effect of the inhibitors. It helps in releasing the inhibitors at the corroding site in required quantity for preventing uncontrolled progress of corrosion activity into the substrates.

The present work is focused on the development of effective anticorrosion coatings for modified 9Cr-1Mo ferritic steels using active corrosion protection. Modified 9Cr-1Mo ferritic steel is a structural and tubing material for various chemical and power plants

industries due to its low thermal expansion, high resistance to chloride stress corrosion cracking in water-steam systems, acceptable mechanical properties at service temperatures and easy control of microstructures by simple heat treatments. However, during fabrication, storage and commissioning stages this class of steel is prone to undergo corrosion in chloride containing humid environments. The objective of the present study is to develop an active corrosion protection system for modified 9Cr-1Mo steels based on self-healing ability of inhibitor loaded ceramic nanocontainers containing novel nanocontainers which can protect the steel from corrosion by releasing the inhibitors on demand. The coatings were prepared on steel substrates by dispersing ceramic nanocontainers ( $\text{TiO}_2$ ,  $\text{SiO}_2$ , and  $\text{ZrO}_2$ ) loaded with non toxic corrosion inhibitors (Benzotriazole and 2-Mercaptobenzothiazole) in zirconia-silane sol. Both the active corrosion protection and barrier property of the coatings were investigated using electrochemical impedance spectroscopy (EIS). Long term stability of the coatings and their self healing ability were also investigated using salt spray test. The thesis consists of eight chapters and the summary of each chapter is given below.

## **Chapter 1**

A brief introduction of corrosion, its manifestations, consequences and methods generally used to prevent corrosion are discussed in this chapter. This chapter introduces the definition of corrosion and its classifications in different ways. Both the direct and indirect consequences of corrosion are discussed. The various methods to control corrosion such as material selection, design, cathodic and anodic protection, inhibitors, and coating are described in this chapter. Corrosion of iron and low alloy steels particularly in coastal and humid atmosphere is described with details of mechanism of uniform and localized corrosion. The necessity to protect them by surface treatment and coatings, and the role of inhibitors and coatings for this purpose

is addressed. The main focus in this chapter is to highlight the necessity to develop surface treatments and coatings for corrosion protection of structural components.

## **Chapter 2**

This chapter gives a general overview about the hybrid sol-gel coatings containing inhibitors for active corrosion protection methods based on self-healing ability. An up to date literature review on various nanocontainers, their synthesis and application in active corrosion protection is covered. The concept of self-healing and how it can be used for corrosion protection of materials is included. A brief history of different self-healing coatings developed so far is also described in this chapter.

## **Chapter 3**

This chapter describes various materials and experimental methods used for the present work. The entire investigation is carried towards the development of nanocontainer mixed hybrid coatings which can impart active corrosion protection based on self-healing ability. The details of 9Cr-1Mo steel for coating and the pretreatments applied on this steel are discussed. The details of synthesis of ceramic nanocontainers ( $\text{TiO}_2$ ,  $\text{SiO}_2$ , and  $\text{ZrO}_2$ ) are described. The various experimental techniques employed to characterize the nanocontainers and the method for loading of inhibitor molecules into the nanocontainers and its sustained release are described. The preparation and application of nanocontainer mixed hybrid coatings and the top epoxy based coatings are included. This chapter also describes electrochemical, microscopy techniques and salt spray test used to evaluate and analyze the short term and long term corrosion protective performance of coatings.

## **Chapter 4**

This chapter describes the fabrication of an active corrosion protection coating system with self-healing ability using hollow mesoporous zirconia nanocontainers. Zirconia

nanocontainers with a hollow core/shell structure were synthesized through a hard templating approach and used as nanocontainers for loading 2-mercatobenzothiazole (2-MBT). A hybrid zirconia-silane sol-gel coating mixed with 2-MBT loaded hollow mesoporous zirconia nanocontainers was deposited on modified 9Cr-1Mo. The corrosion protection performance of coatings with and without the addition of inhibitor loaded nanocontainers was investigated using electrochemical impedance spectroscopy (EIS) technique. Further, artificial defects were made to the coatings in order to analyze the evolution of corrosion activity and to prove active corrosion protection. It was found that the released inhibitor delayed the corrosion process and imparted active corrosion protection.

## **Chapter 5**

Chapter 5 discusses the development of an active corrosion protection system consisting of silane-zirconia hybrid sol-gel coating impregnated with inhibitor loaded hollow mesoporous silica nanocontainers. Hollow mesoporous silica spheres were synthesized through sol-hydrothermal method and used as nanocontainers to load corrosion inhibitor molecule, 2-mercaptobenzothiazole. A silane-zirconia based hybrid coating containing hollow mesoporous silica nanocontainers were applied on modified 9Cr-1Mo ferritic steels. The loading and releasing properties of hollow mesoporous silica nanocontainers were studied using UV-visible spectroscopy. The corrosion resistance and active corrosion protection efficiency of hybrid silane-zirconia coatings with and without the addition of inhibitor loaded hollow mesoporous silica nanocontainers were studied using electrochemical impedance spectroscopy (EIS) and scanning electron microscopy (SEM) techniques. In order to prove the self-healing ability of the coatings, EIS experiments were carried out on coated specimens with artificial scratches. The anticorrosive property of the hybrid coating impregnated with

inhibitor loaded nanocontainers was found enhanced in comparison with that of the plain hybrid coating. This enhancement in corrosion resistance was due to the controlled and sustained release of 2-MBT from hollow mesoporous silica nanocontainers embedded in the hybrid coating.

## **Chapter 6**

This chapter describes a new approach to develop active corrosion protection coating system using TiO<sub>2</sub> nanotube powder. TiO<sub>2</sub> nanotube powder was synthesized by rapid breakdown anodization (RBA) method and loaded with corrosion inhibitors. Benzotriazole (BTA) and 2-mercaptobenzothiazole (2-MBT) were used as inhibitors for encapsulation. The successful loading and controlled release of the inhibitor molecules was investigated using UV-visible spectroscopy. The inhibitor loaded TiO<sub>2</sub> nanotube powder was randomly introduced into a hybrid barrier coating. This hybrid sol-gel barrier coating with random distribution of such inhibitors loaded TiO<sub>2</sub> nanotube powder was coated over modified 9 Cr-1 Mo steel. The corrosion resistance and the self healing effects of this hybrid passive barrier coating with and without the addition of inhibitor loaded TiO<sub>2</sub> nanocontainers were studied using electrochemical impedance spectroscopy (EIS). EIS analysis revealed that inhibitor loaded TiO<sub>2</sub> nanocontainer impregnated coatings showed enhanced corrosion protection due to the release of inhibitor molecules from the nanocontainers.

## **Chapter 7**

A comparison of the active corrosion protection rendered by different nanocontainers, hollow mesoporous silica, hollow mesoporous zirconia, and titania nanocontainers were carried out and presented in this chapter. Titania nanocontainers were found to have better corrosion protective performance considering both the active and barrier protective properties. Hence, this superior corrosion protection system was selected to

study the long term corrosion protection in accelerated corrosive environments. Later these titania nanocontainers were used to fabricate inhibitor loaded nanocontainer mixed hybrid coating with top epoxy coating. Along with the reference (plain top epoxy) coating, these samples were exposed to neutral salt spray test in a salt spray cabinet in order to investigate the long term corrosion protection and the self-healing efficiency of the nanocontainer mixed epoxy coating. The salt spray experiment was carried out according to the standard of ASTM B117. The salt spray chamber test showed sufficient protection even after 1000 h of exposure for inhibitor loaded nanocontainer mixed epoxy coating compared to that of reference (plain top epoxy) coating. Blistering and peeling off of the coating was observed for reference epoxy coating, while insignificant rust markings were observed for the developed coatings.

## **Chapter 8**

This chapter elucidates the important conclusions derived from the investigations carried out on synthesis of nanocontainers, its inhibitor loading and releasing properties and the active corrosion protection efficiency of coatings developed using inhibitor loaded nanocontainers. The self-healing ability of various coatings prepared using nanocontainers was assessed and compared. These results were consolidated and summarized in this chapter. Apart from this, suggestions are provided for further research to be carried out for improving the performance of coatings for enhanced longer active corrosion protection systems with self-healing ability.

## **References**

- [1] P.A. Sorensen, S. Kiil, K.Dam-Johansen, C.E. Weinell, Anticorrosive coatings: a review, *J. Coat. Technol. Res.* **6** (2009) 135-176.
- [2] D. Wang, G.P. Bierwagen, Sol-gel coatings on metals for corrosion protection, *Prog. Org. Coat.* **64** (2009) 327-338.

- [3] S.A.S. Dias, S.V. Lamaka, C.A. Nogueira, T.C. Diamantino, M.G.S. Ferreira, Sol-gel coatings modified with zeolites fillers for active corrosion protection of AA2024, *Corros. Sci.* **62** (2012) 153-162.
- [4] S.K. Ghosh, Functional coatings and microencapsulations: a general perspective in: Functional Coatings, 1<sup>st</sup> Ed., WILEY-VCH Verlag GmbH & Co. KGaA, Weinheim, 2006, 1-26.
- [5] M.L. Zheludkevich, I.M. Salvado, M.G.S. Ferreira, Sol-gel coatings for corrosion protection of metals, *J. Mater. Chem.* **15** (2005) 5099-5111.
- [6] G. Bierwagen, R. Brown, D. Battocchi, S. Hayes, Active metal based corrosion protection coating systems for aircraft requiring no-chromate pretreatment, *Prog. Org. Coat.* **67** (2010) 195-208.
- [7] C.J. Brinker, G.C. Frye, A.J. Hurd, C.S. Ashley, Fundamentals of sol-gel dip coating, *Thin Solid Films*, **201** (1991) 97-108.
- [8] D. Wang, G.P. Bierwagen, Sol-gel coatings on metals for corrosion protection, *Prog. Org. Coat.* **64** (2009) 327-338.
- [9] M.L. Zheludkevich, D.G. Shchukin, K.A. Yasakau, H. Mohwald, M.G.S. Ferreira, Anticorrosion Coatings with self-healing effect based on Nanocontainers impregnated with corrosion inhibitor, *Chem. Mater.* **19** (2007) 402-411.
- [10] E.W. Brooman, Modifying organic coatings to provide corrosion resistance: Part II- Inorganic additives and inhibitors, *Met. Finish.* **100** (2002) 42-53.
- [11] M.L. Zheludkevich, J. Tedim, M.G.S. Ferreira, Smart coatings for active corrosion protection based on multi-functional micro and nanocontainers, *Electrochim. Acta* **82** (2012) 314-323.



- [12] D.G. Shchukin, H. Mohwald, Self repairing coatings containing active nanoreservoirs, *Small* **3** (2007) 926-943.
- [13] C. Arunchandran, S. Ramya, R.P. George, U. Kamachi Mudali, Self-healing corrosion resistive coatings based on inhibitor loaded TiO<sub>2</sub> nanocontainers, *J. Electrochem. Soc.* **159** (2012) C552-C559.
- [14] D.G. Shchukin, G.B. Sukhorukov, H. Mohwald, Smart inorganic/organic nanocomposites hollow microcapsules, *Angew. Chem. Int. Ed.* **42** (2003) 4472-4475.
- [15] D. Borisova, H. Mohwald, D.G. Shchukin, Mesoporous silica nanoparticles for active corrosion protection, *ACS Nano* **5** (2011) 1939-1946.
- [16] A. Vimalandan, L.P. Lv, T.H. Tran, K. Landfester, D. Crepsy, M. Rohwerder, Redox-responsive self-healing for corrosion, *Adv. Mater.* **25** (2013) 6980-6984.
- [17] L.P. Lv, Y. Zhao, N. Vibrandt, M. Gallei, A. Vimalandan, M. Rohwerder, K. Landfester, D. Crepsy, Redox responsive release of hydrophobic self healing agent from polyaniline capsules, *J. Am. Chem. Soc.* **135** (2013) 14198-14205.
- [18] M. Serdechnova, S. Kallip, M.G.S. Ferreira, M.L. Zheludkevich, Active self-healing coatings for galvanically coupled multi-material assemblies, *Electrochem. Commun.* **41** (2014) 51-54
- [19] G.L. Li, M. Schenderlein, Y. Men, H. Mohwald, D.G. Shchukin, Monodisperse polymeric core-shell nanocontainers for organic self-healing anticorrosion coatings, *Adv. Mater. Interfaces*, **1** (2014) 13006-13012.

# LIST OF FIGURES

Figure No.	Figure caption	Page No.
<b>Figure 1.1</b>	Schematics of the common forms of corrosion	2
<b>Figure 1.2</b>	Macroscopic and microscopic forms of localized corrosion	3
<b>Figure 1.3</b>	Electrochemical process of atmospheric rusting	6
<b>Figure 1.4</b>	The process of atmospheric rusting in low concentration of chloride content in atmosphere	11
<b>Figure 1.5</b>	A typical coating system for marine and industrial applications	24
<b>Figure 2.1</b>	Schematic for the sol-gel synthesis of silica materials	32
<b>Figure 2.2</b>	Mechanism of the base catalyzed hydrolysis of silicon alkoxide	34
<b>Figure 2.3</b>	Reaction pathway for acid catalyzed hydrolysis of silicon alkoxide	34
<b>Figure 2.4</b>	Reaction pathway for the sol-gel synthesis of metal alkoxide	35
<b>Figure 2.5</b>	Schematic of different classes of hybrid materials prepared by sol-gel process; (a) no chemical bond between organic and inorganic group; (b) polymerizable organic group is bonded to the inorganic group; (c) non-polymerizable organic groups are bonded to inorganic phase	39
<b>Figure 2.6</b>	Structure of some of the commonly used alkoxysilanes to introduce organic parts into hybrid sol-gel materials	40
<b>Figure 3.1</b>	Experimental setup for the synthesis of TiO <sub>2</sub> nanocontainers using rapid break down anodization method	61
<b>Figure 3.2</b>	Schematic of the synthesis procedure for HMZ nanocontainers	62
<b>Figure 3.3</b>	Schematic drawing of the inhibitor loading into TiO <sub>2</sub> nanocontainers	64
<b>Figure 3.4</b>	Schematic drawing of the inhibitor loading into mesoporous silica and zirconia containers	64
<b>Figure 3.5</b>	Design of the epoxy based coatings for long term corrosion test	69
<b>Figure 3.6</b>	Current versus potential curve showing pseudo-linearity	75
<b>Figure 3.7</b>	Nyquist plot with impedance vector	76
<b>Figure 3.8</b>	Vector representations of $ Z $ and $\emptyset$	76
<b>Figure 3.9</b>	Complex plane representations of $ Z $ and $\emptyset$	77

<b>Figure 3.10</b>	Bode plot for simple electrochemical system	77
<b>Figure 3.11</b>	Equivalent circuit of a coating on metallic substrate	79
<b>Figure 4.1</b>	HRTEM images of solid silica nanoparticles at different magnifications	88
<b>Figure 4.2</b>	HRTEM images of HMZ nanocontainers at different magnifications	88
<b>Figure 4.3</b>	Raman spectra of as prepared HMZ nanocontainers	89
<b>Figure 4.4</b>	N <sub>2</sub> adsorption-desorption isotherms of HMZ nanocontainers and pore size distribution (inset)	90
<b>Figure 4.5</b>	UV-visible spectra of 2-MBT before and after interaction with HMZ	91
<b>Figure 4.6</b>	Raman spectra of HMZ, 2-MBT and 2-MBT loaded HMZ	92
<b>Figure 4.7</b>	UV-vis spectra at different times of the 0.05 M NaCl media in which 2-MBT was released from 2-MBT loaded HMZ nanocontainers (a) at pH 3, (b) at pH 7, (c) at pH 10 and (d) corresponding pH-dependent releasing behaviour of 2-MBT from HMZ-MBT system	94
<b>Figure 4.8</b>	EIS behaviour of BS, CS, CS-I, CS-N, CS-NI after 1 h of immersion in 0.05 M NaCl solution	97
<b>Figure 4.9</b>	EIS behaviour of CS, CS-I, CS-N, and CS-NI after 1 day of immersion in 0.05 M NaCl	98
<b>Figure 4.10</b>	EIS behaviour of CS, CS-I, CS-N, and CS-NI after 1 week of immersion in 0.05 M NaCl solution	99
<b>Figure 4.11</b>	EIS response of CS-NI during 1 week of immersion in 0.05 M NaCl	100
<b>Figure 4.12</b>	Optical photographs of the coated samples after 1 week of immersion in 0.05 M NaCl solution. The drawn circles indicate the exposed area of the coatings	101
<b>Figure 4.13</b>	SEM images and its corresponding EDX spectrum of various coated substrates after 1 week of exposure to 0.05 M NaCl solution	102
<b>Figure 4.14</b>	EIS spectra of CS during immersion in 0.01 M NaCl solution after making an artificial defect	103
<b>Figure 4.15</b>	EIS spectra of CS-NI during immersion in 0.01 M NaCl solution after making an artificial defect	104

<b>Figure 4.16</b>	Equivalent circuits used to fit the experimental EIS data of scratched CS and CS-NI during 1 week of immersion in 0.01 M NaCl solution	105
<b>Figure 4.17</b>	Evolution of hybrid barrier coating resistance ( $R_{coat}$ ) during 1 week of immersion in 0.01 M NaCl solution	106
<b>Figure 4.18</b>	Evolution of polarization resistance of (a) CS-NI, (b) CS during 1 week of immersion in 0.01 M NaCl solution	107
<b>Figure 4.19</b>	Optical photographs of scratched CS-NI and CS after 1 week of immersion in 0.01 M NaCl solution. The drawn circles indicate the exposed area of the coatings	108
<b>Figure 4.20</b>	Self-healing mechanism of active corrosion protection	109
<b>Figure 5.1</b>	Schematic drawing for the formation of HMS nanocontainers	117
<b>Figure 5.2</b>	Low angle XRD pattern for HMS nanocontainers	118
<b>Figure 5.3</b>	HRETM images of HMS nanocontainers at different magnifications	119
<b>Figure 5.4</b>	FESEM images of HMS nanocontainers. Inset shows a magnified view	119
<b>Figure 5.5</b>	$N_2$ adsorption-desorption isotherm of HMS nanocontainers. Inset shows the BJH pore size distribution	120
<b>Figure 5.6</b>	UV-visible spectra of 2-MBT before and after interaction with HMS	121
<b>Figure 5.7</b>	Raman spectra of pure 2-MBT and 2-MBT loaded HMS nanocontainers	122
<b>Figure 5.8</b>	UV-vis spectra at different times of the 0.05 M NaCl media in which 2-MBT was released from 2-MBT loaded HMS nanocontainers (a) at pH 3, (b) at pH 7, (c) at pH 10 and (d) corresponding pH-dependent releasing behaviour of 2-MBT from HMS-MBT system	124
<b>Figure 5.9</b>	FESEM images of the coatings produced on modified 9Cr-1 Mo ferritic steel: (a) hybrid silane-zirconia coating, (b) nanocontainer doped hybrid silane-zirconia coating	126
<b>Figure 5.10</b>	EIS behaviour of BS, CS, CS-I, CS-N, and CS-NI after 1 h of immersion in 0.05 M NaCl solution	128
<b>Figure 5.11</b>	EIS response of CS, CS-I, CS-N, and CS-NI after 1 day of immersion in 0.05 M NaCl solution	129
<b>Figure 5.12</b>	EIS response of CS, CS-I, CS-N, and CS-NI after 1 week of immersion in 0.05 M NaCl solution	130

<b>Figure 5.13</b>	EIS response of CS-NI during 1 week of immersion in 0.05 M NaCl solution	131
<b>Figure 5.14</b>	Optical photographs of the coated samples after 1 week of immersion in 0.05 M NaCl solution. The drawn circles indicate the exposed area of the coatings	133
<b>Figure 5.15</b>	SEM images and its corresponding EDX spectra of various coated specimens after 1 week of immersion in 0.05 M NaCl solution	133
<b>Figure 5.16</b>	EIS behaviour of scratched CS for one week while immersed in 0.01 M NaCl solution	135
<b>Figure 5.17</b>	EIS behaviour of scratched CS-NI for one week while immersed in 0.01 M NaCl solution	136
<b>Figure 5.18</b>	Equivalent circuits used to fit the experimental EIS data of scratched CS and CS-NI during 1 week of immersion in 0.01 M NaCl solution	137
<b>Figure 5.19</b>	Evolution of coating resistance ( $R_{\text{coat}}$ ) of CS and CS-NI during 1 week of immersion in 0.01 M NaCl solution	138
<b>Figure 5.20</b>	Evolution of oxide layer resistance ( $R_{\text{oxide}}$ ) of CS and CS-NI during 1 week of immersion in 0.01 M NaCl solution	139
<b>Figure 5.21</b>	Optical images of artificially scratched CS-NI and CS after 1 week of immersion in 0.01 M NaCl solution	139
<b>Figure 5.22</b>	Proposed mechanism of the active corrosion protection based on self-healing ability	141
<b>Figure 6.1</b>	The current-time behaviour observed during the rapid breakdown anodization of $\text{TiO}_2$ nanotube powder at 20 V at room temperature in 0.1 M $\text{HClO}_4$	149
<b>Figure 6.2</b>	FESEM micrographs of $\text{TiO}_2$ nanocontainers	150
<b>Figure 6.3</b>	The HRTEM images of (a) as synthesized $\text{TiO}_2$ nanotube; (b) calcined $\text{TiO}_2$ nanotube powder at 400 °C; (c) & (d) magnified views	151
<b>Figure 6.4</b>	Raman spectra of (a) the as prepared $\text{TiO}_2$ nanotube powders and (b) Raman spectra of $\text{TiO}_2$ nanotube powders calcined at 400 °C.	152
<b>Figure 6.5</b>	The UV absorbance spectra of ethanolic solution of benzotriazole before and after the interaction with $\text{TiO}_2$ nanocontainers	153
<b>Figure 6.6</b>	The release percentages of benzotriazole from $\text{TiO}_2$ nanocontainers at different pH values. Inset shows the UV-visible absorbance spectra of	154

benzotriazole in the release medium

<b>Figure 6.7</b>	UV absorbance spectra of 2-MBT before and after the interaction with TiO <sub>2</sub> nanocontainers	155
<b>Figure 6.8</b>	UV-vis spectra at different times of the 0.05 M NaCl media in which 2-MBT was released from 2-MBT loaded TiO <sub>2</sub> nanocontainers (a) at pH 3, (b) at pH 7, (c) at pH 10 and (d) corresponding pH-dependent releasing behaviour of 2-MBT from TiO <sub>2</sub> -MBT system	156
<b>Figure 6.9</b>	Raman spectra of (a) TiO <sub>2</sub> , (b) pure 2-MBT, (c) 2-MBT loaded TiO <sub>2</sub> nanocontainer. Inset shows the enlarged view of the Raman features of 2-MBT in 2-MBT@TiO <sub>2</sub> system	158
<b>Figure 6.10</b>	The Bode plots for BS, CS, CS-I, CS-N, CS-NI after 1 h immersion in 0.05M NaCl	160
<b>Figure 6.11</b>	The Bode plots for CS, CS-I, CS-N, CS-NI after 24 h immersion in 0.05M NaCl	161
<b>Figure 6.12</b>	The equivalent circuit (a) for bare Mod.9Cr-1Mo alloy specimen immersed in 0.05M NaCl solution, (b) for coated Mod.9Cr-1Mo alloy specimens immersed in 0.05M NaCl solution	163
<b>Figure 6.13</b>	Evolution of (a) pore resistance $R_{\text{pore}}$ of the coating (b) pseudo-capacitance $Q_{\text{pore}}$ of the coating during immersion in 0.05M NaCl solution.	164
<b>Figure 6.14</b>	Evolution of (a) electrical double layer and oxide layer resistance $R_c$ (b) electrical double layer and oxide layer pseudo-capacitance $Q_{\text{fdl}}$ during immersion in 0.05M NaCl solution	166
<b>Figure 6.15</b>	Graphical representation of the proposed self healing mechanism	167
<b>Figure 6.16</b>	EDX mapping of hybrid coating with TiO <sub>2</sub> nanocontainers for the element Ti	168
<b>Figure 6.17</b>	EIS behaviour of BS, CS, CS-I, CS-N, and CS-NI after 1 h of immersion in 0.05 M NaCl solution	169
<b>Figure 6.18</b>	EIS response of CS, CS-I, CS-N, and CS-NI after 1 day of immersion in 0.05 M NaCl solution	170
<b>Figure 6.19</b>	EIS response of CS, CS-I, CS-N, and CS-NI after 1 week of immersion in 0.05 M NaCl solution	171

<b>Figure 6.20</b>	EIS spectra of CS-NI during 1 week of immersion in 0.05 M NaCl solution	172
<b>Figure 6.21</b>	Evolution modulus of impedance at $10^{-2}$ Hz for CS-NI during 1 week of immersion	173
<b>Figure 6.22</b>	Optical photographs of the coated specimens after 1 week of immersion in 0.05 M NaCl solution. The drawn circles indicate the exposed area of the coatings	174
<b>Figure 6.23</b>	SEM images CS, CS-I, CS-N, and CS-NI after 1 week of immersion in 0.05 M NaCl solution and its corresponding EDX spectra	175
<b>Figure 6.24</b>	EIS spectra of CS during immersion in 0.01 M NaCl solution after making an artificial scratch	176
<b>Figure 6.25</b>	EIS spectra of CS-NI during immersion in 0.01 M NaCl solution after making an artificial defect	177
<b>Figure 6.26</b>	Equivalent circuits used to fit the experimental EIS data of scratched CS and CS-NI during 1 week of immersion in 0.01 M NaCl solution	178
<b>Figure 6.27</b>	Evolution of coating resistance ( $R_{coat}$ ) of CS and CS-NI during 1 week of immersion in 0.01 M NaCl solution	179
<b>Figure 6.28</b>	Evolution of polarization resistance ( $R_p$ ) of (a) CS-NI and (b) CS during 1 week of immersion in 0.01 M NaCl solution	181
<b>Figure 6.29</b>	Photographs of scratched CS-NI and CS after 1 week of immersion in 0.01 M NaCl solution. The drawn circles indicate the exposed area of the coatings	181
<b>Figure 7.1</b>	EIS response of scratched hybrid coatings of 2-MBT loaded zirconia, silica, and titania nanocontainers after 1 week of immersion in the salt solution	185
<b>Figure 7.2</b>	Evolution of $ Z $ at $10^{-2}$ Hz for scratched 2-MBT loaded zirconia, silica, and titania mixed hybrid coatings after 1 week of immersion in salt solution	186
<b>Figure 7.3</b>	Specimens coated with plain epoxy coatings before (A) and after (B) initial adhesion test; specimens coated with epoxy nanocontainer coatings before (C) and after (D) initial adhesion test.	189
<b>Figure 7.4</b>	Photographs of the Epoxy Nanocontainer Coating (ENC) and reference coating (Plain epoxy coating, PEC) after 1000 h of exposure to neutral	190

salt spray test; (A) first set, (B) second set

- Figure 7.5** Photographs of the Epoxy Nanocontainer Coating (ENC) after 2000 h of exposure to neutral salt spray test 191
- Figure 7.6** The photographs of metal surface underneath the coatings after 1000 h of salt spray exposure 192
- Figure 7.7** Raman spectra of plain epoxy coating after 1000 h of salt spray exposure. Inset shows the image of the specimen and the circle indicates the area at which the spectrum was recorded 193
- Figure 7.8** Raman spectra of epoxy nanocontainer coating after 1000 h of salt spray exposure. Inset shows the image of the specimen and the circle indicates the area at which the spectrum was recorded 194



# LIST OF TABLES

<b>Table No.</b>	<b>Table caption</b>	<b>Page No.</b>
<b>Table 1.1</b>	Oxides and hydroxides found in rust layers	7
<b>Table 3.1</b>	List of chemicals used for experiments	58
<b>Table 3.2</b>	List of various instruments and equipment used for thesis work	59
<b>Table 4.1</b>	Raman peak assignments for 2-MBT	93
<b>Table 5.1</b>	Raman peak assignments for 2-MBT	123
<b>Table 6.1</b>	Raman peak assignments for 2-MBT	158
<b>Table 7.1</b>	Characteristic features of three nanocontainer systems	187

# LIST OF ABBREVIATIONS

NACE: National Association of Corrosion Engineers

GDP: Gross Domestic Product

DC: Direct Current

VCI: Volatile Corrosion Inhibitors

PVD: Physical Vapor Deposition

CVD: Chemical Vapor Deposition

TEOS: Tetraethyl orthosilicate

LbL: Layer- by- Layer

PEI: Poly(ethylene amine)

PSS: Poly(styrene sulfonate)

LDHs: Layered Double Hydroxides

XRD: X-ray Diffraction

2-MBT: 2-Mercaptobenzothiazole

BTA: Benzotriazole

SVET: Scanning Vibrating Electrode Technique

UV: Ultra Violet

TTIP: Titanium isopropoxide

GPTMS: (3-Glycidyloxypropyl) trimethoxy silane

TPOZ: Tetra-n-propoxyzirconium

CTAB: Cetyltrimethylammonium bromide

PVP: Poly (vinylpyrrolidone)

RBA: Rapid Breakdown Anodization

HMS: Hollow Mesoporous Silica

HMZ: Hollow Mesoporous Zirconia

SEM: Scanning Electron Microscopy

FESEM: Field Emission Scanning Electron Microscopy

EDX: Energy Dispersive X-ray

TEM: Transmission Electron Microscopy

LRS: Laser Raman Spectroscopy

HRTEM: High Resolution Transmission Electron Microscopy

EIS: Electrochemical Impedance Spectroscopy

BET: Brunauer-Emmett-Teller

BJH: Barrett-Joyner-Halenda

BS: Bare Specimen (Uncoated modified 9Cr-1Mo Ferritic Steel)

CS: Coated Specimen (Hybrid Coated modified 9Cr-1Mo Ferritic Steel)

CS-I: Inhibitor Mixed Coated Specimen (Inhibitor Mixed Hybrid Coated modified 9Cr-1Mo Ferritic Steel)

CS-N: Empty Nanocontainer Mixed Coated Specimen (Empty Nanocontainer Mixed Hybrid Coated modified 9Cr-1Mo Ferritic Steel)

CS-NI: Inhibitor Loaded Nanocontainer Mixed Coated Specimen (Inhibitor Loaded Nanocontainer Mixed Hybrid Coated modified 9Cr-1Mo Ferritic Steel)

EEC: Electrical Equivalent Circuits

ENC: Epoxy Nanocontainer Coating

PEC: Plain Epoxy Coating

# CHAPTER 1

## Introduction to Corrosion and its Prevention

---

*A brief introduction to corrosion, its manifestations, consequences and methods generally used to control corrosion are discussed in this chapter. Both the direct and indirect consequences of corrosion are discussed. The various methods to control corrosion such as material selection, design, cathodic and anodic protection, inhibitors, and coatings are described in this chapter. Corrosion of iron and low alloy steels particularly in coastal and humid atmosphere is described with details of mechanism of uniform and localized corrosion. The necessity to protect them by surface treatment and coatings, and the role of inhibitors and coatings for this purpose is addressed. The main focus in this chapter is to highlight the necessity to develop surface treatments and coatings for corrosion protection of structural components.*

---

### 1.1 Corrosion and its Manifestations

The very common meaning of *corrosion* to the great majority of the people is *rust*. The word “Rust” is more specifically reserved for iron, whereas corrosion is commonly defined as the deterioration of a substance (usually a metal) or its properties because of a reaction with its environment. The terms corrosion and rust are almost synonymous since iron and its alloys are the most commonly used material by mankind and corrosion of iron must have been the one of the first serious corrosion problems affected humans [1]. Corrosion is a naturally occurring phenomenon and just like all natural processes, corrosion of materials is spontaneous and it drives the materials to its lowest possible energy states. Most of the metals and alloys have a natural tendency to combine with water and oxygen present in its environment and return to its most stable state. Iron and steel quite often interact with their environment return to their native and stable oxide states. Similar to any natural disasters such as earthquakes or severe

weather changes, corrosion results in dangerous and expensive damage to everything from automobiles, home appliances, drinking water systems, gas and petroleum pipelines, bridges and buildings [2].

Corrosion takes place in several different ways and it can be classified based on one of the three factors:

- *Nature of the corrodent*: This classification is based on “wet” or “dry” conditions in which corrosion occurs. The presence of moisture is essential for wet corrosion and dry corrosion usually involves reaction with gases at high temperatures.
- *Mechanism of corrosion*: Corrosion can occur either electrochemically or with direct chemical reactions.
- *Appearance of the corroded metal*: Corrosion can be either uniform or localized. The metal corrodes at the same rate over the entire surface for the former and only small areas are affected in localized corrosion.

Classification by appearance is manifested by the morphology of the corrosion attack and this can be visualized either by naked eye or magnification [2]. The schematic given in Figure 1.1 illustrates some of the most common forms of corrosion.

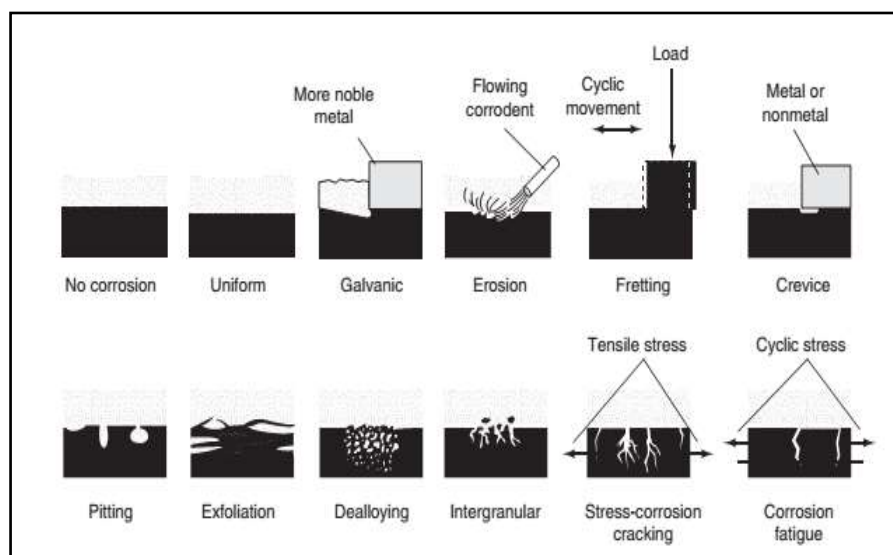


**Figure 1.1: Schematics of the common forms of corrosion [2]**

Based on the appearance of corroded metal, eight forms of wet corrosion can be identified. These are:

- Uniform or general corrosion
- Pitting corrosion
- Crevice corrosion, including corrosion under tubercles or deposits, filiform corrosion, and poultice corrosion
- Galvanic or two metal corrosion
- Erosion-corrosion, including capitation corrosion and fretting corrosion
- Intergranular corrosion, including sensitization and exfoliation
- Environmentally assisted cracking, including stress corrosion cracking, corrosion fatigue and hydrogen damage
- Selective leaching or parting

Even though the eight forms of corrosion are unique, all of them are more or less interrelated. Furthermore, the localized corrosion attack can be classified as microscopic and macroscopic forms. Figure 1.2 depicts microscopic and macroscopic forms of localized corrosion.

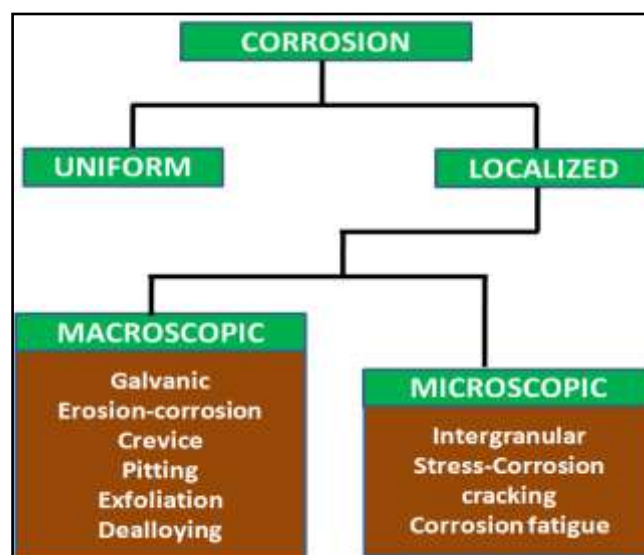


**Figure 1.2: Macroscopic and microscopic forms of localized corrosion [2]**

Macroscopic corrosion affects most of the areas of the metal and which can be observed with the help of naked eye or can be viewed by with the aid of low magnifying power devices. However, microscopic form of corrosion can cause considerable damage to materials before even noticed by naked eye.

## **1.2 Consequences of Corrosion**

Corrosion is having both direct and indirect effects on our daily life. It can affect the useful life of various materials we possess. We can easily recognize corrosion on automobile parts, grills, metal furniture and other household tools made up of metals and alloys. Corrosion can cause far more serious consequences to human lives when a bridge is collapsed due to the corrosion of the steel reinforcing bar in concrete or the collapse of electric towers and damage to buildings. The major cost and consequences of corrosion can be represented in three ways [1-3]:

- ❖ It is extremely expensive financially
- ❖ It is extremely wasteful of natural resources
- ❖ It causes considerable inconveniences and injuries to human beings and sometimes even loss of life.

Corrosion results in tremendous economic loss and it slow down the economic growth of all countries. The annual cost of corrosion worldwide is estimated to be \$ 2.2 trillion [4]. National Association of Corrosion Engineers, NACE estimated that the direct cause of corrosion in the US was \$ 276 billion in 1998, approximately 3.1% of Gross Domestic Product (GDP) [5]. However, by including the indirect losses of corrosion it was estimated to exceed \$1trillion [5]. Our country India loses a staggering amount of Rs 2 lakh crore per year due to corrosion and related issues [6, 7].

The major economic and social consequences of corrosion are described here [1, 2, 8].

- ❖ Replacements of corroded equipments and materials

- ❖ Aesthetic appearance of materials is very important since corroded surfaces are unlikable to the eye. Hence, equipments and structures are required to paint to improve its appearance to the observer.
- ❖ Shutdown of plants and equipments due to corrosion failure. Because of unexpected corrosion failures, electrical, chemical, nuclear power plants are shut down.
- ❖ Contamination of products
- ❖ Loss of valuable products
- ❖ Inability to use otherwise desirable objects
- ❖ Damage of equipments due to corrosion failures
- ❖ Serious damage to the liability of products
- ❖ Safety and health of public, for example, sudden failure of plants can cause fire, explosion, release of toxic gases and acids and other hazardous and flammable materials
- ❖ Depletion of natural recourses, including metals and the fuels used to manufacture them.

Corrosion is causing a huge amount of financial damage to economies, wasting a vast amount of natural recourses and giving rise to a great deal of human sufferings.

### **1.3 Atmospheric Corrosion Behaviour of Iron and Low Alloy Steels**

Atmospheric corrosion is the most visible form of corrosion processes. It is difficult to provide a clear definition for atmospheric corrosion, since it lies in a region between immersed corrosion and dry oxidation. Broadly, atmospheric corrosion can be defined as the corrosion of materials exposed to air and its impurities, rather than immersed in a liquid. The most widely studied corrosion process is the atmospheric corrosion or rusting of iron and steels. Atmospheric corrosion of iron and steels is electrochemical in nature in opposition to dry oxidation [9-11]. Atmospheric corrosion of metals generally



results from surface wetting and it occurs in thin films or adsorbed layers of electrolyte on the metal surface. Due to the thin film nature of atmospheric corrosion, the process is very sensitive and easily influenced by factors such as temperature, relative humidity, precipitation, air currents, orientation of the metal samples and airborne pollutants and particulars [12]. The atmospheric rusting of iron and steels can be considered as wet corrosion in the thin water film formed on the surface of iron and steel and its physical and electrochemical mechanisms are quite complex [12,13].

The following scheme summarizes electrochemical process, which requires aqueous conditions for the atmospheric rusting of iron and alloy steels.

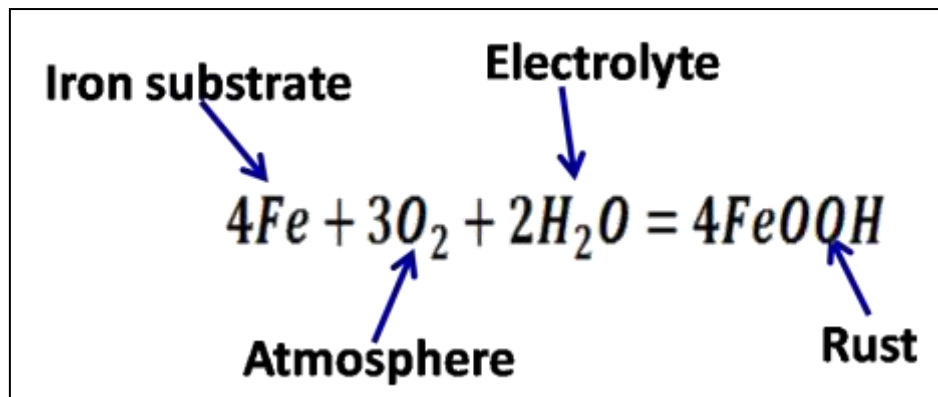


**Figure 1.3: Electrochemical process of atmospheric rusting**

The equation in Figure 1.3 shows that atmospheric oxidizer (O<sub>2</sub>) in the presence of a water layer oxidizes iron substrate and this leads to the formation of rust. In fact, the formed rust layer is quite complex and contains several oxides and hydroxides of iron as presented in Table 1.1[14]. The major parameter influencing the atmospheric corrosion is the interaction between rust layer and electrolyte. An electrolyte layer is formed on the surface of the metal due to the condensation of water. The time of wetness depends on the relative humidity at a given temperature [9, 14]. There is a direct relationship between the amount of relative humidity and thickness of the

electrolyte formed on the metal surface. The variations in relative humidity and temperature form wet-dry cycles on the surface of the metal [14].

Composition	Name	Crystal system
$\text{Fe}_3\text{O}_4$	Magnetite	Cubic (spinel)
$\gamma\text{-Fe}_2\text{O}_3$	Maghemite	Cubic (spinel)
$\alpha\text{-FeOOH}$	Goethite	Orthorhombic
$\gamma\text{-FeOOH}$	Lepidocrocite	Orthorhombic
$\beta\text{-FeOOH}$	Akaganeite	Tetragonal
$\gamma\text{-Fe.OH.OH}$	Reduced lepidocrocite	Orthorhombic
$\text{Fe(OH)}_2$	Ferrous hydroxide	Hexagonal

**Table 1.1: Oxides and hydroxides found in rust layers**

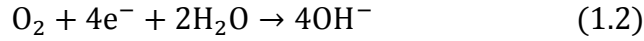
The alternative wet-dry cycle results from the temperature fluctuations between day and night is the most typical feature of atmospheric corrosion which makes drastic changes in the mechanism of rusting in opposition to bulk aqueous corrosion [9,14-16]. According to earlier studies reported by Evans and Taylor and Stratmann, atmospheric corrosion occurs in three stages [9-11, 17]. During the wetting stage, electrolyte is building up on the surface of iron or iron based alloys and this leads to the anodic dissolution of iron. In this first stage (wetting) of atmospheric corrosion, anodic dissolution of iron occurs and it is balanced mainly by the reduction of ferric species within the rust layer and the reduction of oxygen is very little. Even though oxygen is readily available for reduction to balance the anodic dissolution of Fe, the rate of oxygen reduction is very small due to the slow diffusion of oxygen through the thick electrolyte layer on the top of iron surface. However, another oxidizer is available in

the rust layer itself is  $\gamma$ -FeOOH. One of the proposed reduction reactions for  $\gamma$ -FeOOH is as follows.



Hence, during the wetting stage, rust layer itself is responsible for corrosion, i.e. the anodic dissolution of Fe is balanced by the reduction of  $\gamma$ -FeOOH available within the rust layer.

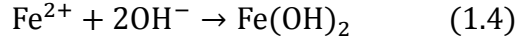
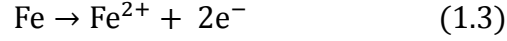
During the second stage (wet stage) of atmospheric corrosion, oxidation of Fe occurs on the small metal area in contact with the electrolyte at the bottom of the pores and oxygen reduction reaction takes place on the large cathodic area of  $\gamma$ -Fe.OH.OH. The oxygen reduction reaction occurring at the cathodic area is as follows



After the wetting stage, adequate amount of  $\gamma$ -FeOOH is reduced and the reduction of oxygen becomes the main cathodic reaction [18]. It is proposed that first atmospheric oxygen is dissolved at the metal/electrolyte interface and then the dissolved oxygen diffuses through the electrolyte and the pores of the rust layer [14].

During the drying stage, the thickness of the electrolyte layer decreases. Due to the decrease in the thickness of the electrolyte layer, the reduction current is also decreased. According to Nishikata et al., at the stage of drying, no more diffusion of oxygen occurs and only oxygen salvation determines the reduction current [19]. Zhang et al. explained that drying results in the decrease of anodic and cathodic area, which would eventually stop the electrochemical reactions due to the scarcity of electrolyte [20]. Another possible mechanism for the decrease of reduction current is related to the phenomenon of passivation. Both the decrease in the electrolyte layer thickness and increase of the concentration of species during the first stage of wet-dry cycle result in the covering of the surface of the metal. This in due course decreases both the cathodic

and anodic areas and hence the covering of small anodic area prevents further iron dissolution. Thus, the blocking of the anodic sites and the diffusion of the dissolved species limit the oxidation current. The anodic sites blocking process is occurring according to the following equation.



At the end of the drying stage, the rust layer is polarized to more positive potential due to the increasing cathodic current and this would in turn results in the regeneration of  $\gamma$ -FeOOH from  $\gamma$ -Fe.OH.OH. This will allow another cycle to occur when the rust is wetted again [21].

In brief, a wet-dry cycle of atmospheric corrosion can be explained as follows [14]:

**Wetting:** The thickness of the electrolyte layer increases from the surface of the rust layer. Fe dissolution occurs. The cathodic reaction is the reduction of  $\gamma$ -FeOOH and the system is under cathodic control.

**Wet Stage:** The thickness of the electrolyte layers remains almost constant. The cathodic reaction is oxygen reduction and the system is under the cathodic control.

**Beginning of the Drying:** The cathodic reaction is oxygen reduction. Anodic sites are being blocked and the system is under anodic control.

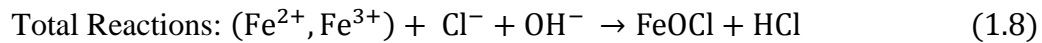
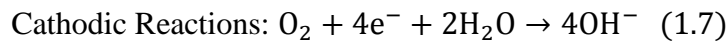
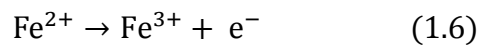
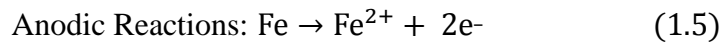
**End of the Drying:** There is no more electrochemical corrosion and the rust layer is re-oxidized to start another cycle.

Marine environment contains significant amounts of chloride ions that have a big role in the corrosion process of iron and steels. The deposition of chloride ions has a significant impact on the composition of the rust layer and its thickness. According to Stratmann et al. and Asami et al., the rust layer formed during atmospheric corrosion mainly constitute goethite ( $\alpha$ -FeOOH), akaganeite ( $\beta$ -FeOOH) and lepidocrocite ( $\gamma$ -

FeOOH) [9, 23]. However,  $\beta$ -FeOOH existed in high chloride containing environments [24, 25]. The phase  $\beta$ -FeOOH accelerates the corrosion process, since its reduction reactivity is higher than that of  $\gamma$ -FeOOH. Antony et al. reported that when both  $\gamma$ -FeOOH and  $\beta$ -FeOOH exists together,  $\beta$ -FeOOH plays the major role in determining the rate of corrosion of Fe [26]. On the other hand, when the concentration of chloride ions is very low, goethite ( $\alpha$ -FeOOH) and lepidocrocite ( $\gamma$ -FeOOH) are the major corrosion products in the rust layer [25]. Generally,  $\beta$ -FeOOH present on the outer surface of the rust layer and it is formed probably due to the reaction between iron ions and atmospherically deposited chloride ions [23]. Sometimes,  $\beta$ -FeOOH appears in the inner layer of the rust also and this may be due to the diffusion of the chloride ions dissolved in the water layer [23, 25].

The detailed mechanism of the accelerated effect of chloride ion deposition is given below. The high amount of chloride ions helps in the formation of  $\beta$ -FeOOH and this in turn decreases the corrosion resistance of steel accelerates the corrosion process [25].

#### ***In Wet Cycle***



#### ***In Dry Cycle***



At low concentration of chloride ions or when the concentration of chloride ion is below the critical concentration, chloride ions help in the transformation of  $\gamma$ -FeOOH to  $\alpha$ -FeOOH. The overall transformation process is given in the following scheme.

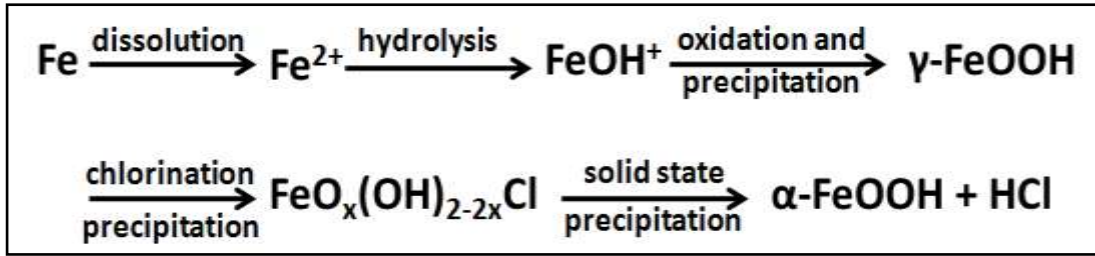


**Figure 1.4: The process of atmospheric rusting in low concentration of chloride content in atmosphere [25]**

#### **1.4 Influence of Cr and Mo on the Atmospheric Corrosion of Steel**

The addition of alloying element chromium to steels has a major influence on atmospheric corrosion and electrochemical properties of steel. Chromium containing steels generally have a surface rust layer with duplex structure, consisting of an outer layer of  $\gamma$ -FeOOH and inner layer of ultra fine chromium enriched  $\alpha$ -FeOOH. It was reported that the Cr enriched  $\alpha$ -FeOOH helped to form a stable protective rust layer [27]. Lai et al. reported that chromium enriched inner most oxide scale resisted the migration of ions and electrons better than FeO [28]. According to Wang et al. chromium could easily enrich in the rust layers compared to that of other alloying elements irrespective of environments [29]. Stratmann et al. pointed out that atmospheric corrosion resistance of chromium containing steel depends on the ratio of crystalline  $\alpha$ -FeOOH (goethite) to all other forms of ferrous oxides such as  $\gamma$ -FeOOH,  $\delta$ -FeOOH. It was found that the atmospheric corrosion resistance enhanced when the mass ratio is higher than 1. The addition of Cr influences the atmospheric corrosion only during the drying stage. According to Stratmann, the reason for higher atmospheric corrosion resistance of chromium containing steel during drying stage might be due to the inhibition of rust reduction and the formation of  $\text{Fe}^{2+}$  states within the rust layer in the presence of Cr enriched oxide layer. This would in turn decrease oxygen reduction rate during drying stage since the electron transfer reaction is the

rate-determining step for the overall reaction [30]. Moreover, in a recent study, Y. Qian reported that higher content of chromium in steel promoted the formation of crystalline  $\alpha$ -FeOOH (goethite) and increases the mass ratio of  $\alpha$ -FeOOH (goethite) to all other forms of ferrous oxides and hence, showed better atmospheric corrosion resistance [31]. According to their study, Cr plays two roles in improving the atmospheric corrosion resistance

- 1) Promotion of formation of rust layers mainly containing  $\alpha$ -FeOOH
- 2) Improving the passivation capability of steels

M. Yashimata and his coworkers conducted investigations on the composition of rust layers containing Cr. Mossbauer spectroscopy studies revealed that the rust layers of Fe-Cr alloy film consisting of supermagnetic ultra fine Cr-goethite with crystal size in the range of 15 nm. The rust layers were mainly composed of  $\gamma$ -FeOOH and ultra fine Cr-goethite with the latter in abundance. Moreover, they proposed a mechanism for the formation of Cr enriched goethite. Due to the solubility difference of  $\text{Cr}^{3+}$  to that  $\text{Fe}^{2+}$  ions, dissolved  $\text{Cr}^{3+}$  ions precipitates as hydroxides at the substrate interface during the initial stages of corrosion.  $\text{Cr}^{3+}$  ions act as nucleus for the growth of Cr-goethite crystals. Moreover, the oxidation of Cr ion is very fast since the diffusion of oxygen through a very thin film is not kinetically limited. This in turn helps in the nucleation of Cr-goethite at various sites on the Fe-Cr alloy surface. The  $\text{Cr}^{3+}$  in the rust layer is coordinated with  $\text{O}^{2-}$  and positioned in the double chains of vacant sites in the network of  $\text{FeO}_3(\text{OH})_3$  octahedra in the goethite crystals [32, 33]. X-ray Absorption Fine Structure (XAFS) spectroscopy studies revealed that  $\text{Cr}^{3+}$  in the rust layer is coordinated with  $\text{O}^{2-}$  and might form  $\text{CrO}_x^{3-2x}$  complex anion and it is located in the double chains of vacant sites in the network of  $\text{FeO}_3(\text{OH})_3$  octahedra as a surface adsorbed or intergranular ion in the ultrafine goethite crystal [34].

The major purpose of adding Mo to steel is to increase the strength and hardness. The influence of Mo addition on corrosion resistance of steels is evident only when Mo is used in combination with other alloying elements and Mo content exceeds 3% simultaneously [35].

### 1.5 Corrosion Prevention Methods

Although corrosion is a natural process, it can be controlled by using effective methods and strategies. There are mainly five primary ways to control corrosion. These are:

- Materials selection
- Design
- Cathodic and anodic protection
- Inhibitors
- Coating

**1.5.1 Materials Selection:** The most common and important method of controlling corrosion is the selection of the right and proper materials for particular corrosive environments. Corrosion behavior of each metal and alloy is unique and inherent and corrosion of metal and alloy has a strong relation with the environment to which it is exposed. A general relation between the rate of corrosion, corrosivity of the environment and corrosion resistance of materials can be elucidated as follows [2]:

$$\text{rate of corrosive attack} \approx \frac{\text{corrosivity of environment}}{\text{corrosion resistance of metal}} \quad (1.10)$$

The rate of corrosion directly depends upon the corrosivity of the environment and inversely proportional to the corrosion resistance of the metal. Hence, the knowledge of the nature of the environment to which the material is exposed is very important. Moreover, the corrosion resistance of each metal can be different in different exposure conditions. Therefore, the right choice of the materials in the given environment (metal-corrosive environment combination) is very essential for the service life of equipments

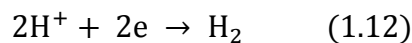
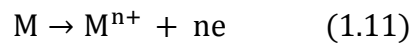


and structures made of these materials. It is possible to reduce the corrosion rate by altering the corrosive medium. The alteration of the corrosive environment can be brought about by lowering temperature, decreasing velocity, removing oxygen or oxidizers and changing concentration. Consideration of corrosion resistance based on the corrosion behaviour of the material and the environment in which it is exposed is an essential step in all industry [1, 2, 8].

**1.5.2 Design:** The design of a structure is as equally important as the choice of materials of construction since it can greatly reduce the time and cost associated with corrosion maintenance and repair [2]. The proper design of equipment or tools made up of metals and alloys must consider mechanical and strength requirements along with corrosion resistance. Prior knowledge about the corrosion resistance of the candidate material and the environment in which it functions is very essential for proper design of any equipment. The most common rule for design is avoiding heterogeneity. It is very important to make all conditions as uniform as possible throughout the entire system [8]. Corrosion frequently happens in dead spaces or crevices and it is highly recommended to eliminate or minimize these areas while designing. All the components and structures should be designed by keeping its expected service life, otherwise premature collapse of the component or structure is the inevitable and large sum of money should be spent for its repair or replacement. The ever-changing environment during the different stages of manufacture, transit and storage as well as the daily and seasonal variations in the environment in which the components are exposed should be considered for its maximum service life. It is highly essential to avoid all unnecessary bimetallic corrosion cells in components by coupling dissimilar metals. The metals involved in coupling should be widely separated in the galvanic series to have a maximum service life of components. Galvanic corrosion can be

controlled effectively by either preventing access of electrolyte to dissimilar metal joints by applying barrier coatings or insulating both the anodes and cathodes to prevent the flow of electrons across the joint. Dissimilar corrosion rate can also be minimized by keeping the anodes as large as possible in the particular component or location to reduce the current density [1, 2, 8].

**1.5.3 Cathodic and Anodic Protection:** Cathodic protection is an electrochemical way of controlling corrosion in which the object to be protected is the cathode. Cathodic protection is achieved by suppressing the corrosion current in a corrosion cell and by supplying electrons to the metal to be protected. The principle of cathodic protection can be explained with the help of a typical corrosion reaction of a metal M in an acid medium [35]. Consider an electrochemical reaction in which metal dissolution and hydrogen evolution are involved; for example



Equations (1.2) and (1.3) show that the addition of electrons to the structure would reduce the metal dissolution and increase the rate of evolution of hydrogen. Cathodic protection of a structure can be achieved by two ways: (1) by an external power supply (2) by appropriate galvanic coupling. Most of the pipelines and marine structures are protected by using an external power supply. Both the buried anodes and the objects to be protected are connected to a direct current (dc) power supply. Generally, the buried anode materials are inert materials and natural cathodes to steel pipelines or tanks to be protected. However, with the aid of the dc power supplies the natural polarities of the materials are reversed and steel pipelines are cathodically protected. Instead of the corrosion reaction of the anodes, some other oxidation reactions such as oxygen or chlorine evolution occur at the anode and thus the anodes are not consumed. Cathodic

coupling by galvanic coupling is realized by using active metal anodes, for example, zinc or magnesium, which is connected to the structure to provide the cathodic protection current. In this case, the anode is called a sacrificial anode, since it is consumed during the protection of the steel structure [2, 8, 36].

In contrast to cathodic protection, anodic protection is one of the more recently developed electrochemical methods for controlling corrosion. Anodic protection is based on the principles of passivity and it is generally used to protect structures used for the storage of sulphuric acid [37, 38]. The difference of anodic protection from cathodic protection is how the metal to be protected is polarized. The component that is to be protected is made as anode in anodic protection. Since the anodic protection is based on the phenomenon of passivity, metals and alloy systems, which exhibit active passive behaviour when subjected to anodic polarization, can be protected by anodic polarization. The corrosion rate of an active-passive metal can be significantly reduced by shifting the potential to the passive range. Anodic protection is used to make a protective passive film on the metal or alloy surface and thereby controlling the corrosion [37].

**1.5.4 Inhibitors:** According to the definition given by NACE International, “inhibitor is a substance that retards corrosion when added to an environment in small concentrations” [39]. An inhibitor can be considered as a retarding catalyst that reduces the rate of corrosion. The mechanism of inhibition is quite complex and it is not well understood. It is established that inhibitors function in more than one way: (a) by adsorption of a thin film on the corroding surface of a metal; (b) by forming a thick corrosion product, or (c) by changing the properties of the environment and thereby slows down the corrosion rate [40]. According to Uhlig et al, inhibitors can be broadly classified as passivators, organic inhibitors and vapor phase inhibitors [35]. The

inhibitors can also be classified based on their mechanism of inhibition and composition [8]. A large number of inhibitors fall under the category of adsorption type inhibitors. These are generally organic compounds and function by adsorbing on anodic and cathodic sites and reduces the corrosion current. Another class of inhibitors is hydrogen evolution poisons. Arsenic and antimony are generally used as hydrogen evolution poisons and they specifically retard the hydrogen evolution reactions. This type of inhibition is very effective only in those environments where hydrogen evolution is the main cathodic reactions and hence these inhibitors are very effective in acid solutions.

The inhibitive substances, which act by removing the corrosive reagents from solution, are known as scavengers. Sodium sulfite and hydrazine are these types of inhibitors, which remove dissolved oxygen from aqueous solutions. These inhibitors function very effectively in those solutions where oxygen reduction is the main cathodic reaction. Oxidizers are also a kind of inhibitors. Substances such as chromate, nitrate, and ferric salts act as corrosion inhibitors in certain systems. Generally, they inhibit the corrosion of metals and alloys that exhibits active-passive transitions. Inorganic oxidizing materials such as chromates, nitrites and molybdates are generally used to passivate the metal surface and shift the corrosion potential to the noble direction. Paint primers containing chromate pigments are widely used to protect aluminum alloys and steel. Inhibitors that are very similar to organic adsorption type with very high vapor pressure are known as vapor phase inhibitors. They are also known as volatile corrosion inhibitors (VCI). According to Miksic and Miller “Volatile corrosion inhibitors are secondary-electrolyte layer inhibitors that possess appreciable saturated vapor pressure under atmospheric conditions, thus allowing vapor-phase transport of the inhibitive substance” [41]. These inhibitors are generally placed very near to the metal

surface to be protected and they are transferred by sublimation and condensation to the metal surface. Hence, these inhibitors can be used to protect metals from atmospheric corrosion without being placed in direct contact with the metal surface. Vapor phase inhibitors are very successful, if they are used in closed packages or the interior of equipments [42].

**1.5.5 Coatings:** Protective coatings are the most generally used method for preventing corrosion. The function of a protective coating is to provide a satisfactory barrier between the metal and its environment. Coatings can be broadly classified into three types. These are:

- ❖ Metallic coatings
- ❖ Inorganic coatings
- ❖ Organic coatings

Usually, an anticorrosive coating system is multifunctional with multiple layers with different properties. A typical multifunctional coating can provide an aesthetic appearance, corrosion control, good adhesion, and abrasion resistance. The functioning of any protective coatings is based upon three basic mechanisms:

- Barrier Protection
- Chemical inhibition
- Galvanic (sacrificial) protection

Completely isolate metals and alloys from its environment achieve barrier protection. Protection of metals through chemical inhibition is achieved by adding inhibitor molecules into the coating system. An active metal is coated on the surface of the metal to achieve sacrificial or galvanic protection [2, 8, 43].

**1.5.5.1 Metallic Coatings:** Metals and sometimes their alloys are applied to other metals and alloys to prevent corrosion. Metallic coatings are applied to a metal surface by using following methods:

- Electroplating
- Electroless plating
- Hot dipping
- Thermal spraying
- Cladding
- Vapor deposition
- Ion implantation
- Laser processing

A metallic coating can function either as noble coatings or as sacrificial coatings.

**Electroplated coatings** are produced by the electrodeposition of an adherent metallic coating upon a metal or alloy which is to be protected [44]. This is carried out by immersing a metal or part of the metal to be coated in a solution of the metal to be coated and passing direct current between the metal and another electrode. It is also known as electroplating and it is generally used for decoration, protection, corrosion resistance, electrical and magnetic properties. The nature of the deposit depends mainly on factors such as temperature, current density, time and composition of the bath. A coating of desired thickness and property can be achieved by changing these variables. Generally zinc and cadmium deposits on steel act as active coatings and protect steel by cathodic protection. Several metals commonly coated on steel are noble to iron. These noble coatings act as an effective barrier to deny access for any corrosive species and to ensure this the noble coating should be pore free and flawless.

**Electroless metal coatings** are prepared without the help of electric current. Electroless nickel coatings are achieved by the autocatalytic chemical reduction of nickel ions from aqueous solution. Generally nickel-phosphorous and nickel-boron coatings are produced. These coatings are amorphous in nature and provide excellent corrosion resistance in a wide range of environments [2].

**Hot-dip coating** is a process in which a low melting point metal is applied as a protective coating on steel wherein the material to be coated is immersed in a molten bath of the coating metal. Although hot dipping method can be applied over a wide variety of materials, it is commonly used to protect steels. Hot-dip coating can be applied by continuous or batch process. Aluminum and zinc are most commonly used metals to be coated to steel. Hot-dip zinc coated steels are generally known as galvanized steels [2, 8].

**Thermal spraying** consists of a group of processes including flame spraying, plasma spraying, arc metallization, detonation gun, high velocity oxyfuel, and cold spray and that can be used to apply a variety of coating materials for corrosion prevention. The coating materials can be powder, rod, wire or liquid. The coating materials are heated to a plastic or molten state and propelled by a stream of compressed gas onto the substrate. When these particles strike the metal surface, they flatten and form thin platelets and adhered to the prepared surface. Generally, a spray gun is used to generate the required heat for melting through combustion of gases, electric arc or plasma [8, 45].

**Cladding** is the bonding together of dissimilar metals. It is achieved by rolling of two sheets of metal together. The principle of cladding includes hot-roll bonding, cold roll bonding, explosive bonding, and weld cladding. For example, a nickel and steel sheets

are hot rolled to get a composite nickel-steel sheet. Similarly, high strength aluminum alloys are clad with commercially pure aluminum to have a good barrier to corrosion.

**Vapor deposited coatings** are accomplished in a high vacuum chamber. There are mainly two types of vapor deposition: physical vapor deposition (PVD) and chemical vapor deposition (CVD). Usually, the coating material is vaporized by heating electrically and the vapors are allowed to deposit on the part to be protected. The major vapor deposition methods are sputtering, evaporation, ion plating (all of which are PVD processes) and CVD. The species to be deposited is transferred and deposited in the form of individual atoms or molecules. The most important advantage of vapor deposited thin coating is that it is pore free and highly dense. However, its application in corrosion protection is limited since this method is more expensive compared to other methods [2].

**Ion implantation** and **laser processing** are two surface modification methods accomplished by the use of high-energy or particle beam. High-energy ion beams are used to modify surfaces to combat issues related to corrosion and wear. By ion implantation, it is possible to enhance the passivation characteristics or create a novel material. Ion implantation commonly finds its application in semiconductor industry. Lasers with output power 0.5 to 10 kW can be employed to engineer the metallurgical structure of a surface and tailor its surface property by leaving its bulk properties intact. Laser processing helps to produce corrosion resistant surface layers. Transformation hardening, surface melting, and surface alloying achieve laser processing [2, 8].

**1.5.5.2 Inorganic Coatings:** Nonmetallic inorganic coatings include ceramic coatings, conversion coatings, and anodized coatings. One of the most widely used ceramic coatings is zinc silicates [46, 47]. Sol-gel based silica and titania coatings are another type of inorganic coatings. The sol-gel process to produce  $\text{ZrO}_2$ ,  $\text{TiO}_2$ ,  $\text{SiO}_2$ ,  $\text{ZnO}$



coatings is very well studied and established [48-52]. The inorganic particles in the sol-gel coatings generally act as a good barrier against corrosive species. These coatings give excellent abrasion resistance, low UV-absorption rate, high abrasion resistance and aesthetic appearance to the metal. However, sol-gel based inorganic coatings cannot be prepared in the thickness required for very high corrosion resistance since it is prone to have cracks in the coating.

Phosphate coating and chromate conversion coatings are two largely used inorganic conversion coatings. Phosphate coating is produced on the metal surface by immersion the metal in a bath mainly contains phosphoric acid and other chemicals. During the immersion, the metal reacts with phosphoric acid and other chemical contained in the bath and produce a crystalline insoluble protective phosphate layer. Phosphate conversion coatings are generally used to improve the corrosion resistance and the adhesion of paints. Commonly used phosphate conversion coatings are zinc phosphate, iron phosphates, and manganese phosphates. The basic principle involves in any phosphate coating is the precipitation of a divalent metal and phosphate ions ( $\text{PO}_4^{3-}$ ) on a metal surface. The phosphate conversion coatings can be applied either by spraying or by immersion [2].

Chromate conversion coatings are produced on the metal surface by a chemical or electrochemical treatment of the metals or metallic coatings in solutions containing hexavalent chromium ( $\text{Cr}^{6+}$ ) and other components. Chromate conversion coatings are primarily applied to improve the corrosion resistance of the metal and to improve the adhesion of paints on the metal surface. Chromate conversion coatings are applied by both spraying and immersion methods. However, various governments and regulatory bodies recommend the replacement of chromate conversion coating with some other green alternative since hexavalent chromium is carcinogenic and toxic [2].

Anodizing is one of the most important surface modifications carried out for aluminum alloys for improving the corrosion resistance and other purposes. Aluminum oxide ( $\text{Al}_2\text{O}_3$ ) films are formed on the surface when aluminum and aluminum alloys are polarized anodically in electrolyte solutions. Since all of the anodic process form porous  $\text{Al}_2\text{O}_3$  films, it is required to seal the pores by immersion the coated materials in hot water. The hot water treatment would hydrate the coating and seal the pores by forming  $\text{Al}_2\text{O}_3 \cdot 3\text{H}_2\text{O}$  [2].

**1.5.5.3 Organic Coatings:** Organic coatings act as relatively thin layer between the substrate materials and the environment. The terms organic protective coatings and paints are generally used interchangeably for both having an organic base. According to the definition of coating mentioned in the *Manuals for Coatings of Light Water Nuclear Plants*, “Coatings (paints) are polymeric materials that applied in fluid stage, cure to form a continuous film”[53, 54]. This is a general definition given very broadly and simply for both coatings and paints. However, as far as corrosion protection is concerned, it is very necessary to define both these terms very specifically. “*Paint can be defined as any liquid material containing drying oils alone or in combination with natural resins and pigments which , when applied to a suitable substrate, will combine with oxygen from air to form a solid, continuous film over the substrate, thus providing a weather resistive decorative surface*”[53]. During its entire lifetime, a paint film continues to oxidize and slowly become porous to oxygen, water and other corrosive species, thus giving a less permanent protection against corrosion than the more sophisticated protective coating.

A protective coating is chemically a considerably different material from paint. It surpasses paint in adhesion, toughness, and resistance to chemical, weather, humidity, and water. “*A protective coating can be defined as any materials composed essentially*

*of synthetic resins or inorganic silicate polymers which, when applied to a suitable substrate, will provide a continuous coating that will resist industrial or marine environments and prevents serious breakdown of the basic structure in spite of abrasion, holidays, or imperfections in the coating”[53].* In order to provide maximum protection, a protective coating should: (a) resist the penetration of ions from salts that are in contact with the coatings; (b) minimize the action of osmosis; (c) expand and contract with the underlying metal surface; and (d) retain the aesthetic appearance over a long period.

### **1.6 The Organic Coating System**

A typical anticorrosive coating system consists of a primer, one or several intermediate coats and a top coat [46, 53, 55]. Figure 1.5 illustrates a typical coating system used for highly corrosive industrial and marine environments.



**Figure 1.5: A typical coating system for marine and industrial applications**

Prior to the application of a primer, the substrates to be coated should be cleaned neatly and pretreated to improve the adhesion of the subsequent coatings. Generally, sand blasting, polishing with emery sheets and pickling are employed for surface finishing.

A primer is considered the most important components of the coating system [8, 46, 53]. The major purposes of a primer are listed as follows:

- Good adhesion to the substrate
- High bond to intermediate coats
- Appropriate flexibility with subsequent coatings
- Strong resistance to corrosion and other chemicals

The primer is the base coat on which the rest of the coating system is applied and hence it should have strong adhesion to the surface of the substrate. The primer generally contains some inhibitive pigments and these pigments used to passivate the metal surface and improve its corrosion resistance. A primer should protect the surface for many days or months prior to the application of top coats and thus the primer coat should be highly adherent and inert.

The specific purpose of the application of intermediate coating is to increase the thickness of the coating system and resist the infiltration of corrosive species to the metal surface [46, 53]. The major use of intermediate coats is to provide:

- Building up the thickness of the coating
- Improve the chemical resistance of the coating
- Retard the moisture vapor transfer
- Increase the electrical resistance of the coating
- Strong cohesion
- Improve the adhesion between the primer and topcoat.

The topcoat is the final finish coat it is always exposed to the external environment. The topcoat should have required colour and gloss to please the eyes of an observer. It is the first line of defense against corrosion in a coating system and hence it should

have enough barrier property to impede the transport of aggressive species through the coating system. The important function of a topcoat is to provide [46, 53, 56, 57]:

- A resistant seal for the coating system
- Initial barrier to the external environment
- Good resistance to water, chemicals, and weather
- Strong and wear resistant surface
- Aesthetic look to the coating system
- High resistance to ultraviolet radiation

The above-mentioned coating system is not necessary for all applications. Different combinations of coating system can be obtained depending upon the corrosive situations. Even a single coat can function satisfactorily for some particular corrosive environment. Sometimes a single coating formulation applied in more than two coats can provide required protection for metals and alloys.

### **1.7 Recent Advances in Protective Coatings**

Application of organic/polymeric coating system is one of the widely used strategies to combat corrosion of metals and alloys under service conditions [46]. Such polymer coating system includes a pre-treatment layer or conversion layer, a primer and a topcoat. These pre-treatment or conversion layers are generally applied to improve the corrosion protection efficiency and to impart good adhesion of organic coatings applied subsequently [58]. Chromate and phosphate conversion coatings are widely used strategies to obtain a pre-treatment layer to improve the adhesion of subsequent organic coatings for both ferrous and non-ferrous alloys [59]. However, the superior oxidation property of Cr (VI) causes several health problems to humans and it is carcinogenic [60]. The main disadvantage of inorganic corrosion inhibitors such as chromates, phosphate is its toxicity. The common usage of chromate is banned in several countries

considering health and safety reasons and the protection of the environment. Similarly, the corrosion protection performance of zinc phosphate treatment is not good enough for outdoor exposure [59]. Hence, the necessity of developing an environmentally friendly surface pre-treatment is vital.

One of the most promising alternatives to aforementioned toxic surface treatment for corrosion protection is sol-gel coatings. A sol-gel based dip coating is a very simple method consists of the withdrawal of a substrate from a fluid sol and this results in the deposition of a thin solid film due to gravitational draining, solvent evaporation and further condensation reactions [61, 62]. Compared to other conventional thin solid film deposition techniques such as chemical vapor deposition (CVD), physical vapor deposition (PVD), electrochemical deposition, and sputtering, sol-gel dip coating method requires considerably less equipments and it is potentially less expensive [63]. The sol-gel process is a chemical synthesis method based on the hydrolysis and condensation reactions of metal alkoxides ( $M(OR)_n$ ). Sol-gel derived coatings have many advantages such as high corrosion resistance, nontoxic and environmentally compatible, and good adhesion to both metallic substrate and organic topcoat. One of the fascinating features of sol-gel based coating is its functionalization and tailoring the properties of the deposited sol-gel film.

The sol-gel process can be used to prepare either organic or inorganic based protective coatings. Moreover, the low reaction temperature required for sol-gel process makes easy the introduction of organic groups in the inorganic material leading to the fabrication of a new class of hybrid coatings consisted of both organic and inorganic components [62]. The functionalities imparted by both organic and inorganic moieties in hybrid coatings are different. The inorganic parts confer enhanced mechanical properties, scratch resistance, durability and adhesion to metallic substrate. On the other

hand, the organic part contributes to the increase of density, flexibility and functional compatibility with polymeric paint systems applied as topcoats. Moreover, organically modified coatings are generally thick and pore free dense coatings [64, 65].

The corrosion resistance of sol-gel derived film is mainly due to its physical barrier property, which obstructs the entry of corrosive species and water through the coatings and protects the underlying metal surface. Corrosion protection provided by a barrier film which avoid any contact between metallic substrate and external environment is known as passive protection. However, sol-gel coatings are not free from cracks and other defects (such as scratches and pores) and this leads to the penetration of electrolyte and water towards metal surface and instigates corrosion. Even though the physical barrier coatings provide resistance against corrosion, any occurrence of failure in this barrier layer leads corrosive ions to permeate to the metal surface leading to the onset of corrosion. Hence, it is required to introduce active agents or corrosion inhibitors into the barrier coatings to improve its anticorrosion property. Corrosion protection provided by active agents or corrosion inhibitors is known as active corrosion protection. In active corrosion protection methods, corrosion inhibitors are incorporated into the protective barrier layers to decrease the corrosion rate when the passive barrier layer starts deteriorating [58, 66]. The corrosion inhibitor can be introduced into the coatings in two ways: (i) adding the inhibitors directly into the coating (ii) loading or encapsulating the inhibitors in some containers or reservoirs and then adding into the coating [58].

It was proved that the direct addition of inhibitors had a negative effect on the stability of the sol-gel coating and thereby deteriorates the physical barrier functionality of the coating [66]. Hence, the second approach, loading or encapsulating the inhibitors in containers prior to mixing with coating, is the favored one. Recent developments in

nanotechnology and surface engineering pave avenues for fabricating novel class of coatings, which can impart both barrier protection and active functionalities. Nano or microcontainers with sustained release properties can be used in a new class of self-healing coatings. When the environment around the coatings changes, the inhibitor from the nanocontainers would be released quickly and delays corrosion activity. There are many advantages in adopting this novel strategy for corrosion protection compared to conventional barrier coatings. This strategy avoids the direct contact between the inhibitor molecules and barrier coatings and hence reduces the negative effect of the inhibitors on the integrity of the coating. It helps in releasing the inhibitors at the right time in the right quantity and thereby no uncontrolled leaching of the inhibitors into the coatings [58, 66, 67].

## **1.8 Summary**

Corrosion of materials and structures is a big hindrance to the development of the economy and cause a lot of damage to our life and hence its prevention is a great challenge for humanity. Corrosion prevention by protective coatings has a greater role to play in curbing this menace. Sol-gel based protective layers equipped with active functionalities is the ideal replacements for both chromate and phosphate coatings as pre-treatment or conversion layers, since sol-gel derived coatings are eco-friendly. However, it is required to utilize the recent developments in nanotechnology to improve the properties of coatings to have multifunctional capabilities.



## CHAPTER 2

### A Review on Protective Sol-Gel Coatings and Active Corrosion

#### Protection Methods Based on Self-Healing Ability

---

*This chapter gives a general overview on the fundamentals of sol-gel method and hybrid sol-gel coatings containing inhibitors for active corrosion protection methods based on self-healing ability. An up to date literature review on various nanocontainers, their synthesis and application in active corrosion protection is covered. The concept of self-healing and how it can be used for corrosion protection of materials is described. A brief description of different self-healing coatings developed so far is also included in this chapter.*

---

#### 2.1 Fundamentals of Sol-Gel Coatings

The sol-gel process has a long history dating back to 1846, when Ebelmen employed this simple chemical synthesis method to prepare silica gels from alkoxides [68]. Sol-gel method is a chemical synthesis method in the beginning used to fabricate inorganic materials such as glass and ceramics. Ebelmen reported that hydrolysis of tetraethyl orthosilicate (TEOS) under acidic conditions yielded  $\text{SiO}_2$  in the form of a “glass like substance”. Later Roy and co-workers employed sol-gel process to synthesize new ceramic oxides of Al, Si, Ti, Zr, etc [69-71]. The potential of sol-gel films as corrosion resistance coatings for metallic substrates was extensively investigated [72-91]. Sol-gel thin film coatings are proposed to be the green replacement for toxic chromate conversion coatings as pretreatments or primer coatings. There are other methods such as chemical vapor deposition (CVD), physical vapor deposition (PVD), electrochemical deposition, and plasma spray process for deposition of coating on metallic substrates. Compared to these techniques, sol-gel coating process has some advantages and they are listed below.

- Sol-gel process is a low temperature chemical synthesis; generally, sol-gel synthesis takes place at room temperature.
- It is possible to apply coatings on substrates of any shapes since sol-gel coating process involves the dipping of substrate in liquid sol.
- The sol-gel coating is a “green” method.

### ***2.1.1 Synthesis of Sol-Gel Coatings***

As the name implies, sol-gel process involves the evolution of a colloidal system through the formation of an inorganic or hybrid sol and followed by the gelation of the sol into a continuous liquid phase colloidal network (gel). Sols are dispersions of colloidal particles with diameters of 1-100 nm in a liquid. A gel is a three dimensional continuous network in the liquid phase which is built by the agglomeration of colloidal particles. During sol-gel process, a compound is “dissolved” in liquid in order to bring it back as a solid in a controlled manner. Sol-gel coatings can be synthesized in two ways: inorganic method and organic method. Inorganic method involves the formation of a colloidal sol and its gelation and eventually resulted in a continuous liquid phase network. But organic method involves either base or acid catalyzed hydrolysis of monomeric metal or metalloid alkoxide precursors  $M(OR)_n$  in alcohol or other low-molecular weight organic solvents. Here M is representing the network forming element such as Si, Ti, Zr, Al, Fe, B, etc.,; and R is an alkyl group ( $C_nH_{2n+1}$ ) [92]. The important steps involved in a sol-gel process are given as follows:

- a) Hydrolysis
- b) Condensation and polymerization of monomers to form chains and particles
- c) Growth of the particles
- d) Agglomeration of the polymer structure followed by the formation of a continuous network in the liquid phase and resulting in the formation of a gel

A schematic of the hydrolysis and condensation during the preparation of sol-gel derived silica materials is presented in Figure 2.1.

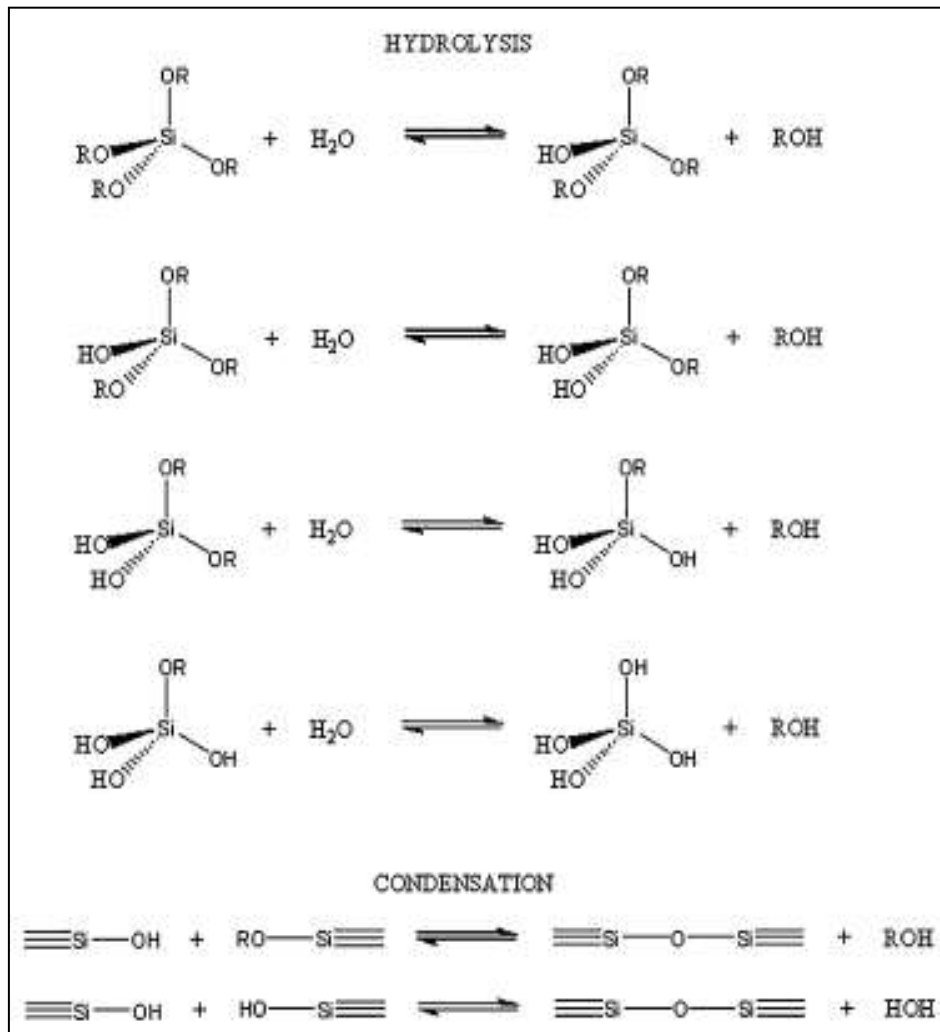


**Figure 2.1: Schematic for the sol-gel synthesis of silica materials [92]**

Generally, alkoxides of Si, Zr, Ti and Al are used to prepare their corrosion resistant sol-gel coatings. During the hydrolysis stage, silicon alkoxides interact with water and alkoxide groups (-OR) are replaced by hydroxyl groups (-OH). In the condensation step, the condensation of two -OH groups or -OH group with -OR groups results in the formation of a continuous network of Si-O-Si bonds, water, and alcohol. In fact, both the hydrolysis and condensation occur simultaneously once the hydrolysis has initiated.

Usually, the rate of hydrolysis is greater than that of the condensation reaction [93-95].

The major factors influence the sol-gel process is given below:

- a) Initial reaction conditions such as pH, temperature
- b) Molar ratio of the reactants
- c) Solvent composition

The nature of the mutual solvent controls significantly the kinetics of the sol-gel reactions [93]. Since the metal alkoxide and water are immiscible, the addition of a mutual solvent like alcohol is essential to achieve homogeneity of the reaction mixture.

The concentration of the solvent used has a significant effect on the thickness of the sol-gel film produced on the metal substrate and hence its corrosion resistance too. Moreover, the effect of concentration depends on the nature of the solvent used. Metroke et al. reported that high concentration of diluent provided enhanced corrosion resistance when aprotic solvents were used. Low concentration of diluent provided higher corrosion protection when small alcohols were used. It was found that the use of high concentration of large alcohol diluents found to decrease the corrosion resistance of sol-gel coatings [96]. Hence, the appropriate selection of the solvent has a huge role in determining the thickness and corrosion resistance of the sol-gel coatings.

Different metal alkoxides with similar alkoxy groups have different chemical reactivity during sol-gel reaction. A general chemical reactivity series can be given as follows:  $\text{Si(OR)}_4 \lll \text{Sn(OR)}_4 < \text{Ti(OR)}_4 < \text{Zr(OR)}_4 < \text{Ce(OR)}_4$  [97]. The sol-gel chemistry of silicon precursor solution is different from that of other metal alkoxide precursor solutions. The key difference in reactivity of alkoxides of transition metals such as Ti, Zr from that of silicon alkoxide is their reaction with water. Silicon alkoxides or the alkoxy silanes are very stable to hydrolysis by water in the absence of water. Hence, the hydrolysis of alkoxy silanes are generally either base catalyzed or acid catalyzed. The

hydrolysis of silicon alkoxide results in the formation of a reactive Si-OH group. The scheme for the base catalyzed hydrolysis of silicon alkoxide is given in Figure 2.2.

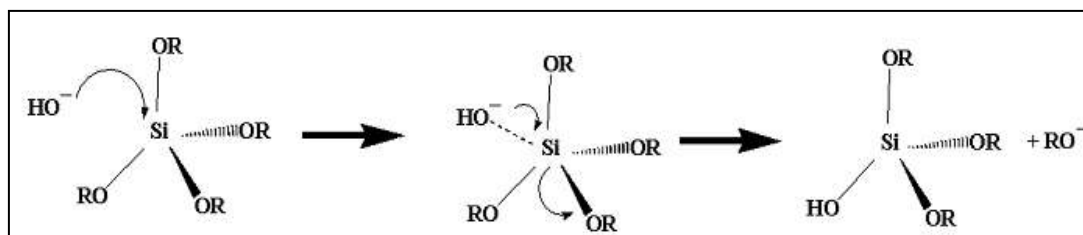


**Figure 2.2: Mechanism of the base catalyzed hydrolysis of silicon alkoxide [103]**

At first, a hydroxide anion attacked the positively charged Si atom. This results in the formation of a highly reactive transition state with Si atom having a coordination number of 5. In the second step, an alkoxide anion is released from transition state and leads to the formation of a reactive Si-OH group. The released alkoxide ion reacts with water and regenerate hydroxide anion.

The reaction pathway of acid catalyzed hydrolysis of alkoxy silane is presented in Figure 2.3.

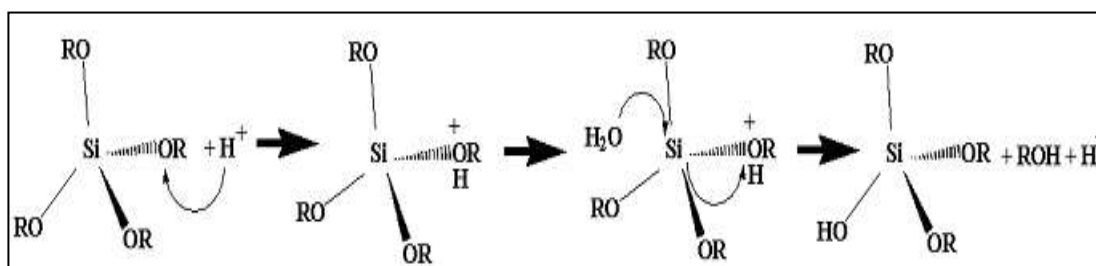


**Figure 2.3: Reaction pathway for acid catalyzed hydrolysis of silicon alkoxide [103]**

Initially, the addition of acid leads to the protonation of an oxygen atom of alkoxy group and hence the formation of a reactive cationic species. This is the first and rate-determining step of the reaction pathway. In the second step, a water molecule attacks this cationic species and leads to the release of a molecule of alcohol and the formation of a reactive Si-OH bond. This in turn regenerates the proton catalyst. Since the silicon

alkoxides are stronger Lewis bases than Lewis acids, acid catalyzed hydrolysis is much quicker compared to that of base catalyzed one.

On the other hand, the sol-gel reaction chemistry of transition metal alkoxides is facile and rapid even in the absence of any catalyst. The hydrolysis of  $\text{Ti}(\text{OR})_4$  occurs within milliseconds and the reaction time for the hydrolysis of  $\text{Zr}(\text{OR})_4$  is in the order of magnitude of microseconds. Compared to that of a semi metal like Si, metals in general and main group and transition metals in particular form stable cationic complexes very easily. Moreover, these metal alkoxides are very strong Lewis bases and hence they are very easily undergoing proton assisted  $\text{S}_{\text{N}}1$  reaction mechanism [93-101]. The high reactivity of metal alkoxides towards water leads to rapid and uncontrolled hydrolysis and eventually ends up in phase separation or precipitation. This limitation is successfully overcome by chemically modifying the metal alkoxides prior to hydrolysis and condensation and the addition of water to this modified precursor results in the formation of a clear and homogeneous sol. A general reaction pathway for the synthesis of sols of metal alkoxide is given in Figure 2.4.

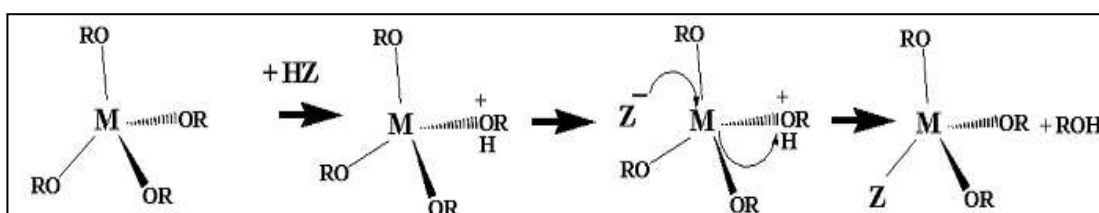


**Figure 2.4: Reaction pathway for the sol-gel synthesis of metal alkoxide [103]**

Compounds such as  $\beta$ -diketones, acetic acids, acetoacetates are generally used as chelating agents to avoid uncontrolled precipitation [102]. The addition of chelating agents does result in slowing down or even preventing gelation and uncontrolled precipitation on the addition of water. According to Kessler et al. the whole sol-gel chemistry of transition metal alkoxide precursor solution is largely controlled by the mobility of chelating ligands and their self-assembly [103]. The modifying ligands

interact with the alkoxide solution and work like a surfactant in stabilizing the sol and help in the formation of clear and homogeneous sol [103].

The stability of the prepared sol is another factor significantly influencing the corrosion resistance of the sol-gel films produced on the metal substrate. The aging of the sol has a crucial role to play on the stability of the sol as it helps in additional condensation and cross-linking between sol particles. The aging of sols result in the formation of a more porous structured sol-gel coating while drying the coating owing to the formation of a stronger gel network and more resistant to capillary driven collapse [104].

### ***2.1.2 Deposition and Curing of Sol-Gel Coatings***

The major methods of applying sol-gel coatings on metal surfaces are dip coating, spin coating, spray coating and electrodeposition [105-112]. Dipping and spin coating methods are generally used to coat flat samples and electrodeposition is very useful for samples with complex geometry. The sol-gel coatings obtained through electrodeposition method is generally thicker, less porous [112-114]. Sintering of the deposited sol-gel film is another important step. There will be a considerable amount of contraction in volume and accumulation of internal stress while drying the sol-gel coating due to the loss of solvents and water [92, 97]. Due to the generation of internal stress, it is very common to have cracks and pores in the dried sol-gel coating. Generally, the corrosion resistance of sol-gel coating decreases as the sintering temperature increases due to cracks induced by thermal stresses [115-118]. Normally, there are two ways of drying sol-gel films produced on metallic substrates: high temperature sintering and low temperature sintering [97]. High temperature sintering leads to decrease in corrosion resistance due to the generation of porosity while improving the mechanical properties of the produced coatings [119]. Usually, the high temperature sintered sol-gel coatings are used as wear resistant layers or barriers

against high temperature oxidation of metallic substrates [76, 107, 120-122]. These coatings are commonly not used for wet corrosion protection due to the presence of large pores [76, 108]. In low temperature sintering, sol-gel films are dried at temperature less than 200 °C. While drying at this temperature the evaporation of solvents and water occurs and further gelation of the formed gel happens. Low temperature curing is generally employed to obtain hybrid organically modified sol-gel coating with crack free compact film [80, 123-125]. Sol-gel derived coatings cured at low sintering temperature can render better corrosion resistance compared to that of high temperature sintered coatings against wet corrosion.

## **2.2 Types of Protective Sol-Gel Coatings**

### ***2.2.1 Inorganic Corrosion Protective Sol-Gel Coatings***

Inorganic sol-gel coatings or metal oxide coatings are the first type of sol-gel derived coatings used to protect metallic substrates from corrosion. SiO<sub>2</sub>, ZrO<sub>2</sub>, TiO<sub>2</sub>, CeO<sub>2</sub>, etc. are the very commonly used metal oxide coatings over different types of metallic substrates. Normally, the corrosion protection performance of sol-gel derived metal oxide coatings is comparable or equally good to that of conventional chromate conversion layer and phosphate pretreatment. However, inorganic sol-gel derived protective coatings failed to offer good corrosion resistance when scribed coated panels were exposed to corrosive environments [126]. The major drawbacks of sol-gel derived metal oxide coatings are the breakdown of the coating layer at isolated sites, generation of porosity while increasing the thickness of the coatings. Normally, the thin layer of sol-gel film developed on the metallic substrates generates cracks or pores while curing at high temperature due to the disparity in thermal expansion co-efficient of sol-gel derived metal oxide layer and underlying metal surface [97]. The properties such as high heat resistance and chemical resistance make sol-gel silica films an ideal



coating to enhance the oxidation and corrosion resistance in acidic media at different temperatures [75, 80]. Owing to very high expansion coefficients very close to many bulk metals, zirconia coatings appear less porous after sintering at high temperature [72, 82]. The inorganic sol-gel derived protective films functions as an adhesion layer between metallic substrate and organic coatings [122, 127, 128].

### ***2.2.2 Organic-Inorganic Hybrid Sol-Gel Coatings***

Even though inorganic sol-gel derived coatings could offer good protection to metallic substrates from corrosion, it has two major deficiencies and it is given below

- a) Metal oxide sol-gel films are breakable and it is difficult to achieve thicker coatings ( $> 1\mu\text{m}$ ) without any thermally induced cracking.
- b) High temperature sintering is often required to have good optimum properties [92, 119].

Both the brittleness and requirement of high temperature sintering of purely inorganically derived sol-gel coating are overcome by the introduction of organic moieties into the coating matrix. Hybrid coatings impart the properties of both the organic polymeric and inorganic ceramic materials. The inorganic part of the hybrid system increases the scratch resistance, durability and adhesion to the metallic substrates while the organic functional groups help to prepare thick crack free hydrophobic surfaces. Furthermore, the organic functionality improves the compatibility and adhesion of thin protective hybrid sol-gel films to top organic paint systems [97]. Wang et al. reported that there are three major approaches according to the chemical bond between the inorganic and organic groups to prepare hybrid sol-gel films [92]. The three different approaches are: (1) by direct mixing of both organic and inorganic sol-gel systems and here the product is a simple mixture and no chemical bond exists between the organic moiety and inorganic group; (2) introducing a

chemical bond between organic and inorganic parts and this is achieved by using already existing functional group within the polymeric/oligomeric species to react with the hydrolyzed inorganic precursor solution; (3) using alkoxysilane as the sole or one of the precursors of the sol-gel process with alkyl group being a second stage polymerizable organic group often carried out by either photochemical or thermal curing following the sol-gel reaction [92]. Structural models for different types of hybrid sol-gel coatings are given in Figure 2.5. In the first type of hybrid sol-gel system, no chemical bond exist between the organic and inorganic group, however, weak dispersion forces like van der Waals force of interactions exist between them.

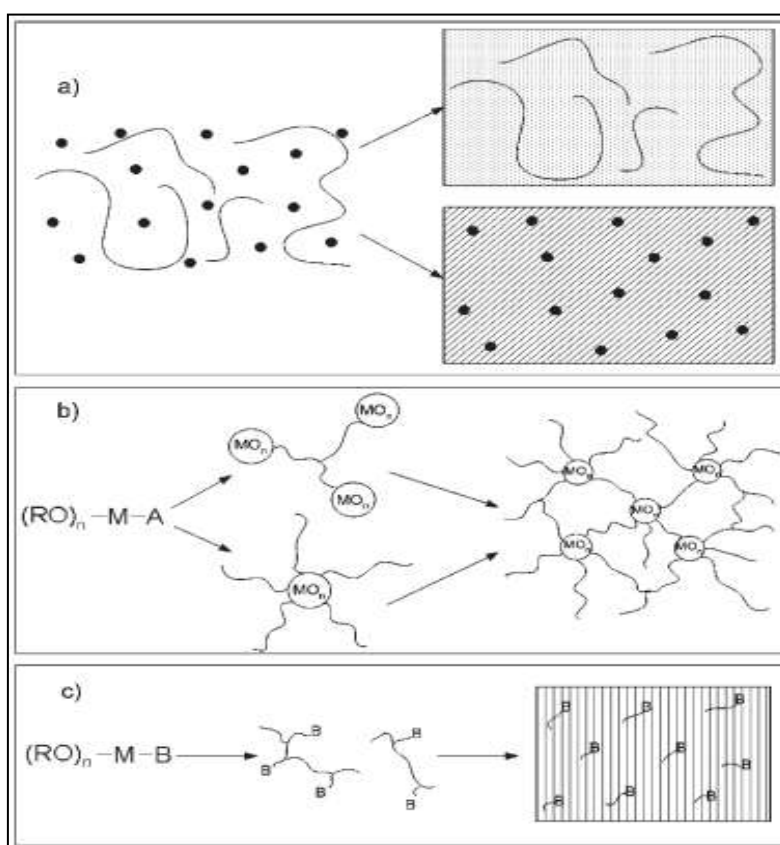


**Figure 2.5: Schematic of different classes of hybrid materials prepared by sol-gel process; (a) no chemical bond between organic and inorganic group; (b) polymerizable organic group is bonded to the inorganic group; (c) non-polymerizable organic groups are bonded to inorganic phase [97, 130]**

In the case of second and third types of hybrid materials, strong chemical bonds are existing between the organic moieties and hydrolyzed inorganic phase.

Organoalkoxysilanes and metal alkoxides are commonly used precursor solutions to obtain organic and inorganic sol-gel systems respectively. Based on the type of organoalkoxysilanes used to introduce organic group into the sol-gel system, organically modified sol-gel system can be classified into two: (1) non functional organoalkoxysilanes; (2) organo functional alkoxysilanes [97, 122]. The structure of some of the commonly used alkoxysilanes is presented in Figure 2.6.

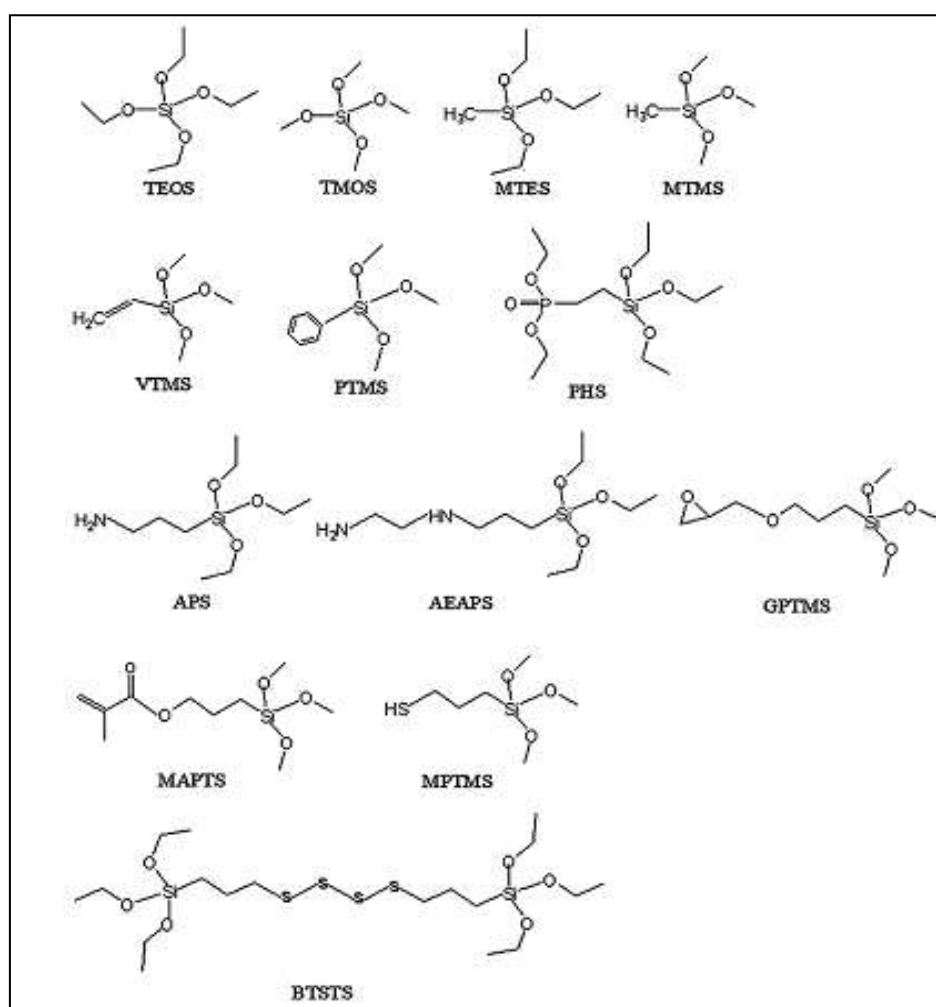


**Figure 2.6: Structure of some of the commonly used alkoxysilanes to introduce organic parts into hybrid sol-gel materials [92]**

For the preparation of hybrid sol-gel coatings having non-functional component, alkoxy silanes containing methyl groups are commonly used [111, 118, 131-135]. Commonly used organofunctional precursors are epoxy, methacrylic, acrylic, allyl, alkyd, phenyl, pyridine, amino or vinyl functional organo silanes [136-148]. Organofunctional groups such as epoxy, vinyl and methacrylic undergo further polymerization and this will lead to a higher cross-linking and better mechanical properties [140, 149]. The additional polymerization of these organofunctional groups during the preparation of the coatings helps to improve the barrier property of the coatings.

### ***2.2.3 Additives Doped Hybrid Sol-Gel Protective Coatings***

Other than the organic components, additives such as inhibitors and nanoparticles are added into the sol-gel systems in order to enhance the corrosion resistance of the sol-gel coating system. Though the addition of organic component helps to form thicker and crack free films, it reduces the wear resistance and other mechanical properties of the sol-gel films [150]. The hybrid sol-gel films can be toughened by dispersing inorganic nanoparticles into the coating matrix. Inorganic particles of size less than 500 nm are generally used since they can be homogeneously dispersed in the sol-gel matrix to have uniform coatings [119]. The addition of nanoparticles into hybrid sol-gel coatings increases the corrosion resistance of the metallic substrates due to the increased thickness and reduced porosity of such coating system [151, 152]. There are two approaches for the incorporation of nanoparticles into the hybrid coating matrix; (1) direct introduction of nanopowders into sol-gel system [119, 132, 152]; (2) direct synthesis of oxide nanoparticles during sol-gel process [95, 112, 151, 153-168]. Even though the direct mechanical addition of nanoparticles into the hybrid sol-gel materials improves the corrosion resistance of the coatings, it does not make any direct chemical bond with the hybrid coatings. Hence, the direct synthesis of nanoparticles during the

sol-gel process is a better alternative to the mechanical introduction of nanoparticles. Another class of effective additives to enhance the corrosion resistance of the coatings is inhibitors. Inhibitors resist or control corrosion by affecting anodic or cathodic reactions [169].

### **2.3 “Smart” Coatings for Active Corrosion Protection**

The hybrid sol-gel coating can offer only *passive protection* by creating a barrier or physical layer to avoid the contact between the metallic substrates and water and other corrosive species. However, sol-gel coatings can offer adequate protection only if they are intact and devoid of any mechanical defects. Therefore, it is necessary to add some active agents to impart *active protection*. In active corrosion protection methods, corrosion inhibitors are incorporated into protective barrier layers and this decreases the corrosion rate when the passive barrier layer starts deteriorating. Active and passive protection methods are the two main approaches currently used to prevent corrosion [170].

Active protection of metallic substrates from corrosion can be achieved by the introduction of inhibitors into the coating system. The corrosion inhibitors can be added into the different components of coating system: pretreatment, primer or topcoat. Conventionally, substances containing lead, hexavalent (chromates) or trivalent chromium (dichromate) are used as corrosion inhibitive additives and this type of inhibitive species are found in pretreatment layers. However, stringent environmental regulations and legislation lead to look for an alternative to these toxic inhibiting additives. Therefore, the introduction of environmentally friendly corrosion inhibitors for protective coatings is essential. Organic corrosion inhibitors are not harmful to the environment and very effective to control corrosion. In order to have the optimum corrosion control by the inhibitors, their solubility should be in the right range in the

corrosive medium. Very low solubility of inhibitors results in the deficit of inhibitive species to diffuse or migrate to the metal surface to protect it. On the other hand, very high solubility of inhibitors may give sufficient protection for a relatively short period since the active agents will be leached out. Moreover, higher concentration of inhibitors in the coating may have negative effects on the coating by either degrading its physical and mechanical properties or causing blistering and delamination of the coating [169, 170]. To overcome this, the inhibitors can be entrapped in some containers and thereby prevents the direct interaction of the inhibitive species to the coating matrix.

A novel strategy widely employed by corrosion scientists and engineers is the encapsulation of active agents in some micro/nano structured reservoirs and disperse them uniformly into the coating systems. Based on this strategy, a new class of anticorrosion coatings that possess both passive barrier protection and active functionality in response to any changes in the local environment has been developed by material scientists. The encapsulation of inhibitors into nanocontainers helps in the smart release of inhibitive species on demand in the right quantity. Active corrosion protection helps to restore the integrity of the coating when the passive coating matrix is broken and corrosion of metallic substrates has instigated. The active corrosion protection is achieved by a self-healing mechanism.

The term self-healing in material science implies the self-recovery of all the properties and functionalities of the materials after the detrimental action of the environment. This definition of self-healing can be applied to functional coatings also. Skorb et al. reported that the partial recovery of main functionality of a material could also be considered as self-healing [171]. In fact, there has been a difference in opinion about the definition of self-healing ability of functional coatings. One school of thought is focused on the recovery of the coating integrity after the destructive action of the

external environment, i.e. the recovery at the structural level [172]. Other authors argue that the recovery of the coatings properties for a specific application (e.g. anticorrosion property) to which the coatings were prepared can be equally considered as self-healing coatings [173-175]. The argument of the latter category is as follows. The major function of a corrosion protective coating is to protect the underlying metallic substrates from corrosion and it is not mandatory to recover all the properties of the coatings. The self-delaying and protection from corrosion activity of a defect causing corrosion in a coated material by any mechanism can be considered as “self-healing”.

There are mainly two approaches to prepare self-healing coatings. The first of its kind is polymer based self-healing coatings and the concept of this class of coating is as follows: Containers in the micrometer regimes are synthesized and filled with monomers similar to that of the polymer matrix and a suitable catalyst or ultraviolet sensitive agent to initiate the polymerization of the monomer. When any damages occurred on the coatings, the coating integrity would be disrupted and this in turn resulted in the release of the entrapped polymer. The released polymer would undergo polymerization in the presence of the catalyst and repair the coatings. The commonly used sealing agents are methyl methacrylate, 2-ethylhexyl methacrylate, tertiary butylaminoethyl methacrylate and lauryl methacrylate [176-180]. White et al. first reported a structurally polymeric material having ability to automatically heal cracks [180]. In their work the healing was accomplished by incorporating a microencapsulated healing agent and a catalytic chemical trigger within the epoxy matrix. Ruthenium based Grubbs’ catalyst was used to initiate the ring opening metathesis polymerization of dicyclopentadiene. Keller et al. reported the development of poly (dimethyl siloxane) based self-healing elastomeric polymer [181]. Another approach employed to achieve hybrid self-healing coatings is based on the use of

inhibitors that can be released from the coating system. Since the direct addition of the inhibitor component into the protective coating system very frequently leads to either the deactivation of the corrosion inhibitor or degradation of the polymer matrix, it is ideal to entrap the corrosion inhibitor and avoid its any direct interaction with coating matrix [182].

The most essential part of this second approach is to fabricate nanocontainers with good compatibility with the protective coating matrix. The nanocontainers should have a shell with permeable properties to load and release the active materials in response to external stimuli. The size of the nanocontainers should be less than 300-400 nm since nanocontainers of larger size can affect the integrity of the coating matrix and thereby reducing the passive protection of the coatings [182]. When the environment of the coating changes, these nanocontainers respond rapidly by releasing the entrapped active agents onto the metallic substrates and delay corrosion [174, 183-185]. Various stimuli, which can induce the release of corrosion inhibitors from nanocontainers, are pH, temperature, redox, optical and magnetic field [186-194]

## **2.4 Active Corrosion Protection Based on Nanocontainers**

Various methods have been tried until now to develop micro and nanocontainers to host active agents. An essential requirement for a nanocontainer to be employed in a self-healing anticorrosion coating is to make the nanocontainer shell sensitive to corrosion process. The corrosion process and subsequent changes in external environment due to corrosion should trigger the release of the entrapped active agent (corrosion inhibitor). The initial approaches developed to achieve self-healing ability to provide active corrosion protection was the direct introduction of inhibitor molecules into the sol-gel coating system. A hybrid sol-gel system functions very well to host the active agents or reservoirs containing the active agents. From a corrosion perspective, the major



function of the hybrid sol-gel film is a pretreatment or primer layer for various metals and alloy surfaces and it works only as a physical barrier layer. These thin hybrid films could provide protection from corrosion for a short period of time due to the presence of cracks and pores in the coating. Zheludkevich et al. reported an enhancement in the corrosion protective performance by the incorporation of corrosion inhibitors and addition of  $\text{ZrO}_2$  nanoparticles into the sol-gel system [97, 151, 195, 196].  $\text{ZrO}_2$  nanoparticles were used as a reinforcement of hybrid sol-gel system and a reservoir for loading corrosion inhibitor [195].  $\text{Ce}(\text{NO}_3)_3$  was used as a corrosion inhibitor for loading  $\text{ZrO}_2$  nanoparticles and prolonged release of  $\text{Ce}^{3+}$  ions was observed from the reservoir to ensure self-healing ability to the hybrid coatings.

Another strategy employed to provide self-healing ability to coatings was Layer-by-Layer (LbL) assembly method in the formation of nanocontainer shell [170, 173, 174]. A change in local pH around local anodic and cathodic site is the trigger for the release of corrosion inhibitor through the shells of the nanocontainer. One such nanocontainer system was fabricated using  $\text{SiO}_2$  nanoparticles [170]. Using the LbL assembly method, charged species were coated on the surface of the nanoparticles. Here the charged nanoparticles would be the core of the smart container. The negatively charged silica nanoparticles were coated with a layer of positively charged poly(ethylene amine) (PEI), followed by the deposition of negatively charged poly(styrene sulfonate) (PSS). Then the positively charged corrosion inhibitor, benzotriazole was incorporated into the system. The inhibitor loading in the nanocontainer was increased by repeating the PSS/benzotriazole deposition [170]. LbL films made up of polyelectrolyte monolayers assembled on the surface of a nanoparticle have controlled permeability properties. Polyelectrolyte layers are permeable to small ions and organic molecules and it can contain large organic molecules and nanomaterials. Moreover, with a change in pH,

polyelectrolyte films would change their chemical composition since their degree of dissociation is pH sensitive [197]. From a corrosion protective coating perspective, polyelectrolytes have two major roles to play: (i) segregate the inhibitor molecules from the passive barrier coating matrix and thereby reducing the negative effect of the inhibitor on the integrity of the coatings, (ii) helps in the smart release of the corrosion inhibitors by controlling the permeability of polyelectrolyte layers in response to any changes in local pH, temperature, irradiation conditions and humidity [170]. Sonawane et al. reported the fabrication of self-healing coatings based on inhibitor loaded polyelectrolyte layers for corrosion protection of mild steel [198]. In their approach, inhibitor molecules (benzotriazole) and oppositely charged polyelectrolyte layers were adsorbed on the surface of ZnO nanoparticles. Their corrosion results from Tafel plot and corrosion rate analysis confirmed that the 5 wt% loading of nanocontainers was useful and optimum for the sustained release of inhibitor for the applications in the marine coatings irrespective of the operating pH [198]. Even though LbL assembled nanocontainer based coating system can provide active corrosion protection with self-healing ability, their complexity hinders their up-scaling and industrial applications.

Another approach for the development of smart nanocontainers for corrosion inhibitors for active corrosion protection is based on the release of inhibitors by ion-exchange. Bohm et al. reported ceramic corrosion inhibitor pigments containing Ce(III) and Ca(II) cation exchanged bentonite to provide effective corrosion protection to organic coated galvanized steel [199]. The bentonite pigments were dispersed in polyester resin based primer and it was compared with two other primer systems containing  $\text{Ca}^{2+}$  exchanged silica pigments and strontium chromate dispersion. The corrosion protection performance of all the three different primer systems was investigated by measuring the rate of corrosion driven organic coating delamination from the cut edge of samples

during 1000 h of salt spray testing. Their results showed that Ce-bentonite pigment showed superior corrosion protection performance to that of strontium chromate pigments at all time during salt spray testing.

Layered Double Hydroxides (LDHs) are another type of ion-exchangers used for interacting with corrosion inhibitors. LDHs contain layers of positively charged mixed metal hydroxides stabilized by anions and solvent molecules between positively charged metal hydroxide layers. The corrosion protection using LDHs is achieved by the release of inhibitors in exchange of anions from the corrosive medium. They can function either by releasing anionic corrosion inhibitors or by entrapping corrosive anionic species like chloride ions. Moreover, the LDH layers are pH specific: at high pH the inhibitors can be exchanged with OH<sup>-</sup> ions and at low pH entrapped inhibitors are released due to the dissolution of LDHs [200].

A work by Buchheit and his colleagues demonstrated the active corrosion protection for Al alloys rendered by Al-Zn-decavanadate hydrtalcite pigments in amide cured bisphenol epoxy resin [201]. The results showed that corrosion protection was achieved by the release of decavanadate from Al-Zn hydroxide based hydrtalcite particles. Corrosion inhibition was realized by the release of both vanadates and Zn<sup>2+</sup> which are anodic and cathodic inhibitors, respectively, for Al alloys. Moreover, the attacking chloride ion was exchanged for inhibiting decavanadate ion and this was proved by XRD measurements.

Williams et al. prepared hydrtalcite pigments incorporating various organic corrosion inhibitors (benzotriazole, ethyl xanthates, and oxalates) and compared their filiform corrosion efficiency on AA 2024-T3. It was proved that the inhibitor efficiency was anion dependent and benzotriazole was most efficient anion for corrosion protection, but not as efficient as chromate [202].

Zheludkevich et al. prepared a new Mg/Al and Zn/Al LDH nanocontainers doped with divanadate anion as corrosion inhibitors for aluminum alloy 2024-T3 [203]. The results of their study showed that the coatings mixed with Zn/Al LDH nanocontainers conferred well defined self-healing ability and their corrosion protection efficiency was superior to that of chromate based systems. In another work reported by Poznyak et al. from the same group organic corrosion inhibitors quinaldate and 2-mercaptobenzothiazole were incorporated into Zn-Al and Mg-Al LDH nanocontainers. The corrosion protection performance of LDH loaded with organic corrosion inhibitors towards AA 2024 aluminum alloy were studied using impedance spectroscopy and a significant reduction in the corrosion rate was observed [204].

Tedim et al. reported an enhancement in active corrosion protection using a combination of inhibitor loaded nanocontainers [205]. LDH nanocontainers were loaded with vanadates, phosphate and 2-mercaptobenzothiazole and the anticorrosion activity of these nanocontainers towards AA 2024 aluminum alloy was studied using impedance spectroscopy. In order to understand the mechanism of corrosion inhibition, the bare alloy sample was immersed in chloride solution containing inhibitor loaded LDH nanocontainers in addition to the incorporation of these nanocontainers in commercial coatings. Their results showed that the combination of various inhibitors can be effectively improving the active corrosion protection efficiency of the coatings.

LDH can also be used as traps for aggressive corrosive species such as chlorides when no inhibitors are incorporated into LDH layers. In another work by Tedim et al. Zn-Al layered double hydroxides intercalated with nitrate anions were used as chloride nano traps for protective organic polymeric coatings [206]. They reported that the incorporation of nitrate anion intercalated LDH into polymeric coatings significantly decreased the infiltration of chloride ions through the protective coatings. Williams and

McMurray also showed an anion exchange inhibition of filiform corrosion on organic coated AA2024-T3 Aluminum alloy by hydrotalcite based pigments [207]. Anions such as carbonates, nitrates and chromates were intercalated in LDH layers and successfully demonstrated as traps for chloride ions and thereby reducing the delamination rate of organic coatings.

The use of natural or artificially synthesized nanocontainer host for corrosion inhibitor is another approach for developing self-healing coatings for active corrosion protection. Naturally available halloysite clay nanotubes are a good container for storing active agents for controlled release. Many researchers [208-214] investigated the utility of halloysite nanotubes for active corrosion protection based on self-healing ability. Halloysite is naturally occurring alumina silicate clay with an outer diameter of 0.3  $\mu\text{m}$  and a length of 3.0  $\mu\text{m}$ . These nanocontainers are environmentally-friendly and available in thousands of tons at very low price. The interaction of halloysite nanotubes with corrosion inhibitors is pH dependent [197].

Abdullayev et al. employed halloysite tubes as nanocontainers for anticorrosion coating with benzotriazole (BTA) for 2024 aluminum alloy and copper alloy [210, 213]. They could achieve a maximum BTA loading of 5% by weight. Moreover, they could control the release rate of BTA by the formation of a metal (Cu) - BTA stoppers at the tube endings. This functionalization could enhance the loading efficiency of halloysite nanocontainers and ensure longer release time. Better loading of BTA in the nanocontainer was achieved through the formation of tube end stoppers by the successful complexation of leaking BTA with copper ions. Later this BTA loaded halloysite nanocontainers were mixed with paints and its corrosion protection performance was assessed by monitoring the localized corrosion current density on the scratches in the coating.

Recently, Joshi et al. reported an interfacial modification of clay nanotube for sustained release of corrosion inhibitors such as BTA, 2-MBT, 2-mercaptobenzimidazole for the corrosion protection of ASTM A366 steel plates [214]. The clay nanotubes were modified with release stoppers urea-formaldehyde copolymer and copper-inhibitor complexation at the tube endings. These interfacial modified clay nanotubes were added into acrylic coating for corrosion protection and the protection efficiency was investigated by microscanning the corrosion current on the scratched made in the coatings. They found that the stopper formation with urea-formaldehyde copolymer provided enhanced corrosion protection due to a longer release of corrosion inhibitors.

Shchukin and coworkers developed active anticorrosion coatings with 2-mercaptobenzothiazole (2-MBT) loaded halloysite nanotubes for 2024 aluminum alloys. Since the inhibitor loaded nanotube has no desired releasing ability and loaded 2-MBT can be leached spontaneously due to the partial solubility in water, loaded halloysite nanotube surfaces were modified with polyelectrolyte layers. 2-MBT loaded halloysite nanotubes were mixed with silane-zirconia hybrid sol-gel coatings and active corrosion protection performance was studied using electrochemical impedance spectroscopy [215]. Their study confirmed that the enhanced long-term corrosion protection for halloysite doped sol-gel coating compared to that of undoped sol-gel coating was due to the self controlled release of the corrosion inhibitor from the halloysite nanocontainers in response to corrosion process.

The major limitations of using halloysite nanotubes are its poorly defined composition, its particle size, the size of its inner hollow lumen, and the presence of 10-20 % of dense, non-hollow material in the commercially available clay tubes [197]. This limitation can be overcome by using artificially synthesized mesoporous and microporous nanomaterials as host for loading corrosion inhibitors.

Andreeva et al. developed mesoporous SiO<sub>2</sub> nanoparticles based coatings for active corrosion protection [197]. Mesoporous SiO<sub>2</sub> nanocontainers loaded with corrosion inhibitor, 2-(benzothiazol-2-ylsulfanyl)-succinic acid) were covered with polyelectrolyte layers to avoid any unwanted leakage of inhibitors. This nanocontainer system was incorporated into silane-zirconia hybrid films and applied over Al alloys using dip coating. The release of 2-(benzothiazol-2-ylsulfanyl)-succinic acid) from nanocontainer with polyelectrolyte was observed at pH 10. The self-healing ability of this coating was confirmed by Scanning Vibrating Electrode Technique (SVET) studies.

Light sensitive nanocontainers were also used as nanocontainers so that the nanocontainer can be opened under the irradiation of light at specific wavelengths. One such nanocontainer system was developed using light sensitive porous TiO<sub>2</sub> as nanocontainers for loading inhibitors [197]. This benzotriazole loaded TiO<sub>2</sub> nanocontainer was covered with polyelectrolyte layers to avoid the spontaneous releasing of benzotriazole due to its solubility in water. The Ultra Violet (UV) activated opening of TiO<sub>2</sub> nanocontainers and the release of inhibitors to retard corrosion process was confirmed by SVET experiments.

Nanocapsules developed thorough LbL assembly of oppositely charged species and emulsion polymerization can be successfully overcome by using mesoporous inorganic nanoparticles as host materials for loading corrosion inhibitors. The biggest drawback of LbL based nanocontainers is low amount of loaded inhibitors, complex design of the nanocontainer systems. This restricts their application for scaling up and long term anticorrosion performance [216]. This disadvantage could be surmounted by using porous organic microcapsules formed by emulsion polymerization and nanoparticles stabilized polymer nanocontainers based on Pickering polymerization [217, 218].

However, these nanocontainers are also having significant restrictions and limitations as far as corrosion protection is concerned [216]. The limitations suffered by these nanocontainers are (i) deactivation of the inhibitors due to the negative interaction of inhibitors with the containers, (ii) loading efficiency of the container is limited to the solubility of the inhibitors in the emulsion oil phase forming the container core, (iii) uncontrolled shorter release of inhibitors affecting long-term corrosion protection. Recently, more simple mesoporous SiO<sub>2</sub> nanoparticles without any polyelectrolyte shell coverings were demonstrated to be effective nanocontainers for storage and sustained release of inhibitors [184]. Due to their high pore volume, surface area, and high inhibitor loading efficiency mesoporous silica can be used as nanocontainers for active corrosion protection. The incorporation of these nano sized mesoporous containers would reinforce the sol-gel coating matrix and coating barrier property due to their mechanically stable and robust nature. Moreover, higher inhibitor loading was achieved using mesoporous nanoparticles as containers for corrosion inhibitors [184, 219, 220]. Borisova et al. studied protection efficiency of anticorrosive coatings containing benzotriazole loaded mesoporous silica nanoparticles [184]. Their study demonstrated pH dependent controlled release of BTA from mesoporous silica nanoparticles without additional polyelectrolyte shells and suggested inhibitor release triggered by the corrosion process itself.

Maia et al. prepared a novel self-healing protective coating with silica nanocontainers for long-term corrosion protection application [172]. They reported a one-stage synthesis of 2-MBT loaded silica nanocapsules (SiNC) through an oil-in-water microemulsion polymerization using cetyl trimethyl ammonium bromide (CTAB) as template-surfactant and ethyl ether as co-solvent. Their results showed that when SiNC loaded with 2-MBT were dispersed in NaCl solution, corrosion rate of aluminum alloy



2024 was reduced considerably. Moreover, when 2-MBT-SiNC nanocontainer system was mixed with conventional coatings, they performed better than coatings in which 2-MBT was added directly.

Yasakau et al. reported the utility of cerium molybdate nanowires prepared via a new method based on a low-temperature, controlled rate mixing process for active corrosion protection on aluminum alloys [221]. They observed that the corrosion activity at local cathodic zones in aluminum alloys were inhibited by Ce and Mo oxide/hydroxide precipitates. In addition to that, the alloy surface was covered with a dense barrier layer mainly consisting of molybdenum oxides. Mekeridis et al. reported the development of a multilayer organic-inorganic coating containing  $\text{TiO}_2$  nanocontainers for corrosion protection of AA2024-T3 [222].  $\text{TiO}_2$  nanocontainers were loaded with 8-hydroxyquinoline and incorporated into multilayer coatings made up of (3-Glycidyloxypropyl) trimethoxysilane (GPTMS) and epoxy resins. The enhanced corrosion resistance of inhibitor loaded  $\text{TiO}_2$  nanocontainer doped coatings compared to that of undoped plain coating was demonstrated using electrochemical impedance spectroscopy.

Another study reported by Balaskas of the same group showed improvement of corrosion protection efficiency of epoxy coating with  $\text{TiO}_2$  nanocontainers loaded with 8-hydroxyquinoline [223]. They observed a continuous increase in total impedance value with the time of immersion suggesting a possible self-healing effect due to the release of 8-hydroxyquinoline from  $\text{TiO}_2$  nanocontainers. Kartsonakis and colleagues incorporated cerium molybdate nanocontainers into the protective coatings for active corrosion protection of hot dip galvanized steel, magnesium alloy ZK10, and aluminum alloys 2024-T3 [224-226]. Li et al. reported the utility of Silica/polymer double walled hybrid nanotubes as stimuli responsive nanocontainers in self-healing coatings for

carbon steel [227]. The corrosion inhibitor BTA was encapsulated in the hybrid nanotubes. The BTA loaded silica/poly (methacrylic acid) nanotube containers were doped into a silane-zirconia film to obtain a self-healing coating on carbon steel. A preliminary corrosion test of carbon steel coated with pure sol-gel silane zirconia coating and self healing coating was carried out and the results confirmed that self-healing coatings with BTA loaded hybrid nanotube could hinder the corrosion process efficiently.

## **2.5 Motivation for the Present Study**

Modified 9Cr-1Mo ferritic steel is extensively used in power generation, chemical processing, and petroleum industries due to its excellent mechanical properties and corrosion resistance. This material is the favored tubing material for steam generators in fast reactors. This is also the proposed candidate material for sodium to air decay heat exchangers to be used during emergency shutdown [228-230]. Modified 9Cr-1Mo ferritic steel is also being considered for fast-reactor structural components, such as wrappers due to its low cooling rate, low irradiation creep rate, and resistance to high-temperature embrittlement.

Even though these classes of steels have good corrosion resistance, they are susceptible to localized corrosion in humid environments containing chloride anions [229]. The present operating test fast breeder reactor and commercial reactors planned for future power generation in India are located in the coastal areas. During the various stages of fabrication, transportation, and storage, the steam generator tubing materials are exposed to humid coastal environments at ambient temperature. Moreover, there is an inevitable time lag between installation and commissioning and this will lead to the exposure of modified 9Cr-1Mo ferritic steel to outside environment. Therefore, these materials should be protected from general and localized corrosion. The motivation for

the present study is to design active corrosion protection system based on novel nanocontainers to protect modified 9Cr-1Mo ferritic steel from corrosion on demand.

## **2.6 Objective of the Present Study**

Literature survey revealed that there is a need for the development of pre-treatment layer in protective coating system to replace chromate and phosphate conversion coatings, which are environmentally unfriendly. Organic-inorganic hybrid sol-gel film based coatings containing nanocontainers loaded with inhibitors are turned out to be a green alternative to toxic chromate based pretreatments. Even though active corrosion protection based on inhibitor loaded nanocontainer impregnated sol-gel hybrid coatings has been reported in the literature, there are a very few reports on the synthesis and corrosion protection application of simple nanocontainer systems. The present study focuses on the synthesis of cost effective and easily synthesizable nanocontainers that can be easily scaled up for industrial needs.

Most of the studied substrates for active corrosion protection based on inhibitor loaded nanocontainers are either aluminum or magnesium based alloys. The applicability of inhibitor loaded nanocontainer impregnated hybrid sol-gel coatings for active corrosion protection for Fe based alloys is very few and the present study looks into the corrosion protection of modified 9Cr-1Mo ferritic steels, which is an important class of material widely used in power plants for steam generator and other applications. In order to achieve these goals, three nanocontainer systems such as zirconia, silica and titania were prepared and loaded with corrosion inhibitors (BTA and 2-MBT). Later these inhibitor-loaded nanocontainers were introduced into barrier sol-gel coatings and its active and passive corrosion protections were investigated using electrochemical impedance spectroscopy studies and salt spray test. The materials, experimental methods used, and results of the studies are described in the subsequent chapters.

## CHAPTER 3

### EXPERIMENTAL: MATERIALS AND METHODS

*This chapter describes the experimental methods and materials used for this thesis work. The entire investigation is carried out towards the development of inhibitor loaded nanocontainer mixed hybrid coatings which can impart active corrosion protection based on self-healing ability. The selection of the substrate material for coating and the pretreatments applied on this substrate are discussed. The various experimental techniques employed to characterize the nanocontainers and the method for loading of inhibitor molecules into the nanocontainers and its sustained releases are described. The preparation and application of nanocontainer mixed hybrid coatings and epoxy-based coatings are included in this chapter. This chapter also describes electrochemical, corrosion and microscopy techniques and other standard methods used to evaluate and analyze the corrosion protection efficiency of various coatings.*

#### 3.1 Materials and Chemicals

All the chemicals used for the present work were of reagent grade and used without further purification. The water used in the study was purified in a three stage Millipore Milli-Q plus 185 purification system, which had a resistivity higher than 15 MΩ. cm. List of all the chemicals used for experiments are given in Table 3.1.

Name of the chemical	Abbreviations	Supplier/Manufacturer
Ethyl alcohol	C <sub>2</sub> H <sub>5</sub> OH	Merck
Isopropyl alcohol	C <sub>2</sub> H <sub>7</sub> OH	Merck
Acetone	(CH <sub>3</sub> ) <sub>2</sub> CO	Merck
Nitric acid	HNO <sub>3</sub>	Merck

Hydrochloric acid	HCl	Merck
Titanium isopropoxide	TTIP	Merck
(3-Glycidyloxypropyl) trimethoxysilane	GPTMS	Sigma-Aldrich
Benzotriazole	BTA	Sigma-Aldrich
2-Mercaptobenzothiazole	2-MBT	Sigma-Aldrich
Perchloric acid 70%	HClO <sub>4</sub>	Fisher Scientific
Sodium Chloride	NaCl	Fisher Scientific
Sodium Hydroxide	NaOH	Merck
tetra-n-propoxyzirconium	TPOZ	Sigma-Aldrich
Ammonium hydroxide	NH <sub>4</sub> OH	Merck
Tetraethoxysilane	TEOS	Sigma-Aldrich
Zirconium butoxide solution (80 wt. % in 1-butanol)	Zr(OC <sub>4</sub> H <sub>9</sub> ) <sub>4</sub>	Sigma-Aldrich
Polyethylene glycol dodecyl ether	Brij 30	Sigma-Aldrich
Ethyl acetoacetate	EAA	LOBA Chemie
Hydrofluoric acid	HF	LOBA Chemie
Hexadecyltrimethylammonium bromide	CTAB	Sigma-Aldrich
Poly (vinylpyrrolidone)	PVP	LOBA Chemie
Bisphenol-A (Epichlorohydrin) Epoxy Resin	Araldite GY 257	Huntsman
Polyaminoimidazoline	Aradur 140	Huntsman

**Table 3.1: List of chemicals used for experiments**

### 3.2 Equipments

Various instruments and equipments used for this thesis work are given in Table 3.2.

<b>Name of the Equipment with Model No.</b>	<b>Manufacturer/ Supplier</b>
IVIUMSTAT.XRe Electrochemical Interface	Ivium Technologies, Netherlands
Magnetic stirrer with hot plate	REMI
Laboratory Centrifuge R-8C	REMI
Analytical Balance BSA224S-CW	Sartorius
Ultrasonicator	PCi Analytics Pvt. Ltd, India
Hot air oven	TECHNICO, India
Dip Coating Unit Model No. HO-TH-02	HOMARC OPTOMECHATRONICS Pvt. Ltd, India
Ag/AgCl Reference electrode	Techscience, India
Field emission scanning electron microscopy	ZEISS system with electron beam energy of 10kV, Germany
High resolution transmission electron microscopy	JEOL JEM 2100, Japan
Laser Raman spectroscopy	Lab RAM HR 800, HORIBA JOBIN YVON, France
UV-visible spectroscopy	UV-2450, SHIMADZU make, Japan
Surface profiler	DEKTAK 3030 A, Sloan make, USA
Low angle XRD	STOE high resolution X-ray diffractometer, Germany
BET isotherm: Sorptomatic 1990	Thermo Quest, CE Instruments, Italy
Salt spray	Salt spray cabinet model SF/100, CW Specialist Equipment, England

**Table 3.2: List of various instruments and equipment used for thesis work**

### **3.3 Substrate for Coating**

Modified 9Cr-1Mo ferritic steel with the following chemical composition (wt %); 8.72 Cr, 0.90 Mo, 0.096 C, 0.32 Si, 0.46 Mn, 0.22 V, 0.08 Nb, 0.006 S, 0.012 P, 0.051 N, 0.1 Ni and Fe balance was used as substrate material for coating. The substrate was cut into desired dimensions for different analyses of anticorrosive properties.

#### ***3.3.1 Pretreatment of Substrate***

Modified 9Cr-1Mo ferritic steel substrates were cleaned and etched according to the following procedure. Modified 9Cr-1Mo ferritic steel sheet was cut into 20 mm×15 mm×3 mm specimens and abraded with SiC emery sheet up to 600 grit, followed by ultrasonic cleaning in acetone, deionized water and finally in ethanol. Afterwards, the substrates were cleaned in an alkaline solution containing NaOH (10 vol. %) at 60 °C for 10 min. Then the substrates were rinsed with water and dipped in another beaker containing 10 vol. % HNO<sub>3</sub>. After 10 minutes of immersion, the substrates were lifted out and rinsed with water and dried at room temperature.

### **3.4 Synthesis of Nanocontainers**

#### ***3.4.1 Synthesis of TiO<sub>2</sub> Nanocontainers***

TiO<sub>2</sub> nanotube powders were synthesized via rapid breakdown anodization (RBA) method [231]. Pretreated Ti foil was immersed directly into the electrolyte solution, 0.1 M HClO<sub>4</sub>. Anodization was performed in a two- electrode cell with a titanium foil as a working electrode and a platinum foil (4 cm ×2 cm) as a counter electrode, at a constant potential of 20 V at room temperature. A computer controlled electrochemical interface (IVIUMSTAT.Xre, IVIUM Technologies, Netherlands) was used to supply the constant potential and to record the current versus time behaviour during the anodization process. A schematic of the experimental setup for the synthesis of TiO<sub>2</sub> nanocontainers is presented in Figure 3.1. The anodization continued till the Ti foil

completely transformed into  $\text{TiO}_2$  nanotube powder. The white colored  $\text{TiO}_2$  powder was collected after several rounds of washings with deionized water. The washed  $\text{TiO}_2$  nanotube powder was mixed with ethanol and dried overnight at room temperature. After drying,  $\text{TiO}_2$  powder was calcined at  $400^\circ\text{C}$  for 2 h at a heating rate of  $10^\circ\text{C}/\text{min}$  using a muffle furnace. This  $\text{TiO}_2$  nanotube powder was used as the nanocontainer for inhibitor loading.

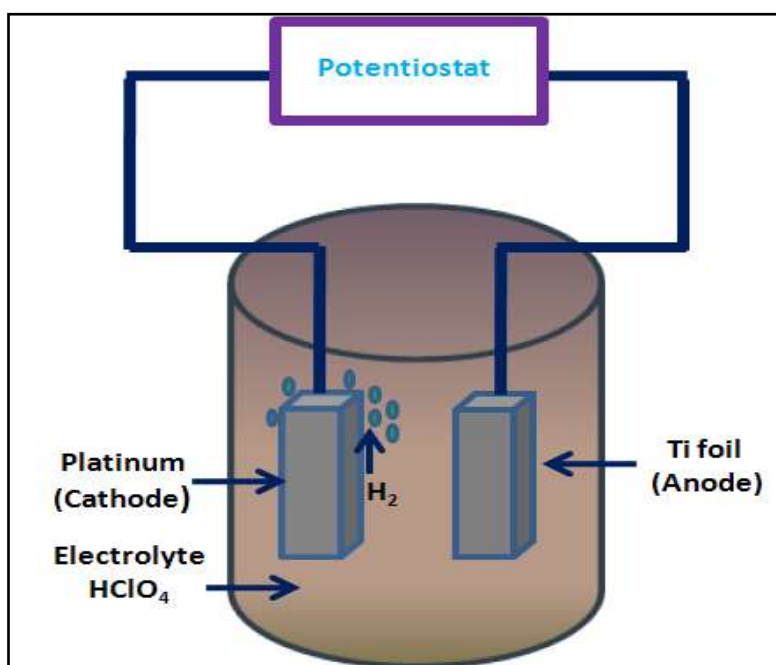


**Figure 3.1: Experimental setup for the synthesis of  $\text{TiO}_2$  nanocontainers using rapid break down anodization method**

### ***3.4.2 Synthesis of Hollow Mesoporous Silica (HMS) Nanocontainers***

The hollow mesoporous silica nanocontainer synthesis procedure adopted in this work was reported elsewhere [232]. 500 mg of Poly(vinylpyrrolidone) (PVP) and 230 mg of NaOH were dissolved in 60 ml water with stirring. When the solution turned clear, 700 mg of cetyltrimethylammonium bromide (CTAB) was added into the above solution. After the complete dissolution of CTAB, 2.3 ml of TEOS was poured into the PVP/CTAB solution under vigorous stirring. Subsequently, a white turbidity appeared



in the solution and stirring was continued for 24 h. Then the solution was transferred into a teflon lined stainless steel autoclave and sealed and heated at 80 °C for 48 h. The white solid product was recovered by filtration and dried at room temperature. The as-prepared powder was subsequently calcined at 550 °C for 10 h to remove the templates.

### 3.4.3 Synthesis of Hollow Mesoporous Zirconia (HMZ) Nanocontainers

Hollow mesoporous zirconia nanocontainers with a hollow core/porous shell structure were synthesized through a hard template method [233-235]. A schematic of the synthesis procedure is given in Figure 3.2.

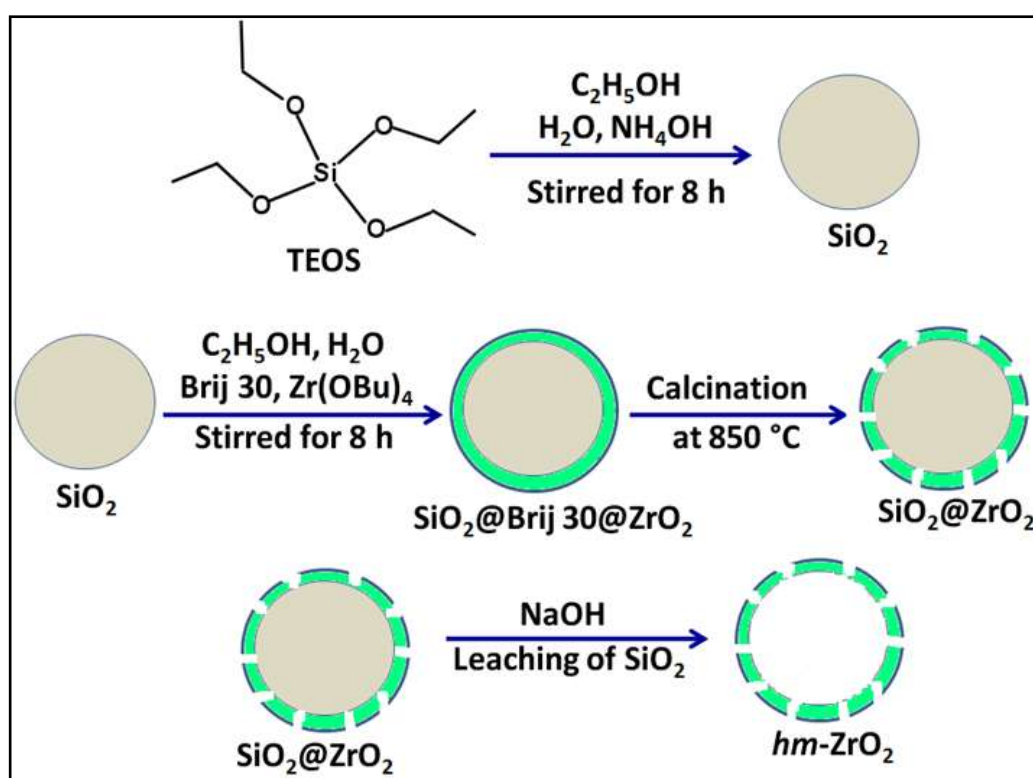


**Figure 3.2: Schematic of the synthesis procedure for HMZ nanocontainers**

Monodispersed solid silica nanoparticles were used as template for the synthesis of HMZ nanocontainers. The Stober method was used to synthesize monodispersed silica nanoparticles [236]. 75 mL of ethanol, 10 mL of water and 3.15 mL of concentrated ammonia solution were mixed and stirred. After 30 minutes of stirring, 6 mL of TEOS was added dropwise and the reaction mixture was stirred for 8 h. The resultant white

silica powders were collected by centrifugation and washed several times with water and ethanol. Then the solid silica powders were again dispersed in water and dried at room temperature.

2 g of SiO<sub>2</sub> template particles were dispersed in 200 mL of ethanol and 1 mL Brij 30 and 1 mL water was added into it. After 30 m of stirring of the reaction mixture, 6 mL of Zr (BuO)<sub>4</sub> was added and the mixture was further stirred for 8 h. The white coloured powder was collected after centrifugation and redispersed in water. These particles were aged in water for 3 days at 298 K and this aging step has a significant role on the structure of the shell. After aging, the removal of the organic material and the crystallization of the amorphous zirconium oxide layer were carried out by calcination. The white powder was calcined at 850 °C for 2 h. Finally, the silica templates were removed by a treatment with NaOH (5M) for 48 h. The powders were kept in NaOH solution with stirring and after 24 h NaOH solution was exchanged with fresh alkaline solution and the stirring continued for another 24 h. After removing the silica template, the core-shell zirconia spheres were washed five times with water and dried at 100 °C for further use.

### **3.5 Inhibitor Loading and Releasing**

Benzotriazole (BTA) and 2-mercaptobenzothiazole (2-MBT) were the corrosion inhibitors used for encapsulation. BTA was proved to be one of the effective corrosion inhibitors for various metals and alloys. BTA was used as the corrosion inhibitor which was already reported for corrosion protection of the ferrous alloys in both acidic and neutral media [237-241]. Since BTA is not effective in alkaline media, 2-MBT, which is a good corrosion inhibitor for ferrous alloys in acidic as well as alkaline media, was used [224, 242, 243]. BTA was loaded into TiO<sub>2</sub> nanocontainers only.

### 3.5.1 Loading of Inhibitor

The general procedure used for loading of inhibitors (both BTA and 2-MBT) into  $\text{TiO}_2$ , HMS, and HMZ nanocontainers is given below. Inhibitor molecules were dissolved in ethanol or acetone at desired concentration. About 100 mg of nanocontainers ( $\text{TiO}_2$ , HMS, and HMZ) was added to 50 mL of inhibitor solution and the vial was sealed in order to avoid any evaporation of solvent and stirred electromagnetically for 24 h. A schematic of the loading of inhibitors into  $\text{TiO}_2$  nanocontainers is depicted in Figure 3.3.

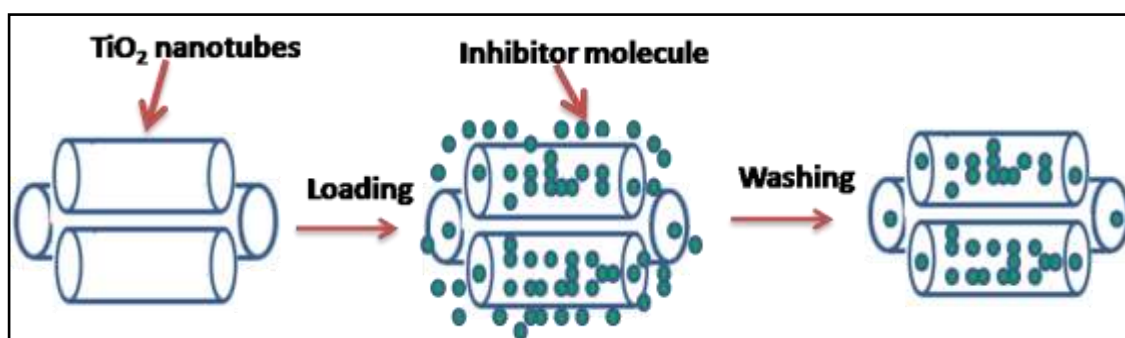


**Figure 3.3: Schematic drawing of the inhibitor loading into  $\text{TiO}_2$  nanocontainers**

Figure 3.4 shows the schematic drawing of the inhibitor loading into HMS and HMZ nanocontainers.

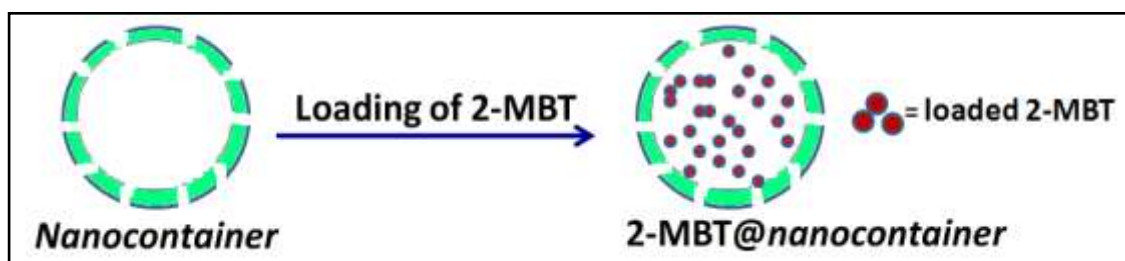


**Figure 3.4: Schematic drawing of the inhibitor loading into mesoporous silica and zirconia containers**

The loading process was carried out in the dark to prevent the photo degradation of inhibitor molecules if any. Nanocontainers loaded with inhibitor molecules were collected by centrifugation and cleaned several times in ethanol to remove inhibitors

adsorbed on the surface of the nanocontainer. The inhibitor loaded nanocontainers were obtained by drying it in air at room temperature. The filtrate was extracted out from the vial and used to determine the free inhibitor content in solution with the help of UV-visible spectroscopy studies. Laser Raman spectroscopy was also used to confirm the successful loading of inhibitors into nanocontainers.

### ***3.5.2 Releasing of Inhibitor***

Briefly, 50 mg of 2-MBT/BTA loaded nanocontainers was dispersed in 150 mL of 0.05 M NaCl at different pH values of 3, 7 and 10 (releasing medium) at room temperature and the resulting solution was stirred at a rate of 500 rpm using a magnetic stirrer. The releasing experiments for BTA@TiO<sub>2</sub> nanocontainer system was carried out at pH 2, 4 and 7, since the inhibitive effect of BTA in alkaline solution on ferrous alloy is insignificant. NaCl solution with acidic pH was obtained by adding 0.1 M HCl drop by drop to NaCl solution. NaCl solution with alkaline pH was obtained by adding 0.1 M NaOH drop by drop to NaCl solution. The pH of the solution was monitored by a pH meter. The pH of the NaCl solution was considered to be neutral since neither Na<sup>+</sup> nor Cl<sup>-</sup> would undergo hydrolysis with water molecules and hence there would not be any changes in the concentrations of H<sup>+</sup> and OH<sup>-</sup> ions. 2 mL of the solution was extracted out using a micropipette at known time intervals for analysis. Then the extracted suspension was centrifuged to remove any suspended mesoporous silica powder. The supernatant solution was measured by UV-vis absorption analysis. After being measured, the upper solution and the suspended solid particles were immediately poured back. The releasing of inhibitors was monitored by absorption intensity peak at *ca.* 325 nm for 2-MBT and 260 nm for BTA. A calibration curve for both BTA and 2-MBT was obtained by taking absorbance vs 2-MBT concentration between 0.01

mg/mL to 1 mg/mL as parameters. For this interval, the calibration curve fit the Lambert-Beer law for 2-MBT,

$$A = 4.41754 \times C + 0.08424 \quad (3.1)$$

where A is the absorbance and C is the concentration in mg/mL. The absorbance values obtained at given intervals of time from the releasing experiments are incorporated in the above-mentioned equation and corresponding concentration and amount of inhibitor released is estimated.

### **3.6 Preparation of Hybrid Barrier Coatings**

Two types of hybrid sol-gel coatings were applied on modified 9Cr1Mo ferritic steels. The first type of hybrid coating applied and tested was silane-titania hybrid coatings. The second hybrid coating used was zirconia-silane hybrid coatings. Both the coatings were synthesized through sol-gel route. Since the barrier property of the zirconia-silane coating was found to be better during initial studies, it was preferred over silane-titania hybrid coatings for long term corrosion studies.

#### ***3.6.1 Silane-Titania Hybrid Barrier Coatings***

The synthesis procedure for silane-titania sol-gel coating is given below. The organosilane sol for this purpose was prepared using 8 ml of (3-Glycidyloxypropyl) trimethoxysilane (GPTMS) added drop wise to a mixture containing 8 ml of isopropyl alcohol and 1 ml of acidified water. This silane solution was then kept for stirring for 1 h [244]. The titania sol was prepared by using mixed solution of titanium isopropoxide and ethanol, which was added to a mixed solution of ethanol and water acidified with 70% nitric acid. These solutions were stirred vigorously for 24 h to carry out the hydrolysis. Then the titania sol and the organo silane sol was mixed in a 1:1 volume ratio and stirred vigorously for another 1 h. This hybrid sol was then kept for aging for 24 h. Ethanol based solutions of benzotriazole was used instead of ethanol during the

preparation of titania sol for the direct impregnation of the inhibitor molecule to the sol-gel coatings. In order to get the inhibitor loaded nanocontainer doped sol-gel coatings, the nanocontainers loaded with the inhibitor ( $3 \text{ mg mL}^{-1}$ ) was dispersed in the final hybrid sol and ultrasonicated for 5 minutes.

### ***3.6.2 Silane-Zirconia Hybrid Barrier Coatings***

The second hybrid organic (silane)-inorganic (zirconia) films were prepared using sol-gel route by mixing an organosiloxane alkosol and an alkosol containing zirconia precursor. The silane based alkosol was prepared by hydrolysis of GPTMS in 2-propanol adding aqueous  $\text{HNO}_3$  solution in an 8:8:1 (GPTMS/2-propanol/water) volume ratio. This silane solution was then stirred for 1 h. The second sol was obtained by hydrolyzing tetra-n-propoxyzirconium (TPOZ) precursor. Initially equal volumes of TPOZ (70 wt% in 1-propanol) and ethylacetoacetate were mixed and ultrasonically agitated in water bath at room temperature for 20 min to stabilize TPOZ by ethylacetoacetate complexant. About 10 vol. % of acidified water ( $\text{HNO}_3$ , pH  $\sim 1$ ) was added dropwise to the sol after 20 minutes ultrasonic agitation. The resulting sol was again agitated for 2 h for complete hydrolysis. Then the zirconia sol and the organosiloxane sol were mixed in a 1:2 volume ratio and stirred vigorously for another 1 h [244]. This hybrid sol was then aged for 24 h prior to the application of the coating. Four different types of coatings were prepared. At first, coatings free of any inhibitor and nanocontainer were prepared and this is named as CS i.e. plain silane zirconia hybrid barrier coating. Secondly, the coating with the direct addition of 2-MBT was prepared and it is referred as CS-I. Then the coatings incorporated with empty nanocontainers were prepared and it is referred as CS-N. Finally, coatings containing inhibitor loaded nanocontainers were prepared and it is referred as CS-NI.

### **3.7 Deposition of Hybrid Barrier Coatings**

The hybrid barrier coatings on modified 9Cr-1Mo ferritic steel with and without inhibitor loaded nanocontainers were obtained via dip coating method. The hybrid sol-gel films were deposited on the substrate using dip coating unit (model no HO-TH-02) obtained from Holmarc Optomechatronics Pvt.Ltd, India. The substrates cut into appropriate dimensions were immersed in the hybrid sol and allow staying in the sol for 100 s. Thereafter the immersed specimen was withdrawn at a constant lifting speed of 2 mm s<sup>-1</sup>. The dipping procedure was repeated three times in order to cover any cracks and defects including any pores present in the previous coating. The coated substrate was dried in air and then baked at 120 °C for 1 h.

### **3.8 Preparation of Epoxy Based Coating for Long Term Corrosion Test**

The major steps involved in the preparation and application of epoxy based coating is given below:

- Preparation of modified 9Cr-1Mo ferritic steel coupons of dimension 60×50×3 mm
- Grinding the coupon surface with SiC emery paper up to 600 grade
- Cleaning the coupons in acetone ultrasonically
- Dipping the cleaned coupons in 10 wt% NaOH solution for surface activation
- Dipping the coupons in 10 vol.% HNO<sub>3</sub>
- Applying the nanocontainer mixed hybrid coating
- Applying the red oxide rich epoxy primer coat
- Applying epoxy based topcoat

Plain epoxy coated specimens' corrosion protective properties were compared with that of epoxy coating nanocontainer mixed hybrid coating.

The design of the epoxy coatings developed for long term corrosion test is given in Figure 3.5.

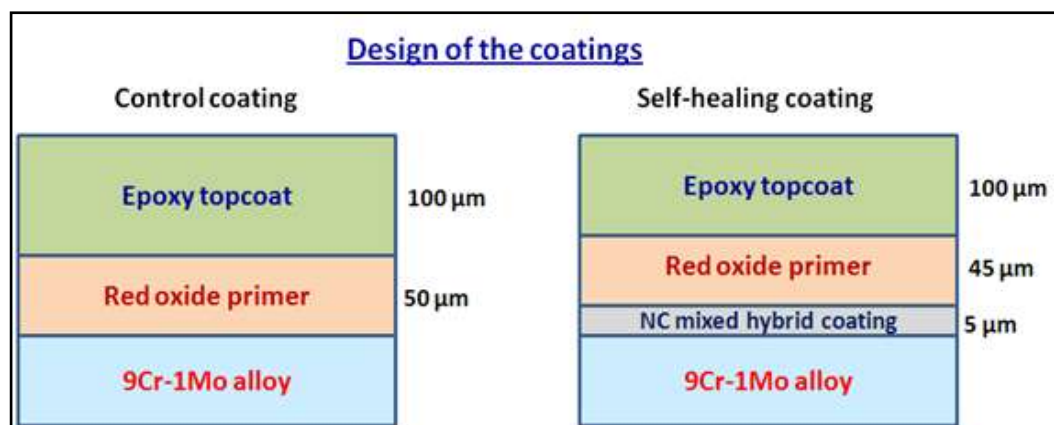


**Figure 3.5: Design of the epoxy based coatings for long term corrosion test**

Nanocontainer mixed hybrid coating was prepared and applied on the substrate using the dip coating method. Araldite GY 257 with Aradur 140, the solvent free low viscosity epoxy system obtained from Huntsman Advanced Materials (India) Pvt. Ltd. was used for epoxy coating. Araldite GY 257 is a low viscosity, Bisphenol-a based crystallization free epoxy resin modified with a reactive diluent with attractive processing properties. Aradur 140 is a high viscosity polyamidamine curing agent for the formulation of flexible coatings and to provide excellent adhesion properties to the coatings. The weight ratio of the epoxy resin to curing agent was 2:1. Red oxide particles supplied by Huntsman was used to make red oxide rich epoxy primer coating. About 2 wt% of red oxide paste was added into 20 g of the epoxy resin, Araldite GY 257 and mixed thoroughly in a mortar using a pestle. After the well dispersion of the red oxide particles in the resin, 10 g of the curing agent was added and the resulting mixture was stirred and mixed thoroughly to obtain well dispersed slurry of epoxy coating system. This epoxy coating was applied over the substrate by using a brush. The transparent epoxy top coat was prepared by mixing Araldite GY 257 and Aradur 140 in 2:1 weight ratio and applied over the substrate using brush.



### **3.9 Characterization Methods**

#### ***3.9.1 Scanning Electron Microscopy (SEM)***

A field emission scanning electron microscopy, FE-SEM, ZEISS system with EDX (Oxford) was used to view the morphology of nanocontainers and hybrid coatings and also to get the chemical composition. Nanocontainers were dispersed in acetone using ultrasonication bath and few drops of this dispersion was placed on a glass slides and images were obtained using both InLens and SE2 detectors and the electron accelerating voltage (EHT) was kept at 10 to 15 kV.

The morphology of various hybrid coatings after immersion in NaCl solution was viewed using Desktop Mini-SEM, SNE 3000 M with EDX. The coated samples were directly glued on the carbon tape on the sample holder and the images of the coatings were obtained using SE detectors at an electron accelerating voltage of 25 kV at different magnifications. Energy dispersive-X-ray (EDX) spectroscopy was performed using a scanning electron microscope (Mini-SEM, SNE 3000 M) coupled with EDX, liquid nitrogen free XFlash silicon Drift Detectors (SDD), QUANTAX, Bruker.

#### ***3.9.2 Transmission Electron Microscopy (TEM)***

High resolution transmission electron microscopy, HRTEM (JEOL JEM 2100, Japan) was employed to characterize the morphology, size and the porous structure of the nanocontainers. A small quantity of nanocontainers was dispersed in ethyl alcohol under ultrasonication and few drops of the dispersed samples were placed on the sample holder and analyzed without further treatment. The TEM images of the samples were obtained with an accelerating voltage of 200 kV.

#### ***3.9.3 Laser Raman spectroscopy (LRS)***

Laser Raman spectroscopy, LRS (Lab RAM HR 800, HORIBA JOBIN YVON Raman spectrometer equipped with 1800 grooves/mm holographic grating) was used for the

phase analysis of nanocontainers and to confirm the loading of inhibitor molecules into nanocontainers. LRS was also used for investigating the surface of the epoxy coated specimen during salt spray test. The sample was placed under Olympus BXFM-ILHS microscope mounted at the entrance of the Raman spectrograph. Ar<sup>+</sup> laser of 488 nm was used as excitation source and the power of the laser at the sample was ~8.6 mW. The Raman spectra were recorded using a super cooled (<-110 °C) 1024×256 pixels charge coupled detector (CCD) in static mode over the range of 80-1000 cm<sup>-1</sup> with 10 s exposure time and 10 CCD accumulations.

#### ***3.9.4 Nitrogen Adsorption/Desorption***

The surface area and porous structure of hollow mesoporous silica and zirconia nanocontainers were determined using N<sub>2</sub> sorption method. Nitrogen adsorption/desorption isotherms were recorded at 77 K on a Sorptomatic 1990 (Thermo Quest, CE Instruments, Italy). The nanocontainers were first degassed for 24 h at 150 °C in vacuum. The specific surface area was calculated by Brunauer-Emmett-Teller (BET) method [245]. The average pore size and pore size distributions were obtained from the desorption branch using Barrett-Joyner-Halenda (BJH) method [246].

#### ***3.9.5 Low Angle X-ray Scattering***

Low angle X-ray powder diffraction pattern for mesoporous silica was obtained using a STOE high resolution X-ray diffractometer (Germany). The low angle XRD measurement was recorded in the 1-5°, 2θ range at a step size of 0.05° using Cu Kα radiation with a wavelength of 1.54 Å.

#### ***3.9.6 UV-Vis Spectroscopy***

UV-Vis spectroscopy was used to investigate the loading of inhibitors into nanocontainers and to analyze the controlled release of the inhibitors from the nanocontainers. A UV-vis spectrophotometer, UV-2450, SHIMADZU make was used

to record the absorbance spectra in the wavelength region 200-800 nm. The absorbance measurements of the inhibitor solutions were made in a quartz cuvette with path length of 1 cm.

### ***3.9.7 Surface Profiler***

In order to estimate the thickness of the hybrid coatings, a using a surface profiler, DEKTAK 3030 A, Sloan make, USA was used to measure the height difference between the coated and uncoated regions.

### ***3.9.8 Cross-Hatch Tape Adhesion Test***

Tape peel test was carried out according to ASTM D 3359-09 to assess the adhesion of the coating to the substrate [247]. A square grid was realized on the surface of the coating with 20 mm long cuts at a distance of 1 mm each others. Eclometer 99 pressure sensitive adhesive tape was glued on the surface of the coating using a pencil eraser. After 90 s, the tape was removed with a strong pulling action. The grid area of the coating was examined using a magnifier in order to assess the bonding strength of the coating and photographs were taken. After the test, the samples were ranked on a 0A to 5A scale, 5A corresponding to perfect coating adhesion.

### ***3.9.9 Salt Spray Test***

Epoxy coating with nanocontainer impregnated hybrid coating and a reference epoxy coating was exposed to salt spray test in a salt spray cabinet model SF/100, CW Specialist Equipment, England. The cross scribes were made on the coated specimen using a sharp edged knife to observe the protective action of the coatings. The edges of all the tested specimens were covered with lacquer to avoid any edge attack and subsequent delamination of the coating. Salt spray test is one of the widely used accelerated testing methods to assess the quality of coatings. The salt spray experiment was carried out according to ASTM B117 [248]. The salt spray test consists of

atomizing salt solution into uniform droplets on the test specimens which was kept inside the salt spray chamber at 15° angle from the vertical. The concentration of the salt solution was 5 wt%, more than sea water. The temperature inside the salt-spray chamber was maintained at 35 °C. The pH of the salt solution is such that when atomized at 35 °C the collected solution will be in a pH range 6.5 to 7.2. The test was run continuously for 2000 h (83 days) and during the test, daily monitoring of the test specimens was carried out.

#### ***3.9.10 Electrochemical Impedance Spectroscopy (EIS)***

Various experimental techniques are available to study the corrosion protection performance of coatings. Even though accelerated corrosion tests can be effectively used to compare the protective properties of different types of coatings, these tests cannot shed any light into the mechanism of protection. Similarly, due to high IR drop, conventional DC polarization method is also not a reliable technique to study the protective properties of coatings. Moreover, both the accelerated corrosion tests and DC polarization technique cannot give any useful information on the active corrosion protection and the self-healing ability of protective coatings [249]. Electrochemical impedance spectroscopy (EIS) finds tremendous use at present to characterize the corrosion protection performance of coating systems. The powerful AC impedance technique can be used to compare the corrosion protective performance of different coatings as well as impart information on the kinetics of evolution of coating degradation and corrosion activity while immersed in a corrosive medium.

The term impedance normally refers to the resistance of a system to an excitation from its steady state condition. Impedance can be stated as the “resistance” of a system to a perturbation to its steady state potential or current. Electrochemical impedance is normally measured by applying a sinusoidal potential perturbation to the coating

system under investigation. An AC current signal is the response to this potential perturbation. Impedance gives the measure of the ability of the studied coating to resist current flowing through it [250-253]. In this study all the experiments were carried out under potentiostatic control. In a linear or pseudo linear system, the current response to a sinusoidal potential perturbation is sinusoid at the same frequency but shifted in phase. The applied small sinusoidal potential perturbation as a function of frequency and time can be expressed as:

$$E_t = E_0 \sin(\omega t) \quad (3.2)$$

$E_t$  is the potential at time  $t$ ,  $E_0$  is the amplitude of the signal, and  $\omega$  is the radial frequency. The relationship between radial frequency  $\omega$  (expressed in radians/second) and frequency  $f$  (expressed in Hertz) can be given as:

$$\omega = 2\pi f \quad (3.3)$$

The linear or pseudo linear response signal  $I_t$  for the potential perturbation  $E_t$  will be shifted in phase ( $\phi$ ) and will have a different magnitude  $I_0$ ,

$$I_t = I_0 \sin(\omega t + \phi) \quad (3.4)$$

The magnitude of impedance can be calculated using an expression analogous to Ohm's law and it is:

$$Z = \frac{E_t}{I_t} = \frac{E_0 \sin(\omega t)}{I_0 \sin(\omega t + \phi)} = Z_0 \frac{\sin(\omega t)}{\sin(\omega t + \phi)} \quad (3.5)$$

However, the current response is purely sinusoidal only for linear systems i.e. systems with only first order current response to applied potential excitation. During corrosion and degradation of coating the linearity is not maintained due to passivation or polarization effects. This can be overcome by changing the system to pseudo-linear by applying a small (1 to 10 mV) AC signal to the system and it is illustrated in Figure 3.6.

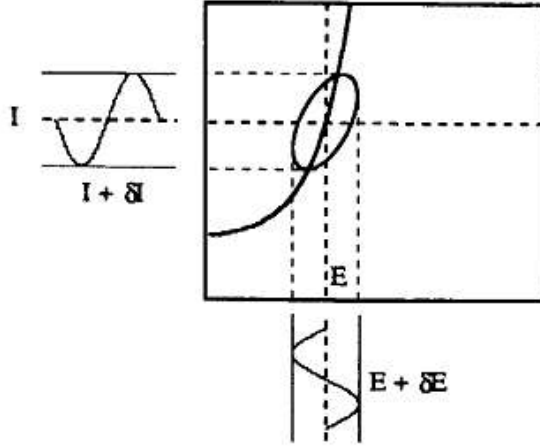


**Figure 3.6: Current versus potential curve showing pseudo-linearity [253]**

Using such a small potential signal the system will be pseudo-linear and since only the system current at the excitation frequency is measured, the large non-linear response of the DC potential cannot come into picture. In order to simplify the calculations further, the potential and its current response can be expressed as complex functions.

Using Eulers relationship,

$$e^{i\phi} = \cos \phi + i \sin \phi \quad (3.6)$$

it is possible to express the impedance as a complex function. The potential can be written as,

$$E_t = E_0 e^{i\omega t} \quad (3.7)$$

and the current response is,

$$I_t = I_0 e^{i(\omega t - \phi)} \quad (3.8)$$

Thus the impedance can be represented as,

$$Z(\omega) = \frac{E}{I} = Z_0 e^{i\phi} = Z_0 (\cos \phi + i \sin \phi) \quad (3.9)$$

From equation 3.9, it is clear that impedance  $Z(\omega)$  is composed of a real and an imaginary part. If the real part is plotted on the X-axis and the imaginary part on the Y-axis, we get a “Nyquist Plot”. A typical Nyquist plot is depicted in Figure 3.7.

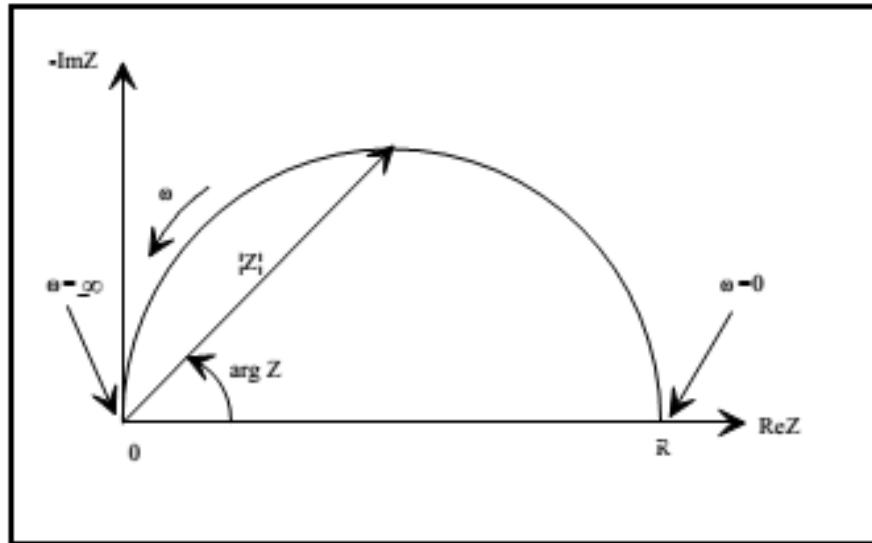


**Figure 3.7: Nyquist plot with impedance vector [254]**

The  $|Z|$  and phase angle,  $\phi$  can be displayed in polar form as a vector as shown in Figure 3.8.  $|Z|$  is the length of the vector and phase angle is the rotation of the vector.

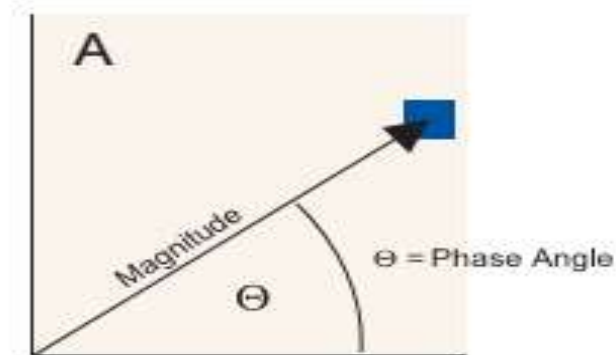


**Figure 3.8: Vector representations of  $|Z|$  and  $\phi$  [250]**

The position of the end of the vector can also be shown as a complex plane representation in Cartesian coordinate system as depicted in Figure 3.9.

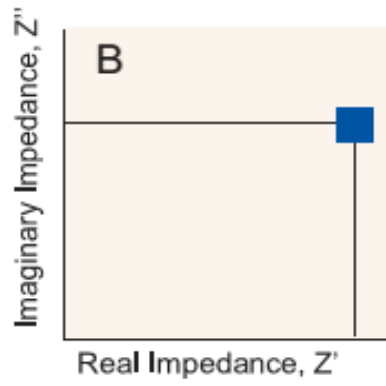


**Figure 3.9: Complex plane representations of  $|Z|$  and  $\phi$  [250]**

The point in the complex plane can be expressed as:

$$Z = Z' + iZ'' \quad (3.10)$$

The absolute magnitude,  $|Z|$  of this complex number can be easily calculated as:

$$|Z| = \sqrt{Z'^2 + Z''^2} \quad (3.11)$$

and the phase angle can be defined by:

$$\tan \phi = \frac{Z''}{Z'} \quad (3.12)$$

In order to characterize impedance, one must define both the modulus of impedance,  $|Z|$  and phase angle,  $\phi$  as well as frequency at which it is measured. When the impedance is plotted using these three parameters, it is known as “Bode Plot” as depicted in Figure 3.10.

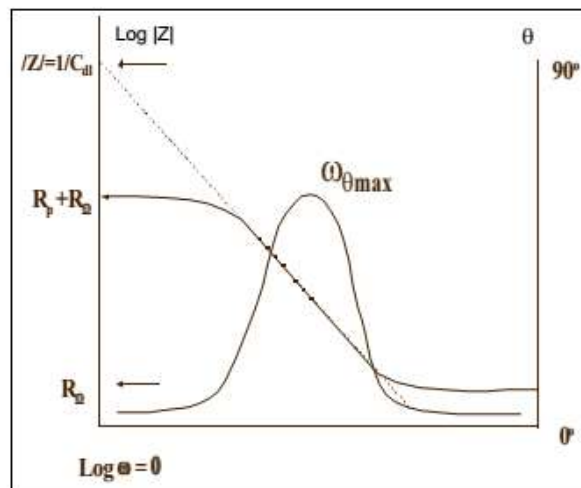


**Figure 3.10: Bode plot for simple electrochemical system [255]**



Bode plots are generally used to display impedance results since it is plotted as a function frequency and hence it shows how the impedance depends on frequency.

In a typical EIS experiment conducted for this thesis work, corrosion resistance of the hybrid sol-gel coatings on modified 9Cr-1Mo and uncoated modified 9Cr-1Mo specimens were assessed and compared. The electrochemical tests were carried out in 0.05 M NaCl at room temperature (25 °C). EIS measurements were performed in a flat cell, which has a teflon O-ring lined hole on one side. The flat surface of the test coupons (the working electrode) was pressed against the O-ring, so that the solution in the cell could access the surface inside the O-ring. On the top of the flat cell, holes are positioned to fix the reference and counter electrodes. The surface area of the working electrode (both coated and uncoated specimens) was 1 cm<sup>2</sup>. An Ag/AgCl electrode and a platinum sheet of surface area 2 cm<sup>2</sup> were used as reference and counter electrodes respectively. EIS studies were carried out with an electrochemical interface (IVIUMSTAT.Xre, IVIUM Technologies make, The Netherlands) at open circuit potential with amplitude of 10 mV. The impedance response was obtained over a frequency range between 10<sup>5</sup> Hz to 10<sup>-2</sup> Hz, recording 10 points per decade of frequency. All the EIS measurements were performed in a Faraday cage in order to avoid electromagnetic interferences. The impedance spectra were collected as a function of time, at regular intervals, up to 168 h of immersion. All the electrochemical testes were repeated three times to verify the reproducibility of the results.

The physicochemical processes take place on the metal substrate when it is immersed in the electrolyte solution for corrosion test can be manifested with the help of electrical equivalent circuits (EEC). A system's EIS spectra can be explained with the help of several cell elements and cell characteristics. The behaviour of each element can be explained using electrical components such as resistor, capacitor and inductors. A

coated sample can be treated as a collection of electrical elements. The equivalent circuit that is most commonly used to describe a coating on metallic substrate is shown in Figure 3.11.

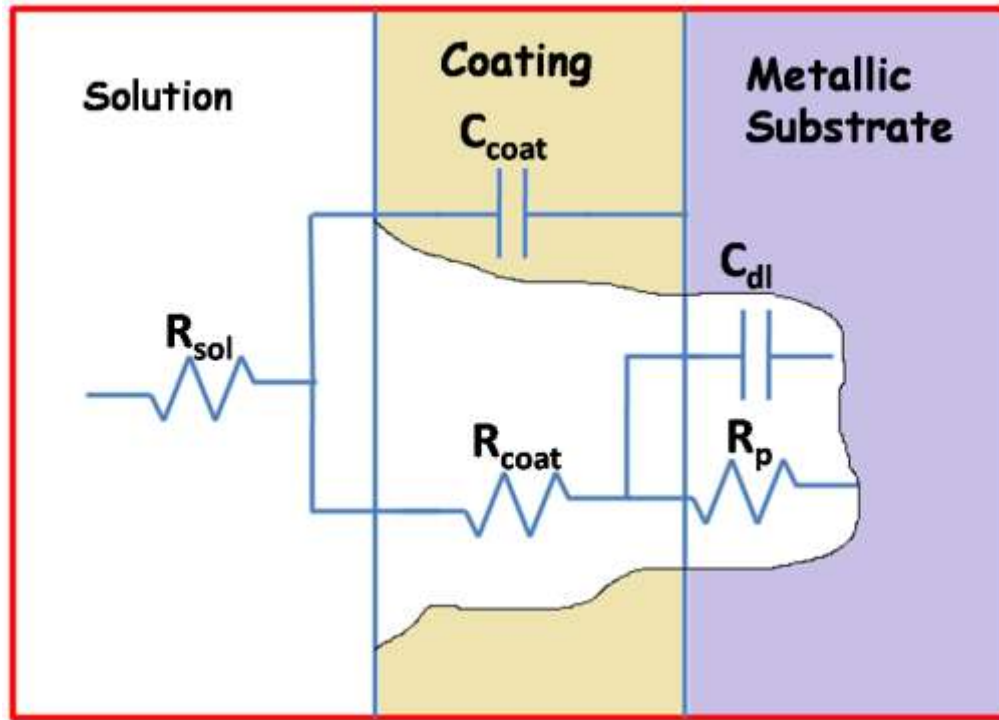


**Figure 3.11: Equivalent circuit of a coating on metallic substrate**

**$R_{sol}$ : Solution Resistance**

The resistance of the electrolyte between the reference and working electrode

**$R_{coat}$ : Coating Resistance**

The coating resistance in general, is related to electrolyte's resistance in the pores and cracks of the coating. Furthermore, the coating resistance gives the measure of obstruction offered by the coating to avoid the conduction between the metal surface and the bulk of the solution. As the immersion time increased, the pore resistance decreased owing to the entry of electrolyte to the coating through the pores. The higher value of coating resistance indicates better barrier protection of the sol-gel coated film [59, 196].

**C<sub>coat</sub>: Coating Capacitance**

C<sub>coat</sub> could be considered as a measure of the water absorption by the sol-gel coating. The coating capacitance is a very important factor for measuring the failure of the coatings. The physical and chemical properties of the coatings that affect the capacitance is given in the following equation.

$$C_{\text{coating}} = \frac{\epsilon\epsilon_0 A}{t} \quad (3.13)$$

where  $\epsilon$  is the dielectric constant of the coating,  $\epsilon_0$  is  $8.85 \times 10^{-14}$  Faraday  $\text{cm}^{-1}$ , A is the area ( $\text{cm}^2$ ), and t is the thickness (cm).

The capacitance is related to the magnitude of impedance |Z| by

$$|Z| = \frac{1}{2\pi f C_{\text{coating}}} \quad (3.14)$$

**R<sub>p</sub>: Polarization Resistance**

Polarization resistance gives a measure of the corrosion rate of a metal under the coating. The corrosion rate can be determined from the R<sub>p</sub> value for a freely corroding metal. Polarization resistance is inversely proportional to the corrosion rate.

**C<sub>dl</sub>: Double Layer Capacitance**

On the interface between an electrode and its surrounding electrolytes, charge separation occurs and an electrical double layer exists at the interface. The double layer is formed due to adsorption of the ions from the solution on the electrode surface. Both the electrode and electrolyte sides are oppositely charged and charges separated by an insulator form a capacitor. Since the interface is generally known as “double layer” in electrochemistry, the capacitance is called as double layer capacitance [254].

In our EIS study, the test specimens were immersed in NaCl solution and the impedance was measured at given time interval and these impedance measurements were analyzed by using appropriate EECs. As immersion time progresses, different

phenomena appear on the surface of the coated specimen. Several electrical equivalent circuits were tried and tested to fit the experimental impedance data and only those electrical equivalent circuits, which are having lowest chi square values, and minimum error was chosen. Impedance fitting was performed using Ivium equivalent circuit evaluator provided by Iviumsoft software.

## CHAPTER 4

### Hollow Mesoporous Zirconia Nanocontainers for Active

#### Corrosion Protection

---

*This chapter describes the fabrication of an active corrosion protection coating system with self-healing ability using inhibitor loaded hollow mesoporous zirconia nanocontainer. Zirconia nanocontainers with a hollow core/shell structure was synthesized through a hard templating approach and used as nanocontainers for loading 2-mercatobenzothiazole (2-MBT). A hybrid zirconia-silane sol-gel coating mixed with hollow mesoporous zirconia nanocontainers loaded with 2-MBT was deposited on modified 9Cr-1Mo. The corrosion protection performance of coatings with and without the addition of inhibitor loaded nanocontainers was investigated using electrochemical impedance spectroscopy (EIS). Further, artificial defects were made on the coatings in order to analyze the evolution of corrosion activity and unambiguously prove the active corrosion protection. It was found that the released inhibitor delayed the corrosion process and imparted active corrosion protection.*

---

#### 4.1 Introduction

Zirconium oxide is one of the widely used materials for various applications because of its interesting physical and chemical properties. Its application includes in refractories, pigments, piezoelectric devices, ceramic condensers, thermal barrier coatings, electrode and oxygen sensors, orthopedic implants and most importantly in catalysis [256]. Zirconia based materials with ordered mesopore structure and high surface area have been synthesized in the recent past [257-259]. Due to their large surface area and controllable pore size, mesoporous zirconia has opened many new possibilities for applications in catalysis, catalyst support and in drug delivery [260]. Due to the availability of interior cavity and highly permeable mesopore shells, hollow

mesoporous zirconia can be effectively used for loading guest species such as drug molecules or corrosion inhibitors and its controlled release.

However, the synthesis of monodispersed hollow mesoporous spheres is a challenging task. To date, template assisted method is commonly used for the synthesis of hollow mesoporous structures. Typically, a template sphere is used and on which the latter shell is deposited [261-264]. These templates are later removed by either calcination or dissolution. Nevertheless, most of this template assisted methods results in the collapse of mesopore structure while removing the templates. The amorphous oxide structure crystallizes with increase in temperature and the resulting crystal growth leads to destruction of the pore structure and disappearance of high surface area and the spherical morphology. Both the spherical micelle templating and emulsion templating generally lacks the perfection of the spheres and having relatively broad size distribution [258, 265-267].

However, it is possible to synthesis hollow mesoporous spheres with very high degree of monodispersity and perfect spherical shapes that is typically not obtained through other methods by using oxidic template spheres instead of polymer templates. Solid silica spheres made by the Stober method can be used as templates for the synthesis of hollow mesoporous zirconia spheres because they are easily obtained in large scale, uniform morphology, and controllable size.

This chapter describes a new contribution to the design of nanocontainer for the encapsulation of corrosion inhibitor and utility of this new nanocontainer system for active corrosion protection. Hollow mesoporous zirconia (HMZ) nanocontainers with a hollow core/porous shell structure were synthesized through a hard template method [233-235]. Monodispersed solid silica nanoparticles were used as template for the synthesis of hollow mesoporous zirconia. The silica nanoparticles were coated with

zirconium oxide layer and later these silica templates were removed using sodium hydroxide. The HMZ were loaded with 2-MBT and this inhibitor nanocontainer system was mixed with hybrid coating. The incorporation of HMZ nanocontainers into sol-gel coatings was not studied earlier. The 2-MBT loaded HMZ were mixed with silane-zirconia hybrid sol and applied on modified 9Cr-1Mo ferritic steel by dip coating method. The corrosion protection efficiency of following four different coatings was studied and compared using EIS in order to ascertain the contribution of each component on the protective properties of silane-zirconia hybrid coating: (i) hybrid sol-gel coated modified 9 Cr-1Mo ferritic steel, (ii) inhibitor mixed hybrid sol-gel coated modified 9 Cr- 1Mo ferritic steel, (iii) empty nanocontainer mixed hybrid sol-gel coated modified 9 Cr-1Mo ferritic steel and (iv) inhibitor loaded nanocontainer mixed modified 9 Cr-1Mo ferritic steel.

## **4.2 Experimental**

### **4.2.1 Materials**

Zirconium butoxide solution (80 wt. % in 1-butanol), tetraethoxysilane (TEOS), ethanol, concentrated ammonia solution (25 %  $\text{NH}_3$  in water), sodium hydroxide (NaOH, Merck), and Brij 30 were used to synthesize hollow mesoporous zirconia nanospheres. 2-mercaptobenzothiazole (2-MBT) was used as corrosion inhibitor, acetone was used for inhibitor loading experiments and sodium chloride (NaCl) was used for releasing experiments.

### **4.2.2 Synthesis of Hollow Mesoporous Zirconia (HMZ) Nanocontainers**

Hollow mesoporous zirconia nanocontainers with a hollow core/porous shell structure were synthesized through a hard templating method. Monodispersed silica nanoparticles were used as template for the synthesis of HMZ. Detailed procedure and

a schematic for the synthesis conditions and method are given in section 3.4.3 of chapter 3

#### ***4.2.3 Characterization of Silica Nanoparticles and HMZ Nanocontainers***

The high-resolution images of silica template and HMZ were taken using a JEOL JEM 2100 electron microscope operated at 200 kV. The powder samples were dispersed in ethyl alcohol under ultrasonication and few drops of the dispersed samples were placed on the sample holder and analyzed without further treatment. The phase analysis of HMZ was carried out using laser Raman spectroscopy (Lab RAM HR 800, HORIBA JOBIN YVON Raman spectrometer equipped with 1800 grooves/mm holographic grating). Nitrogen adsorption/desorption isotherms were recorded at 77 K on a Sorptomatic 1990.

#### ***4.2.4 Loading and Releasing of 2-MBT***

100 mg of HMZ was mixed with 50 mL of 10 mg mL<sup>-1</sup> MBT solution. The mixture was then sonicated for 30 m and stirred further for 24 h in a glass vial. After 24 h of stirring of the mixture, the nanocontainers loaded with inhibitor molecules were taken out by centrifugation and cleaned with water. The MBT loaded HMZ was obtained by drying at room temperature. The filtrate was extracted from the vial and used for UV-visible spectroscopy studies to confirm the encapsulation of MBT. UV-visible spectroscopy (UV-2450, SHIMADZU make, Japan) was used for UV-vis analysis. Laser Raman spectroscopy (LRS) was also used to confirm the loading of 2-MBT into HMZ. A detailed description of loading of 2-MBT into HMZ is given in section 3.5.1 of chapter 3.

50 mg of MBT loaded HMZ was dispersed in 150 mL of releasing medium (0.05 M NaCl) at different pH values of 3, 7 and 10 at room temperature and the solution was stirred at a rate of 500 rpm using a magnetic stirrer. 1 mL of the solution was pipetted



out at given time intervals for UV-visible analysis. After the measurement, the solution was poured back immediately to the solution.

#### ***4.2.5 Development of Coatings on Modified 9Cr-1Mo***

The modified 9Cr-1Mo ferritic steel substrates were cleaned and etched prior to the application of hybrid coating. The procedure employed for the pretreatment of modified 9Cr-1Mo is given in section 3.3.1 of chapter 3. A silane-zirconia hybrid coating was applied on the substrate as barrier coating and its detailed synthesis procedure is described in section 3.6.2 of chapter 3. Four different types of coatings were prepared. At first, coatings free of any inhibitor and nanocontainer were prepared and this is named as CS i.e. plain silane zirconia hybrid barrier coating. Secondly, inhibitors (2-MBT) were mixed directly with the hybrid coating was produced and named it as CS-I. Then the coatings incorporated with empty nanocontainers were prepared and it is referred as CS-N. Finally, coatings containing inhibitor loaded nanocontainers were prepared and it is referred as CS-NI. All the above mentioned three sol solutions were deposited on the modified 9Cr-1Mo steel by dip coating procedure, i.e., immersing a specimen in the hybrid sol-gel mixture for 100 s and thereafter, withdrawn at a constant lifting speed of  $2 \text{ mm s}^{-1}$ . The coated substrate was dried in air and then baked at  $120^\circ\text{C}$  for 1 h.

#### ***4.2.6 Evaluation of Anticorrosion Efficiency of Coatings***

Electrochemical impedance spectroscopy (EIS) was used to assess and compare the anticorrosion efficiency of the developed hybrid coatings on modified 9Cr-1Mo ferritic steel without and with artificial defect, during 1 week of immersion in 0.05 M NaCl solution and in 0.01 M NaCl solution, respectively. EIS measurements were carried out using Iviumstat. XRe. at open circuit potential, by applying a sinusoidal excitation of 10 mV in the frequency range of 100 kHz-10 mHz recording 10 points per decade of

frequency. A flat cell was used consisting of an Ag/AgCl reference electrode, platinum counter electrode and the coated modified 9Cr-1Mo ferritic steel of 1 cm<sup>2</sup> as working electrode. The morphology and composition of the coated substrates after immersion in 0.05 M NaCl solution was analyzed by scanning electron microscope and attached energy dispersive X-ray analysis (EDX) system.

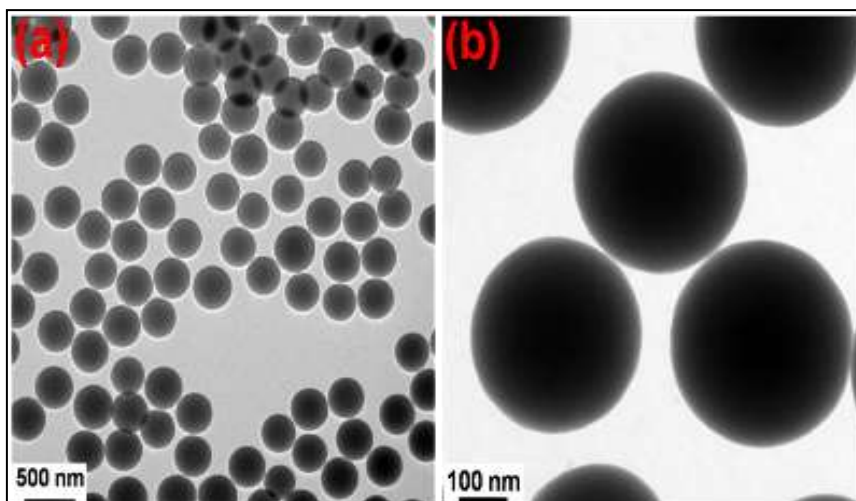
### **4.3 Results and Discussion**

#### ***4.3.1 Synthesis and Characterization of HMZ Nanocontainers***

The five steps involved in the preparation of hollow mesoporous zirconia are described below.

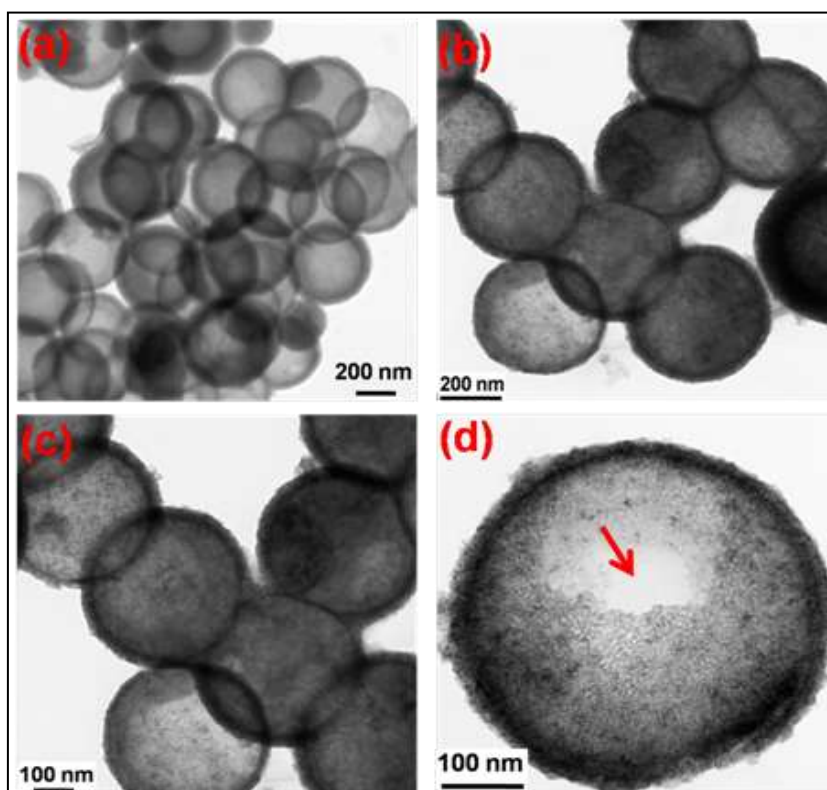
1. Monodispersed silica template nanoparticles were synthesized using the well known Stober method [236].
2. The prepared monodispersed silica nanoparticles were then coated with amorphous layer of zirconium hydroxide during the hydrolysis of zirconium butoxide in the presence of Brij 30.
3. The silica core with the zirconia shell containing Brij 30 was aged in water for 3 days at room temperature.
4. Later the silica core with zirconia shell was calcined at 850°C to remove the organics and to achieve the crystallization of the shell.
5. Finally, the template, silica core was removed using NaOH (5 M) treatment for 48 h. The silica particles were leached out through the pores present in the zirconia shell. The removal of solid silica core particles resulted in the formation of hollow mesoporous zirconia nanocontainers.

Figure 4.1 depicts the HRTEM images of silica template particles having average diameter of 375 nm.



**Figure 4.1: HRTEM images of solid silica nanoparticles at different magnifications**

Figure 4.2 presents the HRTEM images of HMZ nanocontainers obtained after the removal of silica templates.



**Figure 4.2: HRTEM images of HMZ nanocontainers at different magnifications**

As presented in the HRTEM images, the average thickness of zirconia layer was 30 nm. The perfectly shaped spherical morphology of the zirconia nanocontainer was maintained after calcination and the removal of silica template with NaOH treatment (Figure 4.2). The porous structure of the shell helped the NaOH solution to access the core of the nanocontainer and dissolve the silica. The removal of silica particle from the interior confirmed that the zirconia nanocontainer had a porous structure. As shown in the HRTEM image (Figure (4.2d)) the hollowness was the most important structural feature of the as prepared zirconia nanospheres. Both the porous structure and hollowness are very essential for high loading capacity of the inhibitor molecules. During encapsulation, the pores on the shell facilitate the diffusion of the inhibitor molecules and the empty space inside the zirconia sphere facilitates the storage of inhibitor molecules. Moreover, the porous structure of the shell makes ease on demand release of the inhibitor molecules.

The phase of the as prepared hollow mesoporous zirconia was investigated using laser Raman spectroscopy. Figure 4.3 shows the Raman spectrum of hollow mesoporous zirconia.

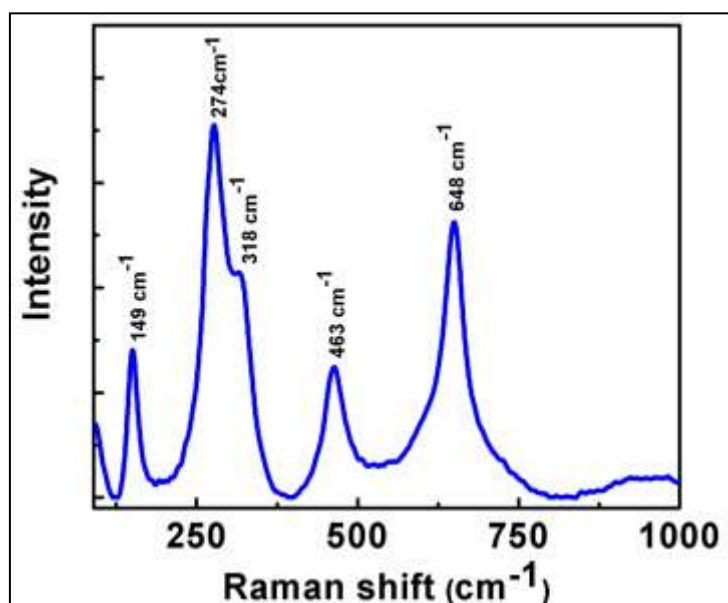


**Figure 4.3: Raman spectra of as prepared HMZ nanocontainers**

As revealed by Figure 4.3, the characteristic phonon modes of tetragonal phase of zirconia were observed in the Raman spectra. Five Raman active modes of tetragonal phase were observed. The bands at  $149\text{ cm}^{-1}$ ,  $274\text{ cm}^{-1}$ , and  $463\text{ cm}^{-1}$  are assigned to the  $E_g$  mode of vibration of tetragonal phase [268]. The bands at  $318\text{ cm}^{-1}$  and  $648\text{ cm}^{-1}$  were of  $B_{1g}$  mode.

The mesoporosity of the sample was confirmed by  $N_2$  adsorption-desorption isotherm analysis presented in Figure 4.4.

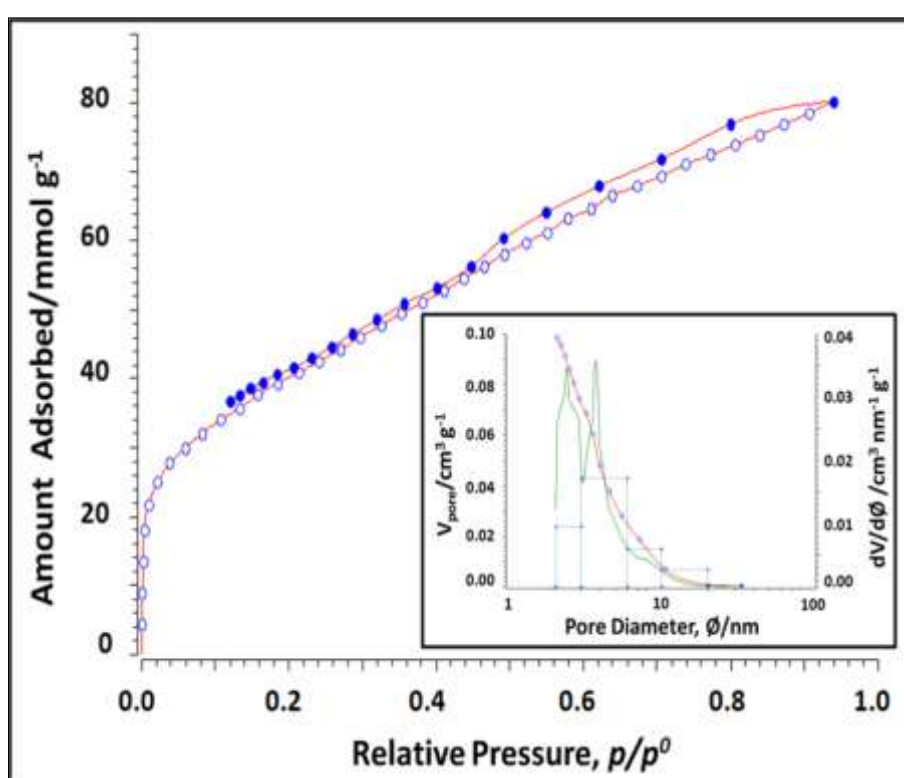


**Figure 4.4:**  $N_2$  adsorption-desorption isotherms of HMZ nanocontainers and pore size distribution (inset)

The hollow zirconia particles showed a sorption isotherm of type IV with a hysteresis loop characteristic for materials with mesoporous structure. The hysteresis loop was due to the capillary condensation in mesopore structures. The type IV adsorption isotherm is a characteristic feature of mesoporous materials. The specific surface area of hollow zirconia products was obtained using the BET method and it was found to be

145.97 m<sup>2</sup> g<sup>-1</sup>. Barrett- Joyner-Halenda (BJH) analyses revealed that the hollow zirconia products exhibited pore size centered at 3.9 nm and cumulative pore volume of 0.0993 cm<sup>3</sup> g<sup>-1</sup>. The high surface area, mesopore distributions and hollow structure of the nanocontainer are very important for inhibitor loading and controlled inhibitor release properties.

#### 4.3.2 Inhibitor Loading and Releasing Properties of HMZ Nanocontainers

2-MBT was successfully loaded into HMZ nanocontainers by mixing HMZ nanocontainers with 2-MBT solution in acetone and followed by stirring for 24 h. Figure 4.5 presents the UV-vis spectra of 2-MBT solution before and after the interactions with HMZ nanocontainers.

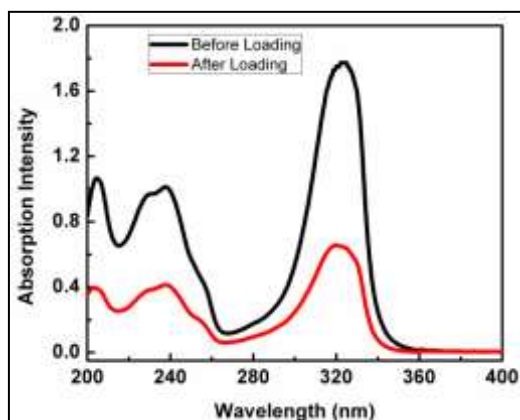


**Figure 4.5:** UV-visible spectra of 2-MBT before and after interaction with HMZ

$\lambda_{\text{max}}$  for 2-mercaptobenzothiazole is at 325 nm. The UV-visible spectra (Figure 4.5) showed that, the absorption maxima for 2-MBT was decreased after the interaction of 2-MBT molecules with HMZ nanocontainers. Moreover, there were no new absorption bands and the position of the peaks was not changed. This decrease in the absorption intensity of 2-MBT after the interaction with HMZ nanocontainers confirmed the decrease of the 2-MBT concentration in the solution as well as the successful loading of the 2-MBT molecules in the pores and interiors of HMZ nanocontainers.

The loading of the organic inhibitor molecules in inorganic nanocontainers are made possible through weak non covalent interactions such as physical adsorption, electrostatic interaction, hydrogen bonding and  $\pi$ - $\pi$  stacking [235]. The loading efficiency was calculated as follows:

$$\text{Loading efficiency} = \frac{\text{Total amount of MBT} - \text{Free MBT in solution}}{\text{Total amount of MBT}} \times 100 \quad (4.1)$$

The loading efficiency of 2-MBT in the HMZ nanocontainer was found to be  $63 \pm 2\%$ .

Furthermore, laser Raman spectroscopy confirmed the loading. Figure 4.6 depicts the Raman spectra of pure 2-MBT, HMZ and 2-MBT@HMZ.

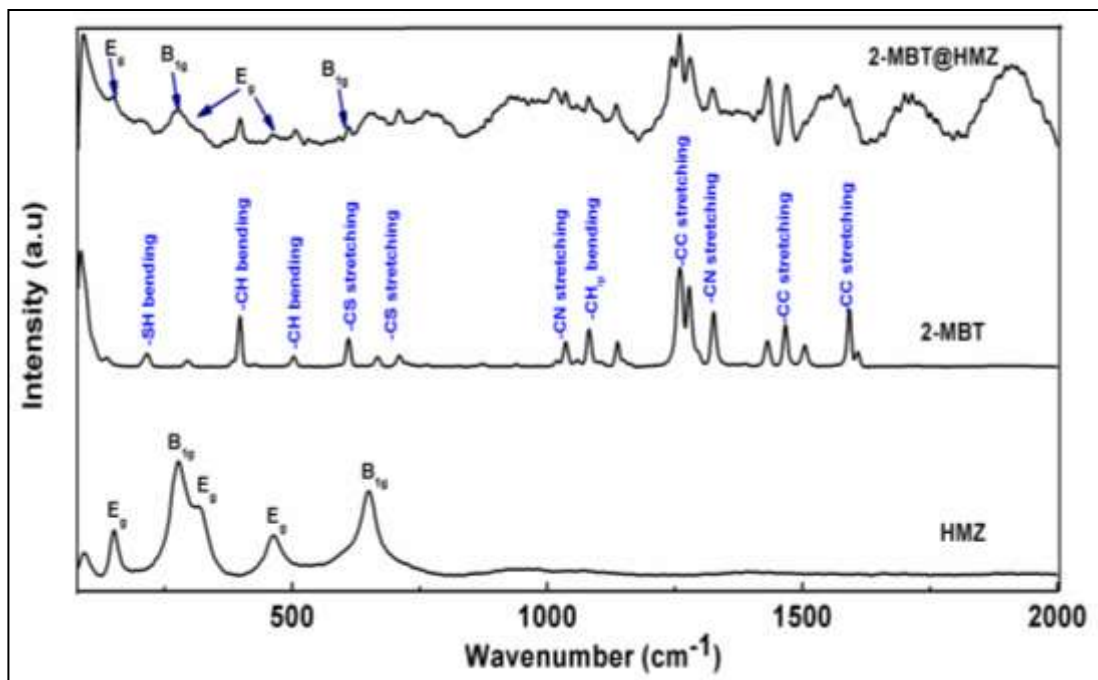


**Figure 4.6: Raman spectra of HMZ, 2-MBT and 2-MBT loaded HMZ**

The characteristic peaks of both 2-MBT and zirconia were present in the spectra of 2-MBT@HMZ. The presence of the peaks of 2-MBT in 2-MBT loaded HMZ confirmed the loading of 2-MBT in HMZ. Five Raman active modes of tetragonal phase of zirconia were observed in the Raman spectra of HMZ. The bands at  $149 \text{ cm}^{-1}$ ,  $274 \text{ cm}^{-1}$ , and  $463 \text{ cm}^{-1}$  are assigned to the  $E_g$  mode of vibration of tetragonal phase [268]. The

bands at  $318\text{ cm}^{-1}$  and  $648\text{ cm}^{-1}$  were of  $B_{1g}$  mode. All the major characteristic peaks and its assignments for 2-MBT are given in Table 4.1. The Raman spectra of MBT loaded HMZ showed the characteristic peaks of both MBT and zirconia and this confirmed the loading of 2-MBT in the HMZ nanocontainers [269-272].

**MBT Peak assignments in detail**

<b>Frequency</b>	<b>Approximate description of vibrations</b>
<b><math>149\text{ cm}^{-1}</math></b>	SH bending
<b><math>294\text{ cm}^{-1}</math></b>	CH bending
<b><math>397\text{ cm}^{-1}</math></b>	CH bending
<b><math>502\text{ cm}^{-1}</math></b>	Bz ring deformation
<b><math>610\text{ cm}^{-1}</math></b>	CS stretching
<b><math>667\text{ cm}^{-1}</math></b>	CS stretching
<b><math>710\text{ cm}^{-1}</math></b>	CS stretching
<b><math>766\text{ cm}^{-1}</math></b>	CH out of plane stretching
<b><math>874\text{ cm}^{-1}</math></b>	CH out of plane bending
<b><math>938\text{ cm}^{-1}</math></b>	CH bending
<b><math>1035\text{ cm}^{-1}</math></b>	CN stretching
<b><math>1081\text{ cm}^{-1}</math></b>	Bz ring or SCS antisymmetric stretching
<b><math>1137\text{ cm}^{-1}</math></b>	CH in plane bending
<b><math>1259\text{ cm}^{-1}</math></b>	NCS ring stretching
<b><math>1277\text{ cm}^{-1}</math></b>	CC stretching
<b><math>1431\text{ cm}^{-1}</math></b>	CC stretching
<b><math>1466\text{ cm}^{-1}</math></b>	CC in plane stretching
<b><math>1504\text{ cm}^{-1}</math></b>	CC stretching
<b><math>1591\text{ cm}^{-1}</math></b>	CC in plane stretching

**Table 4.1: Raman peak assignments for 2-MBT**



The release behaviour of 2-MBT loaded HMZ was investigated by UV-visible analysis of NaCl (0.05 M) suspensions of 2-MBT loaded HMZ at different pH values. The absorption intensity at *ca.* 325 nm was measured at given time interval for 28 h and the results are shown in Figure 4.7.

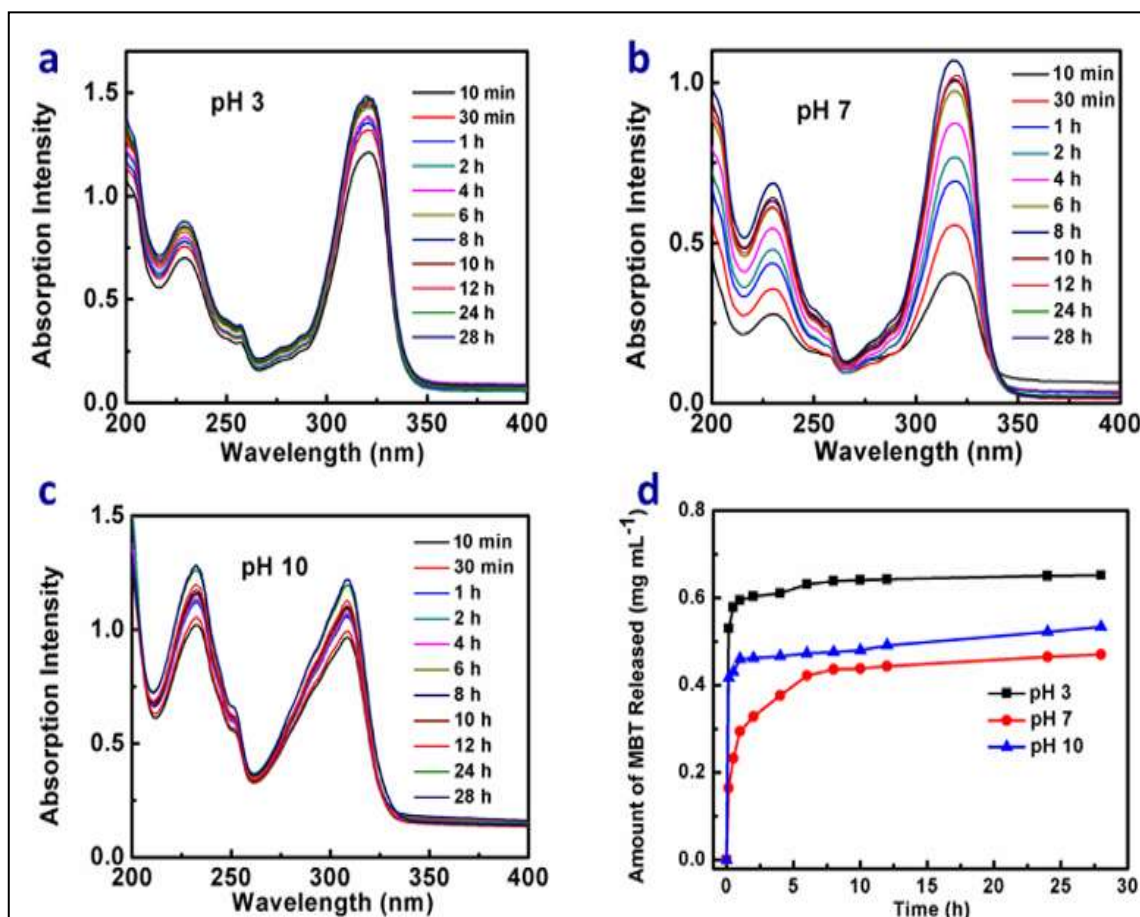


**Figure 4.7: UV-vis spectra at different times of the 0.05 M NaCl media in which 2-MBT was released from 2-MBT loaded HMZ nanocontainers (a) at pH 3, (b) at pH 7, (c) at pH 10 and (d) corresponding pH-dependent releasing behaviour of 2-MBT from HMZ-MBT system**

Figure 4.7 shows the release of 2-MBT and the increase of concentration of 2-MBT with time and attained equilibrium after 5 h. When the releasing medium had infiltrated into the pores and channels of HMZ nanocontainers, the inhibitor molecules (2-MBT) gets dissolved in the medium and released by diffusion through the pores along the aqueous pathways. The releasing of 2-MBT from HMZ followed similar release

kinetics at different pH values. A faster release was observed under alkaline and acidic conditions compared to neutral condition. The release of 2-MBT was leveled off and reached equilibrium in 4 h at pH 10.

It was observed that higher amount of 2-MBT was released from the HMZ at pH 3 and 10 compared to pH 7. The amount of 2-MBT released after 28 h under acidic and alkaline conditions were  $0.66 \text{ mg mL}^{-1}$  and  $0.53 \text{ mg mL}^{-1}$  respectively, while in neutral conditions it was  $0.45 \text{ mg mL}^{-1}$  only. The difference in the release rate and quantity of 2-MBT released from HMZ can be explained by the variation of solubility of 2-MBT and the differences in the surface charge of both 2-MBT and zirconia particles with pH. The solubility of 2-MBT is low in neutral pH, but relatively higher in alkaline and acidic conditions [172]. Both the zirconia particles and the inhibitor molecules have the same surface charge when the pH values vary from neutral pH values. Under acidic pH conditions, zirconia particles have positive surface charge whereas; at alkaline pH zirconia particles acquire negative surface charge [273]. At acidic pH, 2-MBT could be protonated due to the presence of a lone pair of electrons on the N atom and carries a positive charge [274, 275]. Thus under acidic conditions, both the zirconia particles and 2-MBT had positive charge and this led to larger electrostatic repulsion between them, thereby facilitating faster release of 2-MBT from HMZ nanocontainers in high amount. Similarly, under alkaline conditions, 2-MBT exists in ionized form with a negative charge on the S atom and thus the 2-MBT molecules carry negative surface charge [276]. It is clear from Figure 4.7(c) that the absorption band at 325 nm is shifted to 309 nm since in basic medium ( $\text{pH} > 9$ ) 2-MBT exists in ionized form with negative charge on the sulfur atom. Again this led to electrostatic repulsion between the HMZ nanocontainers and 2-MBT, thereby facilitating the diffusion of 2-MBT through the pores of HMZ nanocontainers and faster release under alkaline condition. Hence, it

could be stated that the release of loaded 2-MBT from HMZ nanocontainers was pH specific since when the pH was shifted from neutral value, the amount of 2-MBT release was more. This dependency of inhibitor release on pH confirmed the stimuli responsive intelligent releasing property of HMZ nanocontainers. This observation can be extrapolated to a corrosion process, as corrosion of metals is always accompanied by changes in local pH. Thus, the above-mentioned results are encouraging for the use of inhibitor loaded HMZ nanocontainers in anticorrosive active coating systems with self-healing ability.

#### ***4.3.3 Anticorrosion Efficiency of Various Hybrid Coatings on Modified 9Cr-1Mo Ferritic Steels***

Corrosion protection efficiency of various coatings produced on modified 9Cr-1Mo was investigated using electrochemical impedance spectroscopy (EIS) studies and scanning electron microscopy (SEM) analysis. All the coated modified 9Cr 1Mo steel specimens were immersed in 0.05 M NaCl solution and their impedance response were recorded at regular intervals of time. Figure 4.8 shows the impedance spectra of BS (uncoated modified 9Cr 1Mo specimen), CS (hybrid coating), CS-I (inhibitor mixed hybrid coating), CS-N (nanocontainer impregnated hybrid coating) and CS-NI (inhibitor loaded nanocontainer impregnated hybrid coating) after 1 h of immersion in 0.05 M NaCl solution. As revealed in Figure 4.8, all the coated substrates (CS, CS-N, and CS-NI) performed better than the uncoated modified 9Cr 1Mo ferritic steel (BS) after 1 h of immersion in 0.05 M NaCl solution. The order of corrosion protection efficiency after 1 h of immersion is as follows, CS-NI > CS-I > CS-N > CS > BS. The impedance spectrum of BS was characterized by the combination of a resistive response and a double layer capacitive response.

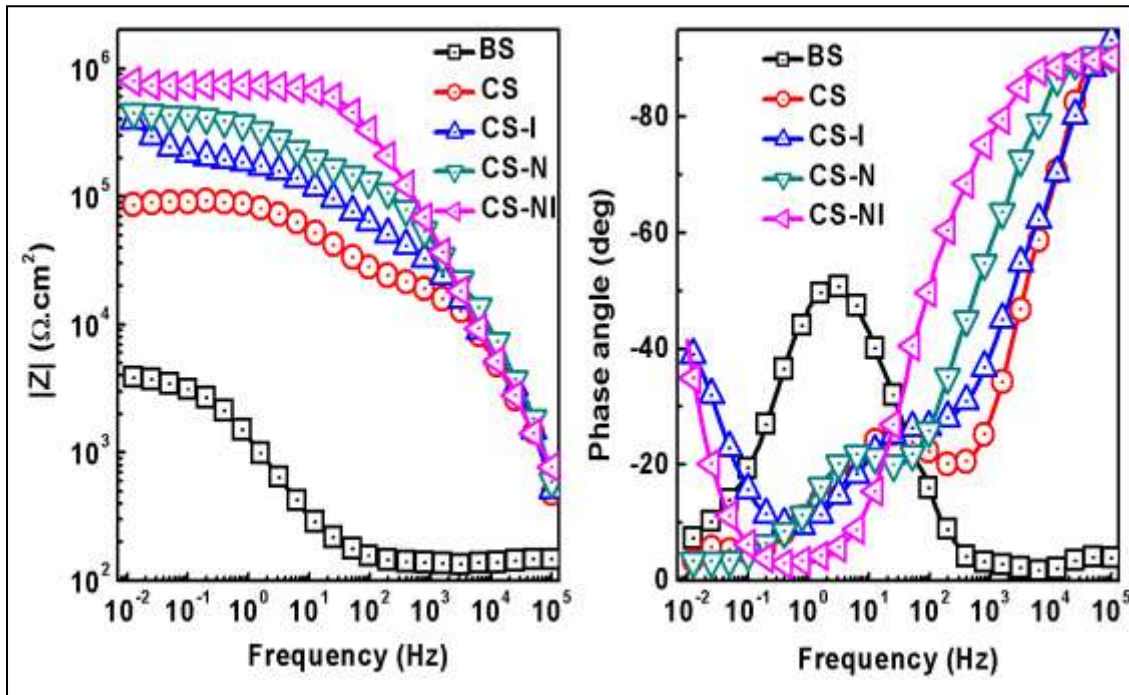


**Figure 4.8: EIS behaviour of BS, CS, CS-I, CS-N, CS-NI after 1 h of immersion in 0.05 M NaCl solution**

CS, CS-I, and CS-N showed three time constants after 1 h of immersion. The first time constant was attributed to the barrier property of the coating, the second time constant to the oxide layer and the third time constant to redox reactions at the underlying metal surface due to corrosion. Impedance response due to corrosion activity was evident at low frequency region in the spectra of CS, CS-I and CS-N even after 1 h of immersion. However, impedance spectrum of CS-NI developed only two time constant after 1 h of immersion in 0.05 M NaCl solution. The time constant at high frequency was attributed to the barrier property of the coatings. The second time constant, which was not developed fully, could be attributed to the response of the oxide film.

Figure 4.9 shows the EIS response of CS, CS-I, CS-N and CS-NI after 1 day of immersion in 0.05 M NaCl solution. Both the CS and CS-N exhibited two time constants. After one day of immersion, for both CS and CS-N, the resistive response in the low frequency region was well evolved and resistance from the oxide layer was

absent, indicating that the coatings developed conductive pathways for electrolyte. The first time constant at high frequency was attributed to the response of the barrier property of the coatings for CS, CS-I, CS-N and CS-NI.

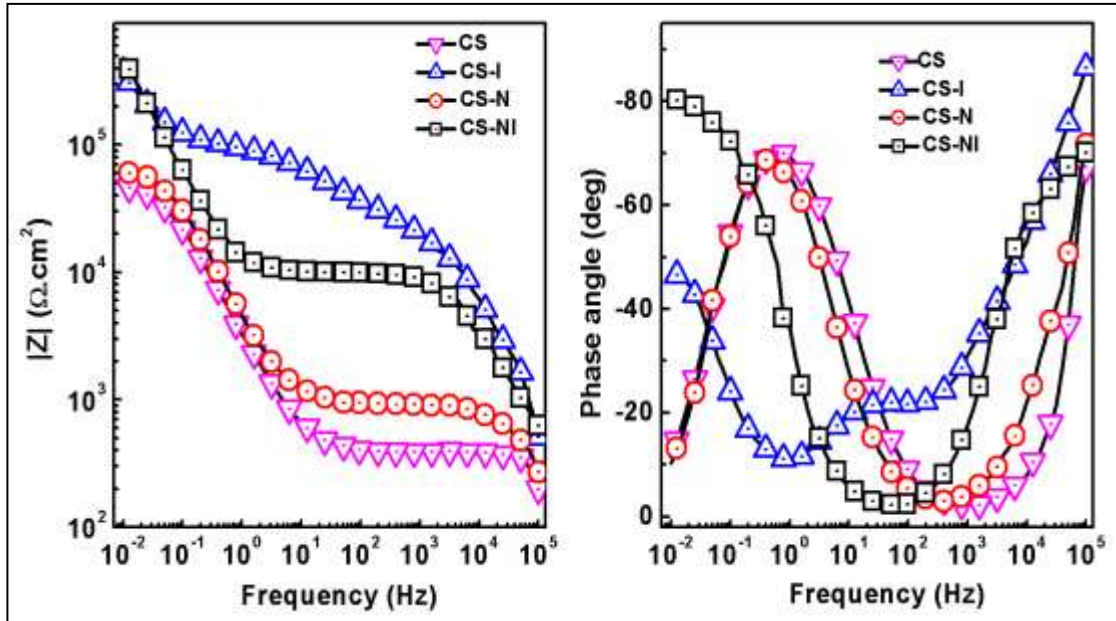


**Figure 4.9: EIS behaviour of CS, CS-I, CS-N, and CS-NI after 1 day of immersion in 0.05 M NaCl**

The second time constant at lower frequency was attributed to the impedance response of the double layer for CS and CS-N. However, the second time constant for CS-NI was attributed to the impedance response of the oxide layer interface, since no signs of corrosion activity were observed in the EIS spectra of CS-NI. As shown in Figure 4.9, the coating barrier property of both CS and CS-N were reduced compared to that CS-I and CS-NI. However, for CS-NI, no clear resistive plateau was observed revealing that the underlying metal surface was protected.

Figure 4.10 shows the EIS response of CS, CS-I, CS-N and CS-NI after 1 week of immersion in 0.05 M NaCl solution. As revealed by Figure 4.10, the barrier property of both CS, CS-I, and CS-N were deteriorated considerably and it was evidenced by the disappearance of capacitive slope in the first time constant at high frequency.

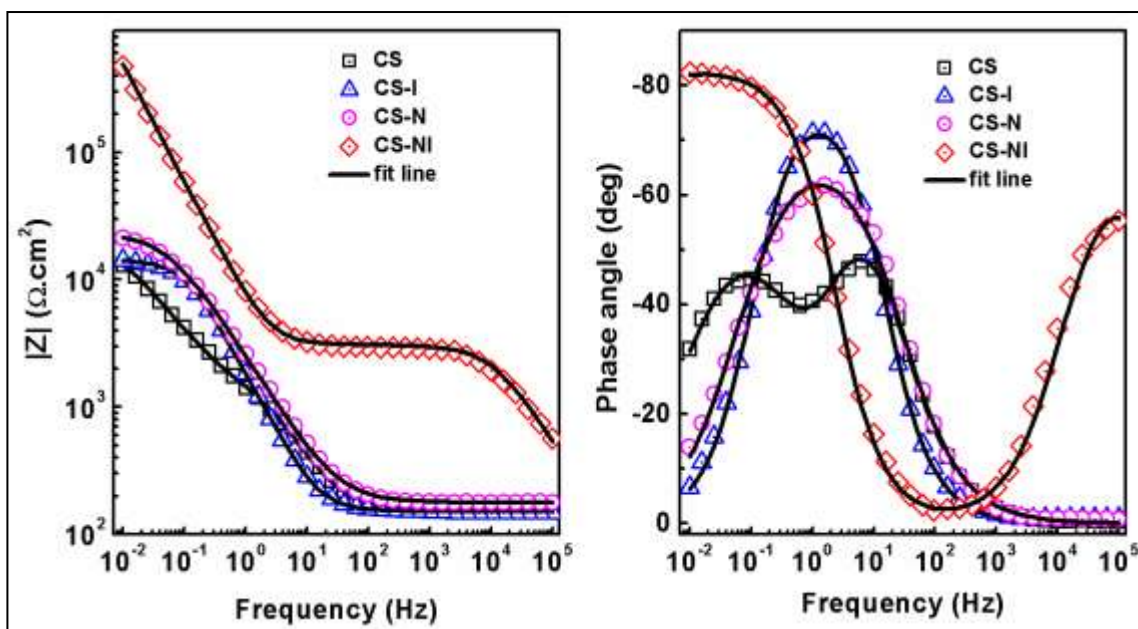


**Figure 4.10: EIS behaviour of CS, CS-I, CS-N, and CS-NI after 1 week of immersion in 0.05 M NaCl solution**

A time constant associated with mass transport of species participating in the redox reactions at the metal surface was also observed for CS. However, CS-NI still had a time constant due to the barrier property of the coatings at high frequency consisting of a capacitive slope and a resistive plateau. The impedance at low frequency can be considered as a measure of the polarization resistance of the coatings and hence can be used to examine the corrosion protection efficiency. The value of modulus of impedance for CS, CS-I, and CS-N was very low compared to CS-NI. Moreover, the value of modulus of impedance at low frequency for CS-NI remains almost unchanged even after 1 week of immersion and this indicates the active corrosion protection rendered by the release of inhibitor molecules from zirconia nanocontainers.

Figure 4.11 shows the evolution of impedance behaviour of CS-NI during 1 week of immersion in 0.05 M NaCl solution. All the impedance spectra have two time constants. The high frequency part of the spectrum is related to the barrier property of the coating and the time constant at lower frequency is attributed to the response of the



oxide film. No time constant due to any redox reactions at the underlying metal surface was observed.

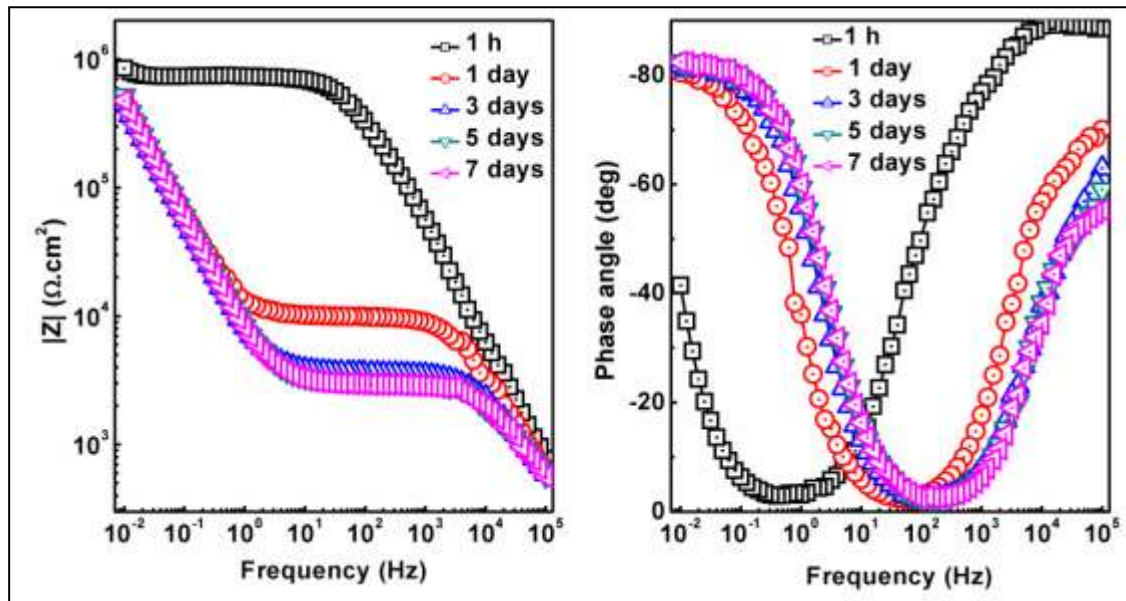


**Figure 4.11: EIS response of CS-NI during 1 week of immersion in 0.05 M NaCl**

Moreover, the second time constant was capacitive in nature since the oxide resistive plateau was not well evolved. It is observed that the resistive plateau corresponding to the coating resistance decreased continuously as the immersion progressed. These results reflect that the coating had conductive pathways for the electrolyte. Nevertheless, the value of modulus of impedance at low frequency remained almost unchanged from 1 day of immersion to 1 week of immersion. The resistance of this oxide interlayer positioned at lower frequency is very important for protecting the underlying metal surface from corrosion, since it is the last barrier for the electrolyte before accessing the metal surface. Even though the barrier property of the coating decreased for CS-NI within 1 day of immersion, the coating resistive plateau remains almost same from 3 day of immersion to 1 week of immersion.

The capacitive slope of second time constant was also did not change with immersion from 1 day to 1 week. However, CS, CS-I, and CS-N did not show this type of behaviour. The impedance response of the oxide layer did not last more than 1 day for

both CS and CS-N. After 1 day of immersion, the time constant due to oxide layer was disappeared from the EIS spectra and corrosion process started on the underlying metal surface (Figure 4.9). This result reflects the hindering of redox reactions due to the action of active agents (inhibitive species) released from the containers and thus providing active corrosion protection to the underlying metal surface for CS-NI. This corrosion protection performance of CS-NI is related to the fact that corrosion inhibitor is released from the nanocontainer mixed in the coating, since CS, CS-I, and CS-N do not show this behaviour.

SEM analysis and photographs of coated modified 9Cr 1Mo ferritic substrates support the above-mentioned EIS analysis after 1 week of immersion in 0.05 M NaCl solution. Figure 4.12 shows the photographs of the coated samples after 1 week of immersion.



**Figure 4.12: Optical photographs of the coated samples after 1 week of immersion in 0.05 M NaCl solution. The drawn circles indicate the exposed area of the coatings**

It is very clear from the figure that both CS and CS-I were badly damaged and the underlying metal surface was visible. Moreover, brown colored corrosion product was also appeared on the coating surface. For CS-N, it is observed that blistering of coatings occurred and corrosion products settled in some areas. However, CS-NI was not



attacked visibly by corrosion. Neither the delamination of coating nor the deposition of corrosion products were observed on the surface of CS-NI. This observation supports the results obtained from EIS analysis of various coatings during 1 week of immersion. Figure 4.13 shows the SEM images of various coated substrates after 1 week of exposure to 0.05 M NaCl solution.

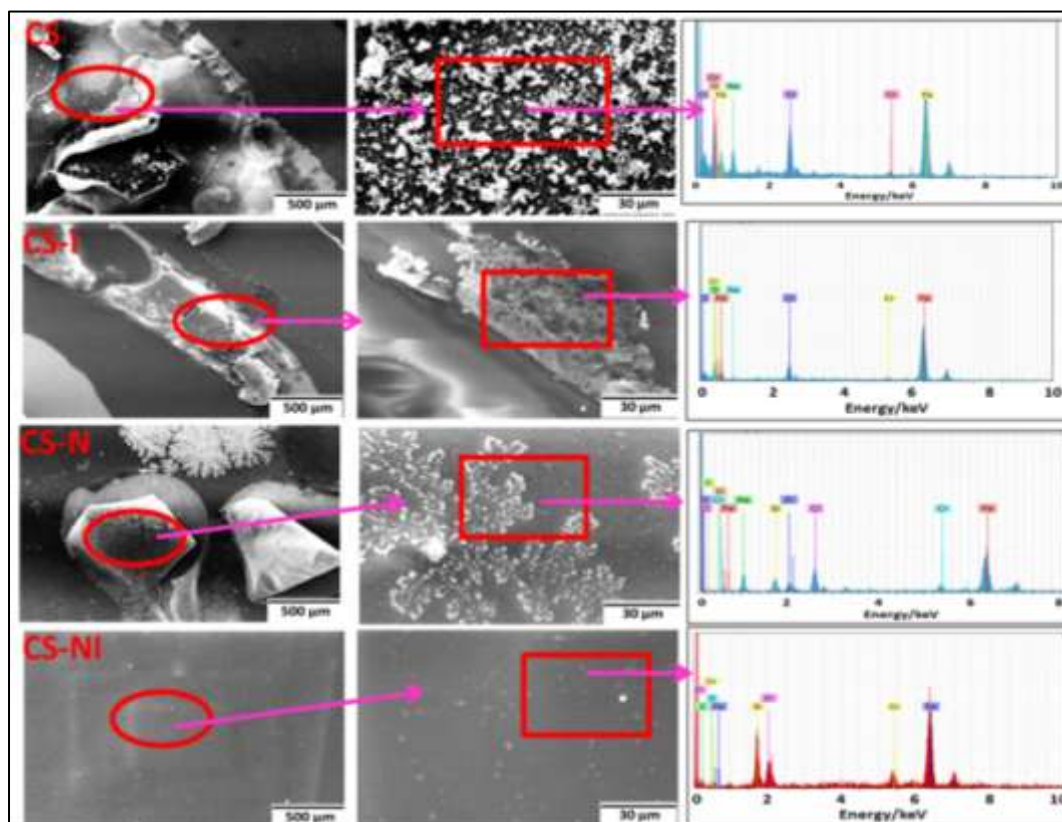


**Figure 4.13: SEM images and its corresponding EDX spectrum of various coated substrates after 1 week of exposure to 0.05 M NaCl solution**

The SEM analysis of the coated substrates after immersion presented similar results obtained from EIS and photographs. Coatings were delaminated and flakes were visible for CS, CS-I, and CS-N. Corrosion products were also visible in the magnified view of the micrograph of CS, CS-I, and CS-N. However, uniform and damage free coating surface was observed for CS-NI after 1 week of immersion. EDX spectrum revealed that chlorine was present on the surface of the coating and Si and Zr peaks were not

observed for both CS and CS-I. Peaks of Si and Zr were present and no peak for Cl was observed for CS-NI.

In order to investigate the active corrosion protection, the coated specimens (CS and CS-NI) were exposed to 0.01 M NaCl solution after making artificial defect on it and impedance response was recorded at given intervals of time. The idea is to destroy the integrity and barrier effect of the coating and to evaluate the corrosion process on the underlying metal surface.

Figure 4.14 shows the evolution of the impedance response of scratched CS for 1 week while immersing in NaCl solution.

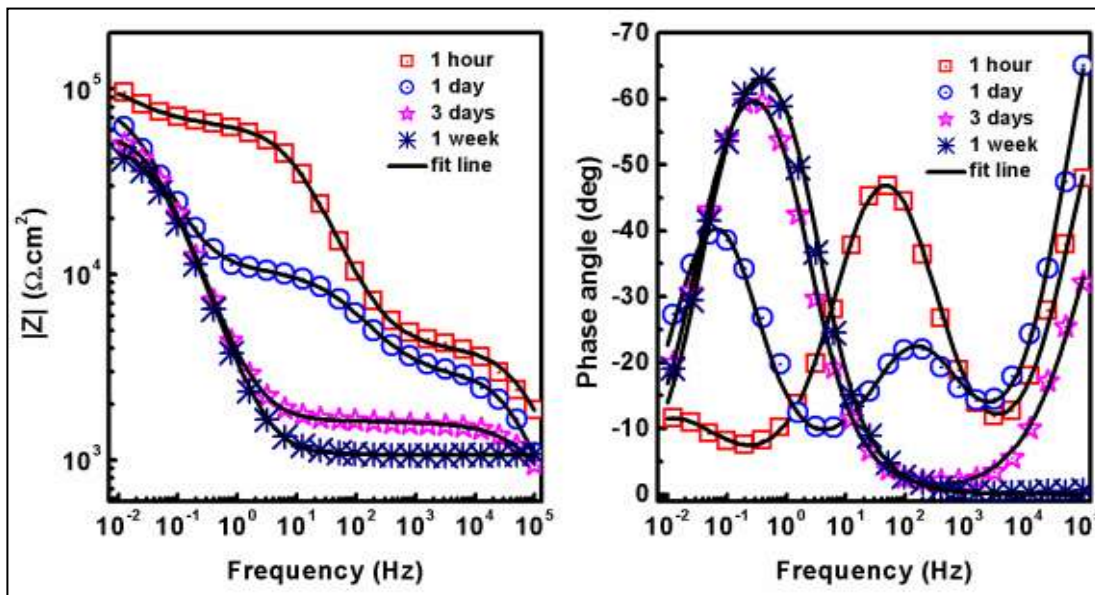


**Figure 4.14: EIS spectra of CS during immersion in 0.01 M NaCl solution after making an artificial defect**

After 1 hour of immersion, scratched CS had three time constant. The first time constant at high frequency is due to the barrier property of the coatings. The second time constant at mid frequency is due to the intermediate oxide layer and third time constant at lowest frequency is due to the corrosion activity. After 3 days of immersion it was observed that the time constant for oxide layer was not identified on the Bode plot and the low frequency impedance value has decreased. Moreover, after 1 week of

immersion, the time constant at high frequency was not present on the Bode plot suggesting that CS completely lost its barrier property. These observations suggested that scratched CS was corroding continually during immersion in NaCl solution.

Figure 4.15 shows the evolution of impedance response of scratched CS-NI for 1 week during immersion in 0.01 M NaCl solution.

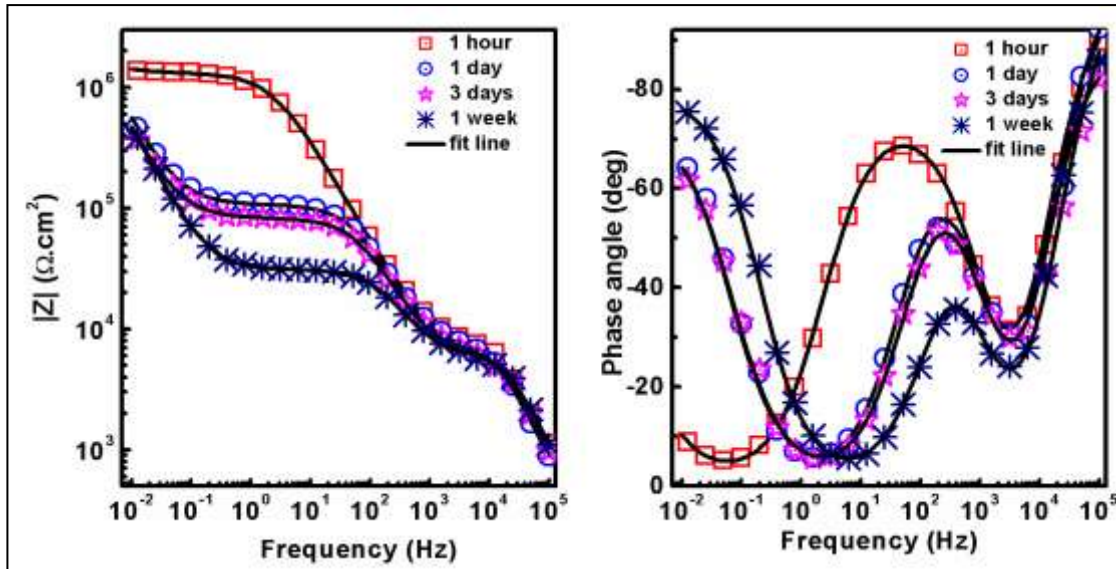


**Figure 4.15: EIS spectra of CS-NI during immersion in 0.01 M NaCl solution after making an artificial defect**

The impedance response after 1 h of immersion had two time constants; one at high frequency was due to the barrier property of the coatings and the second time constant at middle frequency due to the oxide film. No corrosion activity at low frequency was observed. After 1 day of immersion, it was observed that the low frequency impedance value was decreased as identified on the Bode plot. However, the barrier property of the coating remained almost constant. During 1 week immersion, from 24 h to 168 h the low frequency impedance remains unchanged there in suggesting active corrosion protection. For CS-NI, the low frequency time constant was not fully evolved. The resistive plateau was not observed, only the capacitive slope was present in the Bode plot. The abovementioned experiment undoubtedly confirms that the highest value of

low frequency impedance module for CS-NI can be related to the healing of the defect by the inhibitor released from the nanocontainer embedded in the coating, since the coating without inhibitor loaded nanocontainer impregnated coatings did not show this effect.

In order to get a quantitative estimation of corrosion resistance, experimentally obtained impedance spectra for scratched CS-NI and CS were fitted using equivalent circuit (EC) models. The ECs used to fit the impedance spectra were depicted in Figure 4.16.

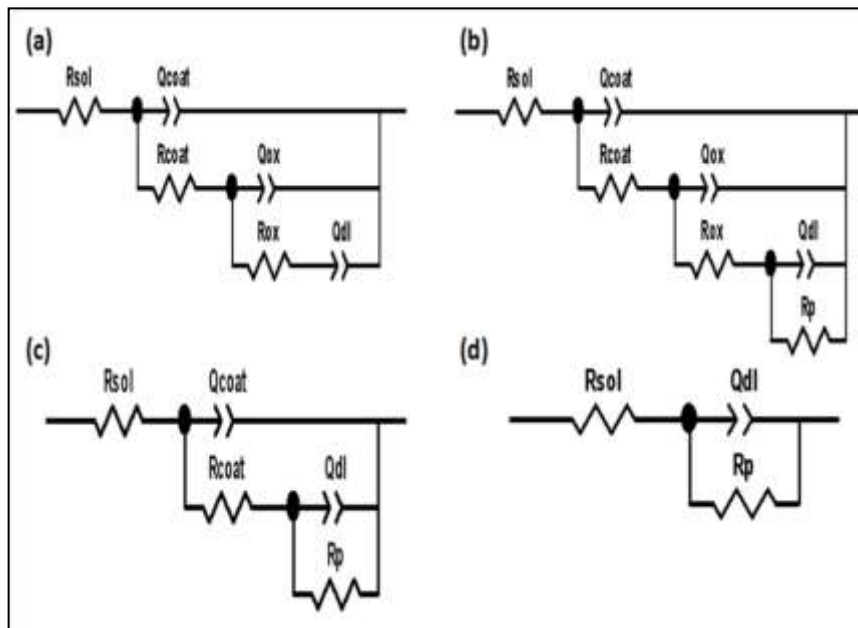


**Figure 4.16: Equivalent circuits used to fit the experimental EIS data of scratched CS and CS-NI during 1 week of immersion in 0.01 M NaCl solution**

$R_{sol}$  is the solution resistance;  $R_{coat}$ ,  $R_{ox}$  and  $R_p$  are respectively the pore resistance of the sol-gel barrier coating, intermediate oxide layer and polarization resistance.  $Q_{coat}$ ,  $Q_{ox}$ ,  $Q_{dl}$  are the constant phase elements of sol-gel hybrid coating, intermediate oxide layer and double layer respectively. Instead of pure capacitance, constant phase elements were used since the phase angle is not equal to  $-90^\circ$ . For scratched CS-NI, in the beginning of the immersion test, two time constants completely appeared in the

impedance spectra and the third time constant at the low frequency was not evolved completely. Hence the impedance spectrum of CS-NI after 1 h of immersion was fitted using EC depicted in Figure 4.16(a). The EC shown in Figure 4.16(b) was used to fit impedance spectra of both scratched CS-NI during immersion of 24 h to 168 h and CS during immersion of 1 h to 24 h. Impedance spectra of CS during immersion of 48 h to 144 h was fitted using EC shown in Figure 4.16(c). Figure 4.16(d) was used to fit the impedance spectra of CS after 168 h of immersion. The error of fitting  $\chi^2$  was less than or equal to  $10^{-3}$  for all the spectra.

Figure 4.17 shows the evolution of  $R_{\text{coat}}$  during immersion in 0.01 M NaCl solution.

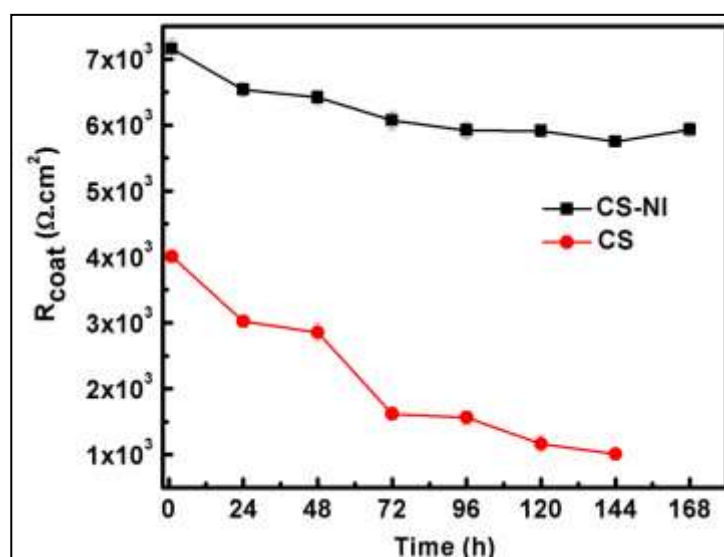


**Figure 4.17: Evolution of hybrid barrier coating resistance ( $R_{\text{coat}}$ ) during 1 week of immersion in 0.01 M NaCl solution.**

The pore resistance of sol-gel barrier coating depends on the porosity, cracks and the amount of water absorbed during immersion in salt solution. For CS-NI, the pore resistance of the coating almost remained constant and the value of  $R_{\text{coat}}$  was almost 6 times more compared to that of CS. The presence of this high frequency time constant even after 1 week of immersion for scratched CS-NI in a corrosive environment shows that CS-NI preserves its barrier property. After 144 h of immersion,  $R_{\text{coat}}$  value of CS

could not be extracted from the impedance spectra and this indicated the complete disruption of the barrier property of CS.

The polarization resistance ( $R_p$ ) is the parameter, which can be directly correlated to the active corrosion protection rendered by corrosion inhibitors [172]. Figure 4.18 presents the evolution of  $R_p$  during immersion.

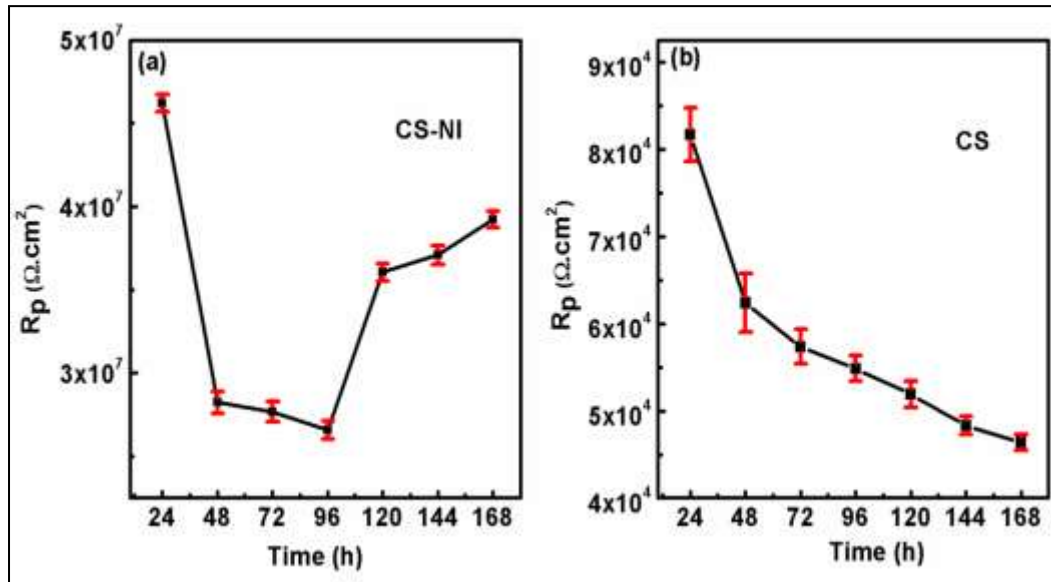


**Figure 4.18: Evolution of polarization resistance of (a) CS-NI, (b) CS during 1 week of immersion in 0.01 M NaCl solution.**

The polarization resistance of CS decreased continuously during 1 week of immersion (Figure 4.18(b)). However, for CS-NI,  $R_p$  value decreased from 24 h to 96 h and from 96 h onwards the value of  $R_p$  increased and showed a stable behaviour (Figure 4.18(a)). The final  $R_p$  value of CS-NI was about three orders of magnitude higher than CS. This may be attributed to the release of 2-MBT from ZrNC and thus provided active corrosion protection to the underlying metal surface.



Figure 4.19 presents the photograph of scratched CS-NI and CS after 1 week of immersion in 0.01 M NaCl solution.

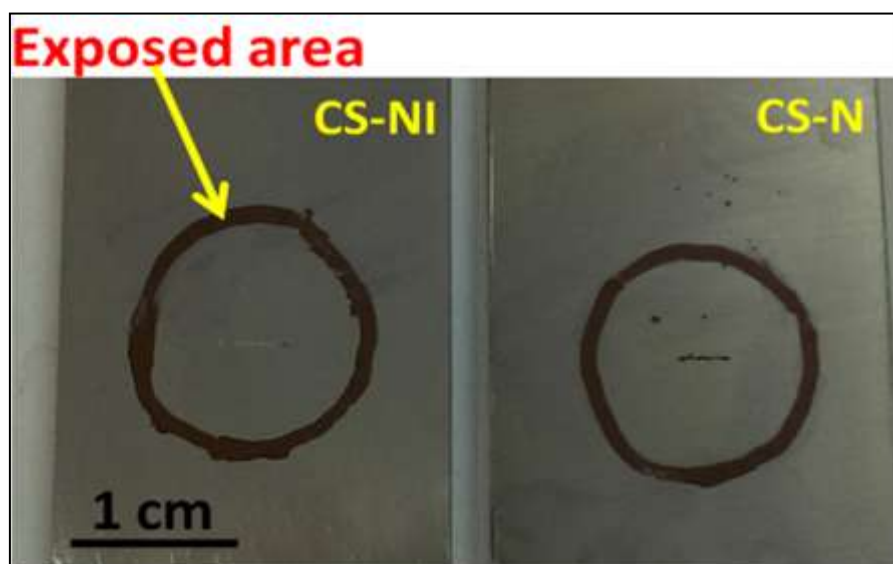


**Figure 4.19: Optical photographs of scratched CS-NI and CS after 1 week of immersion in 0.01 M NaCl solution. The drawn circles indicate the exposed area of the coatings**

Corrosion products appeared on the scratched area and pits were developed on the surface of CS. However, corrosion products were not appeared on the scratched area of CS-NI and the surface was not attacked by corrosion. These observations are in good agreement with the EIS results.

With the aid of the aforementioned results a probable mechanism for active corrosion protection based on the self-healing is depicted in Figure 4.20. When the integrity of the coating is lost due to corrosion or some inherent defects in the coating, it could not function as a barrier against the permeation of any corrosive species. However, the hybrid coating containing inhibitor loaded nanocontainers could effectively delay the corrosion process by releasing the loaded inhibitor molecules. The nanocontainers could release inhibitors around the attacked or scratched region in response to pH

changes. The released inhibitor can delay the corrosion process either by forming a thin layer or by complexing with the metal ions.

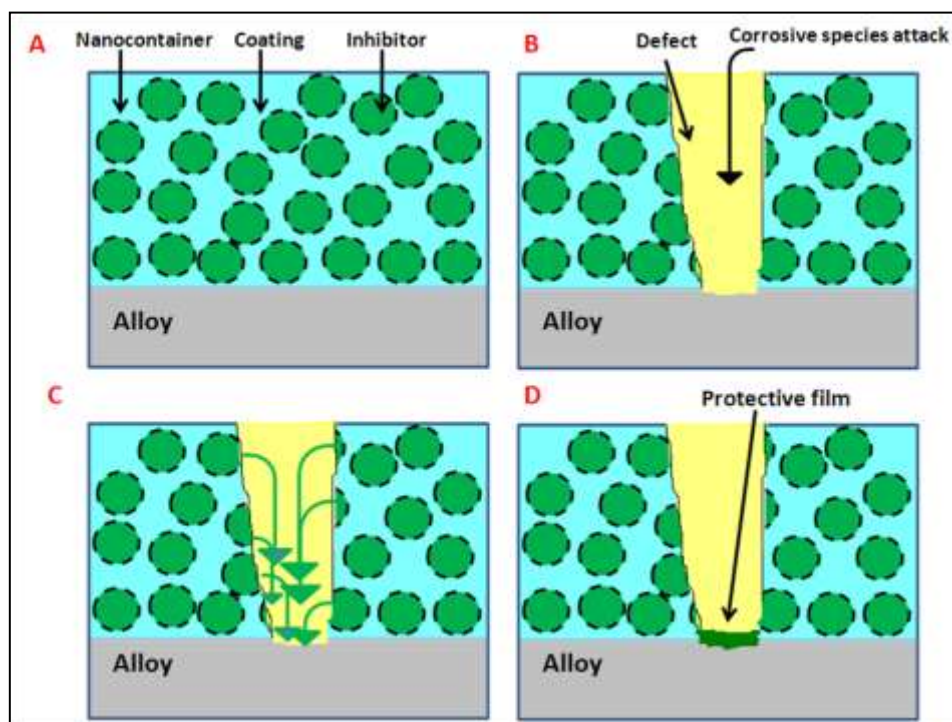


**Figure 4.20: Self-healing mechanism of active corrosion protection**

#### 4.4 Summary

- ❖ Hollow mesoporous zirconia nanocontainers with uniform spherical shape and average diameter of 375 nm were synthesized using a hard templating method. Solid silica nanoparticles were used as the template.
- ❖ Subsequently, HMZ nanocontainers were loaded with 2-MBT molecules and the loading efficiency was found to be 63 %. The successful loading of 2-MBT into HMZ was confirmed by laser Raman spectroscopy.
- ❖ The pH specific release of 2-MBT from HMZ was observed and it was found that the release of 2-MBT was faster and higher in amount when the pH was shifted from neutral values.



- ❖ The enhanced corrosion resistance of 2-MBT loaded HMZ impregnated hybrid coating was established using EIS, SEM and visual inspection.
- ❖ EIS was employed as a useful technique for the study of active anticorrosion performance of 2-MBT loaded HMZ mixed coatings after creating artificial defects on the coating surface. The increase in the low frequency impedance of CS-NI during the immersion is due to the self-healing effect achieved by the releasing of loaded inhibitor from the nanocontainers.

## CHAPTER 5

### Hollow Mesoporous Silica Nanocontainers for Active Corrosion Protection

---

*This chapter discusses the development of an active corrosion protection system consisting of silane-zirconia hybrid sol-gel coating impregnated with inhibitor loaded hollow mesoporous silica nanocontainers. Hollow mesoporous silica spheres were synthesized through sol-hydrothermal method and used as nanocontainers to load corrosion inhibitor molecules, 2-mercaptobenzothiazole. A silane-zirconia based hybrid coating containing hollow mesoporous silica nanocontainers were applied on modified 9Cr-1Mo ferritic steels. The loading and releasing properties of hollow mesoporous silica nanocontainers were studied using UV-visible spectroscopy. The corrosion resistance and active corrosion protection efficiency of hybrid silane-zirconia coatings with and without the addition of inhibitor loaded hollow mesoporous silica nanocontainers were studied using electrochemical impedance spectroscopy (EIS) and scanning electron microscopy (SEM). In order to prove the self-healing ability of the coatings, EIS experiments were carried out on coated specimens with artificial scratches. The anticorrosive property of the hybrid coating impregnated with inhibitor loaded nanocontainers was found enhanced in comparison with that of the plain hybrid coating. This enhancement in corrosion resistance was due to the controlled and sustained release of the corrosion inhibitor from nanocontainers embedded in the hybrid coating.*

---

#### 5.1 Introduction

Ever since the discovery of ordered mesoporous silica materials by researchers at Mobil Research and Development Corporation, it has been considered as a versatile material having a variety of important applications [277]. Mesoporous silica has large surface

area, uniform cylindrical pores with diameter ranging from 2 to 50 nm, very good chemical and thermal stability and versatile chemistry for surface of functionalization. Aforesaid properties made mesoporous silica a breakthrough material for using as a support for adsorption, catalysis, chemical separation and carrying and delivering drugs [278-280]. The use of mesoporous silica for loading and releasing drug molecules at targeted cells has been increased recently. The very high surface area, tunable pore size and non-toxic nature make mesoporous silica a good material for drug delivery. Many research groups have investigated new possibilities in the burgeoning area of drug delivery research using conventional mesoporous silica materials such as MCM-41 and SBA-15 [280-292]. Tunable pore size and suitable pore volume make them ideal host support for loading and further releasing of guest molecules. However, the guest molecule storage capacity for conventional mesoporous materials is relatively low and irregular morphology is also not ideal for a host molecule delivery system. These drawbacks can be overcome by making hollow the interior of the mesoporous silica. The huge hollow interior can make it possible to accommodate more amounts of guest molecules. Hollow mesoporous spheres have made tremendous interest for the facile loading, transport and delivery of guest species such as drugs, catalysts, dyes and corrosion inhibitors due to its high surface area, huge hollow inner space and penetrating pores in the shell.

Templating method is one of the most promising and general approaches employed to control the inner hollow core and this method is also known as core-shell technique. The template method can be generally classified into two: hard-templating methods and soft templating methods. Usually, hard templating materials are non-silica materials having good compatibility and affinity with silica, such as polymer beads, oxide nanoparticles. Generally, the hard templates are coated with sol-gel derived silica gel

and while coating some pore making agents are also added to obtain the mesoporosity. The hollow mesoporous spheres are achieved by selectively removing the templates and pore making agents [293-298]. In soft-templating methods, the co-assembly of the surfactant uses surfactants/microemulsions as templates to obtain mesoporous silica shell with a hollow inner cavity and sol-gel derived silica [299-303].

Borisova et al. reported the application of mesoporous silica nanoparticles for active corrosion protection of aluminum alloy AA2024 [184]. They used mesoporous silica nanoparticles whereas; the present study employs hollow mesoporous silica spheres as nanocontainers. In our study, we synthesized monodispersed hollow mesoporous silica spheres as nanocontainers using both poly(vinylpyrrolidone) (PVP) and cetyltrimethyl ammonium bromide (CTAB) as co-templates under basic conditions. This chapter describes the synthesis of monodispersed hollow mesoporous silica (HMS) nanocontainers having very high surface area and pore volume and its application as nanocontainers for loading corrosion inhibitor (2-mercaptobenzothiazole (2-MBT)). 2-MBT loaded HMS containers were added into a siloxane-zirconia hybrid sol-gel barrier coating. The 2-MBT loaded HMS were mixed with silane-zirconia hybrid sol and applied on modified 9Cr-1Mo ferritic steel by dip coating method. The corrosion protection efficiency of following four different coatings were studied and compared using EIS in order to understand the contribution of each component on the protective properties of silane-zirconia hybrid coating: (i) hybrid sol-gel coated modified 9Cr-1Mo ferritic steel, (ii) inhibitor mixed hybrid sol-gel coated modified 9Cr-1Mo ferritic steel, (iii) empty nanocontainer mixed hybrid sol-gel coated modified 9Cr-1Mo ferritic steel and (iv) inhibitor loaded nanocontainer mixed hybrid sol-gel coated modified 9Cr-1Mo ferritic steel. Thus, the possibility of using 2-MBT loaded HMS nanocontainers

impregnated hybrid sol-gel coating in order to enhance the corrosion protection of modified 9Cr-1Mo ferritic steel substrates is reported in this chapter.

## **5.2 Experimental**

### **5.2.1 Materials**

Poly (vinylpyrrolidone) (PVP), cetyltrimethylammonium bromide (CTAB), sodium hydroxide (NaOH), and tetraethoxysilane (TEOS) were used to synthesize hollow mesoporous silica nanocontainers. (3-Glycidyloxypropyl) trimethoxysilane, zirconium *n*-propoxide (TPOZ), ethylacetoacetate, ethyl alcohol, isopropyl alcohol and nitric acid were used to prepare silane and zirconia based sols. 2-mercaptobenzothiazole (MBT) was used as corrosion inhibitor and sodium chloride was used for electrochemical studies. All the chemicals used were of reagent grade and the water used in the study was purified in a three stage Millipore Milli-Q plus 185 purification system, which had a resistivity higher than 15 M $\Omega$ . cm.

### **5.2.2 Synthesis and Characterization of HMS Nanocontainers**

HMS nanocontainers were synthesized through a sol-hydrothermal method and the details of the synthesis procedure are given in section 3.4.2 of chapter 3.

The HRTEM images of HMS nanocontainers were obtained using JEOL JEM 2100 electron microscope operated at 200 kV. Low angle X-ray powder diffraction pattern for HMS was obtained using a STOE high resolution X-ray diffractometer. Nitrogen adsorption/desorption isotherms were recorded at 77 K on a Sorptomatic 1990.

### **5.2.3 Loading and Releasing of 2-MBT**

2-MBT was dissolved in ethanol at a concentration of 10 mg/ml. About 100 mg of calcined hollow mesoporous silica spheres was added to 50 ml ethanolic 2-MBT solution. The above mixture was ultrasonically agitated for 20 minutes and subsequently kept under magnetic stirring for 24 h. Then the 2-MBT loaded HMS was

separated out and dried at room temperature. The filtrate was extracted out from the vial and used to determine the free 2-MBT content in solution with the help of UV-visible spectroscopy studies. Laser Raman spectroscopy was also used to confirm the loading of 2-MBT into HMS.

50 mg of 2-MBT loaded HMS was dispersed in 150 mL of releasing medium (0.05 M NaCl) at different pH values of 3, 7 and 10 at room temperature and the solution was stirred at a rate of 500 rpm using a magnetic stirrer. 1 mL of the solution was pipetted out at given time intervals for UV-visible analysis. After the measurement, the solution was poured back immediately to the solution.

#### ***5.2.4 Development of Coatings on Modified 9Cr-1Mo Ferritic Steel***

The modified 9Cr-1Mo ferritic steel substrates were cleaned and etched prior to the application of hybrid coating. The procedure employed for the pretreatment of modified 9Cr-1Mo ferritic steel is given in section 3.3.1 of chapter 3. A silane-zirconia hybrid coating was applied on the substrate as barrier coating and its detailed synthesis procedure is described in section 3.6.2 of chapter 3. Four different types of coatings were prepared. At first, coatings free of any inhibitor and nanocontainer were prepared and this is named as CS i.e. plain silane zirconia hybrid barrier coating. Secondly, inhibitors (2-MBT) were mixed directly with the hybrid coating was produced and named it as CS-I. Then the coatings incorporated with empty nanocontainers were prepared and it is referred as CS-N. Finally, coatings containing inhibitor loaded nanocontainers were prepared and it is referred as CS-NI. All the above mentioned three sol solutions were deposited on the modified 9Cr-1Mo steel by dip coating procedure, i.e., immersing a specimen in the hybrid sol-gel mixture for 100 s and thereafter, withdrawn at a constant lifting speed of  $2 \text{ mm s}^{-1}$ . The coated substrate was dried in air and then baked at  $120^\circ\text{C}$  for 1 h.

### ***5.2.5 Evaluation of Anticorrosion Efficiency of Coatings***

Electrochemical impedance spectroscopy (EIS) was used to evaluate the protective performance of the developed hybrid coatings on modified 9Cr-1Mo ferritic steel without and with artificial defect, during 1 week of immersion in 0.05 M NaCl solution and in 0.01 M NaCl solution, respectively. EIS measurements were carried out using Iviumstat. XRe. at open circuit potential, by applying a sinusoidal excitation of 10 mV in the frequency range of 100 kHz-10 mHz recording 10 points per decade of frequency. A flat cell was used consisting of an Ag/AgCl reference electrode, platinum counter electrode and the coated modified 9Cr-1Mo ferritic steel of 1 cm<sup>2</sup> as working electrode. The morphology and composition of the coated substrates after immersion in 0.05 M NaCl solution was analyzed by scanning electron microscope and attached energy dispersive X-ray analysis (EDX) system.

## **5.3 Results and Discussion**

### ***5.3.1 Synthesis and Characterization of HMS Nanocontainers***

Hollow mesoporous silica spheres with very high surface area were prepared through a sol-hydrothermal method. Both PVP and CTAB were used as templates. In fact, PVP acted as a co- template and helped in the formation of hollow mesoporous silica spheres. The hollow mesoporous silica spheres were formed based on the following mechanism. When PVP was added to a basic aqueous solution, spherical aggregates were formed. When CTAB was poured into the solution, an interface between CTAB molecules and PVP was formed due to the hydrophilic interaction between these two molecules. When TEOS was added into the above solution, it underwent hydrolysis under basic condition. Shortly, these hydrolyzed TEOS self-assembled with the CTAB molecules, resulting in the formation of an ordered mesostructured shell. After

calcination at 550 °C, both the PVP and CTAB were removed and HMS nanocontainers were obtained.

A schematic drawing for the suggested formation of hollow core shell structured mesoporous silica nanocontainers is given in Figure 5.1.

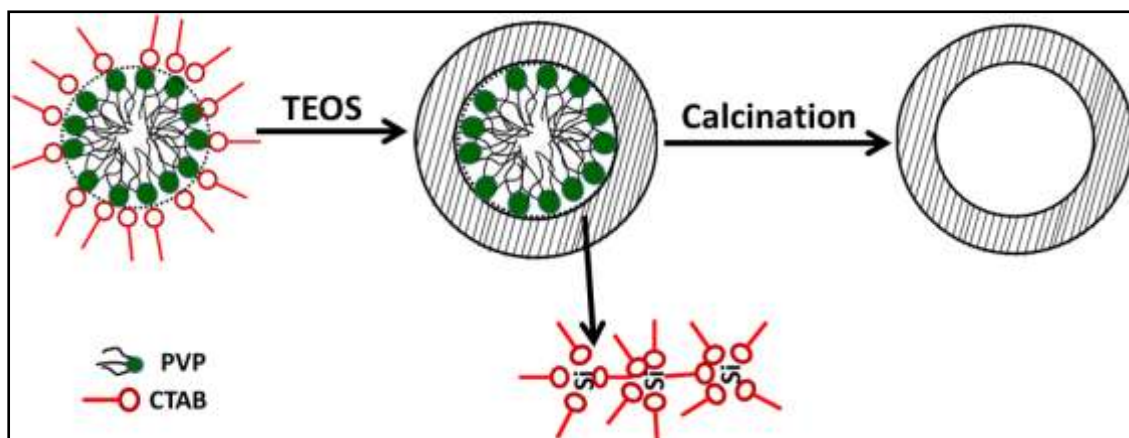


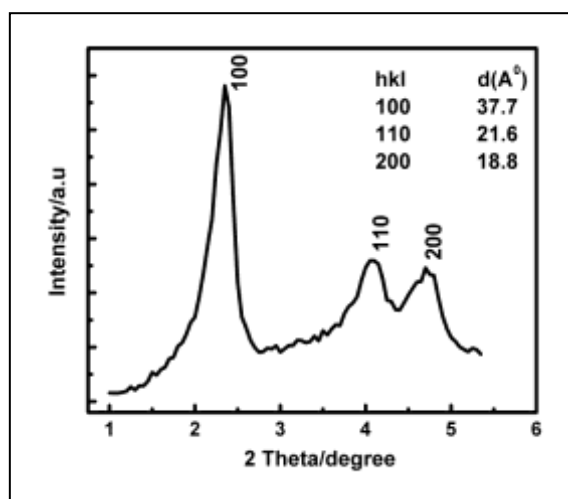
**Figure 5.1: Schematic drawing for the formation of HMS nanocontainers**

PVP plays a significant role in the formation of hollow core of the core-shell mesoporous silica spheres. A conventional MCM-41 materials or partially hollow spheres might form in the absence of the addition of PVP to the reaction mixture. When PVP is added to the basic solution, spherical aggregates would form and PVP would assemble in such a way that its hydrophilic group will extend the outer interface with the solvent molecules. Due to the affinity between two kinds of hydrophilic groups, PVP aggregates would interact with the dissolved CTAB molecules and this would result in the formation of an interface between PVP aggregates and CTAB molecules. Here PVP has a crucial role since it is believed that self-assembly can only take place around PVP aggregates due to the hydrophilic interaction between PVP and CTAB. When TEOS was added into the aforesaid basic solution containing PVP and CTAB, TEOS would undergo hydrolysis. Subsequently, the hydrolyzed TEOS molecules self assembled with CTAB molecules around the PVP aggregates and followed by the formation of a well ordered meso structured shell. After calcination, the PVP



aggregates and CTAB molecules were removed and eventually obtained the monodispersed silica spheres with hollow core and mesoporous shell.

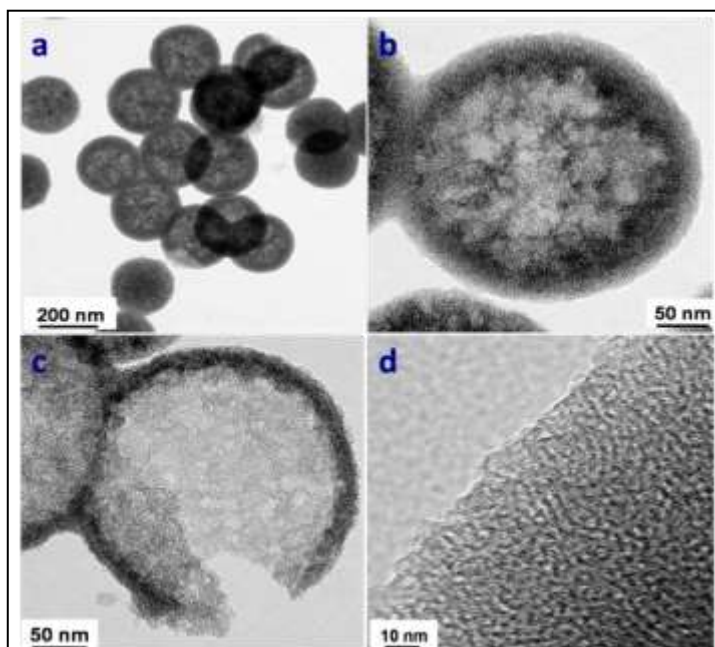
Figure 5.2 shows the low angle XRD pattern of HMS nanocontainers. Three well resolved Bragg diffraction peaks can be observed from the XRD pattern. These three obvious diffraction peaks can be assigned to the (1 0 0), (1 1 0) and (2 0 0) reflections of an ordered hexagonal array of parallel silica tubes resulting in a hexagonal symmetry structure ( $P6mm$ ) typical for MCM-41 [277]. The intense peak at  $2\theta = 2.35$  have a  $d$ -spacing of 3.7 nm. The  $d$ -spacing corresponding to diffraction peaks at  $2\theta = 4.1$  and  $2\theta = 4.7$  are 2.2 and 1.9 nm respectively. Aforesaid results suggest that the HMS spheres have a hexagonal mesostructure.



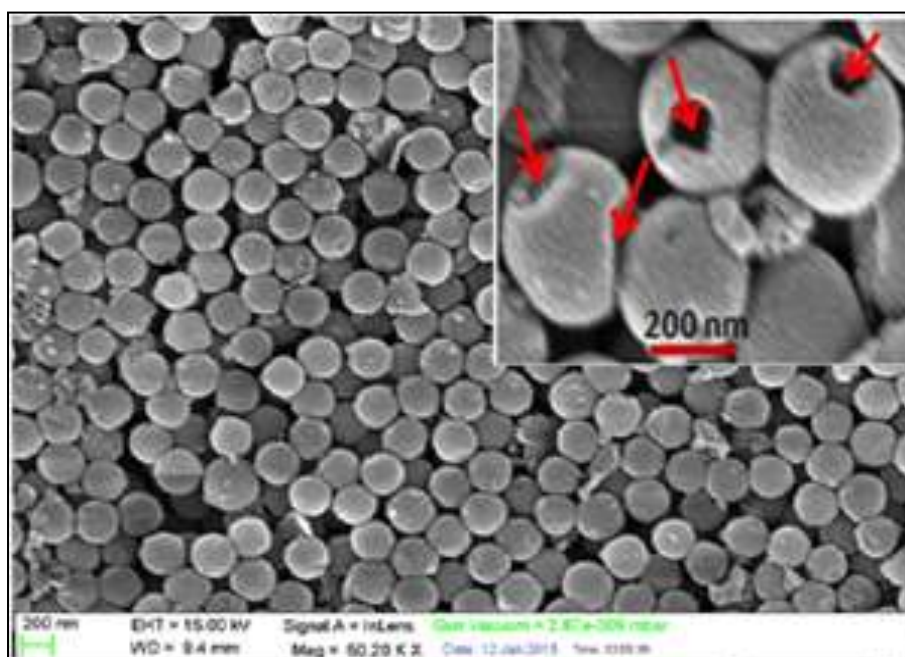
**Figure 5.2: Low angle XRD pattern for HMS nanocontainers**

Figure 5.3 depicts the HRTEM micrograph of the calcined mesoporous silica particles. The particles are spherical in shape and channel like ordered pores *ca.* 2.5 nm in width are clearly visible on the silica spheres. In addition to that, a remarkable contrast between the shell and the core can be observed. The HRTEM analysis indicates that HMS spheres have a uniform, well-defined hexagonal mesostructure.

Figure 5.4 presents the FESEM images of the calcined HMS spheres. As shown in Figure 5.4, the HMS products are monodispersed uniform spheres having average diameter 200 nm. The broken silica spheres as arrowed (inset) reveals that these silica spheres are hollow in nature.



**Figure 5.3: HRTEM images of HMS nanocontainers at different magnifications**



**Figure 5.4: FESEM images of HMS nanocontainers. Inset shows a magnified view**

The mesoporosity of the sample was further confirmed by N<sub>2</sub> adsorption-desorption isotherm analysis, as shown in Figure 5.5.

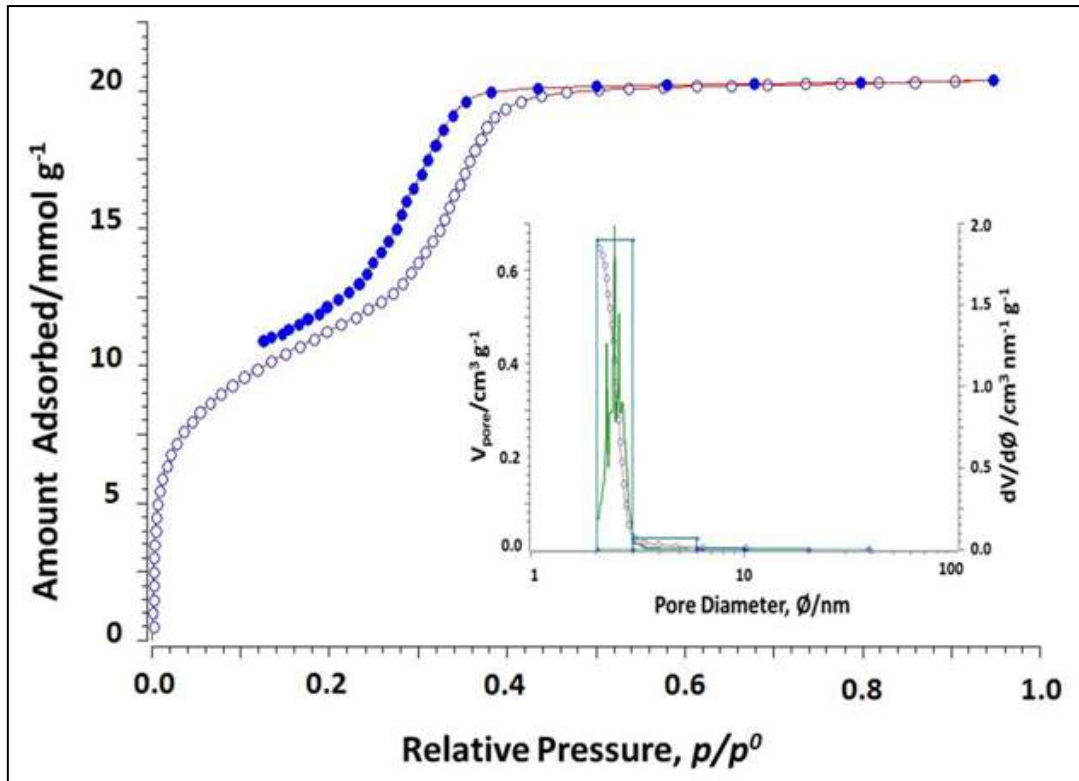


**Figure 5.5: N<sub>2</sub> adsorption-desorption isotherm of HMS nanocontainers. Inset shows the BJH pore size distribution**

The nitrogen adsorption-desorption isotherms of calcined HMS spheres are basically of type IV with an H1 hysteresis loop. The pronounced hysteresis loop is primarily associated with capillary condensation in mesopore structures. The type IV adsorption isotherm is a characteristic feature of mesoporous materials. The H1 hysteresis loop reveals that the HMS nanocontainers consisting of agglomerates or compacts of approximately uniform spheres in fairly regular array with a narrow distribution of pore size [304]. The adsorption isotherm was very flat at high pressure region, therein indicating low external surface area and the absence of any secondary mesoporosity. The specific surface area of the MS products was obtained using the BET method and it was found to be 940.57 m<sup>2</sup> g<sup>-1</sup>. Barrett- Joyner-Halenda (BJH) analyses revealed that the

calcined MS products exhibited pore size of 2.5 nm and cumulative pore volume of  $0.66 \text{ cm}^3 \text{ g}^{-1}$ . The very high surface area, narrow mesopore distributions and hollow structure of the nanocontainer are very important for inhibitor loading and controlled inhibitor release properties.

### 5.3.2 Inhibitor Loading and Releasing Properties of HMS Nanocontainers

2-MBT was loaded into HMS spheres by dispersing HMS spheres with ethanolic solution of 2-MBT and followed by stirring for 24 h. Figure 5.6 presents the UV-vis spectra of 2-MBT solution before and after the interactions with HMS nanocontainers.

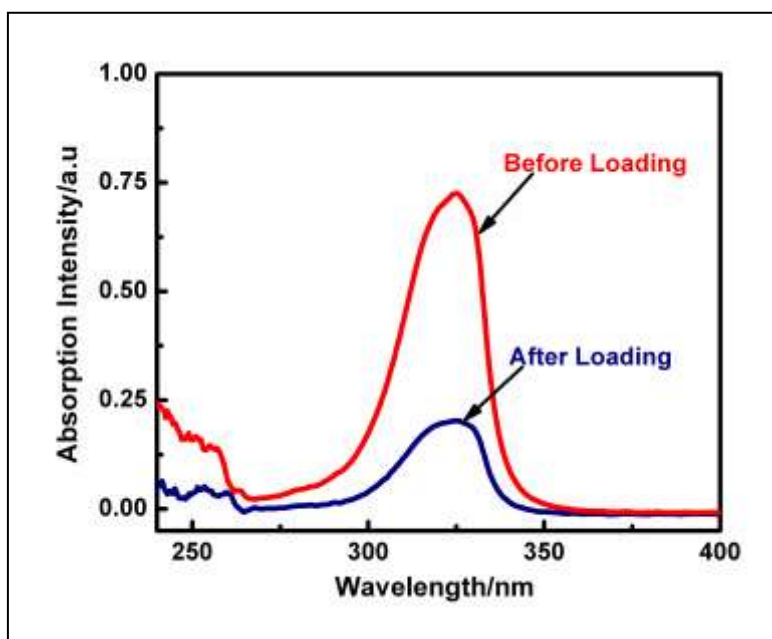


**Figure 5.6: UV-visible spectra of 2-MBT before and after interaction with HMS**

$\lambda_{\text{max}}$  for 2-mercaptobenzothiazole is at 325 nm. As depicted in Figure 5.6, the intensity of the absorption maxima decreased after the interaction of the 2-MBT molecules with HMS nanocontainers and no new absorption bands appeared. Moreover, the position of the absorption band also did not change, which indicated the stability of 2-MBT molecules after the loading procedure. This decrease in the absorption intensity of 2-MBT after the interaction with HMS nanocontainers revealed both the decrease of the

2-MBT concentration in the solution and the successful loading of the 2-MBT molecules in the pores and interiors of HMS nanocontainers. Typically, the organic inhibitor molecules are loaded in inorganic high surface area containers through weak non-covalent interactions such as physical adsorption, electrostatic interaction, hydrogen bonding and  $\pi$ - $\pi$  stacking [235]. The loading efficiency was calculated as follows:

$$\text{Loading efficiency} = \frac{\text{Total amount of MBT} - \text{Free MBT in solution}}{\text{Total amount of MBT}} \times 100 \quad (5.1)$$

The loading efficiency of MBT in the HMS nanocontainer was found to be  $72 \pm 2 \%$ .

Moreover, the successful encapsulation of 2-MBT into HMS nanocontainers was confirmed by laser Raman spectroscopy. Figure 5.7 presents the Raman spectra of pure 2-MBT and MBT loaded HMS.

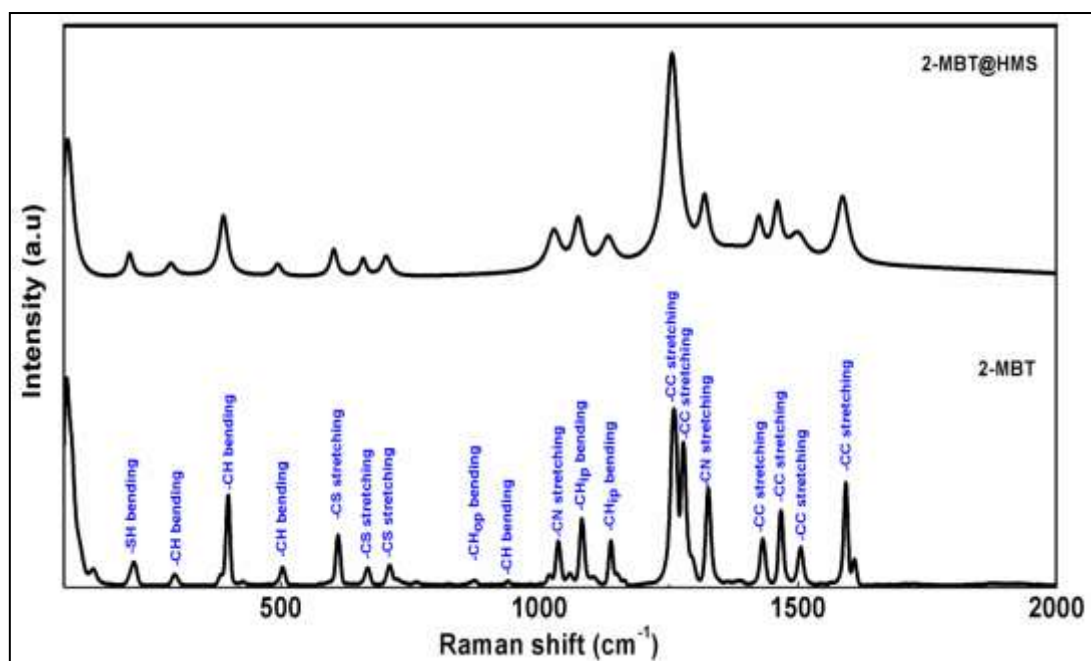


**Figure 5.7: Raman spectra of pure 2-MBT and 2-MBT loaded HMS nanocontainers**

Most of the characteristic Raman features of 2-MBT was present in the spectra of 2-MBT@HMS. The presence of peaks of 2-MBT in the Raman spectra of 2-MBT@HMS confirmed the successful encapsulation of 2-MBT into HMS nanocontainers. However,

the Raman features of silica did not appear in the spectra of MBT@HMS, since silica is a very weak Raman scatterer [305]. All the major peaks and its assignments are given in Table 5.1 [269-272].

**MBT Peak assignments in detail**

<b>Frequency</b>	<b>Approximate description of vibrations</b>
<b>149 cm<sup>-1</sup></b>	SH bending
<b>294 cm<sup>-1</sup></b>	CH bending
<b>397 cm<sup>-1</sup></b>	CH bending
<b>502 cm<sup>-1</sup></b>	Bz ring deformation
<b>610 cm<sup>-1</sup></b>	CS stretching
<b>667 cm<sup>-1</sup></b>	CS stretching
<b>710 cm<sup>-1</sup></b>	CS stretching
<b>766 cm<sup>-1</sup></b>	CH out of plane stretching
<b>874 cm<sup>-1</sup></b>	CH out of plane bending
<b>938 cm<sup>-1</sup></b>	CH bending
<b>1035 cm<sup>-1</sup></b>	CN stretching
<b>1081 cm<sup>-1</sup></b>	Bz ring or SCS antisymmetric stretching
<b>1137 cm<sup>-1</sup></b>	CH in plane bending
<b>1259 cm<sup>-1</sup></b>	NCS ring stretching
<b>1277 cm<sup>-1</sup></b>	CC stretching
<b>1431 cm<sup>-1</sup></b>	CC stretching
<b>1466 cm<sup>-1</sup></b>	CC in plane stretching
<b>1504 cm<sup>-1</sup></b>	CC stretching
<b>1591 cm<sup>-1</sup></b>	CC in plane stretching

**Table 5.1: Raman peak assignments for 2-MBT**

Figure 5.8 shows the results of MBT released from mesoporous silica nanocontainers. The controlled and sustained release of 2-MBT from HMS nanocontainers was investigated by redispersing 2-MBT loaded silica nanocontainers in 0.05 M NaCl solution of pH 3, 7 and 10.

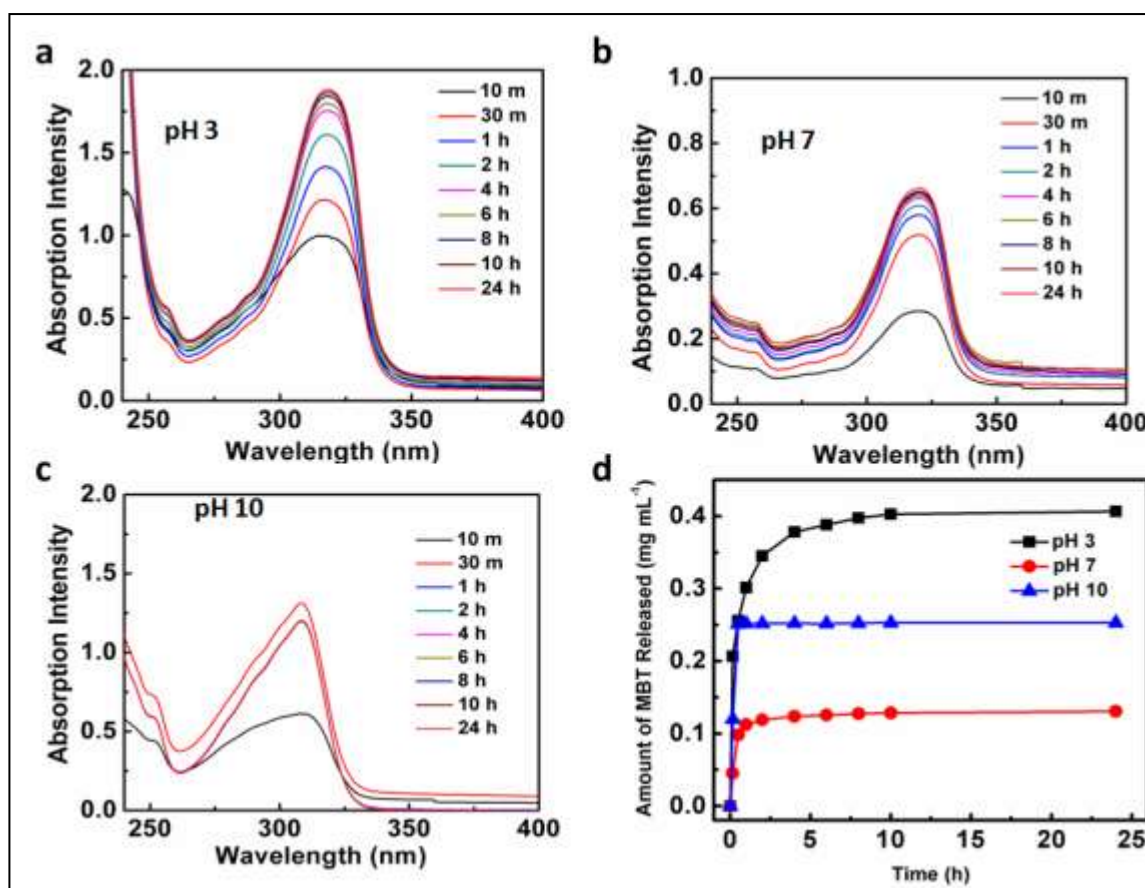


**Figure 5.8:** UV-vis spectra at different times of the 0.05 M NaCl media in which 2-MBT was released from 2-MBT loaded HMS nanocontainers (a) at pH 3, (b) at pH 7, (c) at pH 10 and (d) corresponding pH-dependent releasing behaviour of 2-MBT from HMS-MBT system

The releasing of 2-MBT was monitored by absorption intensity peak at *ca.* 325 nm. As shown in Figure 5.8, the release of 2-MBT was observed and the concentration of 2-MBT in the releasing medium increased with time and reached equilibrium after 10 h. The release of 2-MBT from HMS nanocontainers occurs only after the releasing medium has infiltrated into the pores and channels of HMS. Thus the inhibitor molecules gets dissolved in the medium and released by diffusion through the pores along the aqueous pathways. As presented in Figure 5.8, the releasing of 2-MBT from HMS follows similar release kinetics at different pH conditions. Initially, the release was relatively faster in both alkaline and acidic conditions compared to neutral

condition. In fact, the release of 2-MBT was leveled off and reached equilibrium in 1 h at pH 10. As shown in the Figure 5.8, more amount of 2-MBT was released from the HMS at pH 3 and 10 compared to pH 7. The quantity of 2-MBT released after 24 h under acidic and alkaline conditions are  $0.41 \text{ mg mL}^{-1}$  and  $0.25 \text{ mg mL}^{-1}$  respectively, while in neutral conditions it is  $0.13 \text{ mg mL}^{-1}$  only.

The difference in the release rate and quantity of 2-MBT released from HMS can be explained by the variation of solubility of 2-MBT and the differences in the surface charge of both 2-MBT and silica particles with pH. The solubility of 2-MBT is low in neutral range, but relatively higher in alkaline and acidic conditions [172]. When the pH is less than 6, silica particles have positive surface charge whereas; at pH values higher than 6 silica particles acquire negative surface charge [184]. In acidic conditions, 2-MBT gets protonated due to the presence of a free pair of electrons on the N atom and carries a positive surface charge [274, 275]. Thus under acidic conditions, both the HMS spheres and 2-MBT have positive charge and this leads to larger electrostatic repulsion between them, thereby facilitating faster release of 2-MBT from HMS sphere in high amount. Furthermore, the faster release in acidic condition may also be attributed to the hydrolysis of any non-hydrolyzed TEOS that might have sealed some pores in the nanocontainer and this can ease the diffusion of 2-MBT into the solution. Similarly, under alkaline conditions, 2-MBT exists in ionized form with a negative charge on the S atom and thus the MBT molecules carry negative surface charge when pH is more than 7 [276]. Again this leads to electrostatic repulsion between the HMS nanocontainers and 2-MBT under alkaline condition, thereby facilitating the diffusion of 2-MBT through the pores of HMS and releasing into the solution. Hence, it can be stated that the release of loaded 2-MBT from HMS was pH specific since when the pH was shifted from neutral value, the amount of 2-MBT release was more. This



dependency of inhibitor release on pH confirms the stimuli responsive intelligent releasing property of HMS spheres. This observation can be extrapolated to a corrosion process, because corrosion of metals always accompanies by changes in local pH.

### 5.3.3 Surface Characterization of the Sol-Gel Coating

The structure and surface morphology of the coatings were examined using FESEM. Figure 5.9 shows the FESEM images of hybrid barrier coating and nanocontainer (HMS) impregnated hybrid barrier coating.

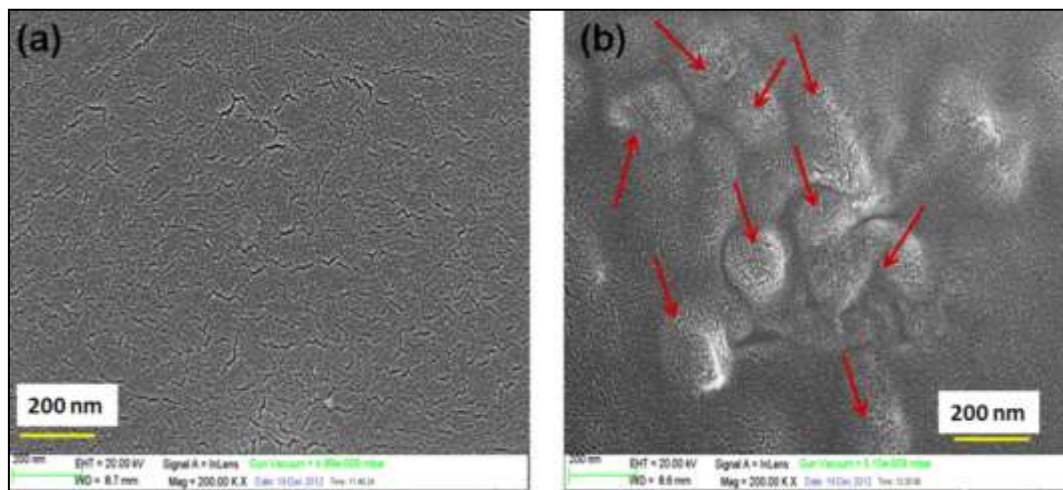


**Figure 5.9: FESEM images of the coatings produced on modified 9Cr-1 Mo ferritic steel: (a) hybrid silane-zirconia coating, (b) nanocontainer doped hybrid silane-zirconia coating**

Figure 5.9(a) depicts the micrograph of hybrid coating without any nanocontainers and as shown in the image, the coating is uniform and homogenous. Moreover, no agglomeration was observed on the surface of the hybrid coating. However, the surface of the baked sol-gel passive barrier coatings had “nano cracks” on the surface and this may have negative impact on the barrier property of the coating. The FESEM image of nanocontainer impregnated hybrid coating is presented in Figure 5.9(b) and nanocontainers are clearly visible on the surface of the coating as “bumps”. The FESEM micrograph confirms the uniform distribution of nanocontainer in the hybrid

barrier coating. Surface profiler measured the thickness of the coating and it was about 3  $\mu\text{m}$ .

#### ***5.3.4 Protective Performance of Various Hybrid Coatings on Modified 9Cr-1Mo Ferritic Steels***

Electrochemical impedance spectroscopy (EIS) was employed to investigate both the barrier property and active corrosion protection of coatings with and without inhibitor loaded nanocontainer impregnated hybrid coatings. Zheludkevich et.al reported that EIS can be used to evaluate the decrease in the corrosion rate and healing of the corroded area by correlating an increase in the low frequency impedance of a metal during immersion in a corrosive medium [249]. All the coated modified 9Cr-1Mo alloy steel substrates were immersed in 0.05 M NaCl solution and their impedance behaviour was recorded at regular intervals of time for 1 week. After 1 week of immersion in salt solution, the extent of attack by corrosion was investigated using scanning electron microscopy (SEM).

Figure 5.10 shows the impedance response of BS (uncoated modified 9Cr-1Mo alloy), CS (hybrid coating), CS-I (inhibitor mixed hybrid coating), CS-N (empty nanocontainer impregnated hybrid coating), CS-NI (inhibitor loaded nanocontainer impregnated hybrid coating) after 1 h of immersion in salt solution. It is observed from Figure 5.10 that all the coated alloy substrates had superior corrosion protection compared to that of uncoated alloy substrate. The order of anticorrosion efficiency after 1 h of immersion is as follows, CS-NI > CS-N > CS-I > CS > BS. BS behaved like a typical corroding surface and its impedance response consisted of only one relaxation process and it is a combination of double layer capacitance and polarization resistance.

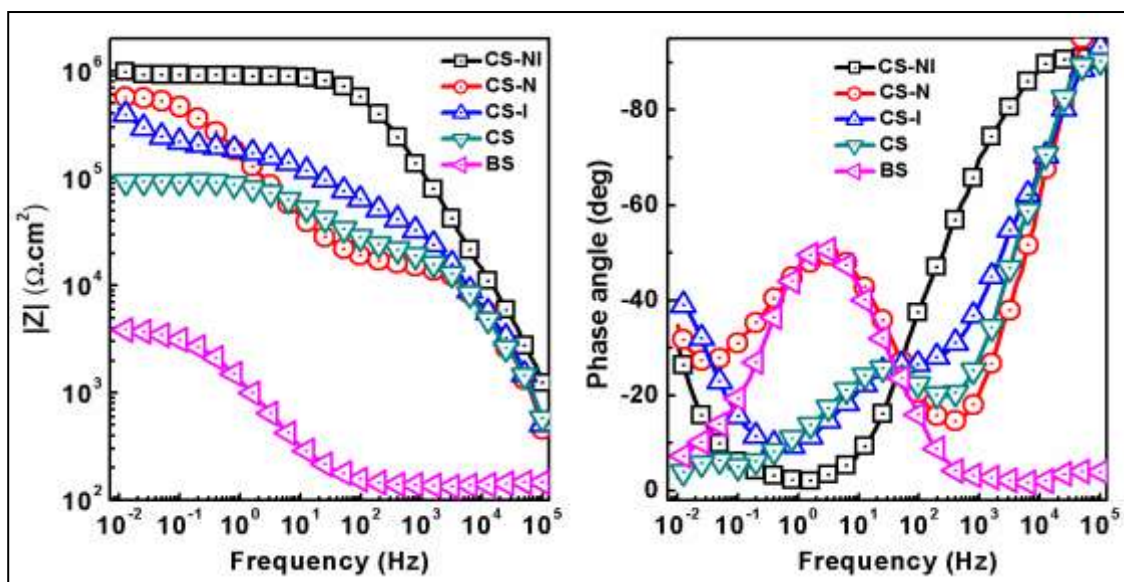


**Figure 5.10: EIS behaviour of BS, CS, CS-I, CS-N, and CS-NI after 1 h of immersion in 0.05 M NaCl solution**

Three relaxation processes were clearly observed in the impedance response of CS. The third relaxation process at low frequency reflects the redox reactions taking place at the metal-electrolyte interface due to corrosion. The relaxation process due to corrosion also appeared in the EIS response of CS-I. Nevertheless, the barrier property of the coating and modulus of impedance at low frequency was higher for CS-I compared to that of CS and this could be attributed to the inhibitive action of 2-MBT mixed in hybrid coating of CS-NI. CS-N had only two time constants in their EIS response and the first at high frequency corresponds to the barrier property of the coating and the second time constant corresponds to the impedance response of the oxide layer. From the Bode phase angle it is observed that a low frequency relaxation process was about to emerge but not developed fully. CS-NI had the highest barrier property after 1 h of immersion in salt solution. Furthermore, the second time constant due to oxide film was not developed also.

Figure 5.11 shows the EIS response of CS, CS-I, CS-N, and CS-NI after 1 day of immersion in 0.05 M NaCl solution.

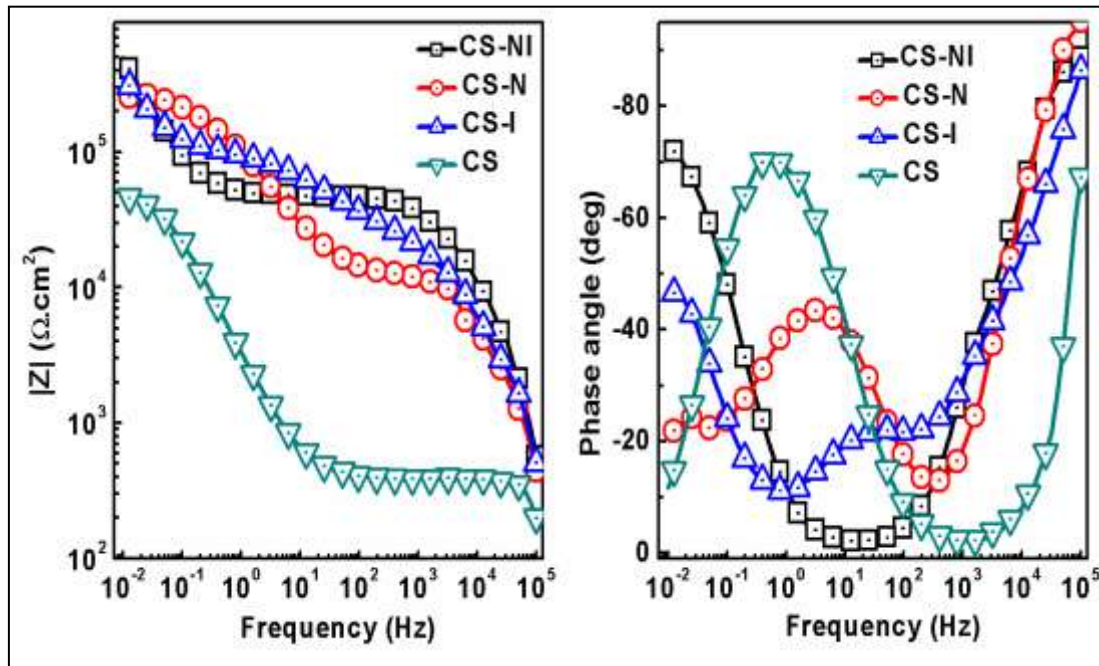


**Figure 5.11: EIS response of CS, CS-I, CS-N, and CS-NI after 1 day of immersion in 0.05 M NaCl solution**

The corrosion protection performance of CS reduced drastically compared to that of CS-I, CS-N, and CS-NI. The second relaxation process at mid frequency disappeared and this observation suggests the complete rupture of the oxide film. The presence of this oxide film is very significant, since it is the last protective layer against the corrosive species. Owing to the complete damage of the oxide film, the salt solution had the direct access to the underlying metal surface through the pores and defects of the coatings and hence the relaxation process due to corrosion was very well evolved. CS-I had better corrosion resistance compared to that of CS-N and this could be attributed to the presence of 2-MBT in the coating of CS-I. The Bode phase angle plot indicated the initiation of corrosion process on the surface of CS-N. After 1 day of immersion, CS-NI had only two time constants and the first at high frequency is related to the barrier property of the coating and the low frequency relaxation process is

associated to the oxide film. From the Bode modulus plot of CS-NI it is observed that the second relaxation process is capacitive in nature since no resistive plateau is observed in the impedance spectrum. This suggests the superior corrosion protection rendered by CS-NI.

The impedance response of CS, CS-I, CS-N, and CS-NI after 1 week of immersion in 0.05 M NaCl solution is depicted in Figure 5.12.

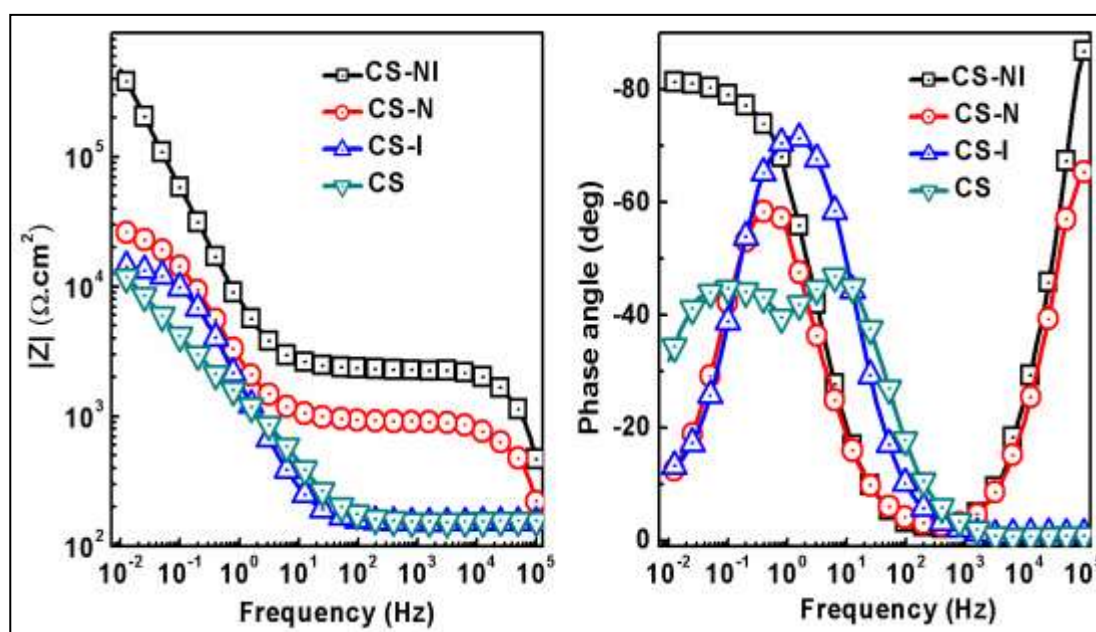


**Figure 5.12: EIS response of CS, CS-I, CS-N, and CS-NI after 1 week of immersion in 0.05 M NaCl solution**

The relaxation process associated with the barrier property of the hybrid coating was completely disappeared from the EIS measurements after 1 week of immersion. Both CS-N and CS-NI retained their barrier property after 1 week of exposure to salt solution. Even though CS-I had inhibitor molecules mixed with the hybrid coatings, it failed to provide protection after 1 week of immersion in salt solution. This clearly demonstrates that the direct addition of inhibitor molecules into the hybrid does not yield any good protection. CS had two relaxation processes in its impedance spectra after 1 week of immersion. A time constant associated with mass transport of species



participating in the redox reactions at metal surface was also present in addition to that of the relaxation process associated with the combination of polarization resistance and double layer capacitance. This shows the severity of damage occurred to CS during 1 week of immersion in salt solution. The value of modulus of impedance at low frequency for CS-NI was superior to that of CS, CS-I, and CS-N and its value did not change considerably with time during immersion. Moreover, the final relaxation process due to the response of the oxide film was capacitive in nature and this show its protective performance achieved by active corrosion protection.

Figure 5.13 shows the EIS measurements of CS-NI during 1 week of immersion in 0.05 M NaCl solution. The EIS response of CS-NI from 1 h to 168 h had two relaxation processes. The relaxation process reflecting the barrier property of the coatings appeared in the high frequency part of the spectra and the response of oxide film reflected in the second relaxation process at lower frequencies

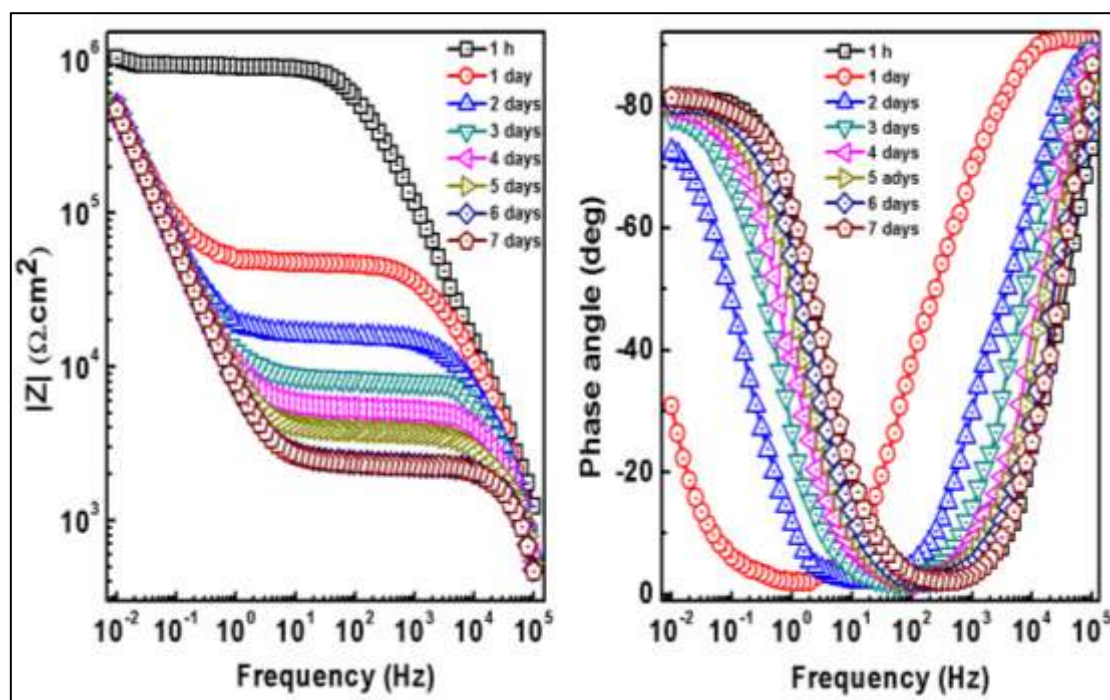


**Figure 5.13: EIS response of CS-NI during 1 week of immersion in 0.05 M NaCl solution**

Relaxation process due to the corrosion reactions was not present in the EIS response of CS-NI even after 1 week of immersion in salt solution. The resistance of the barrier coatings to the infiltration of the electrolyte containing the corrosive species decreased continuously as it is evidenced by the decrease in the resistive plateau in the Bode modulus plot. This is due to the pores and cracks in the coatings. The interesting feature of the EIS response of CS-NI is that the second relaxation process is capacitive in nature and the oxide resistive plateau did not appear. The oxide film is the last barrier layer and it is very important for protecting the underlying metal surface from corrosion, because its damage will give the electrolyte the direct access to the metal surface. The capacitive slope for the second relaxation process also did not change while immersed in salt solution from 1 day to 1 week. This behaviour was not shown by CS, CS-I, and CS-N, when they were immersed in salt solution. The impedance response due to the oxide film was not present in the EIS measurements of CS, CS-I, and CS-N and corrosion was initiated on the metal surface. The aforesaid results reflect the active corrosion protection offered by CS-NI and this is achieved by the release of the inhibitor from the mixed nanocontainers in the coating.

The obtained impedance results are well supported by visual inspection and SEM investigation of the coated specimens after 1 week of immersion in salt solution. Figure 5.14 shows the photograph of various coated samples after 1 week of immersion in salt solution. Visual inspection of the coated specimens (Figure 5.14) clearly shows the damage occurred on all coatings except CS-NI due to corrosion. Flakes and corrosion products were clearly visible on the surface of CS, CS-I, and CS-N. Coating was completely peeled off in CS and brownish corrosion products were deposited on the surface.



**Figure 5.14: Photographs of the coated samples after 1 week of immersion in 0.05 M NaCl solution. The drawn circles indicate the exposed area of the coatings**

The SEM images and corresponding EDX analysis of the coated specimens after immersion in salt solution for one week are depicted in Figure 5.15.

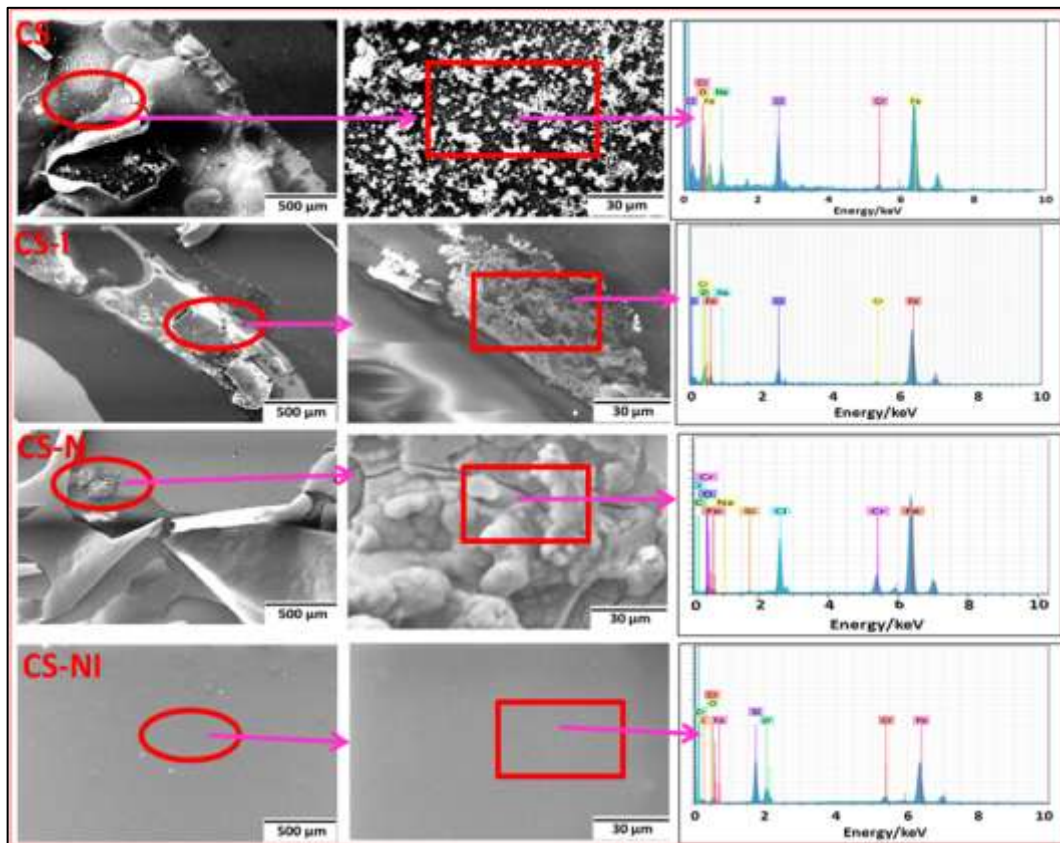


**Figure 5.15: SEM images and its corresponding EDX spectra of various coated specimens after 1 week of immersion in 0.05 M NaCl solution.**



The micrographs of the coatings after 1 week of immersion in salt solution is in good agreement with the results obtained from EIS studies. CS, CS-I, and CS-N underwent severe attack of corrosion after 1 week of immersion. Delamination of the coatings and corrosion products were visible in the images. However, the surface of CS-NI was uniform and coating was not delaminated after 1 week of immersion. The presence of chlorine was identified on the surface of CS, CS-I, and CS-N after EDX analysis. The peaks of Si and Zr were also absent from the EDX spectra and this observation clearly suggests the disruption of coating integrity and the presence of corrosion products on the surface of CS, CS-I, and CS-N. Conversely, Si and Zr were present in the EDX spectra of CS-NI and Cl<sup>-</sup> was absent.

The active corrosion protection of the coatings (CS and CS-NI) was carried out using EIS. Artificial scratches were made on the coatings to disrupt the coating integrity and to induce corrosion on the surface of the coatings. These scratched coatings were exposed to salt solution for one week to study the evolution of corrosion process. Impedance response of the coatings was recorded at regular intervals of time. Figure 5.16 shows the impedance response of CS for one week while immersed in salt solution. Three relaxation processes occurred in the surface of scratched CS after 1 h of immersion in salt solution. The impedance response of the hybrid coatings reflected at the high frequency range and of the oxide film at mid frequency range. The response of the metal-electrolyte interface was present at the low frequency region. After 1 day of immersion the impedance response of oxide film decreased but the relaxation process due to metal-electrolyte interface developed further. After 3 days of immersion, the oxide film was broken as it is evidenced by the disappearance of the relaxation process at mid frequency region and corrosion was initiated on the metal surface. However, the barrier property of CS was retained.

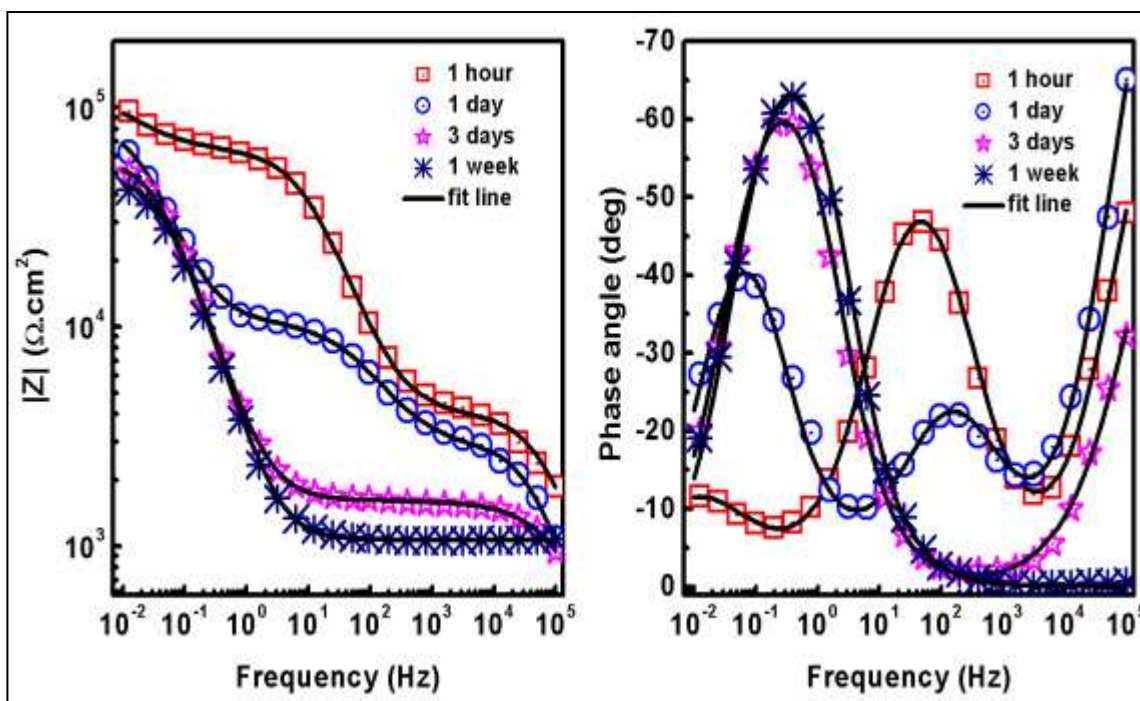
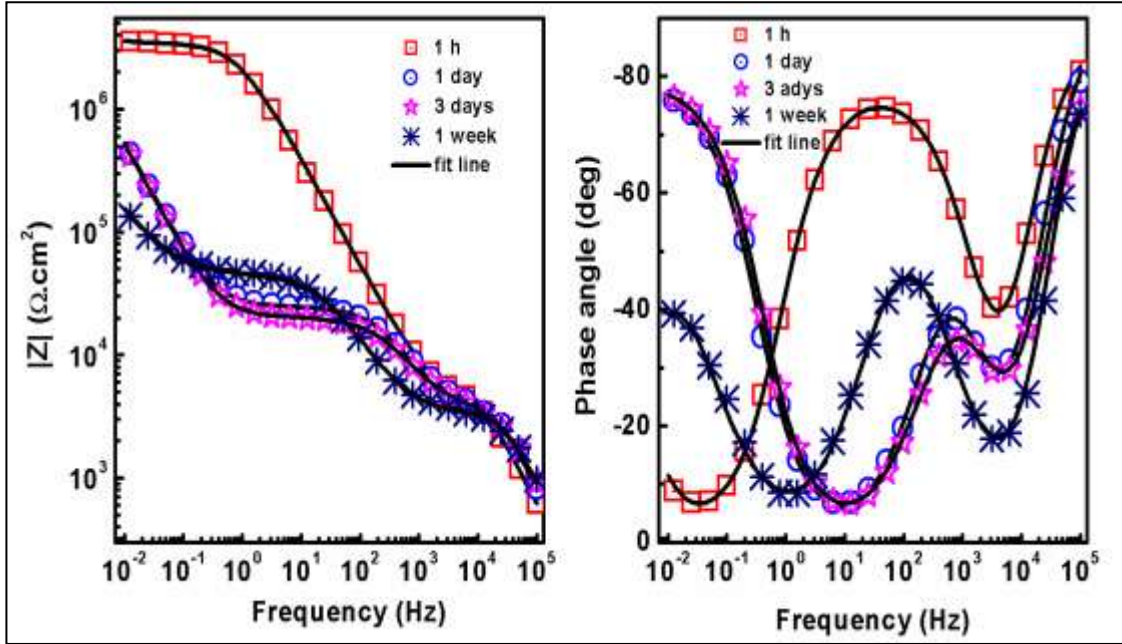


**Figure 5.16: EIS behaviour of scratched CS for one week while immersed in 0.01 M NaCl solution**

After 1 week of immersion, the surface of CS behaved typically like a double layer and the relaxation process due to the barrier property of the coating was not present in the impedance spectra. CS was corroding spontaneously as time progressed while immersing in salt solution.

Figure 5.17 shows the impedance response of artificially scratched CS-NI during one week of immersion in 0.05 M NaCl solution. The EIS behaviour of CS-NI was quite different from that of CS. CS-NI had only two time constants after 1 h of immersion in salt solutions and they are associated with the barrier coatings and the oxide film. No relaxation processes due to corrosion is present on the impedance spectrum after 1 h of immersion. After 1 day of immersion, the relaxation process due to oxide film became narrower (Bode phase angle at mid frequency) and a relaxation process from the metal-electrolyte layer started emerging. However, interestingly, the relaxation process due to

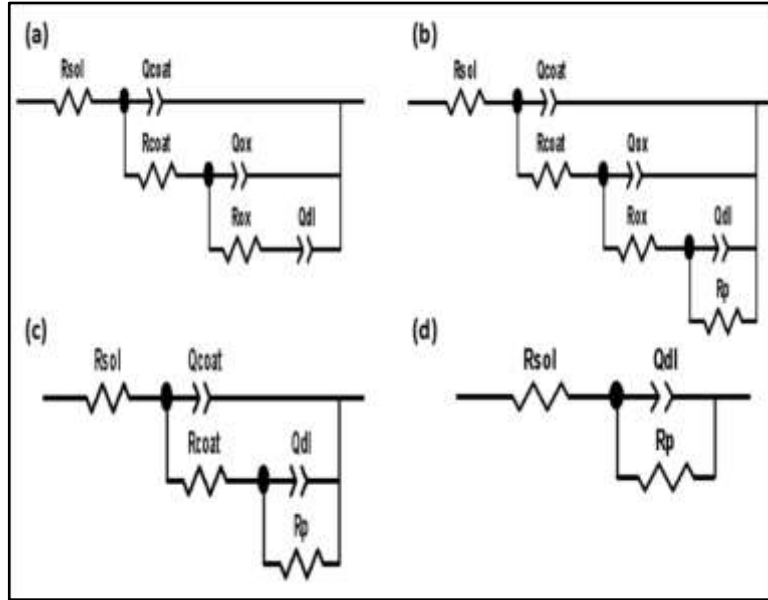
oxide film at mid frequency region became broader as the resistance of the oxide layer increased.



**Figure 5.17: EIS behaviour of scratched CS-NI for one week while immersed in 0.01 M NaCl solution**

This increase can be attributed to the release of MBT from HMS container and the presence of this insulating layer had also contributed to the relaxation process at mid frequency. This behaviour was not present in the impedance response of CS. This observation clearly demonstrated the active corrosion protection offered by CS-NI.

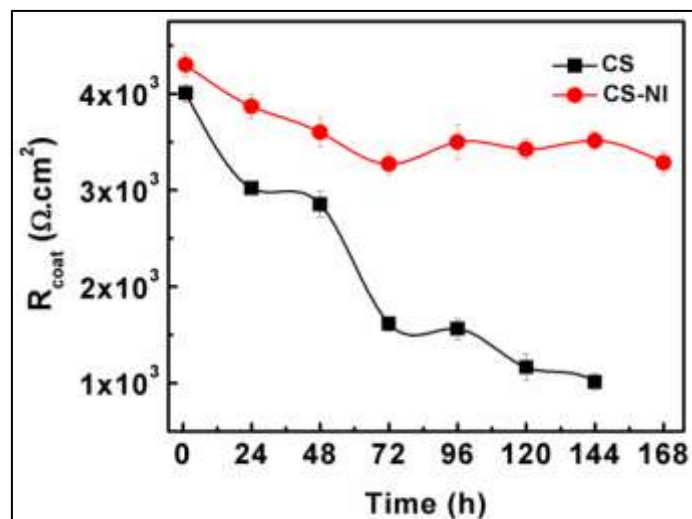
The impedance spectra of both scratched CS and CS-NI were fit using equivalent circuits (ECs) models to quantify the corrosion resistance offered by CS and CS-NI. The ECs used to fit the impedance spectra were depicted in Figure 5.18.  $R_{sol}$  is the solution resistance;  $R_{coat}$ ,  $R_{ox}$  and  $R_p$  are respectively the pore resistance of the sol-gel barrier coating, intermediate oxide layer and polarization resistance.  $Q_{coat}$ ,  $Q_{ox}$ ,  $Q_{dl}$  are the constant phase elements of sol-gel hybrid coating, intermediate oxide layer and double layer respectively. Instead of pure capacitance, constant phase elements were used since the phase angle is not equal to  $-90^\circ$ .



**Figure 5.18: Equivalent circuits used to fit the experimental EIS data of scratched CS and CS-NI during 1 week of immersion in 0.01 M NaCl solution**

For scratched CS-NI, in the beginning of the immersion test, two time constants were completely evolved in the impedance spectra and the third time constant at the low frequency was not evolved completely. Hence the impedance spectrum of CS-NI after 1 h of immersion was fitted using EC depicted in Figure 5.18(a). The EC shown in Figure 5.18(b) was used to fit impedance spectra of both scratched CS-NI during immersion of 24 h to 168 h and CS during immersion of 1 h to 24 h. Impedance spectra of CS during immersion of 48 h to 144 h was fitted using EC shown in Figure 5.18(c). Figure 5.18(d) was used to fit the impedance spectra of CS after 168 h of immersion. The error of fitting  $\chi^2$  was less than or equal to  $10^{-3}$  for all the spectra.

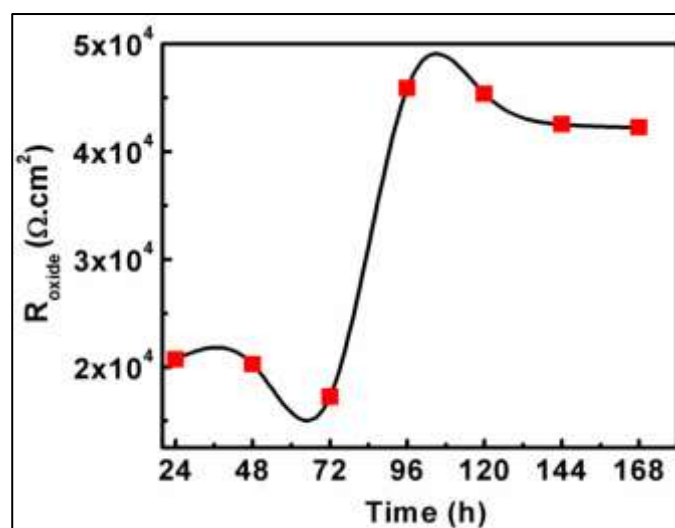
Figure 5.19 depicts the change in coating resistance ( $R_{coat}$ ) of CS and CS-NI while immersed in salt solution for 1 week. The coating resistance or pore resistance of barrier coatings depends on porosity and cracks present in the coatings. Coating resistance of CS decreased continuously as the immersion time progressed and CS did not have  $R_{coat}$  value after 144 h of immersion.



**Figure 5.19: Evolution of coating resistance ( $R_{coat}$ ) of CS and CS-NI during 1 week of immersion in 0.01 M NaCl solution.**

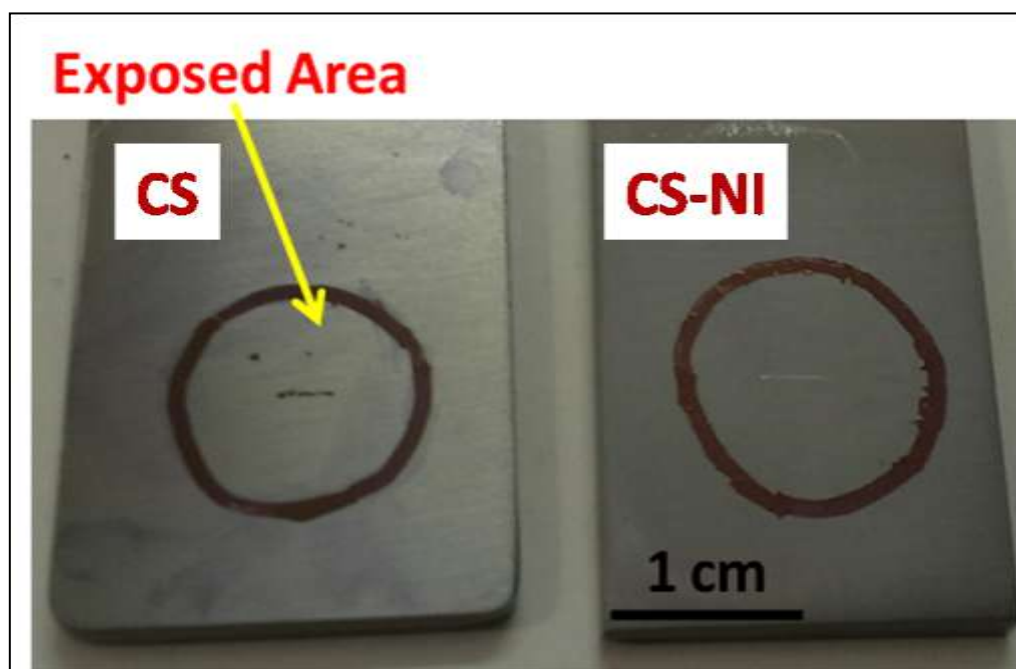
This shows that the barrier property of CS was completely lost. Conversely, CS-NI always had high  $R_{coat}$  value compared to that of CS and retained its barrier property after 1 week of immersion. Moreover, there is a slight increase in  $R_{coat}$  value from 72 h onwards.

Figure 5.20 shows the evolution of oxide layer resistance ( $R_{oxide}$ ) of CS-NI with time during 1 week of immersion. The oxide layer resistance of CS did not consider for a comparison since the oxide layer was no longer present in the EIS response of CS after 1 day of immersion (see Figure 5.15). It is observed that value of  $R_{oxide}$  initially decreased from 24 h to 72 h. However, from 72 h of immersion onwards, resistance of the oxide layer increased and it almost remained constant up to 1 week of immersion. This increase in  $R_{oxide}$  could be attributed to the formation of a new interfacial layer made up of MBT released from HMS nanocontainers on the oxide layer. This increase in oxide film resistance clearly demonstrated the active corrosion protection rendered by the release of the inhibitor from the nanocontainer mixed in the hybrid coating.



**Figure 5.20: Evolution of oxide layer resistance ( $R_{\text{oxide}}$ ) of CS and CS-NI during 1 week of immersion in 0.01 M NaCl solution.**

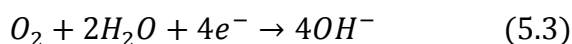
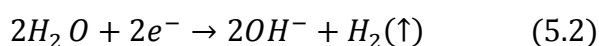
Figure 5.21 shows the photograph of scratched CS-NI and CS after 1 week of immersion in salt solution.



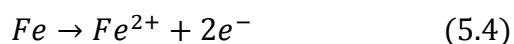
**Figure 5.21: Optical images of artificially scratched CS-NI and CS after 1 week of immersion in 0.01 M NaCl solution**

It is observed from the figure that black coloured corrosion products appeared on the scratched area of CS after 1 week of immersion in salt solution and pits were also present on the surface of CS. Conversely, no sign of corrosion or presence of corrosion products were observed at the scratched area and remaining surface of CS-NI. These observations clearly supported the EIS results.

Thus both the EIS studies and SEM analysis portrayed the superior corrosion protection property of silane-zirconia hybrid coating mixed with inhibitor loaded nanocontainers. Though the silane-zirconia film could act as a good physical barrier coating, any damage occurred on the barrier coating, corrosion process started. However, inhibitor loaded nanocontainer impregnated silane-zirconia coating could demonstrate enhanced corrosion resistance and this was achieved by the active corrosion protection rendered by the release of entrapped 2-MBT. The release of the inhibitor molecules from the nanocontainer is also confirmed from the release studies carried out using UV-visible spectroscopy. The initiation of corrosion process itself can act as a trigger for the release of the inhibitor molecules from the nanocontainer. The improved corrosion protection of the coating can be explained by a self-healing mechanism. A graphical illustration of the proposed mechanism is presented in Figure 5.22. It is well established that the corrosion process always accompanies with pH changes in the corrosive environment. The following electrochemical reactions occur when a ferrous alloy is exposed to neutral aqueous NaCl solution. Cathodic reactions at the local cathodic sites generate hydroxyl radicals.



Anodic reactions at local anodic sites generates of metal cations.



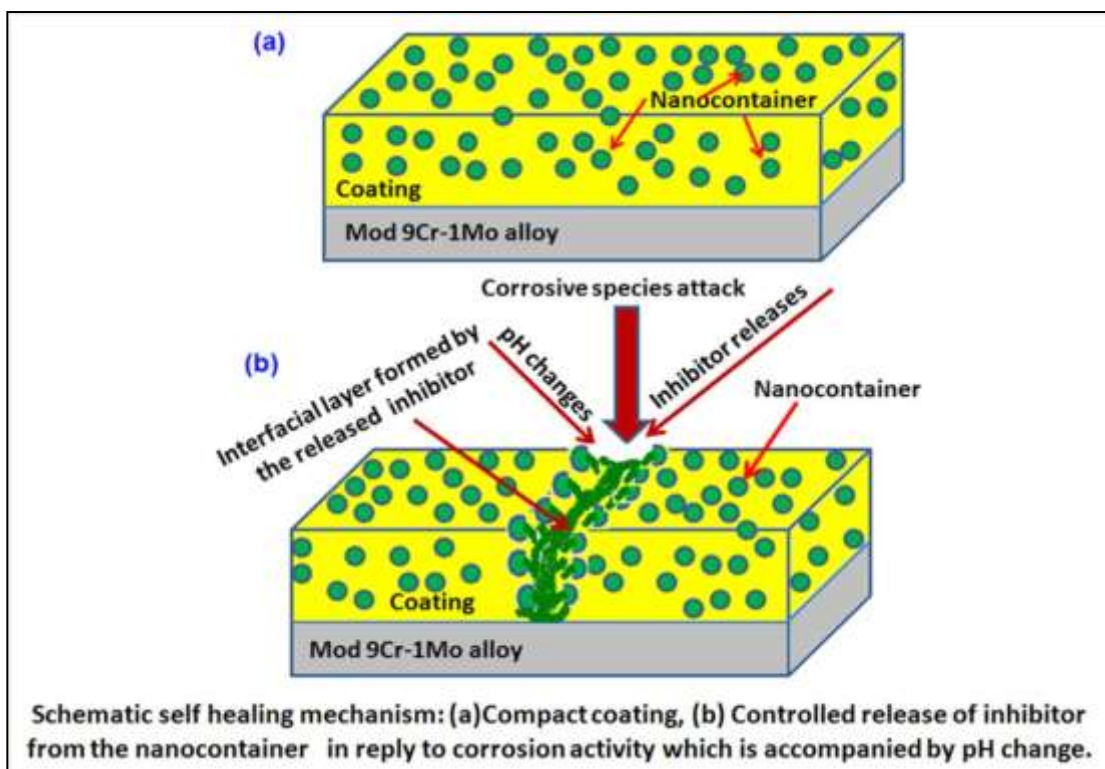


**Figure 5.22: Proposed mechanism of the active corrosion protection based on self-healing ability**

Thus during corrosion acidic pH develops around anodic area and alkaline pH develops at cathodic area. If any local damage occurs in the coating, corrosion will instigate in the alloy surface. Localized corrosion of ferritic steels is commonly accompanied by change in pH at the micro anodes and micro cathodes. Aforementioned, the release of inhibitor molecules happened by diffusion of inhibitor through the channels and pores of the nanocontainers into aqueous NaCl solution. The enhanced corrosion resistance showed by the inhibitor loaded nanocontainer mixed hybrid coating can be explained as follows; as the immersion time increases, the water molecules and corrosive species enters to the coating through the pores and cracks of the coatings. This electrolyte solution could infiltrate into the nanocontainers through the mesopores and the inhibitor molecules could diffuse along this aqueous pathway. When any corrosion activity takes place low pH prevails around the micro anode and alkaline pH develops around the



micro cathode area. This change in local pH will increase the release rate and quantity of the inhibitor released from the nanocontainers. The anticorrosive property of the organic inhibitor 2-mercaptobenzothiazole is based on producing a film on the alloy surface and this layer acts as physical barrier to aggressive corrosive ions [235]. When pitting corrosion is initiated, these organic inhibitor molecules can form complexes with the metal ions and form a protective layer and that stops further dissolution of the metal and alloys.

#### 5.4 Summary

- ❖ Effectiveness of an active coating system consisting of hybrid silane-zirconia film impregnated with 2-MBT loaded HMS nanocontainers for corrosion protection has been discussed in this chapter.
- ❖ Hollow silica spheres with mesoporous structure and extraordinary surface area was synthesized through a sol-hydrothermal method.
- ❖ These porous silica spheres were successfully loaded with corrosion inhibitor 2-MBT. The inhibitor loading efficiency of hollow mesoporous silica containers was about  $72 \pm 2$  %.
- ❖ The pH stimulated intelligent release of 2-MBT from the HMS spheres was demonstrated. The inhibitor was released in right amount from the nanocontainer, without any unwanted leaching, with increase or decrease of local pH.
- ❖ Then these inhibitor filled nanocontainers were embedded in a hybrid silane-zirconia coating and applied on modified 9Cr-1Mo ferritic steel.
- ❖ Both the barrier property and active corrosion protection based on self-healing ability of inhibitor loaded nanocontainer impregnated of the coating was successfully confirmed using electrochemical impedance spectroscopy

## CHAPTER 6

### **TiO<sub>2</sub> Nanocontainers for Active Corrosion Protection**

---

*This chapter describes a new approach to developing active corrosion protection coating system using TiO<sub>2</sub> nanotube powder. TiO<sub>2</sub> nanotube powder was synthesized by rapid breakdown anodization (RBA) method and loaded with corrosion inhibitors. Benzotriazole (BTA) and 2-mercaptobenzothiazole (2-MBT) were the two inhibitors used for encapsulation. The successful loading and controlled release of the inhibitor molecules were investigated using UV-visible spectroscopy. The inhibitor loaded TiO<sub>2</sub> nanotube powder was randomly introduced into a hybrid barrier coating. This hybrid sol-gel barrier coating with random distribution of such inhibitors loaded TiO<sub>2</sub> nanotube powder was coated over modified 9Cr-1Mo steel. The corrosion resistance and the self-healing effects of this hybrid passive barrier coating with and without the addition of inhibitor loaded TiO<sub>2</sub> nanocontainers were studied using electrochemical impedance spectroscopy (EIS). EIS analysis revealed that inhibitor loaded nanocontainer impregnated coatings showed enhanced corrosion protection due to the release of inhibitor molecules from the nanocontainers.*

---

#### **6.1 Introduction**

The nanostructured TiO<sub>2</sub> is one of the very important compounds in the arena of material science due to its outstanding properties. The nontoxic and environmentally friendly nature, biocompatibility and high corrosion resistance made TiO<sub>2</sub> one of the most used materials in various industrial applications. Among the various nanostructures of TiO<sub>2</sub>, nanotubes have numerous applications in solar cells, gas sensing, hydrogen storage and drug delivery [306-309]. TiO<sub>2</sub> nanotubes can be synthesized by various methods such as template-assisted method, sol-gel method,

solvo/hydrothermal method and electrochemical anodization method [310]. The titanium dioxide nanotubes prepared by both precursor and template methods result in single nanotubes as well as bundles of nanotubes. Conversely, the anodization approach for the synthesis of  $\text{TiO}_2$  nanotubes has significant advantages over template assisted and sol-gel/sol-hydrothermal methods.

The anodization can be executed at room temperature and the nanotubes can be grown within a short period. Titanium surface of any shape can be used to fabricate self-organized nanotubes. However, the tubes are not well organized over a very large surface area and not well defined in length distribution [310, 311]. Zwillig et al. first reported the preparation of  $\text{TiO}_2$  nanotubes on Ti foil by anodization in hydrofluoric acid [312]. The fabrication of  $\text{TiO}_2$  nanotubes by electrochemical anodization was thoroughly investigated by both Grimes and Schmki groups [313-316]. In recent times, extensive research was carried out on the rapid fabrication of  $\text{TiO}_2$  nanotubes by electrochemical anodization under breakdown conditions [317-319]. Recently Fahim and Sekino synthesized  $\text{TiO}_2$  nanotube powder for the first time by rapid breakdown anodization method (RBA) [231]. We synthesized  $\text{TiO}_2$  nanotube powder following their method and this  $\text{TiO}_2$  nanotube powder was used for loading corrosion inhibitor molecules.

Benzotriazole (BTA) and 2-mercaptobenzothiazole (2-MBT) were the corrosion inhibitors used for encapsulation. BTA was used as the corrosion inhibitor, which was already reported for corrosion protection of the ferrous alloys in both acidic and neutral media [237-241]. Since BTA is not effective in alkaline media, 2-MBT, which is a good corrosion inhibitor for ferrous alloys in acidic as well as alkaline media, was used [224, 242, 243]. The barrier coatings produced on modified 9Cr-1Mo ferritic steel were silane-titania and silane-zirconia hybrid sol-gel films. The corrosion protection

efficiency of following four coatings was studied and compared using EIS: (i) hybrid sol-gel coated modified 9 Cr-1 Mo ferritic steel, (ii) inhibitor mixed hybrid sol-gel coated modified 9 Cr- 1 Mo ferritic steel, (iii) empty nanocontainer mixed hybrid sol-gel coated modified 9 Cr-1 Mo ferritic steel and (iv) inhibitor loaded nanocontainer mixed modified 9 Cr-1 Mo ferritic steel.

## **6.2 Experimental**

### **6.2.1 Materials**

Commercially pure titanium (Ti) foil (99.8% purity) of 1 mm thickness was used for preparing the  $\text{TiO}_2$  nanotube powder. (3Glycidyloxypropyl) trimethoxysilane, titanium isopropoxide, zirconium-n-propoxide (TPOZ), ethyl alcohol, isopropyl alcohol and nitric acid were used to synthesize silane and titania based sols. Perchloric acid was used as electrolyte for anodizing Ti foil. BTA and 2-MBT were used as inhibitor molecules and NaCl was used for electrochemical studies.

### **6.2.2 Synthesis and Characterization of $\text{TiO}_2$ Nanocontainers**

$\text{TiO}_2$  nanocontainers were synthesized through rapid breakdown anodization method (RBA). Detailed synthesis procedure and schematic for the synthesis condition and set up are given in section 3.4.1 of chapter 3.

The structure, morphology and the phase of the  $\text{TiO}_2$  nanocontainers were studied using field emission scanning electron microscopy (FESEM; ZEISS system with electron beam energy of 10kV, Germany), high resolution transmission electron microscopy (HRTEM; JEOL JEM 2100, Japan) and laser Raman spectroscopy (LRS; Lab RAM HR 800, HORIBA JOBIN YVON, Japan, Raman spectrometer equipped with 1800 grooves/mm holographic grating).

### ***6.2.3 Loading and Releasing of Inhibitors***

Both BTA and 2-MBT were chosen to load into TiO<sub>2</sub> nanocontainers. BTA inhibitor molecule was dissolved in ethanol at a concentration of 10 mg/mL. 100 mg of TiO<sub>2</sub> nanotube powder was added to 50 mL of ethanolic benzotriazole solution and the vial was sealed in order to avoid any evaporation of ethanol and stirred electromagnetically for 24 h. After 24 h of stirring, BTA loaded TiO<sub>2</sub> was taken out by centrifugation and cleaned several times with water. The benzotriazole loaded TiO<sub>2</sub> nanocontainers were obtained by drying it in air at room temperature. The filtrate was extracted out from the vial and used to determine the free BTA content in solution with the help of UV-visible spectroscopy studies. The aforesaid similar procedure was used to load 2-MBT into TiO<sub>2</sub> nanotube powder and the loading efficiency was calculated using UV-visible spectroscopy studies. Laser Raman spectroscopy also used to confirm the successful loading of 2-MBT into TiO<sub>2</sub> nanocontainers.

50 mg of inhibitor (MBT/BTA) loaded TiO<sub>2</sub> nanocontainers was dispersed in 150 mL of 0.05 M NaCl at different pH values of 3, 7 and 10 (releasing medium) at room temperature and the resulting solution was stirred at a rate of 500 rpm using a magnetic stirrer. The releasing experiments for BTA@TiO<sub>2</sub> nanocontainer system was carried out at pH 2, 4 and 7, since the inhibitive effect of BTA in alkaline solution on ferrous alloy is insignificant. A detailed description of loading and releasing procedures of BTA and 2-MBT into TiO<sub>2</sub> nanocontainers is given in sections 3.5.1 and 3.5.2 of chapter 3.

### ***6.2.4 Synthesis and Deposition of Sol-Gel Hybrid Coatings***

Silane-titania and silane-zirconia hybrid sol-gel films were deposited after dispersing with inhibitor loaded TiO<sub>2</sub> nanocontainers on modified 9Cr-1Mo ferritic steel. The pretreatments applied on modified 9Cr-1Mo ferritic steel prior to the coating was

described in detail in section 3.3.1 of chapter 3. The synthesis procedure for organic-inorganic hybrid sol-gel films is described elaborately in section 3.6 of chapter 3. Four different types of coatings were produced. At first, coatings free of any inhibitor and nanocontainers were prepared and this is named as CS i.e. plain silane zirconia/silane titania hybrid barrier coating. Secondly, inhibitors (2-MBT/BTA) were mixed directly with the hybrid coating and it was produced and named as CS-I. Then the hybrid coatings incorporated with empty nanocontainers were prepared and it is referred as CS-N. Finally, coatings containing inhibitor loaded nanocontainers were prepared and it is referred as CS-NI. All the above mentioned three sol solutions were deposited on the modified 9Cr-1Mo steel by dip coating procedure, i.e., immersing a specimen in the hybrid sol-gel mixture for 100 s and thereafter, withdrawn at a constant lifting speed of  $2 \text{ mm s}^{-1}$ . The coated substrate was dried in air and then baked at  $120^\circ\text{C}$  for 1 h.

#### ***6.2.5 Evaluation of Anticorrosion Efficiency of Coatings***

Electrochemical impedance spectroscopy (EIS) was used to assess and compare the anticorrosion efficiency of the developed hybrid coatings on modified 9Cr-1Mo ferritic steel without and with artificial defect, during 1 week of immersion in 0.05 M NaCl solution and in 0.01 M NaCl solution, respectively. The morphology and composition of the coated substrates after immersion in 0.05 M NaCl solution was analyzed by scanning electron microscope and attached energy dispersive X-ray analysis (EDX) system.

### **6.3 Results and Discussions**

#### ***6.3.1 Synthesis of $\text{TiO}_2$ Nanocontainers***

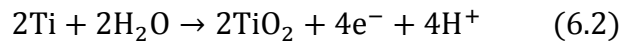
The process and the underlying mechanism of anodization were well-studied and understood [313-316]. When Ti metal is immersed in the electrolyte solution and a

sufficiently high anodic voltage is applied under rapid stirring, the oxidation of Ti metal is initiated.



This  $\text{Ti}^{4+}$  can undergo any of the three possible reactions depending upon the experimental conditions [310]. (I) The  $\text{Ti}^{4+}$  ions are dissolved continuously in the electrolyte; i.e., corrosion takes place. (II) The  $\text{Ti}^{4+}$  ions can react with  $\text{O}^{2-}$  ions present in the aqueous electrolyte solution and form a compact layer of  $\text{TiO}_2$ . (III) A competition between dissolution and oxide formation can take place under certain condition and this equilibrium between these two competing processes resulted in the formation of porous  $\text{TiO}_2$ . Moreover, at certain specific experimental conditions; i.e., anodization at sufficiently high applied anodic potential and under rapid stirring, leads to the rapid formation of disorganized  $\text{TiO}_2$  nanotube bundles.

Figure 6.1 shows the current versus time behavior recorded during the anodization of the Ti foil in 0.1 M  $\text{HClO}_4$ . Initially, within seconds the current showed a steep decrease due to the formation of the passive oxide layer of titanium that is poor in conduction compared to the Ti metal. The anodic reaction leading to the formation of titanium dioxide can be represented as follows:



$\text{TiO}_2$  layer thus formed started growing on both sides of the Ti foil with in a very short period. Then it is observed that the current starts increasing gradually as the white coloured titanium oxide begins dissolving. This is due to the dissolution of the passive  $\text{TiO}_2$  layer and creation of pores by the chloride ions present in the electrolyte. The very high speed of the reaction and the application of sufficiently high anodic voltage resulted in the rapid breakdown of the  $\text{TiO}_2$  layer.

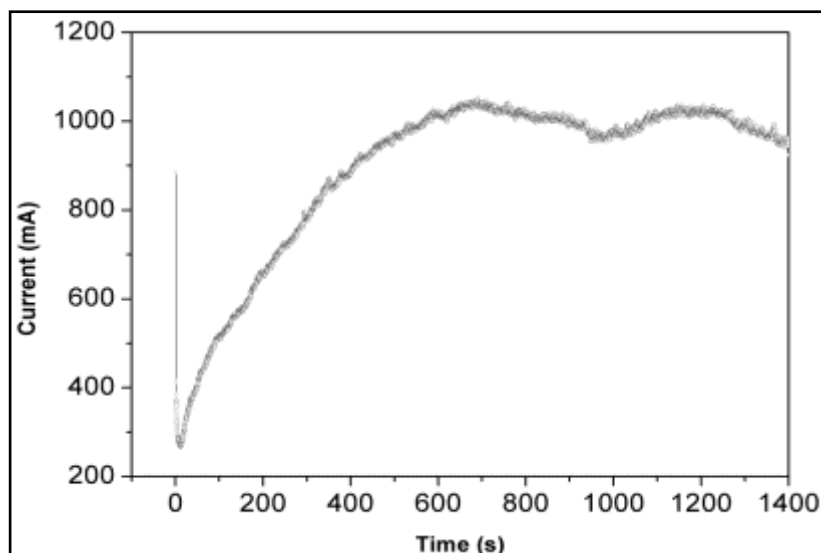
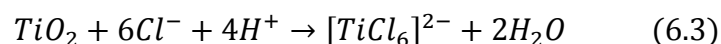


**Figure 6.1: The current-time behaviour observed during the rapid breakdown anodization of TiO<sub>2</sub> nanotube powder at 20 V at room temperature in 0.1 M HClO<sub>4</sub>**

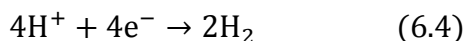
Even though TiO<sub>2</sub> is thermodynamically stable in the pH range of 2-12, the presence of Cl<sup>-</sup> ions lead to the dissolution of TiO<sub>2</sub> according to the following mechanism involving the formation of a complex containing Ti and Cl<sup>-</sup> [231].



Earlier Chassaing et al. [320] suggested the high stability of [TiCl<sub>6</sub>]<sup>2-</sup> with its free energy of formation ranging from -5.12 to -10.90 kcal/mol depend upon the type of the cations. However, the pores created by the pitting of chloride ions also helped in the inward migration of oxygen and thus the oxidation of the Ti foil was simultaneously maintained. From Figure 6.1 it is clear that the current reached a steady state after 10 min when anodizing in 0.1M HClO<sub>4</sub>. The steady state behaviour of the current after 10 min of anodization confirms both the repassivation and the saturation of the nanotube formation. The chemical etching of Cl<sup>-</sup> ion, which creates pits on the compact TiO<sub>2</sub> layer and re-oxidation Ti substrate, causes the repassivation at Ti substrate. The steady state behaviour of the current is observed when equilibrium is attained between the



oxidation of Ti and the solvatization of  $\text{TiO}_2$  by the inhibiting action of chloride ions. More specifically speaking, at the steady state the rate of oxidation is equal to the rate of oxide dissolution. The strong evolution of the bubbles during anodization was due to the hydrogen evolution at the platinum electrode.



### 6.3.2 Characterization of $\text{TiO}_2$ Nanocontainers

The morphology and the phase analysis of the  $\text{TiO}_2$  nanocontainers were examined using FESEM, HRTEM and LRS. Figure 6.2 shows the FESEM micrographs of as prepared  $\text{TiO}_2$  nanotube powder. The tubular structure of the as prepared  $\text{TiO}_2$  powder is evident from the FESEM images (Figure 6.2). The tubes were well ordered and stacked in bundles of length approximately 6-8  $\mu\text{m}$  and diameter about 40 nm. The HRTEM images of as prepared and calcined  $\text{TiO}_2$  nanotube powders at 400  $^\circ\text{C}$  at the heating rate of 10  $^\circ\text{C}$  /min at different magnifications are shown in Figure 6.3. The open end and the hollow structure of  $\text{TiO}_2$  nanotube are visible from Figure 6.3a.

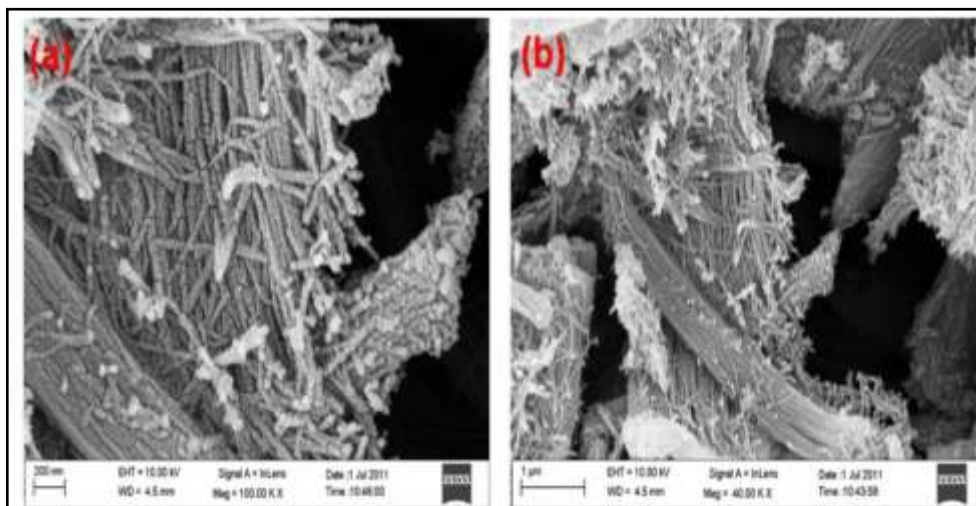


**Figure 6.2: FESEM micrographs of  $\text{TiO}_2$  nanocontainers**

Calcining of TiO<sub>2</sub> nanotube powders resulted in the lost of tubular morphology and the powders became spherical nanoparticles.

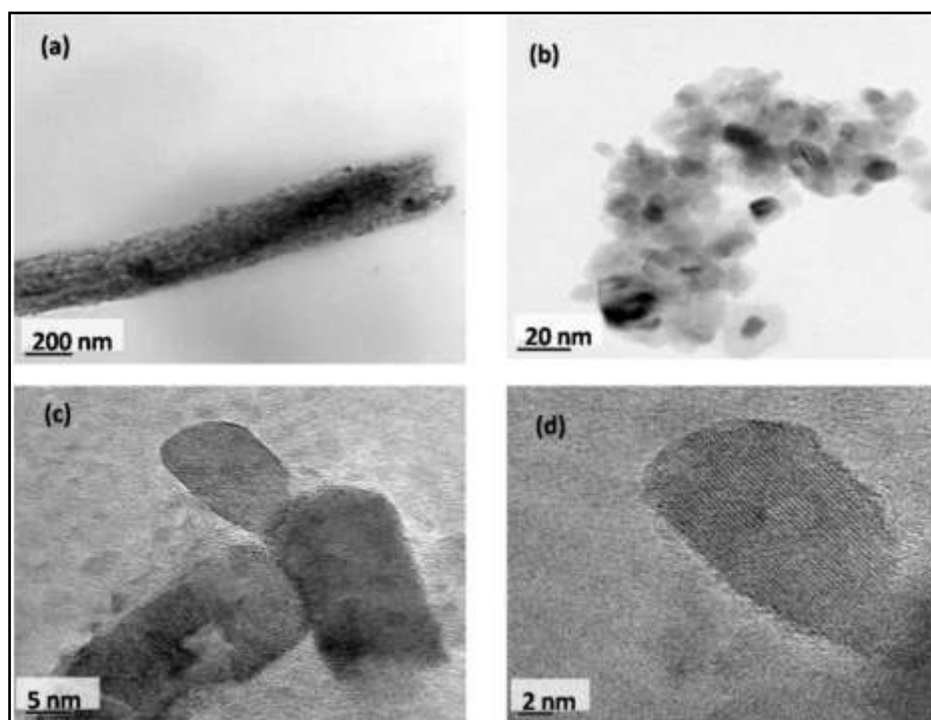


**Figure 6.3: The HRTEM images of (a) as synthesized TiO<sub>2</sub> nanotube; (b) calcined TiO<sub>2</sub> nanotube powder at 400 °C; (c) & (d) magnified views.**

TiO<sub>2</sub> crystallites with a size of approximately 10-30 nm are demonstrated in Figure 6.3(b-d). Crystal fringes (finger prints) and ordered array of micro pores are visible on the surface of this small TiO<sub>2</sub> crystallite (Figure 6.3(d)) and these pores can effectively increase the adsorption of inhibitor while loading the inhibitor.

Figure 6.4 shows the Raman spectra of as synthesized and calcined TiO<sub>2</sub> nanotube powders at 400 °C. The anatase TiO<sub>2</sub> has six Raman active modes in the vibrational spectrum:  $A_{1g}+2B_{1g}+3E_g$  [321]. In the case of the as synthesized TiO<sub>2</sub> nanotube powders, features were very weak and overlapped. Raman lines became weak and broad when the samples have local lattice imperfections [322]. The Raman spectra of the as prepared TiO<sub>2</sub> revealed its amorphous nature (Figure 6.4(a)). When the as

synthesized powders were calcined at 400 °C, the anatase phase appeared and it was revealed by Raman spectra (Figure 6.4(b)).

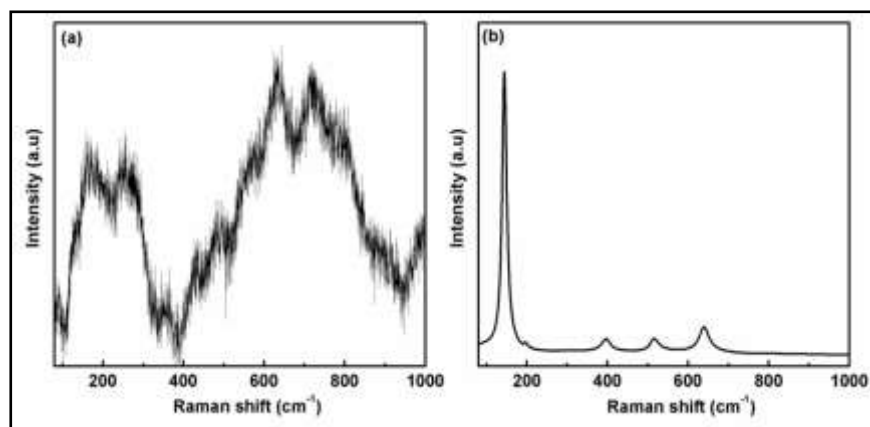


**Figure 6.4: Raman spectra of (a) the as prepared TiO<sub>2</sub> nanotube powders and (b) Raman spectra of TiO<sub>2</sub> nanotube powders calcined at 400 °C.**

All the characteristics phonon modes of the anatase titania was observed in the Raman spectra of the calcined TiO<sub>2</sub> nanotube powder. The band appeared at 144 cm<sup>-1</sup> is the strongest one and this is a clear indication of the anatase phase. The bands at 144 cm<sup>-1</sup>, 196 cm<sup>-1</sup>, and 639 cm<sup>-1</sup> are assigned to the E<sub>g</sub> mode of vibration of anatase phase. The band at 397 cm<sup>-1</sup> is of the B<sub>1g</sub> mode and the band at 515 cm<sup>-1</sup> is a doublet of A<sub>1g</sub> and B<sub>1g</sub> modes [323].

### **6.3.3 Inhibitor Loading and Releasing**

**Loading and releasing of Benzotriazole (BTA):** BTA was loaded into the TiO<sub>2</sub> nanocontainers by mixing the nanocontainer system in inhibitor solution and stirring for 24 h [324, 325]. Figure 6.5 shows the UV absorbance spectra of 10 mg/ml benzotriazole solutions before and after the interactions with the TiO<sub>2</sub> nanotube powders. After the incorporation of the benzotriazole within TiO<sub>2</sub> nanocontainers, the positions of the absorption maxima was the same and no new bands appeared, but the intensity of the absorption maxima decreased. This indicated the stability of the benzotriazole molecule after the loading procedure. The decrease in the intensity of the

UV absorbance of benzotriazole after stirring for 24 h with TiO<sub>2</sub> nanotube powders indicated not only the reduction of the inhibitor concentration but also its storage in the TiO<sub>2</sub> nanocontainer. The loading efficiency of benzotriazole in the TiO<sub>2</sub> nanotube powders was  $73\pm2$  %.

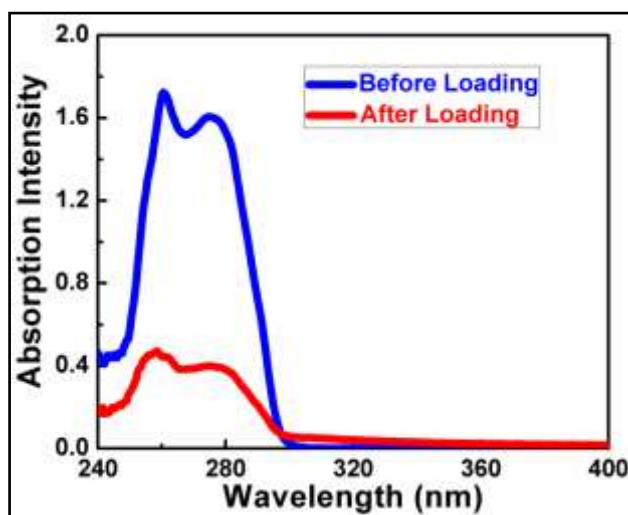


**Figure 6.5: The UV absorbance spectra of ethanolic solution of benzotriazole before and after the interaction with TiO<sub>2</sub> nanocontainers**

Benzotriazole was proved to be an inhibitor for metals and ferrous alloys in acidic as well as neutral solutions and particularly, in acidic conditions it exhibited better protection. Hence, the benzotriazole release from the TiO<sub>2</sub> nanocontainer experiments were conducted in aqueous NaCl solutions of pH 2, 4 and 7 for 24 h. The main idea of this experiment was to find out the optimum pH conditions and how it is released in a controlled and sustained manner. Figure 6.6 shows the release percentage of benzotriazole from TiO<sub>2</sub> nanocontainer in aqueous NaCl medium at different pH values.

Figure 6.6 clearly shows the effect of pH of the release medium on the releasing behavior of BTA from TiO<sub>2</sub> nanocontainers. As anticipated, the high release of BTA from TiO<sub>2</sub> nanocontainer is obtained for the low pH-release medium. At pH 2 almost 90 % of the benzotriazole was released out from the TiO<sub>2</sub> nanocontainer within 24 h. In

the neutral medium (i.e., pH 7), the release is quite slow and only about 64 % released over 24 h. As seen in Figure 6.6, the releasing behavior at pH 4 is intermediate, which is falling between pH 2 and pH 7. The presented results confirm the loading of the inhibitor into the TiO<sub>2</sub> nanocontainers and it proves the sustained as well as controlled releasing behavior on demand.

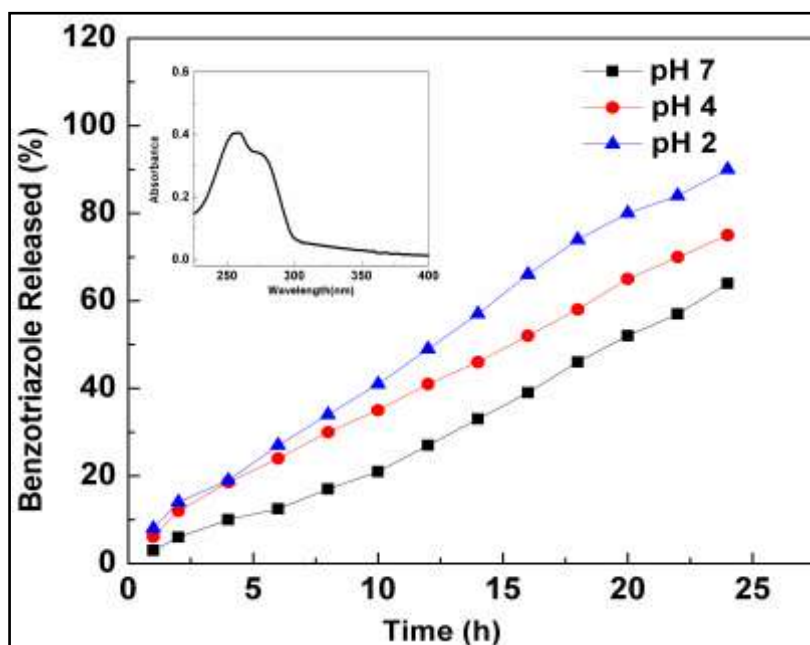


**Figure 6.6: The release percentages of benzotriazole from TiO<sub>2</sub> nanocontainers at different pH values. Inset shows the UV-visible absorbance spectra of benzotriazole in the release medium.**

**Loading and releasing of 2-mercaptobenzothiazole (2-MBT):** 2-MBT was successfully loaded into TiO<sub>2</sub> nanocontainers by mixing TiO<sub>2</sub> nanocontainers with 2-MBT solution in acetone and followed by stirring for 24 h. Figure 6.7 presents the UV-vis spectra of MBT solution before and after the interactions with TiO<sub>2</sub> nanocontainers.  $\lambda_{\text{max}}$  for 2-mercaptobenzothiazole is at 325 nm. The UV-visible spectra (Figure 6.7) showed the successful encapsulation of 2-MBT into TiO<sub>2</sub> nanocontainers. This decrease in the absorption intensity of MBT after the interaction with TiO<sub>2</sub>

nanocontainers confirmed the decrease of the MBT concentration in the solution as well as the successful loading of the MBT molecules into TiO<sub>2</sub> nanocontainers.

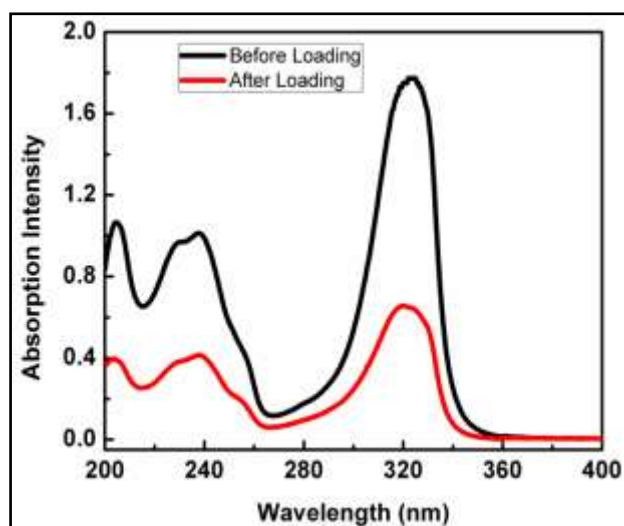


**Figure 6.7: UV absorbance spectra of 2-MBT before and after the interaction with TiO<sub>2</sub> nanocontainers**

The loading efficiency was calculated as follows:

$$\text{Loading efficiency} = \frac{\text{Total amount of MBT} - \text{Free MBT in solution}}{\text{Total amount of MBT}} \times 100 \quad (6.5)$$

The loading efficiency of 2-MBT in the TiO<sub>2</sub> nanocontainer was found to be 73±3 %. The release behaviour of 2-MBT loaded TiO<sub>2</sub> nanocontainer system was investigated by UV-visible analysis of NaCl (0.05 M) suspensions of 2-MBT loaded TiO<sub>2</sub> at different pH values. The absorption intensity at *ca.* 325 nm was measured at given time interval for 36 h and the results are shown in Figure 6.8. When the releasing medium had entered into the pores of TiO<sub>2</sub> nanocontainers, the inhibitor molecules (2-MBT) gets dissolved in the medium and released by diffusion through the pores along the aqueous pathways. The releasing of MBT from TiO<sub>2</sub> followed similar release kinetics at different pH values. A faster release was observed under alkaline and acidic conditions compared to neutral condition. The release of MBT was leveled off and reached equilibrium in 5 h at pH 10.

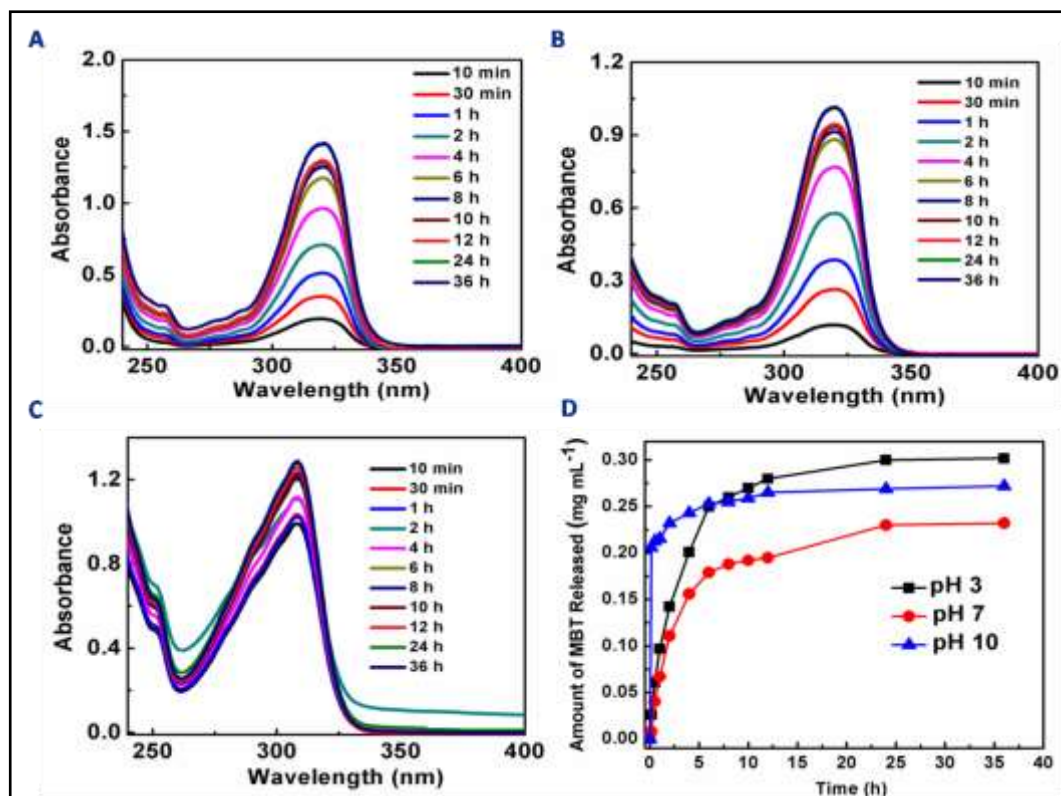


**Figure 6.8:** UV-vis spectra at different times of the 0.05 M NaCl media in which 2-MBT was released from 2-MBT loaded TiO<sub>2</sub> nanocontainers (a) at pH 3, (b) at pH 7, (c) at pH 10 and (d) corresponding pH-dependent releasing behaviour of 2-MBT from TiO<sub>2</sub>-MBT system

It was observed that higher amount of 2-MBT was released from the TiO<sub>2</sub> at pH 3 and 10 compared to pH 7. The amount of MBT released after 28 h under acidic and alkaline conditions were 0.30 mg mL<sup>-1</sup> and 0.27 mg mL<sup>-1</sup> respectively, while in neutral conditions it was 0.23 mg mL<sup>-1</sup> only.

The difference in the release rate and quantity of MBT released from TiO<sub>2</sub> can be explained by the variation of solubility of MBT and the differences in the surface charge of both MBT and titania particles with pH. The solubility of 2-MBT is low in neutral pH, but relatively higher in alkaline and acidic conditions [172]. Both the titania particles and the inhibitor molecules have the same surface charge when the pH vary from neutral pH values. Under acidic pH conditions, titania particles have positive

surface charge whereas at alkaline pH titania particles acquire negative surface charge [326]. At acidic pH, MBT could be protonated due to the presence of a lone pair of electrons on the N atom and carries a positive charge [274, 275]. Thus under acidic conditions, both the titania particles and MBT had positive charge and this led to larger electrostatic repulsion between them, thereby facilitating faster release of MBT from TiO<sub>2</sub> nanocontainers in high amount. Similarly, under alkaline conditions, MBT exists in ionized form with a negative charge on the S atom and thus the MBT molecules carry negative surface charge [276].

It is clear from Figure 6.8(c) that the absorption band at 325 nm is shifted to 309 nm since in basic medium (pH >9) 2-MBT exists in ionized form with negative charge on the sulfur atom. Again this led to electrostatic repulsion between the TiO<sub>2</sub> nanocontainers and 2-MBT, thereby facilitating the diffusion of MBT through the pores of TiO<sub>2</sub> nanocontainers and faster release under alkaline condition. Hence, it could be concluded that the release of loaded 2-MBT from TiO<sub>2</sub> nanocontainers was pH specific since when the pH was shifted from neutral value, the amount of 2-MBT release was more. This dependency of inhibitor release on pH confirmed the stimuli responsive intelligent releasing property of TiO<sub>2</sub> nanocontainers.

The loading of 2-MBT into TiO<sub>2</sub> nanocontainer was further confirmed using Raman spectroscopy. Figure 6.9 depicts the Raman spectra of pure 2-MBT, TiO<sub>2</sub> and 2-MBT@TiO<sub>2</sub>. The characteristic peaks of both 2-MBT and TiO<sub>2</sub> were present in the spectra of 2-MBT@TiO<sub>2</sub>. The presence of the peaks of 2-MBT in 2-MBT@TiO<sub>2</sub> confirmed the successful loading of 2-MBT into TiO<sub>2</sub> nanocontainer. Raman active modes of anatase phase of zirconia were observed in the Raman spectra of TiO<sub>2</sub> nanocontainer. All the major characteristic peaks and its assignments for 2-MBT are given in Table 1 [269-272].



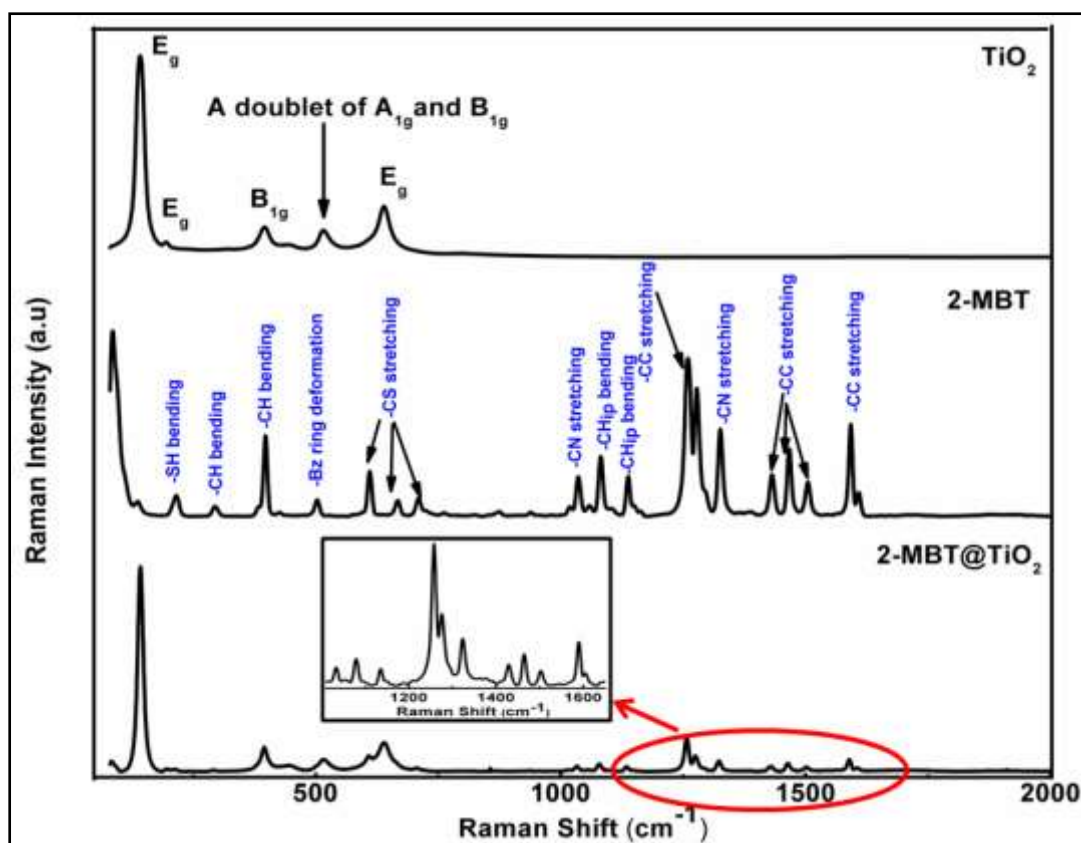


**Figure 6.9: Raman spectra of (a)  $\text{TiO}_2$ , (b) pure 2-MBT, (c) 2-MBT loaded  $\text{TiO}_2$  nanocontainer. Inset shows the enlarged view of the Raman features of 2-MBT in 2-MBT@ $\text{TiO}_2$  system**

#### MBT peak assignments in detail

Frequency	Approximate description of vibrations
149 $\text{cm}^{-1}$	SH bending
294 $\text{cm}^{-1}$	CH bending
397 $\text{cm}^{-1}$	CH bending
502 $\text{cm}^{-1}$	Bz ring deformation
610 $\text{cm}^{-1}$	CS stretching
667 $\text{cm}^{-1}$	CS stretching
710 $\text{cm}^{-1}$	CS stretching

---

<b>766 cm<sup>-1</sup></b>	CH out of plane stretching
<b>874 cm<sup>-1</sup></b>	CH out of plane bending
<b>938 cm<sup>-1</sup></b>	CH bending
<b>1035 cm<sup>-1</sup></b>	CN stretching
<b>1081 cm<sup>-1</sup></b>	Bz ring or SCS antisymmetric stretching
<b>1137 cm<sup>-1</sup></b>	CH in plane bending
<b>1259 cm<sup>-1</sup></b>	NCS ring stretching
<b>1277 cm<sup>-1</sup></b>	CC stretching
<b>1431 cm<sup>-1</sup></b>	CC stretching
<b>1466 cm<sup>-1</sup></b>	CC in plane stretching
<b>1504 cm<sup>-1</sup></b>	CC stretching
<b>1591 cm<sup>-1</sup></b>	CC in plane stretching

---

**Table 6.1: Raman peak assignments for 2-MBT**

#### ***6.3.4 Protective Performance of Various Hybrid Coatings on Modified 9Cr-1Mo Ferritic Steels***

Two types of TiO<sub>2</sub> nanocontainer mixed organic-inorganic hybrid coatings, silane-titania (SiO<sub>x</sub>-TiO<sub>x</sub>) and silane-zirconia (SiO<sub>x</sub>-ZrO<sub>x</sub>), were applied on modified 9Cr-1Mo ferritic steels and its anticorrosion property was investigated using EIS. Initially silane-titania hybrid coatings mixed with BTA loaded TiO<sub>2</sub> nanocontainers were prepared and its corrosion resistance was studied while immersing in 0.05 M NaCl solution. Since its corrosion resistance was not high and it could not retain its barrier property more than 24 h and BTA's inhibitive action is negligible under alkaline conditions, silane-zirconia hybrid coatings and 2-MBT replaced BTA. Nevertheless, BTA loaded TiO<sub>2</sub> dispersed SiO<sub>x</sub>-TiO<sub>x</sub> coating system (CS-NI) showed better corrosion resistance and active corrosion protection compared to that of BTA mixed SiO<sub>x</sub>-TiO<sub>x</sub>

coating system (CS-I), plain  $\text{SiO}_x\text{-TiO}_x$  coating system (CS), and empty  $\text{TiO}_2$  mixed  $\text{SiO}_x\text{-TiO}_x$  coating system (CS-N).

#### 6.3.4.1 EIS Studies of $\text{SiO}_x\text{-TiO}_x$ Hybrid Coating System

The corrosion protection property of all the four coating systems (CS, CS-I, CS-N, and CS-NI) was investigated during immersion in 0.05 M NaCl solution for 24 h. During the initial time of immersion (within 1 h), the resistance of the sol-gel coating was the highest and the capacitance was the lowest. Figure 6.10 presents the impedance bode plots for CS-NI, CS-N, CS-I, CS and BS specimens after immersion in 0.05M NaCl solution for 1 hour. The concentration of NaCl solution was chosen as 0.05M, since it was earlier reported that 9Cr-1Mo ferritic steel had undergone pitting at 0.05 M NaCl solution [230, 327].

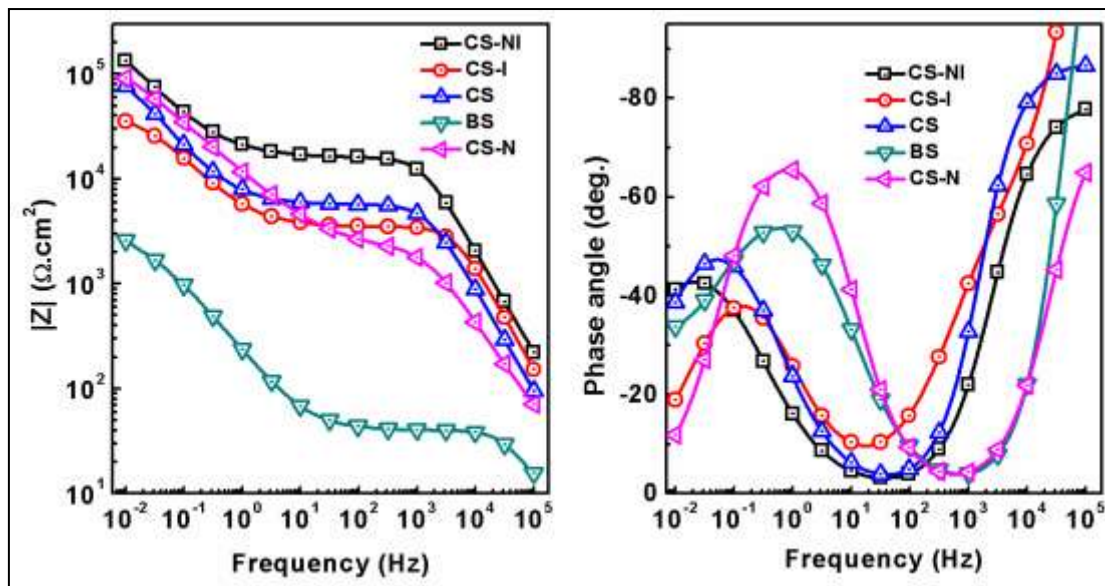


**Figure 6.10: The Bode plots for BS, CS, CS-I, CS-N, and CS-NI after 1 h immersion in 0.05M NaCl**

It was observed that during the initial immersion itself the inhibitor loaded nanocontainer impregnated sol-gel coated specimens showed better corrosion protection efficiency than other three types of coated specimens. The low frequency impedance is the main parameter which gives the direct comparison of the corrosion

protection efficiency of different coating systems. The higher impedance modulus in the low frequency region suggests a lower corrosion activity on the alloy surface. The corrosion resistance of the different types of coating during 1 hour immersion in 0.05M NaCl was as follows: CS-NI > CS-N > CS > CS-I.

Figure 6.11 presents bode plots for BS, CS, CS-I, CS-N, CS-NI after 24 hours immersion in 0.05M NaCl solution. Two different time constants in the bode plots reflects two relaxation process on the metal surface during immersion in 0.05M NaCl. The relaxation process due to the coating appeared at high frequency region and the corrosion activity was revealed by the low frequency time constant.

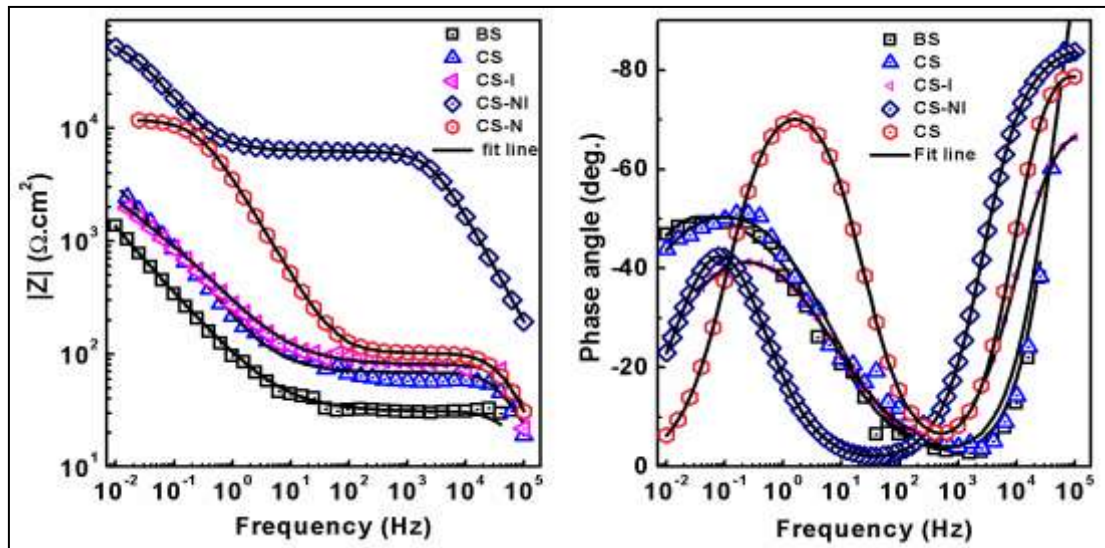


**Figure 6.11: The Bode plots for BS, CS, CS-I, CS-N, and CS- NI after 24 h immersion in 0.05M NaCl**

It is clear from the figure that the alloy coated with benzotriazole loaded  $\text{TiO}_2$  nanocontainer impregnated (CS-NI) showed the highest impedance value of  $5.5 \times 10^4$  at 0.01 Hz among the five specimens after exposed in 0.05M NaCl solution indicating better corrosion protection performance. The low frequency impedance value for both the sol-gel coated (CS) and inhibitor doped sol-gel coated (CS-I) was almost an order of 10 less than that of the nanocontainer impregnated (CS-N I) specimen. At the same

time, the inhibitor doped sol-gel coated (CS-I) specimen's low frequency impedance value was less than that of sol-gel coated specimen (CS). This indicated the negative effect of the inhibitor when directly added to the barrier coating. It was reported that the inhibitor can damage the cross linking of the sol-gel coating during the hydrolysis and condensation process. This can destroy the homogenous nature of the sol-gel coating and can lead to the formation of pores or cracks. Moreover, it was observed that CS-N performed better than CS and CS-I. Hence it could be concluded that CS-N provided better barrier property than CS and CS-I. However, CS-N could not offer better protection than CS-NI. This observation indicates that the better corrosion protection provided by CS-NI was due to the active corrosion protection provided by benzotriazole loaded in  $\text{TiO}_2$  nanocontainer.

EIS can be effectively used for the evaluation of the various components of the coated system such as pore resistance, pore capacitance of the barrier sol gel film, the polarization resistance and double layer capacitance [59, 196, 328]. The expression of these parameters as the function of immersion time gives a clearer picture about the behavior of the coatings. Figure 6.12 illustrates the EEC models used to fit the electrochemical impedance measurements [251, 329]. A simple EEC was used to simulate and fit the measured impedance data of the uncoated alloy (Figure 6.12(a)). This EEC represents a basic corrosion process where electric double layer and surface oxide film act as a set of parallel combination of resistance ( $R_p$ ) and capacitance ( $Q_{dl}$ ).  $R_s$  correspond to the resistance offered by the electrolyte solution. All the coated alloy specimens were simulated and fitted by EEC consisting of two time constant (Figure 6.12(b)). The first time constant was represented by a parallel combination of  $R_{pore}$  and  $Q_{pore}$  which represent the pore resistance and the pseudo capacitance of the coating respectively. Similarly, the second time constant was simulated by a parallel

combination of  $R_c$  and  $Q_{fdl}$  which stands for the combined responses of both the electrical double layer and surface oxide layer. The selection of this particular EEC for simulating the measured data for all coated alloy specimens is explained in detail when the evolution of various components of the EEC is discussed during immersion in 0.05M NaCl. Instead of ideal capacitance, the constant phase elements were used for the construction of the equivalent circuit and fitting of the impedance data.

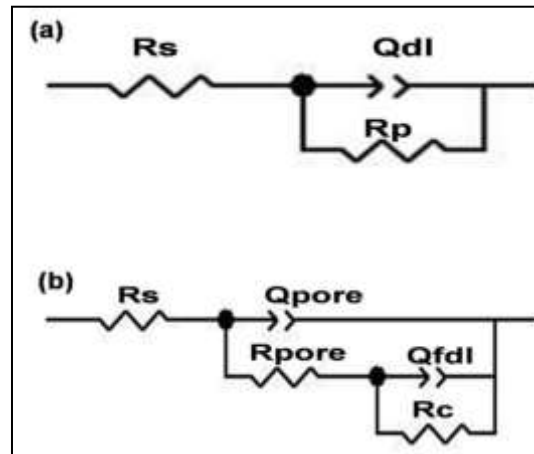


**Figure 6.12: The equivalent circuit (a) for bare Mod.9Cr-1Mo alloy specimen immersed in 0.05M NaCl solution, (b) for coated Mod.9Cr-1Mo alloy specimens immersed in 0.05M NaCl solution**

The use of the constant phase element is a must since the phase angle of the capacitance is deviated from  $-90^\circ$ . The corresponding capacitance value can be calculated by using the following formula [328].

$$C = Q(\omega_{max})^{n-1} \quad (6.6)$$

where  $\omega_{max}$  is the frequency at which the imaginary impedance reaches a maximum for the respective time constant and  $Q$  and  $n$  are the parameters which characterizes the capacitance of the respective film [249, 330].

Figure 6.13 shows the behavior of the pore resistance ( $R_{pore}$ ) and pseudo sol-gel capacitance ( $Q_{pore}$ ) of the sol-gel barrier coating of CS-NI, CS-N, CS-I and CS while immersed in 0.05M NaCl solution. The pore resistance arises from the electrolyte

resistance from the pores and micro cracks present in the sol-gel coating [59]. This resistance of the coatings changes during immersion due to the penetration of the electrolyte in to the micro pores and the cracks of the sol-gel network. The higher value of the pore resistance reflects the better barrier property of the sol-gel passive barrier coating. The plot shows that CS-NI had very high pore resistance when immersed for 1, 4, 24 hours (Figure 13(a)).

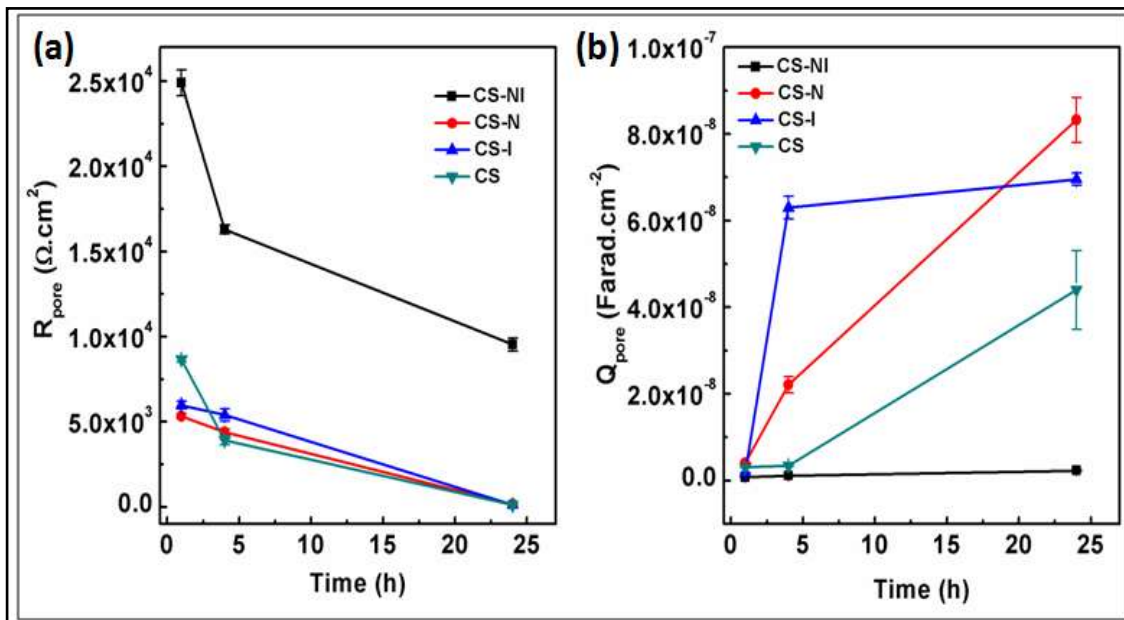


**Figure 6.13: Evolution of (a) pore resistance  $R_{pore}$  of the coating (b) pseudo-capacitance  $Q_{pore}$  of the coating during immersion in 0.05M NaCl solution**

This observation suggests that CS-NI could provide better protection since the damage in the coating is less due to the uptake of the water. The decrease in the pore resistance is due to the penetration of the electrolyte and that making a path to the metal surface via the intermediate oxide layer. CS registered a higher  $R_{pore}$  value than CS-I and CS-N during 1 hour immersion. This might be due to the presence of less pores and more compact nature of the coating. However, after 24-hour immersion pore resistance of CS-N, CS-I, CS became identical. The variation of the pseudo sol-gel capacitance ( $Q_{pore}$ ) during the immersion of the specimen is presented in Figure 13(b). Inhibitor

loaded nanocontainer impregnated sol-coated specimen (CS-NI) recorded the lowest pseudo-capacitance value. The increase in the value of the pseudo- capacitance ( $Q_{\text{pore}}$ ) is due to the uptake of water into the coating. A continuous increase in the pore capacitance at given time interval was observed for CS-N, CS-I and CS coated alloys during 24 h immersion in 0.05M NaCl solution, while the pore capacitance values of the CS-NI coated alloy did not change with time. The nature of the evolution of both pore resistance ( $R_{\text{pore}}$ ) and pseudo- capacitance ( $Q_{\text{pore}}$ ) are in good agreement.

The passive protection effect of the intermediate oxide layer is very important, because the corrosive species can directly access the bare metal surface once the breakdown of this passive oxide layer happens [59, 329]. Therefore, the compactness and the stability of this passive oxide layer are essential for better corrosion protection of metals and alloys. The evolution of the combined resistance and capacitance effect of electric double layer and intermediate passive oxide layer is presented in Figure 6.14. Even though  $Q_{\text{pore}}$  for all coated alloy specimens are similar,  $Q_{\text{fdl}}$  varies significantly during immersion in 0.05M NaCl. Moreover,  $Q_{\text{fdl}}$  values obtained for different coated alloy specimens were deviated from the typical electrical double layer values recorded by metals and alloys, which in general is in the  $\mu\text{F}/\text{cm}^2$  range [329]. Hence, the time constant, consisting of  $Q_{\text{fdl}}$  and  $R_c$  appeared due to a combined response of the surface oxide film and the electrical double layer. The value of  $Q_{\text{fdl}}$  for CS-NI after 1 h immersion in 0.05M NaCl was 2 orders of magnitude lower than CS-I and CS. From Figure 6.14(a) it is observed that  $R_c$  values of all different types of coated alloy specimens decreased as the immersion progressed. Except CS-NI, all other coated alloys had very lower  $R_c$ . The higher  $R_c$  value for CS-NI after 24 h immersion can be attributed to the active protection provided by the controlled release of the BTA inhibitor loaded in  $\text{TiO}_2$  nanocontainer.



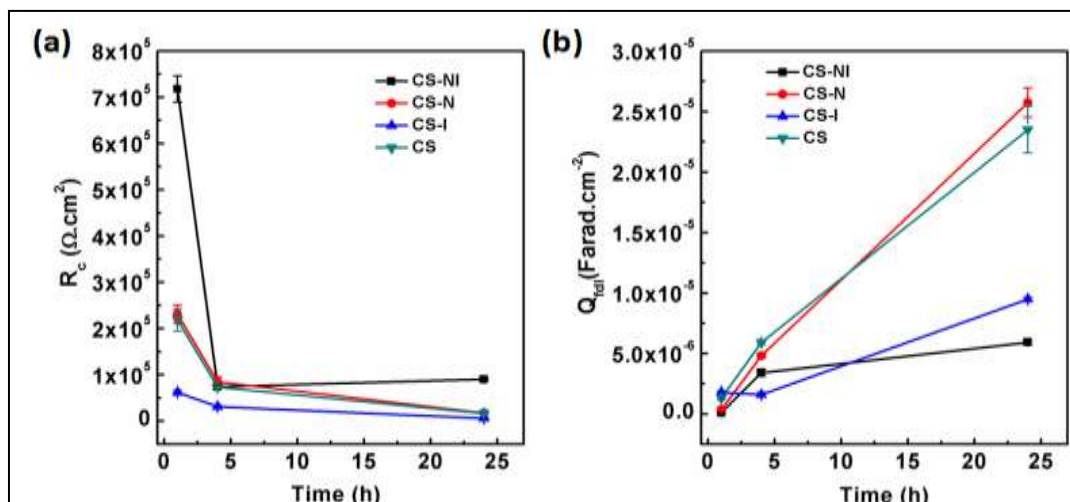


**Figure 6.14: Evolution of (a) electrical double layer and oxide layer resistance  $R_c$  (b) electrical double layer and oxide layer pseudo-capacitance  $Q_{fdl}$  during immersion in 0.05M NaCl solution**

This released inhibitor could heal the damage caused by the corrosive species that entered through the pores and cracks in the coating. Thus, the damaged oxide layer was recovered by the self-healing effect of the inhibitor encapsulated in the nanoreservoir. The higher  $R_c$  value of the CS compared to CS-I can be attributed to the compactness of the intermediate oxide layer of CS [59]. The evolution of  $Q_{fdl}$  as a function of immersion time was in good agreement with the behavior of  $R_c$  during immersion (Figure 6.14(b)). CS-NI recorded the lowest  $Q_{fdl}$  value after 24 h immersion in 0.05M NaCl. As capacitance is directly proportional to the area of the specimen exposed in the electrolyte, the lower capacitance value of CS-NI suggests that relatively lower area of metal/hydroxide interface was exposed to the electrolyte. This can be attributed to the fact that the coating of CS-NI was less damaged and subsequent protection was achieved by an active corrosion protection mechanism.

The passive barrier coating can offer effective protection from corrosion activity only if the barrier sol-gel film remains intact. Any damages present on the passive barrier layer

immediately instigate corrosion processes especially in a pitting electrolyte like NaCl solution. Therefore, the addition of active agents such as BTA is required. However, it is observed that the addition of inhibitive species directly into the sol gel network can cause damage to the barrier property of the coating. The active corrosion protection of the alloy surface can be explained by a self-healing mechanism.

The graphical illustration of the proposed mechanism is presented in Figure 6.15.

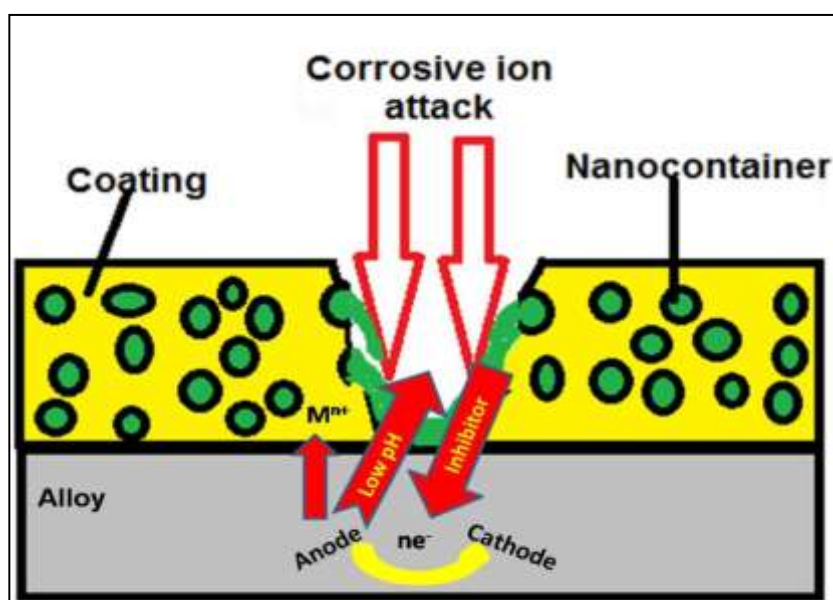
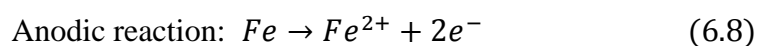
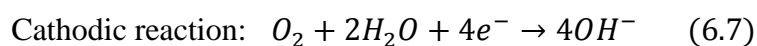


**Figure 6.15: Graphical representation of the proposed self-healing mechanism**

No coating is free from any kind of micro cracks or pores. The aggressive corrosive species can penetrate through these pores and access the alloy surface and instigate corrosion. The typical electrochemical phenomena taking place in a neutral aqueous NaCl solution can be represented as follows:



In the case of localized corrosion such as pitting corrosion, the anodic reaction takes place in a very confined area and the metal ions produced are precipitated as solid corrosion products such as iron oxide, and the mouth of the pit is covered by these solid

corrosion precipitates. Further this porous corrosion product layer helps in the gradual accumulation of hydronium ion,  $H^+$  inside the pit. In effect when pitting corrosion takes place, acidic pH develops around the anode area, where as around cathode area alkaline pH develops [331]. At acidic pH, BTA releases from  $TiO_2$  nanocontainers. The released BTA inhibitor forms complexes with the dissolved metal ion and this metal-complex film prevents further attack of the corrosive species and protects the metal surface.

#### **6.3.4.2 EIS studies of $SiO_x$ - $ZrO_x$ hybrid coating system**

Corrosion protective performance of  $SiO_x$ - $ZrO_x$  hybrid coatings was studied using EIS measurements, while immersing in 0.05 M NaCl solution for one week. All the tested samples were coated with silane-zirconia hybrid sol at the same time and the average thickness of the coatings was around 2  $\mu m$ . The titanium elemental mapping of the coated sample with  $TiO_2$  nanocontainers is depicted in Figure 6.16.

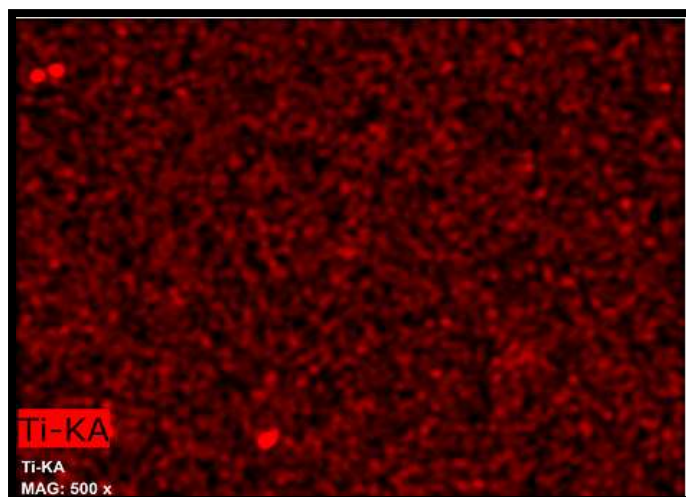


**Figure 6.16: EDX mapping of hybrid coating with  $TiO_2$  nanocontainers for the element Ti**

It can be observed that the element Ti was present uniformly in the coating. This result allowing to concluding that  $TiO_2$  nanocontainers were very well distributed in the hybrid coatings. After the immersion, the surface of the exposed area of the coated specimen was investigated using SEM and optical photography.

Figure 6.17 shows the impedance spectra of BS (uncoated Mod.9Cr-1Mo specimen), CS (hybrid coating), CS-I (inhibitor mixed hybrid coating), CS-N (empty nanocontainer impregnated coating), and CS-NI (inhibitor loaded nanocontainer impregnated hybrid coating) after 1 h of immersion in 0.05 M NaCl solution.

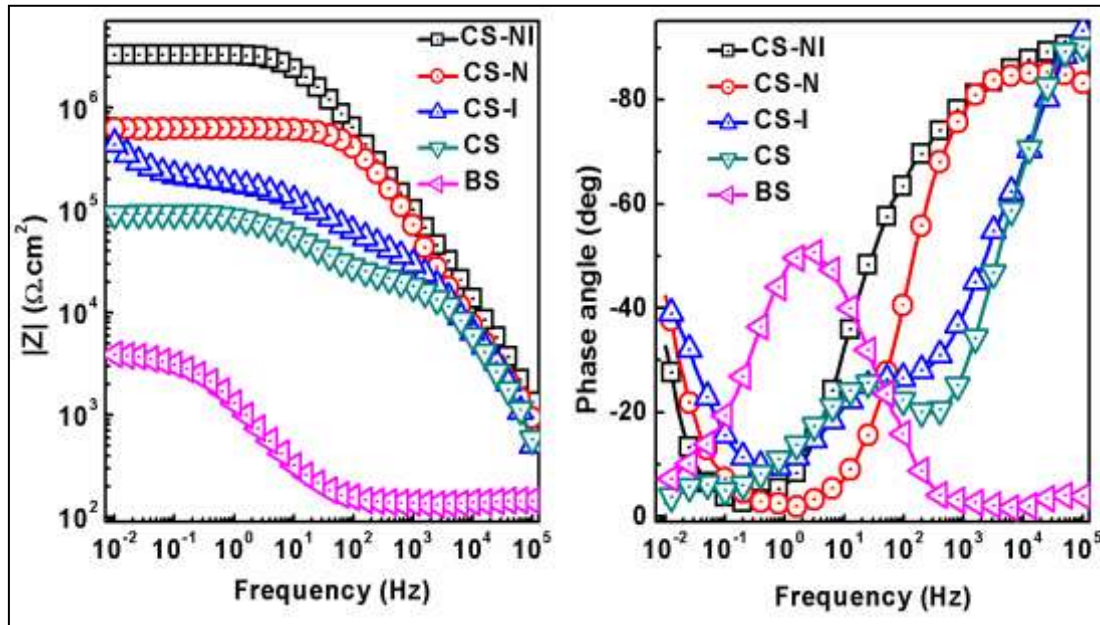


**Figure 6.17: EIS behaviour of BS, CS, CS-I, CS-N, and CS-NI after 1 h of immersion in 0.05 M NaCl solution**

It is clear from Figure 6.17 that all the coated modified 9Cr-1Mo alloy specimens had better corrosion resistance compared to that of uncoated modified 9Cr-1Mo ferritic steel. The order of corrosion resistance of the tested alloy specimens after 1 h of immersion is as follows; CS-NI > CS-N > CS-I > CS > BS. The uncoated alloy typically behaved like an electrical double layer and its impedance spectrum was characterized by the combination of a polarization resistance and a double layer capacitance. Both CS and CS-I had three time constants corresponding to three processes on their surfaces during 1 h of immersion in salt solution. The barrier property of the coating was reflected in the first time constant at high frequency region and the resistance of oxide layer was characterized by the second relaxation process at mid frequency region. The

last and the third time constant could be attributed to the redox reactions at the underlying metal surface due to corrosion. This observation implies that corrosion started in both CS and CS-I after 1 h of immersion in salt solution. However, both CS-N and CS-NI had only two time constant after 1 h of immersion in salt solution. The first time constant could be attributed to the barrier property of the coating and the second time constant was due to the oxide film. The barrier property of CS-NI was superior to CS and this could be attributed to the presence of loaded 2-MBT in the nanocontainer.

Figure 6.18 depicts the EIS response of CS, CS-I, CS-N, and CS-NI after 1 day of immersion in 0.05 M NaCl solution.

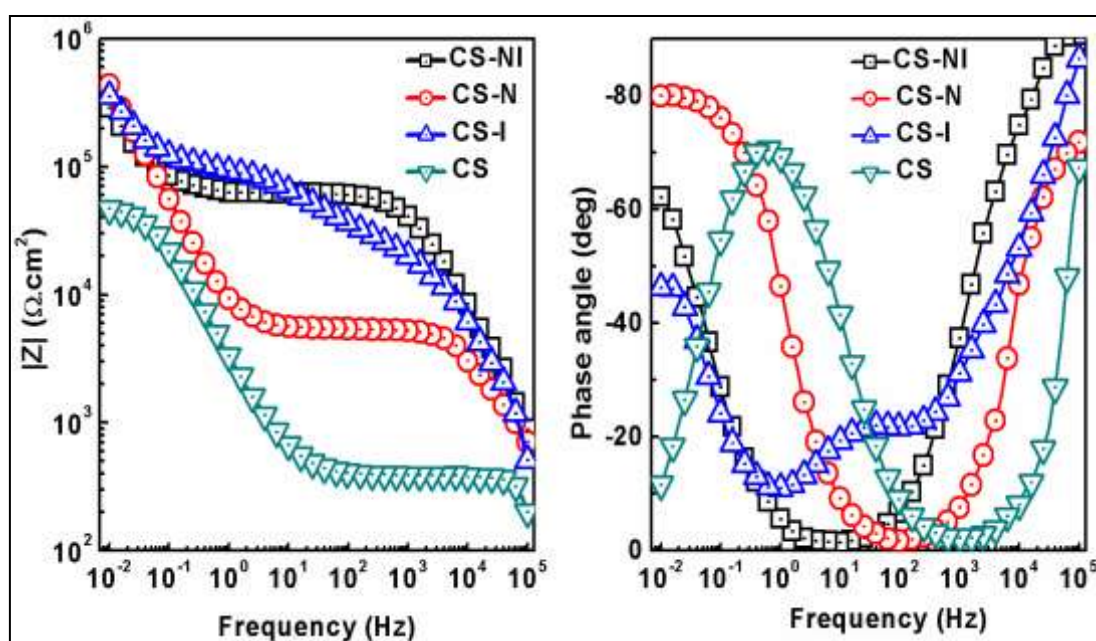


**Figure 6.18: EIS response of CS, CS-I, CS-N, and CS-NI after 1 day of immersion in 0.05 M NaCl solution**

After 1 day of immersion, the oxide film of CS was completely damaged and this observation is supported by the absence of second time constant at mid frequency in the EIS spectrum of CS. Furthermore, the barrier property of CS was deteriorated



considerably and the modulus of impedance at low frequency was decreased. All these observations suggest that corrosion has started and spread on the surface of CS.

But the impedance spectrum of CS-I had a relaxation process at mid frequency and this is attributed to the response of oxide layer and its modulus of impedance value at low frequency was superior to CS. So compared to CS, CS-I has higher corrosion resistance after 1 day of immersion in salt solution. Both CS-N and CS-NI had only two time constants after 1 day of immersion in salt solution. It is observed from figure 6.18 that the barrier property of CS-NI is higher than that of CS-N and CS-I as well as the second time constant for CS-NI is not evolved completely compared to that of CS-N. This observation implies the better corrosion protective performance of CS-NI compared to other coatings and this is achieved due to the controlled release of 2-MBT from  $\text{TiO}_2$  nanocontainers. Figure 6.19 depicts the EIS response of CS, CS-I, CS-N, and CS-NI after 1 week of immersion in 0.05 M NaCl solution.

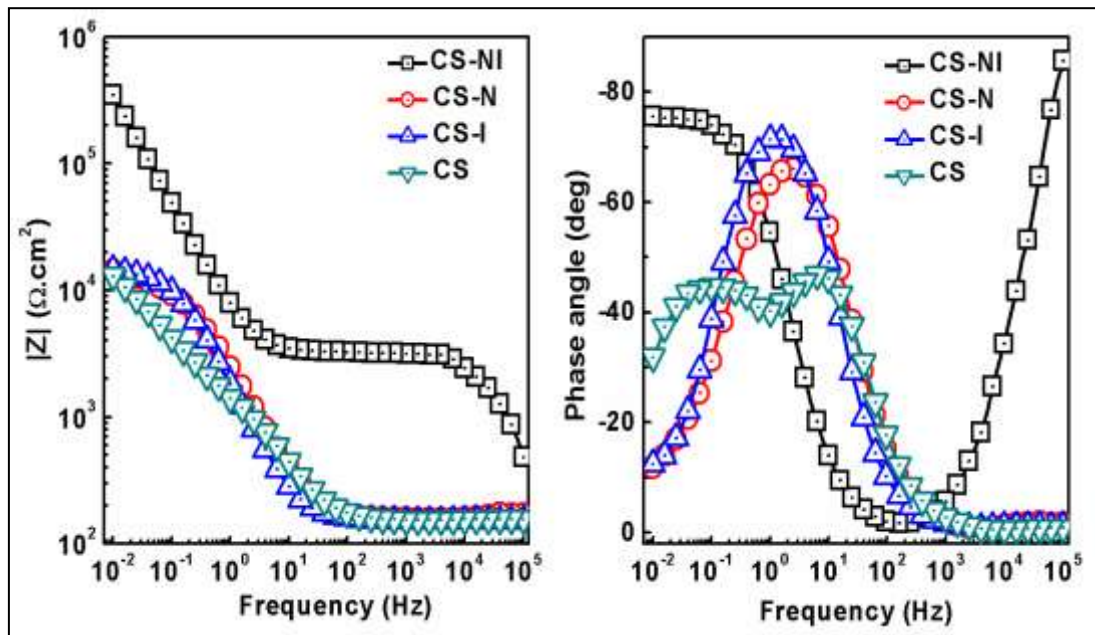


**Figure 6.19: EIS response of CS, CS-I, CS-N, and CS-NI after 1 week of immersion in 0.05 M NaCl solution**

As it is observed from figure 6.19, the barrier property of CS, CS-I, and CS-N was damaged significantly and this observation implies that the coatings no longer offer any protection to the underlying metal surface. The impedance spectra of CS-I and CS-N were characterized by the combination of a resistive response and a double layer capacitive response. A time constant associated with mass transport of species participating in the redox reactions at the metal surface was also observed for CS. Conversely, CS-NI did have a time constant at high frequency due to barrier property rendered by the hybrid coatings. The impedance at low frequency can be considered as a measure of the polarization resistance of the coating systems and hence can be used to assess and compare the performance of corrosion protective coatings. The value of modulus of impedance at low frequency for CS, CS-I, and CS-N is very low compared to that of CS-NI. These observations suggest the superior corrosion protection performance of CS-NI compared to that of other coatings and this is accomplished through an active corrosion protection.

Figure 6.20 shows the EIS response of CS-NI during 1 week of immersion in 0.05 M NaCl solution.

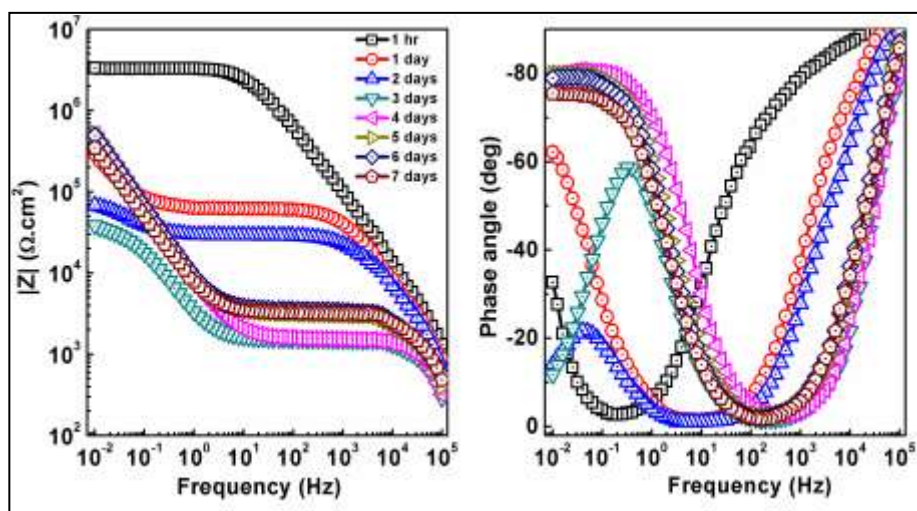


**Figure 6.20: EIS spectra of CS-NI during 1 week of immersion in 0.05 M NaCl solution**

During the immersion study of CS-NI in salt solution, the barrier property of the coatings decreased continuously due to the infiltration of water and chloride ions through the pores and cracks in the hybrid coatings. All the impedance spectra depicted in Figure 6.20 had two time constants. The relaxation process at high frequency is attributed to the barrier property of the coating and the second time constant at low frequency is due to the impedance response of the oxide layer. After 4 days of immersion, the second time constant was capacitive in nature and the oxide resistive plateau was not well evolved. However, the resistive plateau for the coating resistance decreased continuously as the immersion progressed. The capacitive slope of second relaxation process due to the response from the oxide film did not change with immersion from 4<sup>th</sup> day to 1 week. Furthermore, no time constant or relaxation process due to corrosion activity is observed in the EIS spectra. The most striking feature of the impedance response is the evolution of modulus of impedance at low frequency.

Figure 6.21 presents the evolution of modulus of impedance at  $10^{-2}$  Hz during 1 week of immersion.

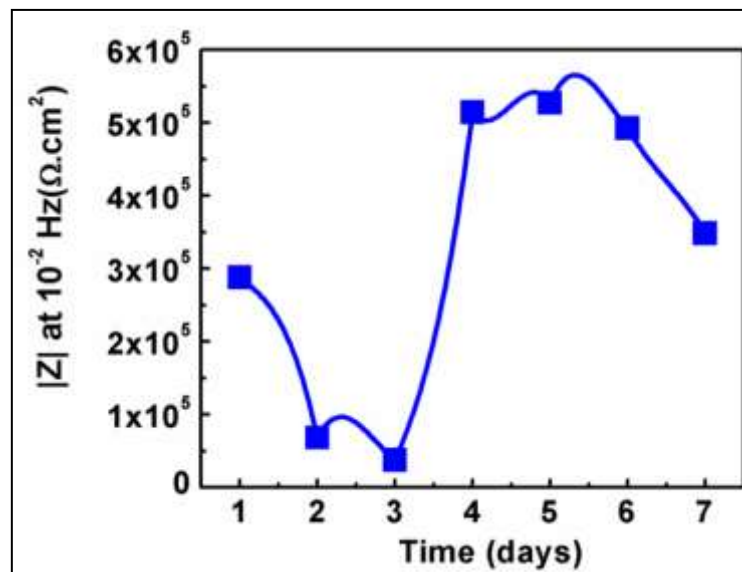


**Figure 6.21: Evolution modulus of impedance at  $10^{-2}$  Hz for CS-NI during 1 week of immersion**



Initially, there was a decrease in the modulus of impedance at  $10^{-2}$  Hz from 1 h to 3 days of immersion in salt solution. Interestingly, after 3 days, the value of modulus started to increase and it was almost unchanged up to one week of immersion. The initial fast drop of impedance at low frequency is related to the access of electrolyte other corrosive species to the underlying metal surface through the pores of the  $\text{SiO}_x$ - $\text{ZrO}_x$  hybrid coatings. The recovery of the low frequency impedance after 3 days can be related to the fact that corrosion inhibitor was released in the coating, since for all the other types coatings (CS, CS-I, and CS-N) did not show this effect.

SEM and visual inspection of the coated specimens after 1 week of immersion in salt solution support the previously mentioned EIS results. Figure 6.22 shows the optical photograph of the coated specimens after 1 week of immersion in 0.05 M NaCl solution.



**Figure 6.22: Optical photographs of the coated specimens after 1 week of immersion in 0.05 M NaCl solution. The drawn circles indicate the exposed area of the coatings.**

Figure 6.22 shows that both CS, CS-I, and CS-N were badly damaged and the underlying metal surface was visible due to the peeling off of the coatings. Furthermore, brown coloured corrosion products were also visible on the surface of the

coatings. However, CS-NI had a slight pit mark on one side of the edge of the circle; the remaining area was protected well. No delamination or blistering was observed on the surface and the surface seemed to be homogenous.

Figure 6.23 shows the SEM images of coated specimens after 1 week of immersion in 0.05 M NaCl solution. The captured SEM images of various coated specimens after immersion of 1 week in salt solution are in agreement with both EIS results and visual inspection.

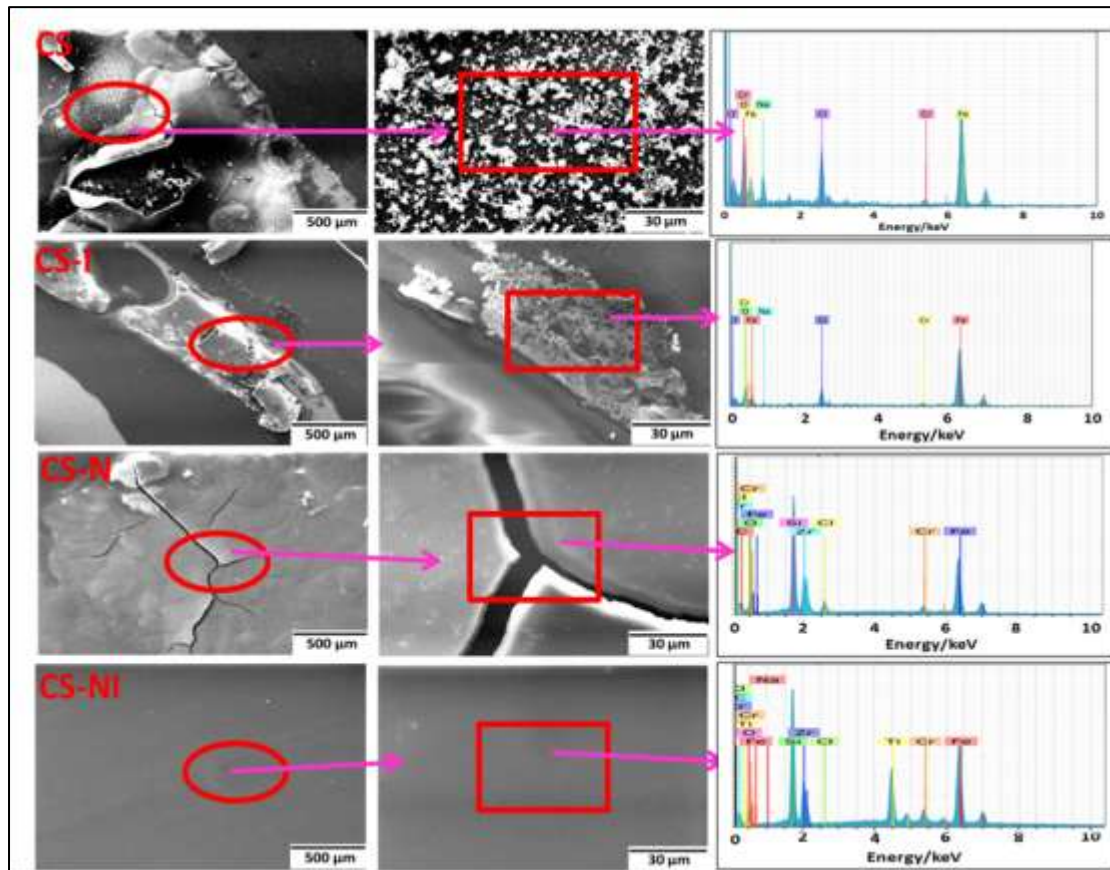


**Figure 6.23: SEM images CS, CS-I, CS-N, and CS-NI after 1 week of immersion in 0.05 M NaCl solution and its corresponding EDX spectra.**

The coatings of CS and CS-I were attacked severely and corrosion products were observed in the SEM images. Coatings were delaminated and flakes were visible for CS and CS-I. Cracks were visible on the SEM image of CS-N. However, uniform and crack or blister free surface was observed for CS-NI after 1 week of immersion in salt

solution. EDX spectrum revealed the presence of chloride ions on the surface of CS, CS-I, and CS-N while the surface of CS-NI was free of chlorine. Peaks corresponding to Si and Zr were absent in the EDX spectra of CS and CS-I, showing the complete disruption of barrier coating matrix due to corrosion.

Artificial scratches were made in CS and CS-NI coatings in order to study the active corrosion protection rendered by the release of 2-MBT from TiO<sub>2</sub> nanocontainers. Figure 6.24 shows the evolution of impedance response of scratched CS for 1 week while immersed in salt solution. After 1 h of immersion itself, three relaxation processes were occurred in the surface of CS. The first relaxation process is the response of the hybrid coating due to its barrier property. The second in the mid frequency range is due to the response of the oxide layer and the third time constant at low frequency region is due to the corrosion activity. This indicates that within 1 h, the electrolyte could access the underlying metal surface and CS failed to give any protection.

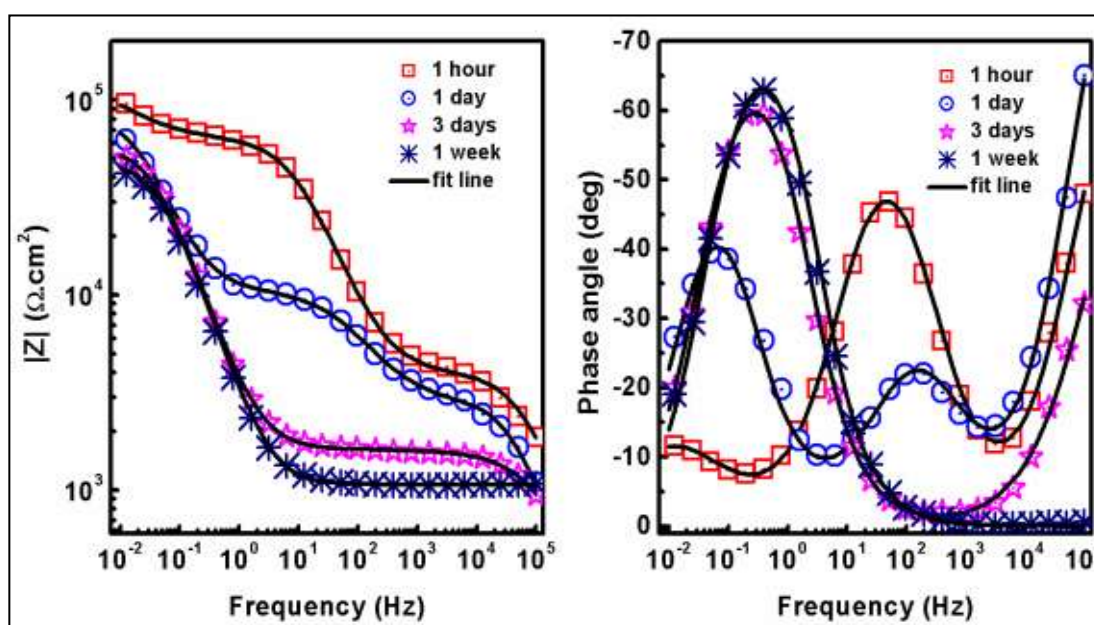


**Figure 6.24: EIS spectra of CS during immersion in 0.01 M NaCl solution after making an artificial scratch.**

After 3 days of immersion, the second time constant disappeared from the EIS spectra and this could be due to the rupture of the oxide layer. Furthermore, CS behaved like a typical double layer having a parallel combination of polarization resistance and double layer capacitance. All the previously mentioned observations indicate that CS was corroding continuously during immersion.

Figure 6.25 shows the impedance response of artificially scratched CS-NI during immersion in 0.01 M NaCl solution. The EIS response of CS-NI after 1 h of immersion had two time constant; the relaxation process occurred at high frequency is assigned to the barrier property of the coating and the second time constant is due to the response of the oxide layer. No relaxation process due to corrosion was observed in the impedance spectra of CS-NI. During 1 week of immersion, from 24 h to 168 h the impedance value at low frequency almost remained unaffected and this suggests active corrosion protection. The relaxation process due to corrosion activity was not developed fully.

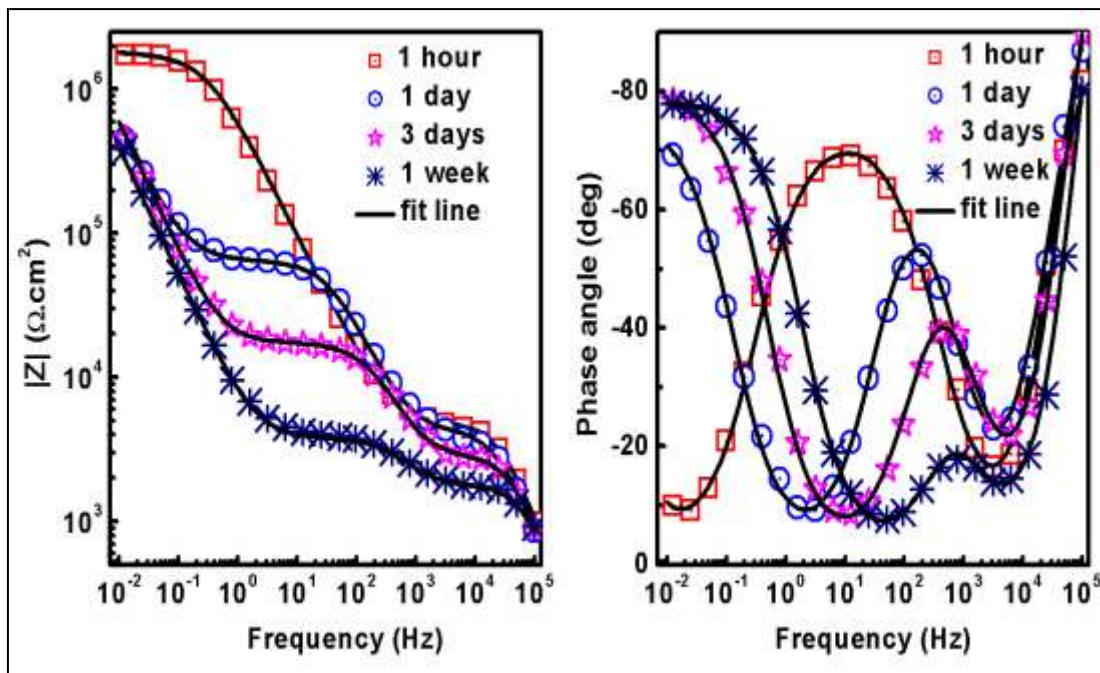


**Figure 6.25: EIS spectra of CS-NI during immersion in 0.01 M NaCl solution after making an artificial defect**

The final relaxation process was more of capacitive in nature and less of resistive. A continuous increase in the theta value of phase angle was observed for the final relaxation process from first day of immersion to 1 week of immersion. This increase in theta value could be attributed to the release of 2-MBT from TiO<sub>2</sub> nanocontainers on the scratched area. The aforementioned results confirmed that the higher corrosion resistance rendered by CS-NI could be due to the release of the inhibitor from nanocontainers embedded in the coating, because CS did not show this effect.

The impedance spectra of both scratched CS and CS-NI were fit using equivalent circuits (ECs) models to quantify the corrosion resistance offered by CS and CS-NI.

The ECs used to fit the impedance spectra were depicted in Figure 6.26.

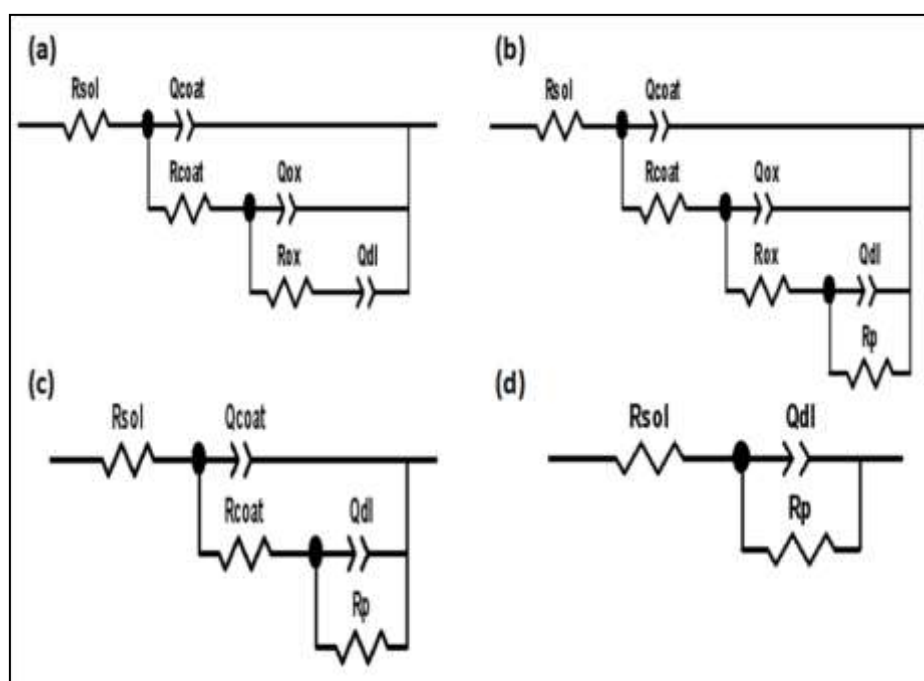


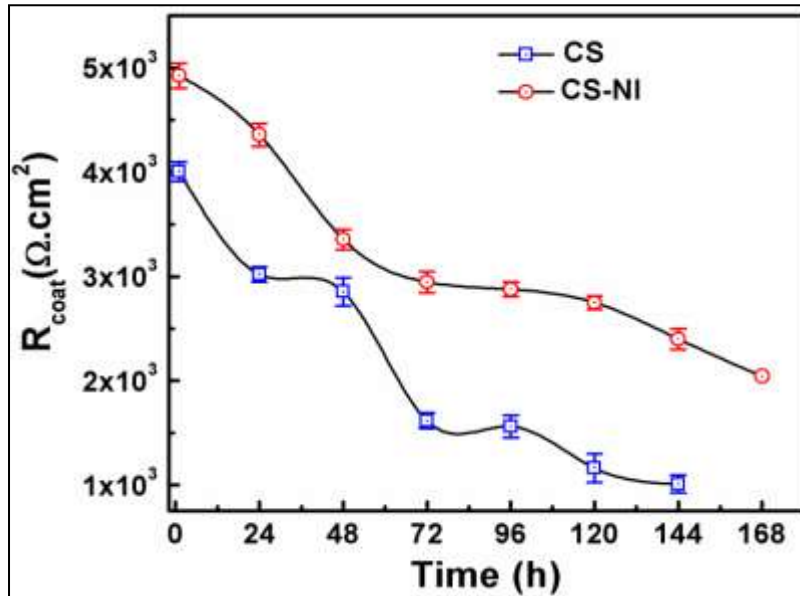
**Figure 6.26: Equivalent circuits used to fit the experimental EIS data of scratched CS and CS-NI during 1 week of immersion in 0.01 M NaCl solution**

$R_{sol}$  is the solution resistance;  $R_{coat}$ ,  $R_{ox}$  and  $R_p$  are respectively the pore resistance of the sol-gel barrier coating, intermediate oxide layer and polarization resistance.  $Q_{coat}$ ,  $Q_{ox}$ ,  $Q_{dl}$  are the constant phase elements of sol-gel hybrid coating, intermediate oxide



layer and double layer respectively. Instead of pure capacitance, constant phase elements were used since the phase angle is not equal to  $-90^\circ$ . For scratched CS-NI, in the beginning of the immersion test, two time constants completely appeared in the impedance spectra and the third time constant at the low frequency was not evolved completely. Hence, the impedance spectrum of CS-NI after 1 h of immersion was fitted using EC depicted in Figure 6.26(a). The EC shown in Figure 6.26(b) was used to fit impedance spectra of both scratched CS-NI during immersion of 24 h to 168 h and CS during immersion of 1 h to 24 h. Impedance spectra of CS during immersion of 48 h to 144 h was fitted using EC shown in Figure 6.26(c). Figure 6.26(d) was used to fit the impedance spectra of CS after 168 h of immersion. The error of fitting  $\chi^2$  was less than or equal to  $10^{-3}$  for all the spectra.

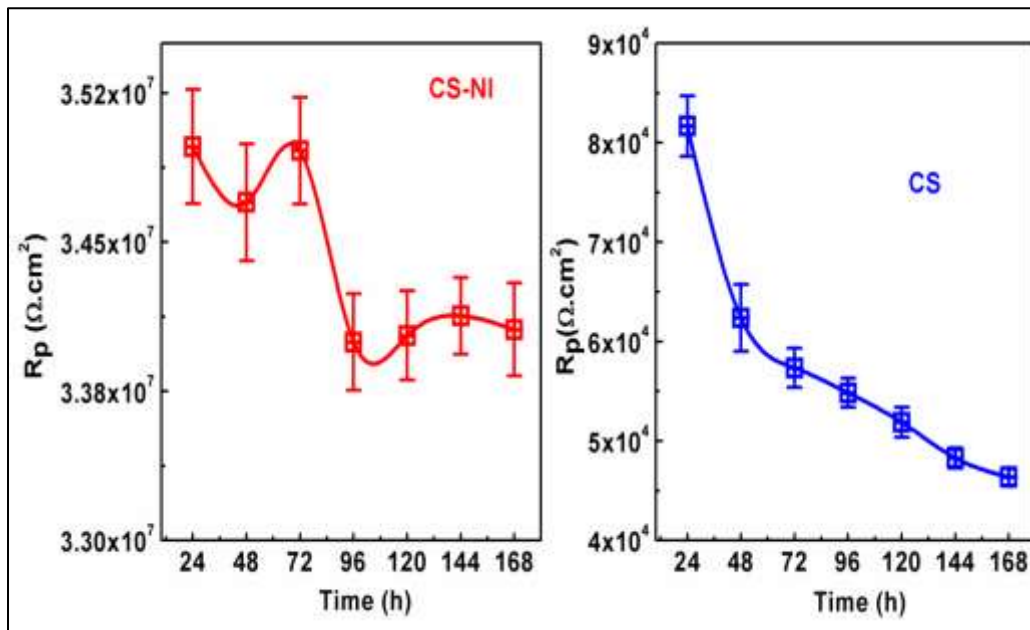
Figure 6.27 depicts the change in coating resistance ( $R_{\text{coat}}$ ) of CS and CS-NI while immersed in salt solution for 1 week. The coating resistance or pore resistance of barrier coatings depends on porosity and cracks present in the coatings.



**Figure 6.27: Evolution of coating resistance ( $R_{\text{coat}}$ ) of CS and CS-NI during 1 week of immersion in 0.01 M NaCl solution.**

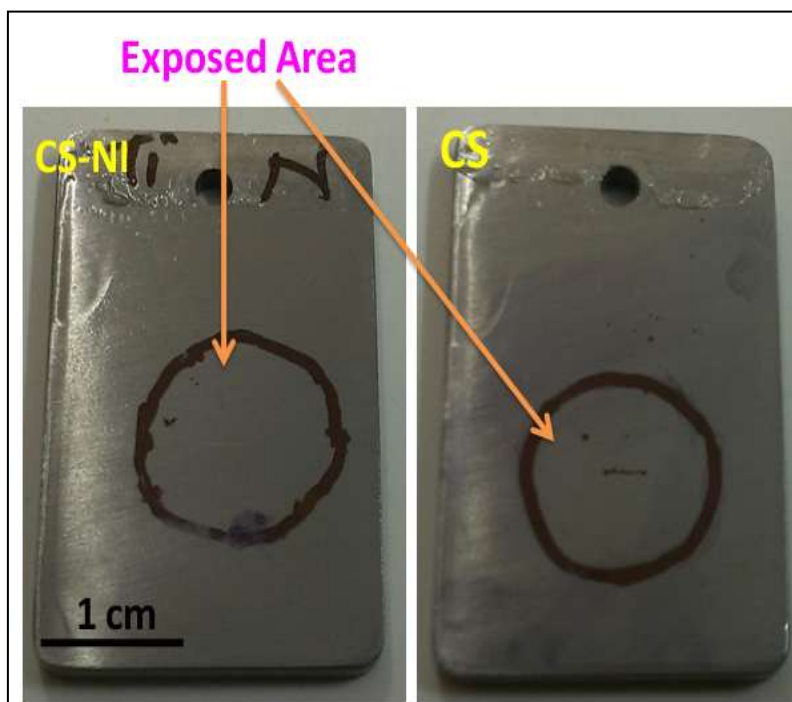
The  $R_{coat}$  of both CS and CS-NI decreased continuously as immersion of the coated specimens progressed. However, CS-NI always had higher  $R_{coat}$  value compared to that of CS and retained its barrier property after 1 week of immersion. The barrier property of CS reduced drastically and it even did not have  $R_{coat}$  value after 168 h of immersion, because the integrity of coating was lost.

Figure 6.28 shows the evolution of polarization resistance ( $R_p$ ) during 1 week of immersion for CS and CS-NI. It is observed from Figure 6.28(b) that  $R_p$  value for CS decreased continuously during one week of immersion. But the  $R_p$  value for CS-NI was superior to that of CS. The polarization resistance can be directly correlated to active corrosion protection offered by the released corrosion inhibitors from the nanocontainers [172]. The  $R_p$  value for CS-NI after 1 week of immersion in salt solution is about three orders higher than that of CS. This can be attributed to the retardation of corrosion at the scratched area due to the release of inhibitor molecules (2-MBT) from  $TiO_2$  nanocontainers.



**Figure 6.28: Evolution of polarization resistance ( $R_p$ ) of (a) CS-NI and (b) CS during 1 week of immersion in 0.01 M NaCl solution.**

Figure 6.29 presents the photograph of scratched CS-NI and CS after 1 week of immersion study.



**Figure 6.29: Photographs of scratched CS-NI and CS after 1 week of immersion in 0.01 M NaCl solution. The drawn circles indicate the exposed area of the coatings**

It is observed from the figure that black coloured corrosion products were appeared on the scratched area of CS after 1 week of immersion in salt solution and pits were also present on the surface of CS. Conversely, no sign of corrosion or presence of corrosion products were observed at the scratched area and remaining surface of CS-NI. These observations are very well supported by obtained EIS results.

#### **6.4 Summary**

- ❖  $\text{TiO}_2$  nanocontainers were synthesized using a rapid breakdown anodization (RBA) method by applying a constant potential of 20 V under vigorous stirring.
- ❖ BTA and 2-MBT were successfully loaded into  $\text{TiO}_2$  nanocontainers and the loading efficiency for both inhibitors was found to be 73 %.



- ❖ The pH-triggered release of BTA from  $\text{TiO}_2$  nanocontainers were carried out at pH of 2, 4 and 7 and it was found out that release was pH specific and more and faster release of BTA was occurred at acidic pH.
- ❖ The pH specific release of 2-MBT from  $\text{TiO}_2$  was observed and it was observed that the release of 2-MBT was faster and higher in amount when the pH was shifted from neutral value.
- ❖ Electrochemical impedance spectroscopy was demonstrated here as a useful technique for the study of active corrosion protection based on self-healing effect of protective coatings on modified 9Cr-1Mo alloy substrates.
- ❖ The increase of low frequency impedance when the coated substrates were immersed could be associated to the active corrosion protection due to the self-healing of the defects in the coatings.

## CHAPTER 7

### Comparison of Corrosion Protective Performance of Silica, Zirconia, and Titania Nanocontainers and Long Term Corrosion Protection Studies

---

*A comparison of the active corrosion protection rendered by different nanocontainers, hollow mesoporous silica, hollow mesoporous zirconia, and titania nanocontainers were carried out and presented in this chapter. Titania nanocontainers were found to have better corrosion protective performance considering both the active and barrier protective properties. Hence, this superior corrosion protection system was selected to study the long term corrosion protection in accelerated corrosive environments. Later these titania nanocontainers were used to fabricate inhibitor loaded nanocontainer mixed hybrid coating with top epoxy coating. Along with the reference (plain top epoxy) coating, these samples were exposed to neutral salt spray test in a salt spray system in order to investigate the long term corrosion protection and the self-healing efficiency of the nanocontainer mixed epoxy coating. The salt spray experiment was carried out according to the standard of ASTM B117. The salt spray test showed sufficient protection even after 2000 h of exposure for inhibitor loaded nanocontainer mixed epoxy coating compared to that of reference (plain top epoxy) coating. Blistering and peeling off of the coating was observed for reference epoxy coating, while insignificant rust markings were observed for the nanocontainer mixed epoxy coatings.*

---

#### 7.1 Introduction

A comparative study of various properties such as cost of fabrication, ease of synthesis, loading efficiency, and sustained release behaviour for enhancing the active corrosion protection of zirconia, silica, and titania nanocontainers were carried out. Based on this

comparative study titania nanocontainers were chosen for evaluating the long term corrosion protection properties. An epoxy coating with pretreatment layer containing inhibitor loaded titania nanocontainers was prepared and applied on modified 9Cr-1Mo ferritic steels. This Epoxy Nanocontainer Coating (ENC) was exposed to neutral salt spray along with Plain Epoxy Coating (PEC) in order to evaluate its long term active corrosion protection efficiency. Laser Raman spectroscopy was used to get the chemical information from the coating surface after salt spray exposure.

## **7.2 Experimental**

### ***7.2.1 Materials and Methods***

Bisphenol- A (Epichlorohydrin) based epoxy, commercially known as Araldite GY 257 (Huntsman), was used as the resin for producing the epoxy coating system. Polyaminoimidazoline, commercially known as Aradur 140 (Huntsman) was used as the curing agent. The weight ratio of the epoxy resin to curing agent was 2:1. Red oxide particles supplied by Huntsman was used to make red oxide rich epoxy primer coating. More details of the preparation and design of epoxy based coatings for long term corrosion test was described in section 3.8 of Chapter 3.

Both the active and barrier protective properties of the hybrid silane-zirconia coatings containing three different nanocontainers, zirconia, silica, and titania have been discussed elaborately in Chapter 4, Chapter 5, and Chapter 6 respectively. All the three 2-MBT loaded zirconia, silica, and titania nanocontainers impregnated hybrid coatings were immersed in 0.01 M NaCl solution for one week after making an artificial scratch on the coatings to induce and observe corrosion activity. Electrochemical Impedance spectroscopy studies were carried out on scratched inhibitor loaded nanocontainer impregnated hybrid coatings for all the three nanocontainers, silica, zirconia, and titania in 0.01 M NaCl solution for 1 week. Tape peel test was carried out according to ASTM

D3359 to assess the adhesion of the coating to the substrate. Neutral salt spray test for the epoxy coated samples (both ENC and PEC) were carried out according to ASTM standard B 117 for 2000 h in a salt spray cabinet model SF/100, CW Specialist Equipment, England. The details of the experiment were given in section 3.9.8 of Chapter 3. Raman spectra of the epoxy coated samples (both ENC and PEC) after the salt spray test were obtained by focusing the laser beam at the centre of the cross mark of the coatings. After salt spray test, the undercoat corrosion was examined after carefully removing the epoxy coating by pulling it off.

### 7.3. Results and Discussions

#### 7.3.1 Comparison of Corrosion Protective Performance of Zirconia, Silica, and Titania Nanocontainers

Figure 7.1 shows the EIS response of scratched hybrid coatings of 2-MBT loaded zirconia, silica, and titania nanocontainers after 1 week of immersion in the salt solution.

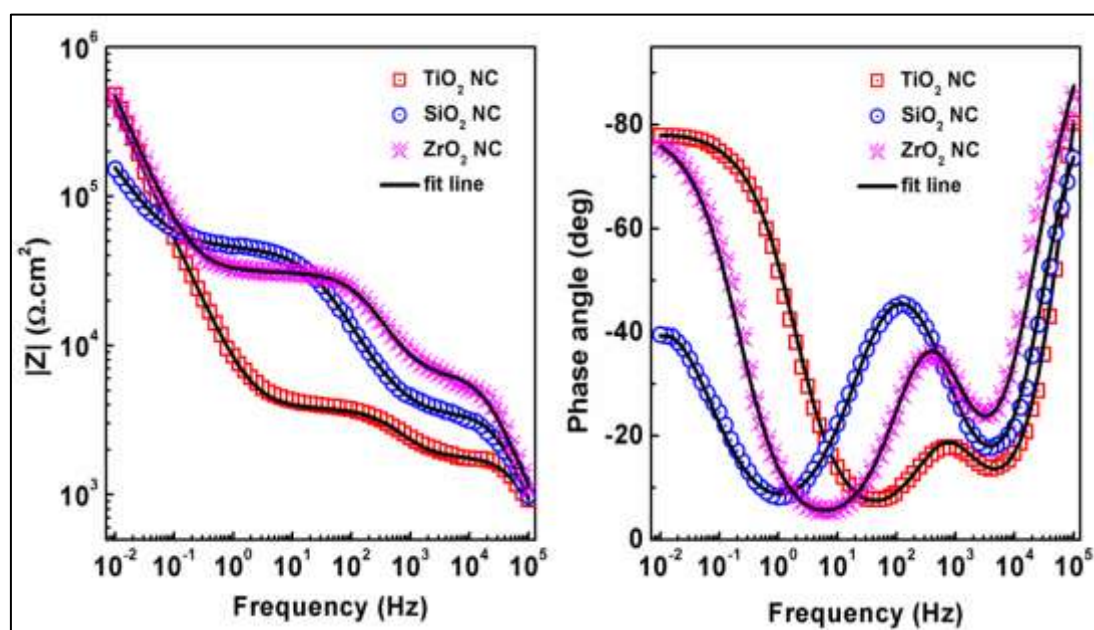


**Figure 7.1: EIS response of scratched hybrid coatings of 2-MBT loaded zirconia, silica, and titania nanocontainers after 1 week of immersion in the salt solution**

The low frequency segment can be related to the active corrosion protection provided by the inhibitive species released from the nanocontainers. The higher value of the low frequency impedance of  $\text{TiO}_2$  nanocontainer system compared to that of  $\text{SiO}_2$  nanocontainer and  $\text{ZrO}_2$  nanocontainer confirmed its better active corrosion protection. Moreover, the final relaxation process of  $\text{TiO}_2$  nanocontainer system had higher phase angle value and it was highly capacitive in nature compared to that of  $\text{SiO}_2$  and  $\text{ZrO}_2$  nanocontainer systems. This also confers the better protective performance of  $\text{TiO}_2$  nanocontainer system.

Figure 7.2 shows the evolution of modulus of impedance at  $10^{-2}$  Hz for scratched 2-MBT loaded zirconia, silica, and titania mixed hybrid coatings during 1 week of immersion in salt solution.

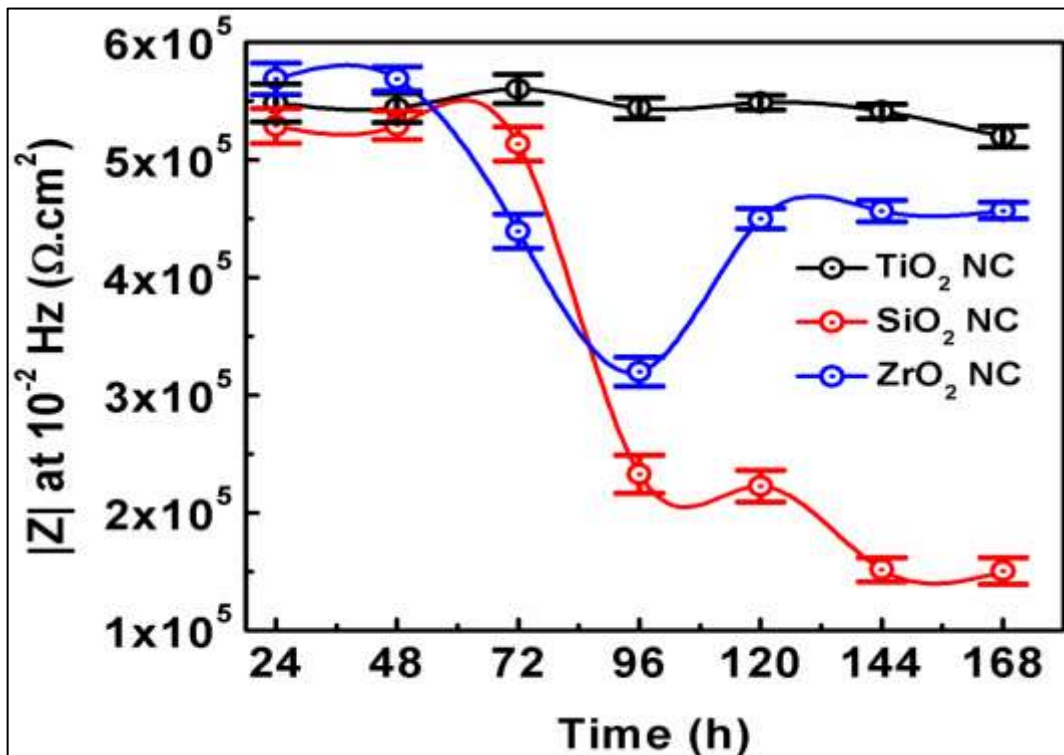


**Figure 7.2: Evolution of  $|Z|$  at  $10^{-2}$  Hz for scratched 2-MBT loaded zirconia, silica, and titania mixed hybrid coatings during 1 week of immersion in salt solution**

The value of  $|Z|$  at  $10^{-2}$  Hz can be correlated to the active corrosion protection conferred by the release of corrosion inhibitors from the nanocontainers. In the case of silica

nanocontainers,  $|Z|$  at  $10^{-2}$  Hz decreased as the immersion progressed in salt solution. For zirconia nanocontainer system,  $|Z|$  at  $10^{-2}$  Hz was initially decreased and then increased. However, in the case of  $\text{TiO}_2$  nanocontainer system,  $|Z|$  at  $10^{-2}$  Hz did not change considerably during immersion and it had highest value of  $|Z|$  at  $10^{-2}$  Hz after 1 week of immersion compared to silica and zirconia nanocontainer systems. The above-mentioned results suggested that hybrid coating containing 2-MBT loaded  $\text{TiO}_2$  nanocontainers has better barrier and active corrosion protection compared to that of hybrid coatings containing silica and zirconia nanocontainers. The following table summarizes different characteristic features of three nanocontainers systems that are described in detail in chapters 4, 5 and 6.

	<b>Titania</b>	<b>Silica</b>	<b>Zirconia</b>
<b>Loading efficiency</b>	<b><math>73 \pm 3 \%</math></b>	<b><math>72 \pm 2 \%</math></b>	<b><math>63 \pm 2 \%</math></b>
<b>Stimuli responsive Release</b>	<b>pH responsive release</b>	<b>pH responsive release</b>	<b>pH responsive release</b>
<b>Active Protection</b>	<b>Best (I)</b>	<b>Good (III)</b>	<b>Better (II)</b>
<b>Cost of fabrication</b>	<b>Economical</b>	<b>Expensive</b>	<b>Expensive</b>
<b>Ease of Synthesis</b>	<b>Simple method and easy to scale up, so easy to adopt industrially</b>	<b>Time consuming, lacking reproducibility</b>	<b>Not a simple method and scaling up need time</b>
<b>Size</b>	<b>Less than 100 nm, easy to disperse in the coating</b>	<b>200 nm</b>	<b>400 nm, can lead to inhomogeneity in the coating</b>

**Table 7.1: Characteristic features of three nanocontainer systems**

From Table 7.1 it is clear that all the three nanocontainers exhibited sustained pH responsive release and which is very essential for active corrosion protection. The loading efficiency of  $\text{TiO}_2$  nanocontainers was slightly higher than that of  $\text{SiO}_2$

nanocontainers where as marginally better than that of  $\text{ZrO}_2$  nanocontainers. From the impedance analysis, the better corrosion protective performance of  $\text{TiO}_2$  nanocontainers was already established. The size of the nanocontainers is a very important factor to be considered for the corrosion protection. Smaller nanocontainers can disperse well in the hybrid coatings and will not affect the homogeneity of the coating matrix. In opposition to that, larger nanocontainers can generate inhomogeneity in the coating matrix and thereby create cracks in the coatings. This in turn will reduce the physical barrier protection offered by the coatings and eventual corrosion of the underlying metallic substrate. The size of  $\text{TiO}_2$  nanocontainers are less than 100 nm and some of them are even smaller and having size of 20-50 nm. This smaller size will help  $\text{TiO}_2$  nanocontainers to be well dispersed in the coating matrix to make crack free homogenous coating with better barrier protection. The cost of fabrication and the ease of synthesis of nanocontainers are key factors to be considered in the economical point of view and scaling up and industrial production of the nanocontainers. The synthesis procedure of  $\text{TiO}_2$  nanocontainer is very easy and which can be easily scaled up for industrial production. Conversely, the synthesis procedure for  $\text{SiO}_2$  and  $\text{ZrO}_2$  nanocontainers required more time and hence the scaling up the production would not be easy. After considering all the previously mentioned facts,  $\text{TiO}_2$  nanocontainers were selected to prepare epoxy-based coatings to test long-term corrosion protection and self-healing ability.

### ***7.3.2 Cross-Hatch Tape Adhesion Test***

Coating adhesion tests were performed according to the ASTM D 3359-09 cross-hatch tape adhesion test. Results of the adhesion test are presented in Figure 7.3. As described in ASTM D 3559-09, both the plain epoxy coating and epoxy nanocontainer coatings

were ranked as 5A. This indicates that both the coatings have perfect adhesion to the alloy surface.

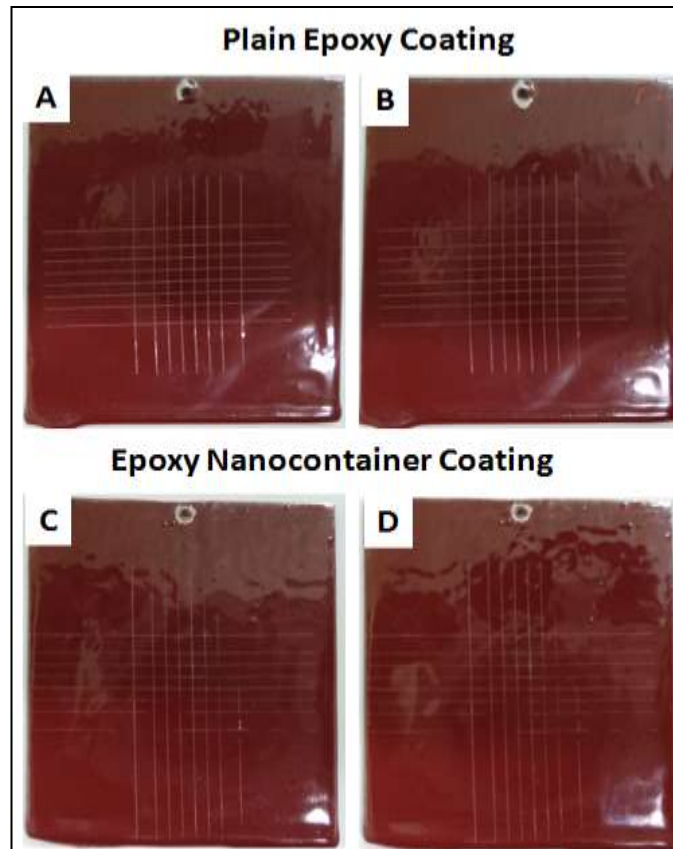


**Figure 7.3: Specimens coated with plain epoxy coatings before (A) and after (B) initial adhesion test; specimens coated with epoxy nanocontainer coatings before (C) and after (D) initial adhesion test**

This result also suggests that the addition of the nanocontainer based pre-treatment layer did not affect the adhesive property of the epoxy coating. The nanocontainer impregnated sol-gel hybrid coating could act as adhesion promoter in addition to imparting active corrosion protection to metallic substrates.

### ***7.3.3 Salt Spray Test for Nanocontainer Based Epoxy Coatings***

Salt spray or salt fog test is an accelerated weathering test to compare the anticorrosive protective performance of various coatings. It is one of the oldest and universally accepted tests to certify the corrosion resistance of materials, even though there are



doubts about its truly predictive characteristics and reliable co-relation between the results of salt spray test and the life of a product [332, 333]. However, this test is widely accepted and a standard test in coating industry. Both the Epoxy Nanocontainer Coating (ENC) and reference coating (Plain epoxy coating, PEC) were exposed to 1000 h of salt spray test. Two sets of coated specimens were exposed to salt spray test. Figure 7.4 shows the photograph of ENC and PEC after 1000 h of salt spray test.

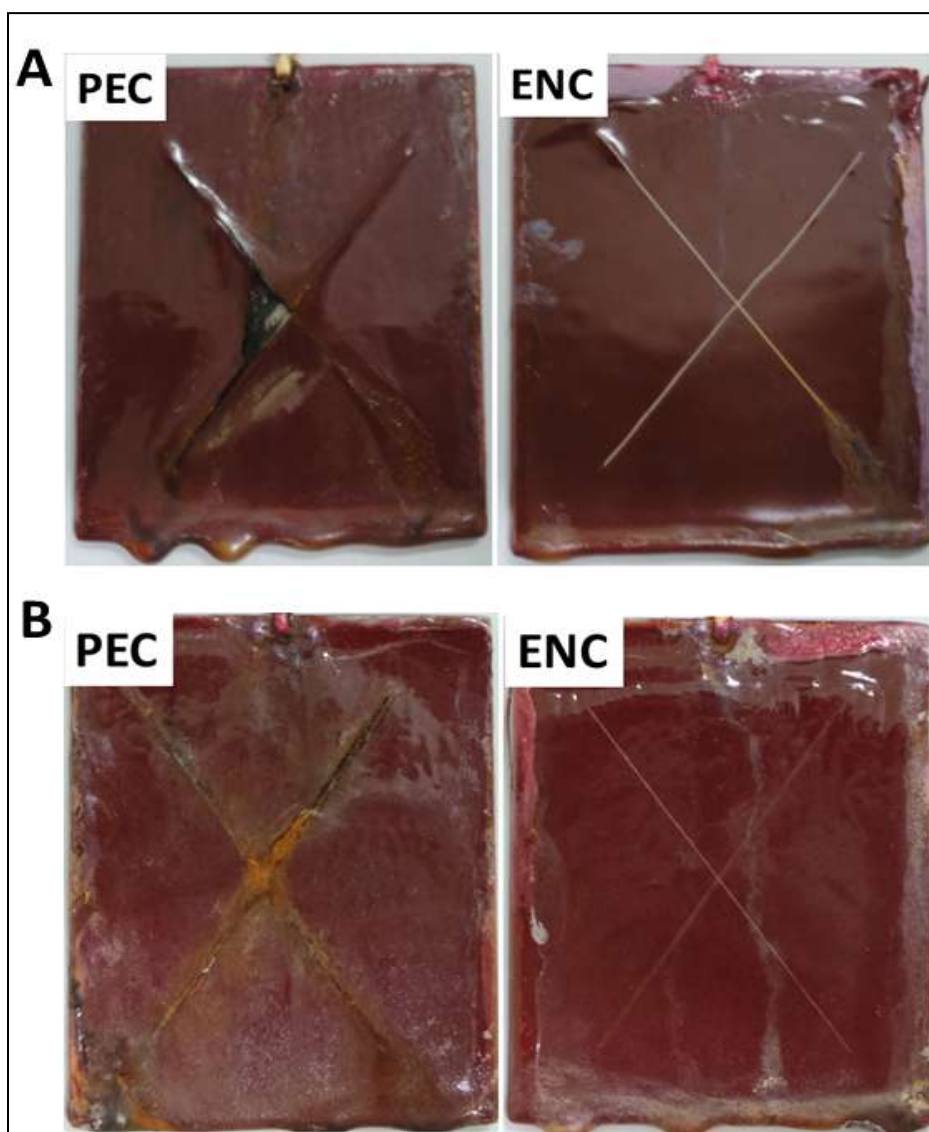


**Figure 7.4: Photographs of the Epoxy Nanocontainer Coating (ENC) and reference coating (Plain epoxy coating, PEC) after 1000 h of exposure to neutral salt spray test; (A) first set, (B) second set**

Blistering of the coatings and under coat corrosion was clearly visible in the case of PEC after 1000 h of salt spray exposure. Moreover, a small flake of the coating was peeled off due to the loss of adhesion to the metallic substrate (Figure 7.4(A)). Conversely, no delamination of coatings was observed for ENC. Insignificant rust markings appeared on one side in the scratched area of the coating (Figure 7.4(A)). However, in the second set of tested samples, such rust markings were not observed on the scratched area (Figure 7.4(B)). The salt spray chamber test showed sufficient protection even after 1000 h of exposure for inhibitor loaded nanocontainer mixed epoxy coating compared to that of reference (plain top epoxy) coating. The salt spray test for ENC was further continued until 2000 h of exposure and the image of the 2000 h salt spray exposed specimen is presented in Figure 7.5



**Figure 7.5: Photographs of the Epoxy Nanocontainer Coating (ENC) after 2000 h of exposure to neutral salt spray test**

It was observed that even after 2000 h of salt spray exposure, the coating was intact and significant damage due to corrosion had not occurred on ENC.

#### ***7.3.4 Analysis of the Undercoat Corrosion***

In order to get a clearer picture about the extent of corrosion attack, the undercoat corrosion was examined after removing the coatings and the results are presented in the

subsequent section. The surface of coated modified 9Cr-1Mo ferritic steel was analyzed after carefully removing the epoxy coating by pulling it off.

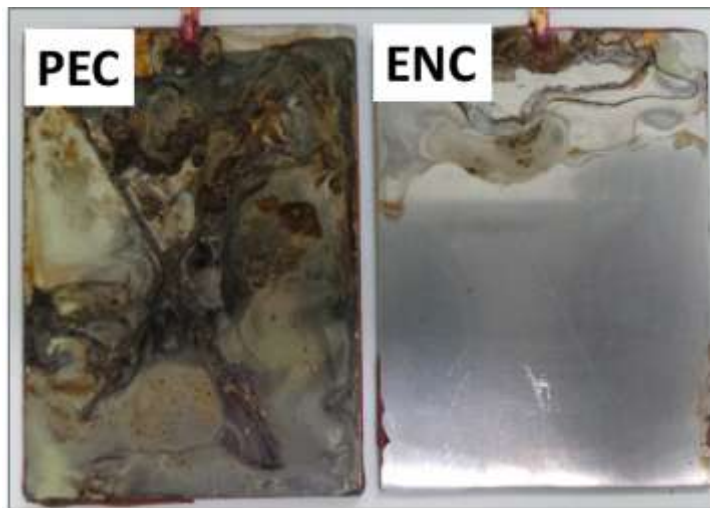


**Figure 7.6: The photographs of metal surface underneath the coatings after 1000 h of salt spray exposure**

The idea is to assess the extent of steel rust formation under the coating. Figure 7.6 shows the photographs of metal surface underneath the coatings after 1000 h of salt spray exposure. In the case of PEC reference coatings, the metal surface corroded uniformly and corrosion products were clearly visible on the surface of the metal. In the case of inhibitor loaded nanocontainer impregnated ENC coatings, corrosion attack was very less. Most of the surface of the alloy was protected except the top part of the surface and this may be due to the attack on the edges and on the sides of the hole on the top of the specimen. The scratched and other areas were protected indicating the inhibition of corrosion due to the presence of 2-MBT loaded  $\text{TiO}_2$  nanocontainers in the coating.

#### ***7.3.5 Raman Analysis of Salt Spray Exposed Coated Specimens.***

Raman spectra were recorded for both plain epoxy coating and epoxy nanocontainer coatings after 1000 h of salt spray exposure. Figure 7.7 shows the Raman spectra of

plain epoxy coating after 1000 h of salt spray test. The various phases of iron oxides and iron-oxy hydroxides, which display stronger Raman scattering, are: Lepidocrocite ( $\gamma$ -FeOOH), Goethite ( $\alpha$ -FeOOH), chlorinated oxyhydroxide Akaganeite ( $\beta$ -FeOOH), Hematite ( $\alpha$ -Fe<sub>2</sub>O<sub>3</sub>), Maghemite ( $\gamma$ -Fe<sub>2</sub>O<sub>3</sub>), and Magnetite (Fe<sub>3</sub>O<sub>4</sub>).

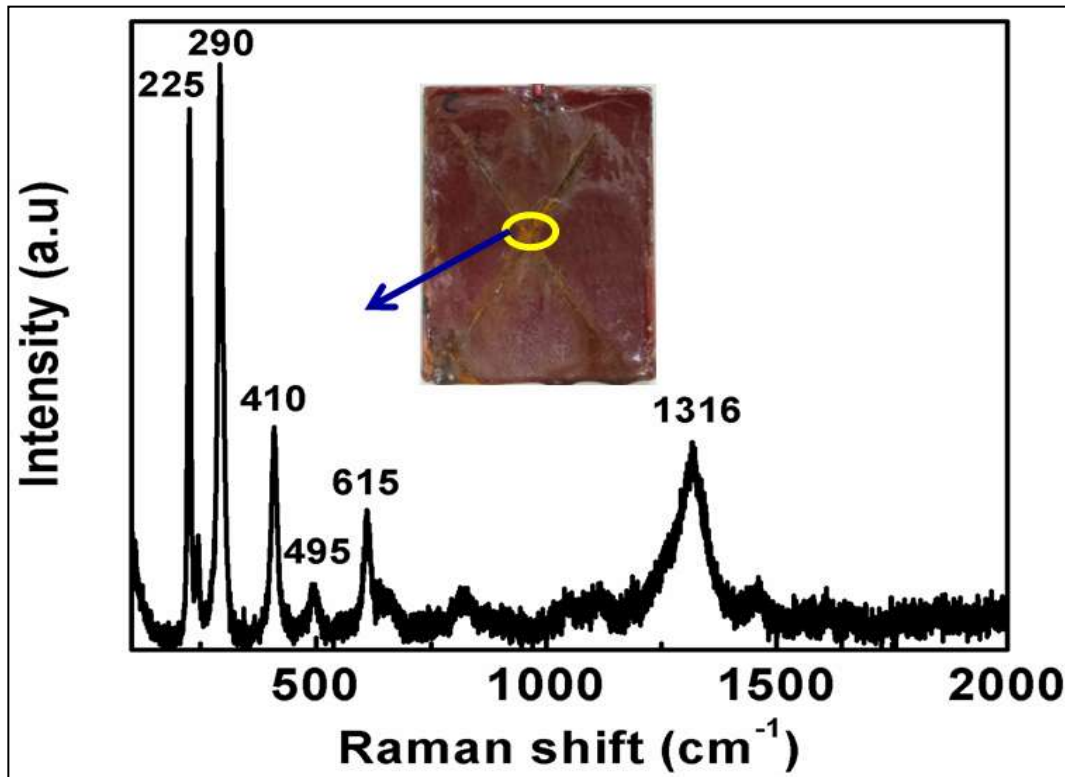


**Figure 7.7: Raman spectra of plain epoxy coating after 1000 h of salt spray exposure. Inset shows the image of the specimen and the circle indicates the area at which the spectrum was recorded**

The Raman spectrum was obtained by focusing the laser beam on the centre of the “X” cut on the coated surface where corrosion products were observed. The intense Raman lines observed were at 225 cm<sup>-1</sup>, 290 cm<sup>-1</sup>, 410 cm<sup>-1</sup>, 615 cm<sup>-1</sup>, and 1316 cm<sup>-1</sup>. These Raman lines are characteristics of Hematite ( $\alpha$ -Fe<sub>2</sub>O<sub>3</sub>) [334, 335]. Other oxides or oxyhydroxides of iron were not present in the obtained Raman spectra, since Hematite was the predominant corrosion product. Moreover, no Raman features for the epoxy

coatings were observed in the Raman spectra. Moreover, no Raman features for the epoxy coatings were observed in the Raman spectra.

Figure 7.8 shows the Raman spectra of epoxy nanocontainer coatings after salt spray experiment.

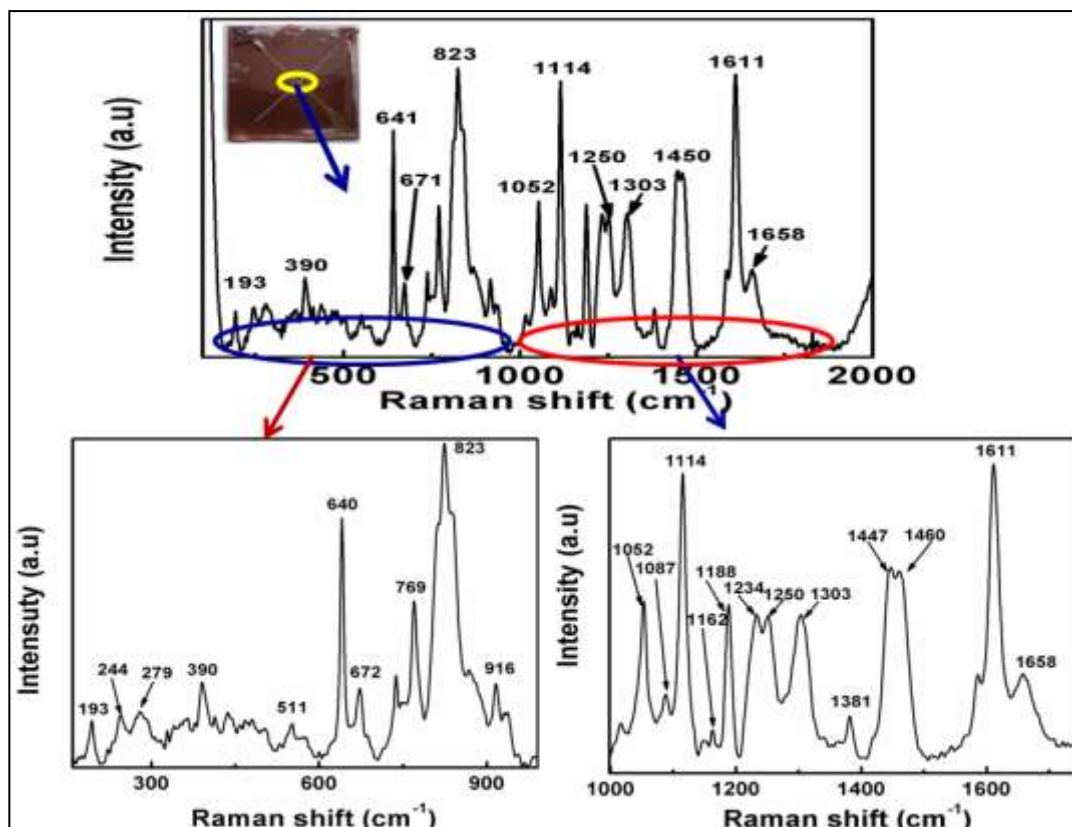


**Figure 7.8: Raman spectra of epoxy nanocontainer coating after 1000 h of salt spray exposure. Inset shows the image of the specimen and the circle indicates the area at which the spectrum was recorded**

The Raman spectra of epoxy nanocontainer coatings (ENC) did not show any peak corresponding to the corrosion products of iron. All the Raman features obtained were of the coatings. The Raman results are in good agreement with the salt spray visual examination results.

The major Raman lines corresponding to the epoxy backbone of the coatings were observed in the spectra. The peaks at 1188, 1460, and 1610  $\text{cm}^{-1}$  corresponded to the stretching vibrations of the disubstituted aromatic rings. The more intense and better

resolved Raman line at  $1610\text{ cm}^{-1}$  was due to the strong stretching of aromatic ring C=C [336]. The breathing vibration mode of epoxide group appeared at 1234 and  $1250\text{ cm}^{-1}$  [337]. The peaks at 824 and  $916\text{ cm}^{-1}$  would have resulted from the symmetric deformation of the epoxy ring. Interestingly, the presence of 2-MBT could detect in the Raman spectra of ENC which reveals the release 2-MBT in the scratched area of the coatings. The Raman lines at 640 and  $672\text{ cm}^{-1}$  may be attributed to –CS stretching vibration mode. The Raman line appeared at  $551\text{ cm}^{-1}$  probably corresponds to CNH bending mode. The in plane ring bending of benzene ring appears at  $769\text{ cm}^{-1}$  [269-272].

#### 7.4 Summary

- $\text{TiO}_2$  nanocontainer based hybrid coating was selected to mix with epoxy coating for long term corrosion evaluation studies.
- Adhesion test for the coatings was performed according to ASTM D 3559-09 and epoxy nanocontainer coating showed perfect adhesion to the alloy surface.
- Salt spray test was carried out for 2000 h according to ASTM B 117. Blistering and peeling off the coating was observed for plain epoxy coating after 1000 h of salt spray exposure. Black coloured corrosion products were observed under the delaminated coatings for control specimen. Insignificant rust markings were observed on the self-healing epoxy nanocontainer coatings and no delamination of the coating was observed even after 2000 h of exposure.
- Raman analysis of the coated specimens after salt spray test showed that corrosion products (mainly  $\alpha\text{-Fe}_2\text{O}_3$ ) were present on the scratched surface of plain epoxy coatings where as no corrosion products appeared on epoxy nanocontainer coatings. Moreover, the presence of 2-MBT was detected in the scratched area of epoxy nanocontainer coatings.

## CHAPTER 8

### Conclusions, Summary and Scope for Future Studies

---

*This chapter elucidates the important conclusions derived from the investigations carried out on synthesis of nanocontainers, its inhibitor loading and releasing properties and the active corrosion protection efficiency of coatings developed using inhibitor loaded nanocontainers. The self-healing ability of various coatings prepared using nanocontainers was assessed and compared. These results were consolidated and summarized in this chapter. Apart from this, suggestions are provided for further research to be carried out for improving the performance of coatings for enhanced longer active corrosion protection systems with self-healing ability.*

---

#### 8.1 Conclusions and Summary

The present work contributes to the development of nanocontainer impregnated hybrid coatings for active corrosion protection based on self-healing ability. The silane-zirconia hybrid coatings with uniformly dispersed inhibitor loaded nanocontainers were investigated. Three different nanocontainers, TiO<sub>2</sub> nanotube powders, hollow mesoporous silica spheres and hollow mesoporous zirconia spheres were synthesized and used as nanocontainers for loading corrosion inhibitors 2-mercaptobenzothiazole (2-MBT) and benzotriazole (BTA). The protective coatings were applied on modified 9Cr-1Mo ferritic steel, which is highly susceptible to atmospheric rusting during fabrication, storage and operation and an important structural material in many sectors such as power generation, chemical processing and petroleum industries. Both the active and passive barrier protection provided by the coatings were investigated using Electrochemical Impedance Spectroscopy (EIS).

Hollow mesoporous zirconia nanocontainers (HMZ) with uniform spherical shape and an average diameter of 400 nm were prepared using a hard templating method. Silica

nanoparticles with an average diameter of 375 nm were used as solid templates. The specific surface area of the HMZ nanocontainers was found to be  $145.97 \text{ m}^2\text{g}^{-1}$  and the pore size was centered at 3.9 nm. Corrosion inhibitor molecules (2-MBT) were successfully loaded into the nanocontainers and the loading efficiency was found to be  $63 \pm 2 \%$ . The entrapment of 2-MBT into the hollow cavity of HMZ was investigated and proved by UV-visible spectroscopy and Raman spectroscopy studies.

Hollow mesoporous silica (HMS) nanocontainers of average size 200 nm were synthesized through a sol-hydrothermal method. The HRTEM investigation of the synthesized HMS revealed that the spheres were spherical in shape and had channel like ordered pores *ca.* 2.5 nm in width. Both the small angle XRD and HRTEM studies showed that HMS nanocontainers had a uniform, well defined hexagonal mesostructure. The specific surface area of the HMS nanocontainers was found to be  $940.57 \text{ m}^2\text{g}^{-1}$  and the pore size was centered at 2.5 nm. The extraordinary surface area, narrow mesopore distributions, and hollow structure of the nanocontainers helped in loading 2-MBT corrosion inhibitors. The loading efficiency of HMS nanocontainers was about  $72 \pm 2 \%$ .

TiO<sub>2</sub> nanocontainers were synthesized using a rapid breakdown anodization (RBA) method by applying a constant potential of 20 V under vigorous stirring. FESEM and HRTEM images of the as-prepared nanocontainers revealed its tubular morphology. The tubes were well ordered and stacked in bundles of length approximately 6-8  $\mu\text{m}$  and diameter about 40 nm. After calcination, the tubular morphology of TiO<sub>2</sub> nanocontainers was lost and the powders became nanoparticles. The sizes of these TiO<sub>2</sub> crystallites were in the range of 10-30 nm. A careful examination on the surface of a single TiO<sub>2</sub> nanocontainers showed ordered arrays of nano pores and these pores could effectively help in the adsorption of inhibitors while loading them. Both BTA and 2-



MBT were successfully loaded into TiO<sub>2</sub> nanocontainers and the loading efficiency of the nanocontainers was about  $73 \pm 3$  %.

The pH stimulated intelligent release of corrosion inhibitors (2-MBT and BTA) from the nanocontainers was demonstrated. It was found that the release of inhibitors from the nanocontainers was faster and higher in amount when the pH was shifted from neutral value. Electrochemical impedance spectroscopy (EIS) was employed in this study as an effective tool for the investigation of active corrosion protection based on self-healing effect of protective coatings on modified 9Cr-1Mo ferritic steels. The size of the nanocontainers had a very important role in the protective performance of the hybrid coatings. It was found that smaller TiO<sub>2</sub> nanocontainers compared to that of SiO<sub>2</sub> and ZrO<sub>2</sub> nanocontainers could impart better active and passive corrosion protection to modified 9Cr-1Mo ferritic steels. The tape peel test showed that the self-healing epoxy coating containing 2-MBT loaded TiO<sub>2</sub> nanocontainers had good adhesion to the alloy surface to provide good protection. A long-term corrosion protection study of TiO<sub>2</sub> nanocontainer based epoxy coatings was carried out and it was found that self-healing epoxy coating containing 2-MBT loaded TiO<sub>2</sub> nanocontainers performed far superior to a reference coating after 2000 h of salt spray exposure. The Raman spectroscopy analysis of salt spray exposed samples revealed the presence of corrosion products on the surface reference epoxy coatings. On the other hand, the Raman spectra of epoxy nanocontainer coatings did not reveal any corrosion products on the scratched area of the coatings. In fact, the Raman lines for 2-MBT appeared in the spectra of epoxy nanocontainer coatings and this can be correlated to the release of 2-MBT to the scratched area. Both the Raman and salt spray results showed the active corrosion protection rendered by the release of the inhibitor from the nanocontainers.

The salient features of the present study are given below:

- Three nanocontainer systems,  $\text{TiO}_2$  NC,  $\text{SiO}_2$  NC,  $\text{ZrO}_2$  NC, were synthesized and loaded with corrosion inhibitor molecules of BTA and 2-MBT
- The sustained and controlled pH responsive release of inhibitors from the nanocontainers were proved
- Later, these inhibitor loaded nanocontainer systems were mixed with hybrid coatings and applied over modified 9Cr-1Mo ferritic steel and their active and barrier corrosion protection properties were studied
- Electrochemical Impedance Spectroscopy (EIS) was used in this study as a useful technique for the investigation of self-healing processes in protective coatings
- Out of three nanocontainer systems,  $\text{TiO}_2$  was selected for long term exposure studies considering the ease of synthesis and scaling up for production and it also provided better active corrosion protection compared to other nanocontainers studied.
- Long term corrosion protection of epoxy coatings containing inhibitor loaded  $\text{TiO}_2$  NC over the control epoxy was demonstrated after 2000 h of salt spray exposure
- Raman spectra of epoxy nanocontainer coatings after 1000 h of salt spray exposure showed the presence of released 2-MBT at the scratched area of the coatings and absence of any corrosion products.

## 8.2 Scope for Future Study

Further research should be carried out to establish and improve the self-healing ability of the coatings. It is also required to prepare coatings with multiple functionalities to protect structural materials from corrosion in different environments. The following are some of the works to be carried out for the aforesaid purpose:

- Development of nanocontainer based corrosion sensing coatings for early detection of the onset of corrosion
- Combination of different inhibitors with various smart nano and microcontainers to obtain multifunctional coating and to have self-healing effect in a synergistic way: an early corrosion protection and a longer time inhibition
- Developing a smart coating with anticorrosive, antibacterial and superhydrophobic functionalities
- Additional studies are required to investigate the kinetic and structural properties of the nanocontainers and the diffusion of the released inhibitor inside the coating matrix
- Investigating the active corrosion protection with the help of a localized electrochemical technique

## References

- 1) K.R. Trethewey, *Corrosion for Students of Science and Engineering*, 1<sup>st</sup> ed., Harlow: Longman Scientific and Technical, 1990
- 2) J.R. Davis, *Corrosion: Understanding the Basics*, 1<sup>st</sup> ed., ASM International, 2000
- 3) G.H. Koch, M.P.H. Brangers, N.G. Thompson, Y.P. Viramani, J.H. Payer, “*Corrosion costs and preventive strategies in United States*”, Publication No. FHWA-RD-01-156, NACE International
- 4) G.H. Hays, “Now is the Time”, <http://corrosion.org/wp-content/themes/twentyten/images/nowisthetime.pdf>
- 5) <http://www.g2mtlabs.com/2011/06/nace-cost-of-corrosion-study-update/> accessed on 14/07/2014
- 6) <http://timesofindia.indiatimes.com/city/vadodara/Corrosion-costs-India-Rs-2-lakh-crore-loss-a-year/articleshow/17484225.cms>
- 7) <http://news.in.msn.com/business/article.aspx?cp-documentid=5137016>
- 8) M.G. Fontana, *Corrosion Engineering*, 3<sup>rd</sup> ed., TATA McGRAW-HILL Edition, 2005
- 9) M. Stratmann, *Ber. Bunsenges. Phys. Chem.*, **94** (1990) 626.
- 10) M. Stratmann, *Corros. Sci.*, **27** (1987) 869.
- 11) M. Stratmann, K. Hoffmann, *Corros. Sci.*, **29** (1989) 1329.
- 12) A. Cox, S.B. Lyon, *Corros. Sci.*, **36** (1994) 1167.
- 13) T. Misawa, K. Asami, K. Hashimoto, S. Shimodaira, *Corros. Sci.*, **14** (1974) 279.
- 14) S. Hörle, F. Mazaudier, Ph. Dillmann, G. Santarini, *Corros. Sci.*, **46** (2004) 1431.

- 15) T. E. Graedel, R. P. Frankenthal, *J. Electrochem. Soc.*, **137** (1990) 2385.
- 16) K. J. Eichhorn, W. Forker, *Corros. Sci.*, **28** (1988) 745.
- 17) U.R. Evans, C. A. J. Taylor, *Corros. Sci.*, **12** (1972) 227.
- 18) M. Stratmann, J. Muller, *Corros. Sci.*, **12** (1994) 327
- 19) A. Nishikata, Y. Ichiara, Y. Hayashi, T. Tsuru, *J. Electrochem. Soc.*, **144** (1997) 1244
- 20) S.H. Zhang, S.B. Lyon, *Corros. Sci.*, **38** (1993) 713
- 21) M. Yamashita, H. Nagano, R.A. Oriani, *Corros. Sci.*, **40** (1998) 1447
- 22) M. Stratmann, K. Bohnenkamp, H.J. Engell, *Corros. Sci.*, **23** (1983) 969
- 23) K. Asami, M. Kikuchi, *Corros. Sci.*, **45** (2003) 2671
- 24) I. Suzuki, Y. Hisamatsu, N. Masuko, *J. Electrochem. Soc.*, **127** (1980) 2210.
- 25) Y. Ma, Y. Li, F. Wang, *Corros. Sci.*, **51** (2009) 997.
- 26) H. Antony, S. Perrin, P. Dillmann, L. Legrand, A. Chausse, *Electrochim. Acta*, **52** (2007) 7754.
- 27) M. Yamashita, H. Miyuki, Y. Matsuda, H. Nagano, T. Misawa, *Corros. Sci.*, **36**, (1994), 283.
- 28) D. Lai, R. Borg, M. Barbas, J. MacKanzie, C. Birchanall, *Corrosion*, **17** (1961) 357.
- 29) Z. Wang, J. Liu, L. Wu, R. Han, Y. Sun, *Corros. Sci.*, **67** (2013) 1.
- 30) T. Kamimura, M. Stratmann, *Corros. Sci.*, **4** (2001) 429.
- 31) Y. Qian, C. Ma, D. Niu, J. Xu, M. Li, *Corros. Sci.*, **74** (2013) 424.
- 32) M. Yamashita, T. Shimizu, H. Konishi, J. Mizuki, H. Uchida, *Corros. Sci.*, **45** (2003) 381.
- 33) M. Yamashita, H. Miyuki, H. Nagano, T. Misawa, *Proceedings of 13<sup>th</sup> International Corrosion Congress*, Melbourne, (1996) 258

- 34) M. Yamashita, H. Konishi, J. Mizuki, H. Uchida, *Mater. T JIM*, **45** (2004) 1920.
- 35) H.H. Uhlig and R.W. Revie, *Corrosion and Corrosion Control*, John Wiley & Sons, 1985
- 36) R.H. Heidersback, Cathodic Protection, *Corrosion: Fundamentals, Testing, and Protection*, Vol 13A, ASM Hand Book, ASM International, 2003, 855.
- 37) C.E. Locke, Anodic Protection, *Corrosion: Fundamentals, Testing, and Protection*, Vol 13A, ASM Handbook, ASM International, 2003, 851.
- 38) O.L. Riggs and C.E. Locke, *Anodic Protection: Theory and Practice in the Prevention of Corrosion*, Plenum Press, 1981
- 39) NACE Glossary of Corrosion Terms, *Mater. Proc.*, Vol 4 (No. 1) 1965 79
- 40) N. Hackerman, *Fundamentals of Inhibitors*, NACE Basic Corrosion Course, NACE International, 1965
- 41) B.A. Miksic and R.H. Miller, *European Symposium on Corrosion Inhibitors*, 5th Proc., 107<sup>th</sup> Manifestation of the European Federation on Corrosion, September 1980, 217
- 42) K.L. Vasanth, Vapor Phase Corrosion Inhibitors, *Corrosion: Fundamentals, Testing, and Protection*, Vol 13A, ASM Handbook, ASM International, 2003, 871
- 43) K.B. Tator, Introduction to Coatings and Linings, *Corrosion: Fundamentals, Testing, and Protection*, Vol 13A, ASM Handbook, ASM International, 2003, 814
- 44) "Standard Definitions of Terms Relating to Electroplating," B 374, Annual Book of ASTM Standards, Vol 02.05, American Society for Testing and Materials

- 45) M.L. Berndt and C.C. Berndt, Thermal Spray Coatings, *Corrosion: Fundamentals, Testing, and Protection*, Vol 13A, ASM Handbook, ASM International, 2003, 803.
- 46) P.A. Sorensen, S. Kiil, K.D. Johansen, C.E. Weinnell, *J. Coating. Tech. Res.*, **6** (2009) 135.
- 47) M.J. Mitchell, M. Summers, *Protect. Coat. Eur. J.*, **12** (2001) 77.
- 48) M. Guglielmi, *J. Sol–Gel Sci. Technol.*, **8** (1997) 443.
- 49) R.L. Ballard, J.P. Williams, J.M. Njus, B.R. Kiland, M.D. Soucek, *Eur. Polym. J.*, **37** (2001) 381.
- 50) G. Schottner, *Chem. Mater.*, **13** (2001) 3422.
- 51) R. Kasemann, H. Schmidt, *New J. Chem.*, **18** (1994) 1117.
- 52) N.N Voevodin, N.T. Grebasch, W.S. Soto, L.S Kasten, J.T. Grant, F.E. Arnold, M.S. Donley, *Prog. Org. Coat.*, **41** (2001) 287.
- 53) C.G. Munger, *Corrosion Prevention by Protective Coatings*, NACE International, 1985.
- 54) ASTM, *Manuals for Coatings of Light Water Nuclear Plants: Primary Containment and Other Safety Related Facilities, Appendix A, Glossary of Terms*, 1979
- 55) D. Kjernsmo, K. Kleven, J. Scheie, *Corrosion Protection*. Bording A/S, Copenhagen, 2003.
- 56) R. Zhang, H. Chen, H. Cao, C.M. Huang, P.E. Mallon, Y. Li, Y. He, T.C. Sandreczki, Y.C. Jean, T. Ohdaira, *J. Polym. Sci.*, **39** (2001) 2035.
- 57) J. Pospisil, S. Nespurek, *Prog. Polym. Sci.*, **25** (2000) 1261.
- 58) S.A.S. Dias, S.V. Lamaka, C.A. Nogueira, T.C. Diamantino, M.G.S. Ferreira, *Corros. Sci.*, **62** (2012) 153.

- 59) S. M. A. Hosseini, A. H. Jafri, and E. Jamalizadeh, *Electrochim. Acta.*, **54**, (2009) 7207.
- 60) R.L. Twite, G.P. Bierwagen, *Prog. Org. Coat.*, **33** (1998) 91.
- 61) C.J. Brinker, G.C. Frye, A.J. Hurd, C.S. Ashley, *Thin Solid Films*, **201** (1991) 97.
- 62) C.J. Brinker and G.W. Scherer, *Sol-Gel Science: The Physics and Chemistry of Sol-Gel Processing*, Academic Press, 1990
- 63) C.J. Brinker, *J. Non-Cryst. Solids*, **100** (1988) 31.
- 64) T.L. Metroke, R.L. Parkhill, E.T. Knobbe, *Prog. Org. Coat.*, **41** (2001) 233.
- 65) C.L. Jackson, B.J. Bauer, A.I. Nakatani, J.D. Barnes, *Chem. Mater.*, **8** (1996) 727.
- 66) G.L. Li, M. Schenderlein, Y. Men, H. Möhwald, D.G. Shchukin, *Adv. Mater. Interfaces*, **1** (2014) 1300019
- 67) D.G. Shchukin, D. O. Grigoriev, H. Möhwald, *Soft Matter*, **6** (2010) 720.
- 68) M. Ebelmen, *Annales de Chimie et de Physique*, **16** (1846) 166.
- 69) R. Roy, *J. Am. Ceram. Soc.*, **39** (1956) 145.
- 70) R. Roy, E.F. Osborn, *Am. Miner.*, **39** (1954) 853.
- 71) R. Roy, *Science*, **238** (1987) 1664.
- 72) M. Atik, P. Neto, L.A. Avaca, M.A. Aegerter, *Ceram. Int.*, **21** (1995) 403.
- 73) M. Atik, F.P. Luna, S.H. Messaddeq, M.A. Aegerter, *J. Sol–Gel Sci. Technol.*, **8** (1997) 517.
- 74) A. Nazeri, P.P. Trzaskoma, D. Bauer, *J. Sol–Gel Sci. Technol.*, **10** (1997) 317.
- 75) P. Galliano, J.J.D. Damborenea, M.J. Pascual, A. Duran, *J. Sol–Gel Sci. Technol.*, **13** (1998) 723.



- 76) M. Mennig, C. Schelle, A. Duran, J.J. Damborenea, M. Guglielmi, G. Brustain, *J. Sol–Gel Sci. Technol.*, **13** (1998) 717.
- 77) F. Perdomo, P.D. Lima, M.A. Aegerter, L.A. Avaca, *J. Sol–Gel Sci. Technol.*, **15** (1999) 87.
- 78) S.H. Messaddeq, S.H. Pulcinelli, C.V. Santilli, A.C. Guastaldi, Y. Messaddeq, *J. Non-Cryst. Solids*, **247** (1999) 164.
- 79) J. Masalski, J. Gluszek, J. Zabrzski, K. Nitsch, P. Gluszek, *Thin Solid Films*, **349** (1999) 186.
- 80) D.C.L. Vasconcelos, J.A.N. Carvalho, M. Mantel, W.L. Vasconcelos, *J. Non-Cryst. Solids*, **273** (2000) 135.
- 81) L. Fedrizzi, F.J. Rodriguez, S. Rossi, F. Deflorian, R.D. Maggio, *Electrochim. Acta*, **46** (2001) 3715.
- 82) H. Li, K. Liang, L. Mei, S. Gu, S. Wang, *J. Mater. Sci. Lett.*, **20** (2001) 1081.
- 83) T.P. Chou, C. Chandrasekaran, S.J. Limmer, G.Z. Cao, *J. Non-Cryst. Solids*, **290** (2001) 153.
- 84) T.P. Chou, C. Chandrasekaran, G.Z. Cao, *J. Sol–Gel Sci. Technol.*, **26** (2003) 321.
- 85) H. Sayilkan, S. Sener, E. Sener, M. Sulu, *Mater. Sci.*, **39** (2003) 733.
- 86) S. Ono, H. Tsuge, Y. Nishi, S. Hirano, *J. Sol–Gel Sci. Technol.*, **29** (2004) 147.
- 87) T. Sugama, *J. Coat. Technol. Res.* **2** (2005) 649.
- 88) L. Jianguo, G. Gaoping, Y. Chuanwei, *Surf. Coat. Technol.*, **200** (2006) 4967.
- 89) A. Conde, J.D. Damborenea, A. Duran, M. Menning, *J. Sol–Gel Sci. Technol.*, **37** (2006) 79.
- 90) A. Pepe, M. Aparicio, A. Duran, S. Cere, *J. Sol–Gel Sci. Technol.*, **39** (2006) 131.

- 91) U. Vijayalakshmi, S. Rajeswari, *J. Sol–Gel Sci. Technol.*, **43** (2007) 251
- 92) D. Wang, G.P. Bierwagen, *Prog. Org. Coat.*, **64** (2009) 327.
- 93) D. Niznansky and J. L. Rehspringer, *J. Sol–Gel Sci. Technol.*, **180** (1995) 191.
- 94) D. Hoebbel, M. Nacken and H. Schmidt, *J. Sol–Gel Sci. Technol.*, **12** (1998) 169.
- 95) M. S. Donley, R. A. Mantz, A. N. Khramov, V. N. Balbyshev, L. S. Kasten and D. J. Gaspar, *Prog. Org. Coat.*, **47** (2003) 401
- 96) T. L. Metroke and A. Apblett, *Prog. Org. Coat.*, **3** (2004) 51.
- 97) M. L. Zheludkevich, I. M. salvado, M.G.S Ferreira, *J. Mater. Chem.*, **15** (2005) 5099.
- 98) M.T. Harris, A. Singhal, J.L. Look, J.R. Smith-Kristensen J.S. Lin, L.M. Toth *J. Sol–Gel Sci. Technol.*, **41** (1997) 8.
- 99) U.H. Schubert, *Synthesis of inorganic materials*, Wiley-VCH, Weinheim, 2000.
- 100) M.H. Chisholm, Z. Zhou *J. Mater. Chem.*, **14** (2004) 3081.
- 101) K.C. Fortner, J.P. Bigi, S.N. Brown, *Inorg. Chem.*, **44** (2005) 2803.
- 102) D.C. Bradley, R.C. Mehrotra, C.P. Gaur, *Metal alkoxides*, Academic Press, London, 1978
- 103) V.G. Kessler, G.L. Spijksma, G.A. Seisenbaeva, S. Hakansson, D.H.A. Blank, H.J.M. Bouwmeester, *J. Sol–Gel Sci. Technol.*, **40** (2006) 40 163.
- 104) T. P. Chou, C. Chandrasekaran, S. J. Limmer, S. Seraji, Y. Wu, M. J. Forbess, C. Nguyen and G. Z. Gao, *J. Non-Cryst. Solids*, **290** (2001) 153.
- 105) R. L. Parkhill, E. T. Knobbe and M. S. Donley, *Prog. Org. Coat.*, **41** (2001) 261.
- 106) T. L. Metroke, O. Kachurina and E. T. Knobbe, *Prog. Org. Coat.*, **44** (2002) 295.

- 107) R. Di Maggio, L. Fedrizzi, S. Rossi and P. Scardi, *Thin Solid Films*, **286** (1996) 127.
- 108) M. Fallet, H. Mahdjoub, B. Gautier and J.-P. Bauer, *J. Non Cryst. Solids*, **293** (2001) 527
- 109) Y. Chen, L. Jin and Y. Xie, *J. Sol–Gel Sci. Technol.*, **13** (1998) 735.
- 110) B. Veeraraghavan, B. Haran, D. Slavkov, S. Prabhu, B. Popov, B. Heimann, *Electrochem. Solid-State Lett.* **6** (2003) B4.
- 111) M. Sheffer, A. Groysman, D. Mandler, *Corros. Sci.* **45** (2003) 2839.
- 112) Y. Castro, B. Ferrari, R. Moreno, A. Duran, *J. Sol–Gel Sci. Technol.* **26** (2003) 735.
- 113) K. Watanabe, M. Sakairi, H. Takahashi, S. Hirai S. Yamaguchi, *J. Electroanal. Chem.*, **473** (1999) 250.
- 114) S. Roux, P. Audebert, J. Pagetti M. Roche, *New J. Chem.*, **26** (2002) 298.
- 115) R. G. Biswas, J. L. Woodhead and A. K. Bhattacharaya, *J. Mater. Sci. Lett.*, **16** (1997) 1628.
- 116) H. Yang and W. J. van Ooij, *Prog. Org. Coat.*, **50** (2004) 149.
- 117) H. M. Hawthorne, A. Neville, T. Troczynski, X. Hu, M. Thammachart, Y. Xie, J. Fu Q. Yang, *Surf. Coat. Technol.*, **176** (2004) 243.
- 118) L. E. Amato, D. A. Lopez, P. G. Galliano S. M. Cere, *Mater. Lett.*, **59** (2005) 2026.
- 119) J. Gallardo, A. Duran, I. Garcia, J. P. Celis, M. A. Arenas A. Conde, *J. Sol–Gel Sci. Technol.*, **27** (2003) 175
- 120) S. Wilson, H. M. Hawthorne, Q. Yang T. Troczynski, *Wear*, **2** (2001) 1042.
- 121) S. Wilson, H. M. Hawthorne, Q. Yang T. Troczynski, *Surf. Coat. Technol.*, **133** (2000) 389.

- 122)H. Zheng, Y. Du, M. Damron, J. Wright, T. Myhanh, *Met. Finish.*, **96** (1998) 35.
- 123)A. N. Khramov, N. N. Voevodin, V. N. Balbyshev M. S. Donley, *Thin Solid Films*, 447 (2004) 549.
- 124)A. N. Khramov, V. N. Balbyshev, N. N. Voevodin M. S. Donley, *Prog. Org. Coat.*, **47** (2003) 207.
- 125)M. Mager, L. Schmalstieg, M. Mechtel H. Kraus, *Macromol. Mater. Eng.*, **286** (2001) 682.
- 126)M. Khobaib, L. B. Reynolds M. S. Donley, *Surf. Coat. Technol.*, **140** (2001) 16.
- 127)G. P. Thim, M. A. S. Oliveira, E. D. A. Oliveira F. C. L. Melo, *J. Non-Cryst. Solids*, **273** (2000) 124.
- 128)M. Mayrand, J. F. Quinson, A. Roche, V. Roisne, H. Guyon, *J. Sol–Gel Sci. Technol.*, **12** (1998) 49.
- 129)J. Wen, G.L. Wilkes, *Chem. Mater.*, **8** (1996) 1667.
- 130)R. L. Ballard, J. P. Williams, J. M. Njus, B. R. Kiland, M. D. Soucek, *Eur. Polym. J.*, **37** (2001) 381.
- 131)F. Rubio, J. Rubio J. L. Oteo, *J. Sol–Gel Sci. Technol.*, **18** (2000) 105.
- 132)A. Conde, A. Duran, J. J. de Damborenea, *Prog. Org. Coat.*, **46** (2003) 288.
- 133)G.-D. Kim, D.-A. Lee, Ji-W. Moon, J.-D. Kim, Ji-Ae Park, *Appl. Organometal. Chem.*, **13** (1999) 361.
- 134)S. M. Kim, K. Chakrabarti, E. O. Oh, C. M. Whang, *J. Sol–Gel Sci. Technol.*, **27** (2003) 149.
- 135)J. Gallardo, P. Galliano, A. Dura'n, *J. Sol–Gel Sci. Technol.*, **21** (2001) 65.

- 136) N. Voevodin, C. Jeffcoate, L. Simon, M. Khobaib, M. Donley, *Surf. Coat. Technol.*, **14** (2001) 29.
- 137) T. L. Metroke, O. Kachurina, E. T. Knobbe, *Prog. Org. Coat.*, **44** (2002) 185.
- 138) F. De. Matteis, P. Proposito, M. Casalboni, M. L. Grilli, E. Di Bartolomeo, E. Traversa, *J. Sol–Gel Sci. Technol.*, **26** (2003) 1081.
- 139) N. N. Voevodin, V. N. Balbyshev, M. S. Donley, *Prog. Org. Coat.*, **52** (2005) 28.
- 140) B. Smarsly, G. Garnweitner, R. Assink, C. J. Brinker, *Prog. Org. Coat.*, **47** (2003) 393.
- 141) S. H. Messaddeq, S. H. Pulcinelli, C. V. Santilli, A. C. Guastaldi, Y. Messaddeq, *J. Non-Cryst. Solids*, **247** (1999) 164.
- 142) J.-I. Chen, R. Chareonsak, V. Puengpipat, S. Marturunkakul, *J. Appl. Polym. Sci.*, **74** (1999) 1341.
- 143) R. L. Ballard, J. P. Williams, J. M. Njus, B. R. Kiland M. D. Soucek, *Eur. Polym. J.*, **37** (2001) 381.
- 144) R. A. Sailer, M. D. Soucek, *Prog. Org. Coat.*, **33** (1998) 36.
- 145) R. A. Sailer, J. R. Wegner, G. J. Hurtt, J. E. Janson, M. D. Soucek, *Prog. Org. Coat.*, **33** (1998) 117.
- 146) T. Sugama, N. Carciello, S. L. Rast, *Thin Solid Films*, **258** (1995) 174.
- 147) H. Ni, W. J. Simonsick, J.A. D. Skaja, J. P. Williams, M. D. Soucek, *Prog. Org. Coat.*, **38** (2000) 97.
- 148) Y. Liu, D. Sun, H. You, J. Shik Chung, *Appl. Surf. Sci.*, **246** (2005) 82.
- 149) K.-H. Haas, *Adv. Eng. Mater.*, **2** (2000) 571.
- 150) A. J. Atanacio, B. A. Latella, C. J. Barbe, M. V. Swain, *Surf. Coat. Technol.*, **192** (2005) 354.

- 151) M. L. Zheludkevich, R. Serra, M. F. Montemor, I. M. Miranda Salvado, M. G. S. Ferreira, *Surf. Coat. Technol.*, **200** (2006) 3084.
- 152) J. Malzbender, G. de With, *Adv. Eng. Mater.*, **4** (2002) 296.
- 153) H. K. Schmidt, *J. Sol–Gel Sci. Technol.*, **8** (1997) 557.
- 154) A. N. Khramov, V. N. Balbyshev, N. N. Voevodin, M. S. Donley, *Prog. Org. Coat.*, **47** (2003) 207.
- 155) H. Schmidt, *Appl. Organomet. Chem.*, **15** (2001) 331.
- 156) H. Schmidt, *Macromol. Symp.*, **159** (2000) 43.
- 157) H. Schmidt, G. Jonschker, S. Goedicke, M. Mennig, *J. Sol–Gel Sci. Technol.*, **19** (2000) 39.
- 158) C. Sanchez, G. J. De, A. A. Soler-Illia, F. Ribot, D. Grosso, *C. R. Chim.*, **6** (2003) 1131.
- 159) N. N. Voevodin, V. N. Balbyshev, M. Khobaib, M. S. Donley, *Prog. Org. Coat.*, **47** (2003) 416.
- 160) M. S. Donley, V. N. Balbyshev, A. J. Vreugdenhil, *J. Coat. Technol.*, **73** (2001) 915.
- 161) A. J. Vreugdenhil, V. N. Balbyshev, M. S. Donley, *J. Coat. Technol.*, **73** (2001) 35.
- 162) L. S. Kasten, V. N. Balbyshev, M. S. Donley, *Prog. Org. Coat.*, **47** (2003) 214.
- 163) V. N. Balbyshev, K. L. Anderson, A. Sinsawat, B. L. Farmer, M. S. Donley, *Prog. Org. Coat.*, **47** (2003) 337.
- 164) J. Jang, H. Park, *J. Appl. Polym. Sci.*, **83** (2002) 1817.
- 165) A. Cellot, S. de Monredon, L. Delattre, L. Gue'neau, F. Ribot, C. Sanchez, *J. Mater. Chem.*, **12** (2002) 2396.
- 166) E. Scolan, C. Sanchez, *Chem. Mater.*, **10** (1998) 3217.

- 167) M. Chatry, M. In, M. Henry, C. Sanchez, J. Livage, *J. Sol–Gel Sci. Technol.*, **2** (1994) 233.
- 168) S. Forster, M. Antonietti, *Adv. Mater.*, **10** (1998) 195.
- 169) E.W. Brooman, *Metal Finishing*, **100** (2002) 42.
- 170) M.L. Zheludkevich, D.G. Shchukin, K.A. Yasakau, H. Mohwald, M.G.S. Ferreira, *Chem. Mater.*, **19** (2007) 402.
- 171) E.V. Skorb, D. Fix, D.V. Andreeva, H. Mohwald, D.G. Shchukin, *Adv. Funct. Mater.*, **19** (2009) 2373
- 172) F. Maia, J. Tedim, A.D. Lisenkov, A.N. Salak, M.L. Zheludkevich, M.G.S. Ferreira, *Nanoscale*, **4** (2012) 1287
- 173) D.G. Shchukin, M.L. Zheludkevich, H. Mohwald, *J. Mater. Chem.*, **16** (2006) 4561.
- 174) D. G. Shchukin, M.L. Zheludkevich, K. Yasakau, S. Lamaka, M.G.S. Ferreira, H. Mohwald, *Adv. Mater.*, **18** (2006) 1672.
- 175) W. Feng, S.H. Patel, M.Y. Young, J.L. Zunino III, M. Xanthos, *Adv. Polym. Technol.*, **26** (2007) 1.
- 176) S.J. Davis, J.F. Watts, *J. Mater. Chem.*, **6** (1996) 479.
- 177) N.A. Allsop, M.R. Bowditch, N.F.C. Glass, A.E. Harris, P.M. O'Gara, *Thermochim. Acta*, **315** (1998) 67
- 178) E.N. Brown, S.R. White, N.R. Sottos, *J. Mater. Sci.*, **39** (2004) 1703.
- 179) Ashok Kumar, L.D. Stephenson, J.N. Murray, *Prog. Org. Coat.*, **55** (2006) 244.
- 180) S.R. White, N.R. Sottos, P.H. Geubelle, J.S. Moore, M.R. Kessler, S.R. Sriram, E.N. Brown, S. Viswanathan, *Nature*, **409** (2001) 794.
- 181) M.W. Keller, S.R. White, N.R. Sottos, *Adv. Funct. Mater.*, **17** (2007) 2399.

- 182) D.G. Shchukin, H. Mohwald, *Small*, **3** (2007), 926.
- 183) D.G. Shchukin, H. Mohwald, *Chem. Commun.* **47** (2011) 8730.
- 184) D. Borisova, H. Mohwald, D.G. Shchukin, *ACS Nano*, **18** (2011) 1939.
- 185) M. Kendig, M. Hon, L. Warren, *Prog. Org. Coat.*, **47** (2003) 183.
- 186) K.T. Kim, S.A. Meuwissen, R.J.M. Nolte, J.C.M. van Heste, *Nanoscale*, **2** (2010) 844.
- 187) K.T. Kim, J.J.L.M. Cornelissen, R.J.M. Nolte, J.C.M. van Heste, *Adv. Mater.*, **21** (2009) 2787.
- 188) K. Yoshimatsu, B.K. Lesel, Y. Yonamine, J.M. Beierle, Y. Hoshino, K.J. Shea, *Angew. Chem. Int. Ed.*, **51** (2012) 2405.
- 189) M.M. Rahman, A. Elaissari, *J. Mater. Chem.*, **22** (2012) 1173.
- 190) H. Cho, J. Bae, V.K. Garripelli, J.M. Anderson, H.W. Jun, S. Jo, *Chem. Commun.*, **8** (2012) 6043.
- 191) D. Klinger, K. Landfester, *Soft Matter*, **7** (2011) 1426.
- 192) J.W. Chung, K. Lee, C. Neikirk, C.M. Nelson, R.D. Priestly, *Small*, **8** (2012) 1693.
- 193) K. Kulbaba, A. Cheng, A. Bartole, S. Greenberg, R. Resendes, N. Coombs, A. Safa-Sefat, J.E. Greedan, H.D.H. Stover, G.A. Ozin, *J. Am. Chem. Soc.*, **124** (2002) 12522.
- 194) S. Bhattacharya, F. Eckert, V. Boyko, A. Pich, *Small*, **3** (2007) 650.
- 195) M.L. Zheludkevich, R. Serra, M.F. Montemor, M.G.S. Ferreira *Electrochem. Commun.* **7** (2005) 836.
- 196) M.L. Zheludkevich, R. Serra, M.F. Montemor, K. Yasakau, I.M.M. Salvado, M.G.S. Ferreira, *Electrochim. Acta*, **51** (2005) 208.
- 197) D.V. Andreeva, D.G. Shchukin, *Materials Today*, **11** (2008) 24.



- 198) S.H. Sonawanec, B.A. Bhanvasea, A.A. Jamali, S.K. Dubeya, S.S. Kalea, D.V. Pinjari, R.D. Kulkarni, P.R. Gogate, A.B. Pandit, *Chem. Eng. J.*, **189** (2012) 464.
- 199) S. Bohm, H. N. McMurray, S. M. Powell D. A. Worsley, *Mater. Corros.*, **52** (2001) 896.
- 200) M.L. Zheludkevich, J. Tedim, M.G.S. Ferreira, *Electrochim. Acta* **82** (2012) 314.
- 201) R. G. Buchheit, H. Guan, S. Mahajanam, F. Wong, *Prog. Org. Coat.*, **47** (2003) 174.
- 202) G. Williams, H.N. McMurray, *Electrochem. Solid-State Lett.*, **7** (2004) B13.
- 203) M.L. Zheludkevich, S.K. Poznyak, L.M. Rodrigues, Kuzentsova, T. Hack, L.F. P. Dick, T. Nunes M.G.S. Ferreira, *Corros. Sci.*, **52** (2010) 602.
- 204) S.K. Poznyak, J. Tedim, L.M. Rodrigues, A.N. Salak, M.L. Zheludkevich, L.F. P. Dick, M.G.S. Ferreira, *ACS Appl. Mater. Interfaces*, **10** (2009) 2353.
- 205) J. Tedim, S.K. Poznyak, A. Kuzentsova, D. Raps, T. Hack, M.L. Zheludkevich, M.G.S. Ferreira, *ACS Appl. Mater. Interfaces*, **2** (2010) 1528.
- 206) J. Tedim, A. Kuznetsova, A.N. Salak, F. Montemor, D. Snihirova, M. Pilz, M.L. Zheludkevich, M.G.S. Ferreira, *Corros. Sci.*, **55** (2012) 1.
- 207) G. Williams, H.N. McMurray, *Electrochem. Solid-State Lett.* **6** (2003) B9.
- 208) D. Fix, D. Andreeva, Y. Lvov, D. Shchukin, H. Mohwald, *Adv. Funct. Mater.*, **19** (2009) 1720.
- 209) D. Shchukin, H. Mohwald, *Adv. Funct. Mater.*, **17** (2007) 1451.
- 210) E. Abdullayev, R. Price, D. Shchukin, Y. Lvov, *ACS Appl. Mater. Interfaces*, **1** (2009) 1437.
- 211) Y. Lvov, D. Shchukin, H. Mohwald, R. Price, *ACS Nano*, **2** (2008) 814.

- 212) V. Vergaro, E. Abdullayev, Y. Lvov, A. Zeitoun, R. Cingolani, S. Leporatti, **11** (2010) 820.
- 213) E. Abdullayev, Y. Lvov, *J. Mater. Chem.*, **20** (2010) 6681.
- 214) A. Joshi, E. Abdullayev, A. Vasiliev, O. Volkova, Y. Lvov, *Langmuir*, **29** (2013) 7439.
- 215) D.G. Shchukin, S.V. Lamaka, K.A. Yasakau, M.L. Zheludkevich, M.G.S. Ferreira, H. Mohwald, *J. Phys. Chem. C*, **112** (2008) 958.
- 216) D. Borisova, D. Akcakayiran, M. Schenderlein, H. Mohwald, D.G. Shchukin, *Adv. Funct. Mater.*, **23** (2013) 3799.
- 217) A. Latnikova, D. Grigoriev, M. Schenderlein, H. Möhwald, D. Shchukin, *Soft Matter* **8** (2012) 10837.
- 218) M. F. Haase, D. O. Grigoriev, H. Möhwald, D. G. Shchukin, *Adv. Mater.*, **24** (2012) 2429.
- 219) D. Borisova, H. Mohwald, D.G. Shchukin, *ACS Appl. Mater. Interfaces*, **4** (2012) 2931.
- 220) M. J. Hollamby, D. Borisova, H. Mohwald, D.G. Shchukin, *Chem. Commun.*, **48** (2012) 115.
- 221) K.A. Yasakau, J. Tedim, M.L. Zheludkevich, R. Drumm, M. Shem, M. Wittmar, M. Veith, M.G.S. Ferreira, *Corros. Sci.*, **58** (2012) 41.
- 222) E.D. Mekeridis, I.A. Kartsonakis, G.C. Kordas, *Prog. Org. Coat.*, **73** (2012) 142.
- 223) A.C. Balaskas, I.A. Kartsonakis, L.A. Tziveleka, G.C. Kordas, *Prog. Org. Coat.*, **74** (2012) 418.
- 224) I.A. Kartsonakis, A.C. Balaskas, E.P. Koumoulos, C.A. Charitidis, G.C. Kordas, *Corros. Sci.*, **57** (2012) 30.

- 225) I.A. Kartsonakis, A.C. Balaskas, E.P. Koumoulos, C.A. Charitidis, G.C. Kordas, *Corros. Sci.* **65** (2012) 481.
- 226) I.A. Kartsonakis, E.P. Koumoulos, A.C. Balaskas, G.S. Pappas, C.A. Charitidis, G.C. Kordas, *Corros. Sci.*, **57** (2012) 56.
- 227) G.L. Li, Z. Zheng, H. Mohwald, D.G. Shchukin, Silica/Polymer Double-Walled, *ACS Nano*, **7** (2013) 2470.
- 228) V.B. Singh, A. Gupta, *Indian. J. Chem. Technol.*, **12** (2005) 347.
- 229) U. Kamachi Mudali, H. S. Khatak, R. K. Dayal, J. B. Gnanamoorthy, *J. Mater. Eng. Perform.* **2** (1993) 135.
- 230) N. Parvathavarthini, R.K. Dayal, G.B. Gnanamoorthy, *Corrosion*, **52** (1996) 540.
- 231) N.F. Fahim, T. Sekino, *Chem. Mater.*, **21** (2009) 1967.
- 232) Y. Zhu, J. Shi, H. Chen, W. Shen, X. Dong, *Microporous Mesoporous Mater.*, **84** (2005) 218.
- 233) P. M. Arnal, C. Weidenthaler, F. Schuth, *Chem. Mater.*, **18** (2006) 2733.
- 234) P. M. Arnal, M. Comotti, F. Schuth, *Angew. Chem. Int. Ed.*, **45** (2006) 8224.
- 235) S. Tang, X. Huang, X. Chen, N. Zheng, *Adv. Funct. Mater.*, **20** (2010) 2442.
- 236) W. Stober, A. Fink, E. Bohn, *J. Colloid. Interface Sci.* **26** (1968) 62.
- 237) P.R.P. Rodrigues, A.H.P. Andrade, S.M.L. Agastinho, *Br. Corros. J.*, **33** (1998) 211.
- 238) K. Babic-Samardzija and N. Hackerman, *J. Solid State Electrochem.*, **9** (2005) 483.
- 239) A. Popova and M. Christov, *Corros. Sci.*, **48**, (2006) 3208.
- 240) K.F. Khaled, *Electrochim. Acta.*, **53** (2008) 3484.

- 241)P. G. Cao, J. C. Yao, J. W. Zheng, R. A. Gu, and Z. Q. Tian, *Langmuir*, **18**, (2002) 100.
- 242)B. Sanyal, *Prog. Org. Coat.* **9** (1981)165.
- 243)H. A. Mohamed, A. A. Farag, B. M. Badran, *J. Appl. Polym. Sci.* **117** (2010) 1270.
- 244)K. A. Yasakau, M. L. Zheludkevich, O. V. Karavai, M. G. S. Ferreira, *Prog. Org. Coat.*, **63** (2008) 352.
- 245)S. Brunauer, P.H. Emmett, E. Teller, *J. Am. Chem. Soc.*, **160** (1938) 309.
- 246)E.P. Barrett, L.G. Joyner, P.P. Halenda, *J. Am. Chem. Soc.*, **73** (1951) 373.
- 247)ASTM D3359- “*Standard Test Method for Measuring Adhesion by Tape Test*”
- 248)ATM B117- “*Standard Practice for operating Salt Spray (Fog) Apparatus*”
- 249)M.L. Zheludkevich, K.A. Yasakau, A.C. Bastos, O.V. Karavai, M.G.S. Ferreira, *Electrochem. Commun.* **9** (2007) 2622.
- 250)D. Loveday, P. Peterson, and B. Rodgers, *J. Coating Technol.*, **8** (2004) 46.
- 251)D. Loveday, P. Peterson, and B. Rodgers, *J. Coating Technol.*, **1** (2004)88.
- 252)D. Loveday, P. Peterson, and B. Rodgers, *J. Coating Technol.*, **3** (2005) 22.
- 253)F. Geenen, “*Characterization of Organic Coatings with Impedance Measurements; A study of Coating Structure, Adhesion and Under film Corrosion*”, Ph-D Thesis, TU Delft 1990.
- 254)[http://www.gamry.com/App\\_Notes/EIS\\_Primer/EIS\\_Primer\\_2007.pdf](http://www.gamry.com/App_Notes/EIS_Primer/EIS_Primer_2007.pdf), “*Basics of Electrochemical Impedance Spectroscopy*”, Gamry Instruments, Inc.
- 255)Appliocation Note AC-1, “*Basics of Electrochemical Impedance Spectroscopy*”, Princeton Applied Research.
- 256)V.G. Dheshmane, Y.G. Adewuyi, *Microporous and Mesoporous Mater.*, **148** (2012) 88.

- 257)J.S. Reddy, A. Sayari, *Catalysis Letters*, **38** (1996) 219.
- 258)F. Schuth, *Chem. Mater.*, **13** (2001) 3184.
- 259)M. S.Wong, D. M. Antonelli, J.Y. Ying, *Nanostruct. Mater.*, **9** (1997) 165.
- 260)G. Duan, C. Zhang, A. Li, X. Yang, L. Lu, X. Wang, *Nanoscale Res. Lett.*, **3**, (2008) 118.
- 261)F. Caruso, A. Caruso, H. Mohwald, *Science*, **282** (1998) 1111.
- 262)X.W. Lou, L.A. Archer, Z. Yang, *Adv. Mater.*, **20** (2008) 3987.
- 263)Y. Sun, B. Mayers, Y. Xia, *Adv. Mater.*, **15** (2003) 641.
- 264)K. An, T. Hyeon, *Nano Today*, **4** (2009) 359.
- 265)G.J.D. Soler-Illia, C. Sanchez, B. Lebeau, J. Patarin, *Chem. Rev.*, **102** (2002) 4093
- 266)A. Taguchi, F. Schuth, *Microporous Mesoporous Mater.*, **77** (2005) 1.
- 267)X. Fang, X. Zhao, W. Fang, C. Chen, N. Zheng, *Nanoscale*, **5** (2013) 2205.
- 268)P. Bouvier, G. Lucazeau, *J. Phys .Chem. Solids*, **61** (2000) 569.
- 269)N. Sandhyarani, G. Skanth, S. Brerchmans, V. Yengnaraman, T. Pradeep, *J. Colloid. Interf. Sci.* **209** (1999) 154.
- 270)G. Wang, A. Harrison, X. Li, G. Whittaker, J. Shi, X. Wang, H. Yang, P. Cao, Z. Zheng, *J. Raman Spectrosc.* **35** (2004) 1016.
- 271) R. Woods, G.A. Hope, K. Watling, *J. Appl. Electrochem.* **30** (2000) 1209.
- 272)C.J. Lee, S.Y. Lee, M.R. Karim, M.S. Lee, *Spectrochim. Acta A*, **68** (2007) 1313.
- 273)V.V. Srdic´, M. Winterer, A. Mo¨ller, G. Miehe, H.Hahn, *J. Am. Ceram. Soc.*, **84** (2001) 2771.
- 274)R. K. Shervedani , A. H. Mehrjardi, M. K. Babadi, *Electrochim. Acta*, **52** (2007) 7051.

- 275)J. Wang, B. Zeng, C. Fang, X. Zhou, *Anal. Sci.*, **16** (2000) 457.
- 276)M. Oshawa, W. Suetaka, *Corros.Sci.*, **19** (1979) 709.
- 277)C.T. Kresge, M.E. Leonowicz, W.J. Roth, J.C. Vartuli, J.S. Beck, *Nature*, **359** (1992) 710.
- 278)W.H. Zhang, J. Lu, B. Han, M. Li, J. Xiu, P. Ying, C. Li, *Chem. Mater.*, **14** (2002) 3413.
- 279)L.X. Zhang, W.H. Zhang, J.L. Shi, Z.L. Hua, Y.S. Li, J.N. Yan, *Chem. Commun.*, **2** (2003) 210.
- 280)C. Yang, H. Sheu, K. Chao, *Adv. Funct. Mater.*, **12** (2002) 143.
- 281)M. Vallet-Regí, A.Ra´mila, R.P. del Real, J. Pe´rez-Pariente, *Chem. Mater.*, **13** (2001) 308.
- 282)H. Hata, S. Saeki, T. Kimura, Y. Sugahara, K. Kuroda, *Chem. Mater.*, **11** (1999) 1110.
- 283)C. Tourne´-Pe´teilh, D.A. Lerner, C. Charnay, L. Nicole, S. Be´gu, J.-M. Devoisselle, *Chem. Phys. Chem.*, **3** (2003) 281.
- 284)K.A. Fisher, K.D. Huddersman, M.J. Taylor, *Chem. Eur. J.* **9** (2003) 5873.
- 285)A. Ra´mila, B. Mun˜oz, J. Pe´rez-Pariente, M. Vallet-Regi´i, *J. Sol–Gel Sci. Technol.*, **26** (2003) 1199.
- 286)B. Mun˜oz, A. Ra´mila, J. Pe´rez-Pariente, I. Di´az, M. Vallet-Regi´, *Chem. Mater.*, **15** (2003) 500.
- 287)C. Tourne´-Pe´teilh, D. Brunel, S. Be´gu, B. Chicle, F. Fajula, D.A. Lerner, J.-M. Devoisselle, *New J. Chem.*, **27** (2003) 1415.
- 288)C.-Y. Lai, B.G. Trewyn, D.M. Jeftinija, K. Jeftinija, S. Xu, S. Jeftinija, V.S.-Y. Lin, *J. Am. Chem. Soc.*, **125** (2003) 4451.
- 289)N.K. Mal, M. Fujiwara, Y. Tanaka, *Nature*, **421** (2003) 350.

- 290) N.K. Mal, M. Fujiwara, Y. Tanaka, T. Taguchi, M. Matsukata, *Chem. Mater.*, **15** (2003) 3385.
- 291) A.L. Doadrio, E.M.B. Sousa, J.C. Doadrio, J. Pe ´rez-Pariente, I. Izquierdo-Barba, M. Vallet-Regi ´, *J. Control. Release*, **97** (2004) 125.
- 292) P. Horcajada, A. Ra ´mila, I. Diaz, J. Pe ´rez-Pariente, M. Vallet-Regi ´, *Micropor. Mesopor. Mater.* **68** (2004) 105.
- 293) M. Chen, L. Wu, S. Zhou, B. You, *Adv. Mater.*, **18** (2006) 801.
- 294) W. Zhao, M. Lang, Y. Li, L. Li, J. Shi, *J. Mater. Chem.*, **19** (2009) 2778
- 295) J. Yang, J. U. Lind, W. C. Trogler, *Chem. Mater.*, **20** (2008) 2875
- 296) H. Blas, M. Save, P. Pasetto, C. Boissiere, C. Sanchez, B. Charleux, *Langmuir*, **24** (2008) 13132.
- 297) G. Qi, Y. Wang, L. Estevez, A. K. Switzer, X. Duan, X. Yang, E. P. Giannelis, *Chem. Mater.*, **22** (2010) 2693.
- 298) Y. Yamada, M. Mizutani, T. Nakamura, K. Yano, *Chem. Mater.*, **22** (2010) 1695.
- 299) J. Wang, Q. Xiao, H. Zhou, P. Sun, Z. Yuan, B. Li, D. Ding, A. C. Shi, T. Chen, *Adv. Mater.*, **18** (2006) 3284.
- 300) M. Yu, H. Wang, X. Zhou, P. Yuan, C. Yu, *J. Am. Chem. Soc.*, **129** (2007) 14576.
- 301) Z. Feng, Y. Li, D. Niu, L. Li, W. Zhao, H. Chen, L. Li, J. Gao, M. Ruan, J. Shi, *Chem. Commun.*, **23** (2008), 2629.
- 302) J. G. Wang, F. Li, H. J. Zhou, P. C. Sun, D. Ding, T. H. Chen, *Chem. Mater.*, **21** (2009) 612.
- 303) L. Han, P. Xiong, J. F. Bai, S. Che, *J. Am. Chem. Soc.*, **133** (2011) 6106.

- 304) K. S. W. Sing, D. H. Everett, R. A. W. Haul, L. Moscou, R. A. Pierotti, J. Rouquerol, T. Siemieniewska, *Pure & Appl. Chem.* **57** (1985) 603.
- 305) Vaughn M. Nace, *Nonionic surfactants: Polyoxyalkoxylene block copolymers*, *Surfactant Science series* Vol.60, 1996, Marcel Dekker Inc., New York
- 306) G.K. Mor, K. Shankar, M. Paulose, O.K. Varghese, C.A. Grimes, *Nano. Lett.*, **6** (2006) 215.
- 307) G.K. Mor, M.A. Carvalho, O.K. Varghese, M.V. Pishko, C. A. Grimes, *J. Mater. Res.*, **19** (2004) 628.
- 308) D.V. Bavykin, A.A. Lapkin, J.M. Friedrich, F.C. Walsh, *J. Phys. Chem. B*, **109** (2005) 19422.
- 309) Y.Y. Song, F. Schmidt-Stein, S. Bauer, P. Schmuki, *J. Am. Chem. Soc.*, **131** (2009) 4230.
- 310) P. Roy, S. Berger, P. Schmuki, *Angew. Chem. Int. Ed.*, **50** (2011) 2904.
- 311) E. Panaitescu, C. Ritcher, L. Menon, *J. Electrochem. Soc.*, **155** (2008) E7.
- 312) V. Zwillling, E. Darque-Certti, A. Boutry-Forveille, D. David, M.Y. Perrin, M. Aucouturier, *Surf. Interface Anal.*, **27** (1999) 629.
- 313) S.P. Albu, A. Ghicov, J.M. Macak, R. Hahn, P. Schmuki, *Nano Lett.*, **7** (2007) 1286.
- 314) G.K. Mor, O.K. Varghese, M. Paulose, C.A. Grimes, *Adv. Funct. Mater.*, **15** (2005) 1291.
- 315) H. Tsuchiya, J.M. Macak, L. Taveira, E. Balaur, A. Ghicov, K. Sirotna, P. Schmuki, *Electrochem. Commun.*, **7** (2005) 576.
- 316) A. Ghicov, H. Tsuchiya, J.M. Macak, P. Schmuki, *Electrochem. Commun.*, **7** (2005) 505.



- 317) N.F. Fahim, T. Sekino, M.F. Morks, T. Kusunose, *J. Nanosci. Nanotechnol.*, **9** (2009) 1803.
- 318) R. Hahn, J.M. Macak, P. Schmuki, *Electrochem. Commun.*, **9** (2007) 947.
- 319) N.K. Allam, C.A. Grimes, *J. Phys. Chem. C*, **111** (2007) 13028.
- 320) E. Chassaing, F. Basile, G. Lorthioir, *J. Less-Common Met.*, **68** (1979) 153.
- 321) X. Chen and S. S. Mao, *Chem. Rev.*, **107** (2007) 2891.
- 322) W. F. Zhang, Y. L. He, M. S. Zhang, Z. Yin, and Q. Chen, *J. Phys. D: Appl. Phys.*, **33**, (2000) 912.
- 323) U. Balachandran and N. G. Eror, *J. Solid State Chem.*, **42** (1982) 276.
- 324) F. Torney, B. G. Trewyn, V. S. Y. Lin, and K. Wang, *Nature Nanotech.*, **2** (2007) 295.
- 325) J. Lu, M. Liong, J. I. Zink, F. Tamanoi, *Small*, **3** (2007) 1341
- 326) J. Jiang, G. Oberdorster, P. Biswas, *J. Nanopart. Res.*, **11** (2009) 77.
- 327) M. G. Pujar, C. R. Das, S. Thirunavukkarasu, U. Kamachi Mudali, A. K. Bhaduri, J. Brijitta, B. V. R. Tata, *Mater. Chem. Phys.*, **130** (2011) 536.
- 328) C. H. Hsu F. Mansfeld, *Corrosion*, **57** (2001) 747.
- 329) P. C. Banerjee R. K. S. Raman, *Electrochim. Acta.*, **56** (2011) 3790.
- 330) W. Trabelsi, P. Cecilio, M. G. S. Ferreira, M. F. Montemor, *Prog. Org. Coat.*, **54** (2005) 276.
- 331) F. J. Maile, T. Schauer, C. D. Eisenbach, *Prog. Org. Coat.*, **38** (2000) 111.
- 332) Z. Wicks, *Organic Coatings: Science and Technology*, 3<sup>rd</sup> Edition, Wiley-Interscience, Hoboken, 2007.
- 333) S.B. Lyon, G.E. Thompson, J.B. Johnson, *Materials evaluation using wet-dry mixed salt spray test*, ASTM STP 1134, 20-31, (1992).

- 334) D. Neff, L. Bellot-Gurlet, P. Dillmann, S. Reguer, L. Legrand, *J. Raman Spectrosc.*, **37** (2006) 1228.
- 335) L. Bellot-Gurlet, D. Neff, S. Reguer, J. Monnier, M. Saheb, P. Dillmann, *J. Nano Res.*, **8** (2009) 147.
- 336) L. S. Cividanes, D. D. Brunelli, E. F. Antunes, E. J. Corat, K. K. Sakane, G. P. Thim, *J. Apply. Poly. Sci.*, **127** (2012) 544.
- 337) H. Vaskova, V. Kresalek, Raman spectroscopy of epoxy resin cross linking, In: 13th WSEAS International Conference. Island (Spain); Lanzarote, Canary; (2011) 357.